

**CHARACTERIZATION OF HARMONIC PHASE MRI:
THEORY, SIMULATIONS, AND APPLICATIONS**

by

Vijay Parthasarathy

A dissertation submitted to The Johns Hopkins University in conformity with the
requirements for the degree of Doctor of Philosophy.

Baltimore, Maryland

April, 2006

© Vijay Parthasarathy 2006

All rights reserved

Abstract

Motion of a human heart is a sensitive indicator of heart disease. Magnetic resonance (MR) tagging has emerged as the gold standard for visualizing the detailed motion of a beating heart. Motion is measured from tagged MR images using Harmonic Phase (HARP)-MRI, which is an image processing method that allows for fast automated processing of tagged MR images. This dissertation investigates the ability of HARP-MRI to provide significant diagnostic information. The goal of this dissertation is to translate this qualitative clinical question into quantifiable engineering problems and to solve them.

In this dissertation, we characterize both the optimal and peak performances of HARP-MRI. We study the optimal performance by investigating HARP-MRI's accuracy and by deriving protocols for its optimal use. We characterize the peak performance of HARP-MRI by deriving three performance measures: ranges of measurable motion, spatial resolution, and the ability to detect small abnormalities. We also explain the presence of artifacts in the outputs of HARP-MRI, and propose an algorithm to reduce them. Finally, we use our understanding of peak performance of HARP-MRI to adapt it to track the motion of the tongue during speech.

Advisor: Dr. Jerry Prince. Additional readers: Dr. Trac Tran, Dr. Sanjeev Khudanpur, and Dr. Maureen Stone

This thesis is dedicated with love and respect to

Amma and Appa

Acknowledgements

I am greatly indebted to my research advisor and my mentor Dr. Jerry Prince. His guidance and insights have had untold value in shaping the course of my research. The confidence and trust that he has had on me were instrumental in my successful completion of the PhD program. He has been very patient with me all these years, and I am very grateful for that. He has been an exceptional personal mentor, and an exemplary role model for me in many aspects. Everything that I know about research, writing, time and people management have been his lessons. After all these years of working with him, I have begun to realize how blessed I should have been to have had him as my advisor.

I would like to thank Dr. Maureen Stone, our collaborator at the University of Maryland Dental School. I would like to acknowledge her guidance in my research and her financial support in pursuing my research goals. I am grateful to Dr. Trac Tran and Dr. Sanjeev Khudanpur for patiently reading my thesis and giving me feedback. I am grateful to Dr. Moriel NessAiver for his help in collecting data for my research.

It has been an honor to be a part of the Image Analysis and Communications Lab. I would like to thank all former and current members of this lab for making this a wonderful place as it is right now. Dr. Chenyang Xu was my first mentor in the lab. Dr. Nael Osman has been of great support, especially in the beginning phases of my thesis work. The research in this thesis is based on the work done by Nael. Dr. Maryam Rettmann has been a wonderful friend all these years and I will always cherish the refreshing discussions that I have had with her. Dr. Smita Sampath has been a great friend and I would like to thank her for support, both personal and academic. It is a privilege to have shared the lab space with Drs. Xiao Han and Xiaodong Tao; two exceptionally talented people from whom I learnt a lot. I would like to thank Dr. Dzung Pham for his guidance. I also greatly appreciate

the help of Dr. William Kerwin during the initial parts of my research. Dr. Dugyu Tosun has been a very nice colleague and taught me MATLAB, which later became one of the mainstays of my research. Dr. Krishnakumar Ramamurthi has been a good friend and I thank him for all the discussions we have had, which included cricket, music, photography, and south Indian movies. Harsh Agarwal and Xiaofeng Liu have been great people to work with. Prasanna Anbazhagan has been a very good friend. I also want to thank members of the Vocal Tract Visualization lab; Dr. Emi Murano, Dr. Marianne Pouplier, and Dr. Melissa Epstein have been wonderful to work with. I also want to thank Ahmed Fahmy and Dr. Li Pan for their help during the initial phase of my thesis work.

I especially want to thank Laura Libertini for her dedication in making our lab function very smoothly. A special thanks goes to my colleague and friend Khaled Abd-Elmoniem. The discussions that I have had with Khaled have been of great assistance to my research. He has been an exceptional person to work with and has had a calming influence on me. My deepest gratitude goes to Aaron Carass, who has not only been a great colleague, but also an exceptionally good friend. I am greatly indebted to him for his support in stressful times and thank him for lending a very patient ear to all that I have to say.

My gratitude goes to the staff of the Department of Electrical Engineering, especially Ms. Gail O'Connor. I also want to thank the entire Johns Hopkins Community, especially the people in the security department. A special thanks to Dr. Nick Arrindell, director of the Office of International Students.

My friends here in Baltimore have been like family to me. They have made my stay in Baltimore worth cherishing all my life. I doubt if I would have been able to complete my PhD without their support. My biggest and heart-felt gratitude goes to my close friend and roommate for many years Dr. Karthik Viswanathan. His friendship has made me a better person. The discussions with him have been refreshing, relaxing, and thought-provoking. Another exceptional friend is Dr. Arun Sripathi. His friendship has made me see life differently. Interactions with Arun regarding Indian history and culture have influenced me in profound ways. Another person who deserves a special mention is my close cricketer friend Dr. Amit Paliwal. His understanding of me is exceptional. I can never forget the long walking discussions we have had on cricket and career choices. His wife Vaishali Paliwal has also been a great friend. I also want to thank Dr. Veera Venkataramani, who

has been an exceptional friend. I also want to acknowledge Prabhakar Kadavasal whose friendship has been invaluable.

I should have been blessed to have such a exceptional set of friends. I want to acknowledge the friendship of Venk Kambhampati, a fellow cricketer and refreshingly funny person. Subbu Ramakrishnan has been constant source of encouragement and support. Dr. Amitabha Bagchi has been a great friend and a mentor in many ways. I will always cherish my interactions with Dr. Sathya Sriram, Kapil and Divya Gupta, Dr. Sachin and Neha Gangaputra, Swati Mehta, and Uttara Sengupta. Each of them has enriched my life experiences in many different ways.

Many of my memorable moments in Baltimore have been through my involvement with various student groups. Each of these moments have not only resulted in personally enriching experiences, but also in memorable friendships. My interactions with members of Season for Non-violence are invaluable. I will always cherish the time I spent with Dr. Jaya Jaya, Anubha Dhasmana, Ameet Jain, and Sushruti Santhanam. Nirveek Bhattacharjee of the Association of India's Development taught me the importance of perseverance.

Out of all the groups that I have been involved in, if there is one group that has literally kept my sanity over the years, it is the Johns Hopkins Cricket Club. I am deeply grateful to some wonderful cricketer friends, who have been great people to interact both on and off the field. I would like to acknowledge the friendship of Vivek Haridas, Himanshu Saraf, Dr. Sameer Jadhav, Puneet Bajpai, and Dr. Utkarsh Sharma.

Apart from my friends in Baltimore, I would like to acknowledge the love and support of many of my high school and college friends, especially Dr. Ganesh Balasubramaniam, Kamesh Narasimhan, Bharathan Aravamudhan, Ganesh Natarajan, Sardal Gautham, and Padmanabhan Kothandapani. A special thanks goes to Karthik's aunt Indru, whose energy and enthusiasm has been a source of inspiration for me.

Finally, I owe a special thanks to my uncle Vasudevan Narayanan, my aunt Prema Vasudevan, and my cousin Prasanna Vasudevan. Their affection and encouragement have guided many actions in my life. I am also greatly indebted to the love and support of my extended family, especially my grandparents. I would like to express my deepest gratitude to my sister Priya for her love and affection and all that she has done for me all these years. Finally I want to thank my mother Vijayalakshmi and my father Parthasarathy whose love,

dedication, understanding, and emotional support will go unmatched. All through these years they have been there whenever I have needed them. Irrespective of their state of mind, they have shared a laughter when I was happy, and have cried with me when I was sad. They have been concerned about my progress more than I was. I owe this thesis to their unflinching support, unconditional love, unwavering discipline, and their unshakable faith in God. I dedicate this thesis to them.

Contents

Abstract	ii
Acknowledgements	iv
List of Tables	xiv
List of Figures	xv
Abbreviations	xxiii
1 Introduction	1
1.1 Clinical and Economical Significance	1
1.2 The Human Heart	3
1.3 Cardiovascular disease	4
1.4 Methods for diagnosing CAD	5
1.4.1 Gold standard in CAD diagnosis	5
1.4.2 Imaging techniques	5
1.4.3 Regional ventricular function	6
1.5 MR Tagging	8
1.6 HARP-MRI and Clinical Challenges	9
1.7 Thesis Contributions	10
1.7.1 Optimal parameter selection for HARP-MRI	10
1.7.2 Performance limits of HARP-MRI	10
1.7.3 Artifact reduction in HARP-MRI strain maps	11
1.7.4 Pushing the envelope of HARP-MRI: tracking the tongue during speech	12
1.8 Organization	12
2 Background	14
2.1 Introduction	14

2.2	MR Physics	14
2.2.1	Microscopic perspective	16
2.2.2	Macroscopic perspective	17
2.2.3	Precession and Larmor frequency	18
2.2.4	Transverse and longitudinal magnetization	19
2.2.5	Free induction decay	20
2.2.6	Relaxation	20
2.2.7	Rotating frame of reference	21
2.2.8	Excitation	22
2.3	Physics of Tagging	23
2.3.1	1-1 SPAMM pulse sequence	23
2.3.2	Sinusoidal modulation of magnetization	25
2.3.3	Tag Fading	28
2.3.4	CSPAMM	28
2.4	Image Acquisition	30
2.5	Encoding tissue motion using tagging	32
2.6	Harmonic Phase (HARP) MRI	36
2.6.1	HARP Tracking	38
2.6.2	Eulerian Strain Calculation	39
2.7	Miscellaneous Background Material	42
2.7.1	VENC and DENSE	42
2.7.2	Nyquist Sampling	42
2.7.3	Spatial resolution	43
3	Optimizing HARP-MRI using Simulations	45
3.1	Introduction	45
3.2	HARP Vector Field	46
3.3	Sources of Error in HARP-MRI	48
3.3.1	Voxel-based Errors	48
3.3.2	Spectral Interference	50
3.3.3	Image Noise	51
3.4	Methods	52
3.4.1	Simulation Methodology	53
3.4.2	Relative Magnitude of Error Sources	56
3.4.3	Optimization Methodology	56
3.4.4	Invivo Data	59
3.5	Results	59
3.5.1	Relative Magnitude of Error Sources	59
3.5.2	A typical optimality analysis	60
3.5.3	Organization of Results	62
3.5.4	Analysis 1.1: Selection of Optimal Filter Size for {27 39} and 7 mm tag separation	62

3.5.5	Analysis 1.2: Variation of Optimal Filter Sizes with LV size for 7 mm tag separation	68
3.5.6	Analysis 2: Selection of Optimal Tag Separation for a mid-systolic strain	68
3.5.7	Comparison with Region-based Cost Function	71
3.5.8	In vivo Results	74
3.5.9	HARP-MRI Optimization Toolbox	75
3.6	Discussion	76
3.6.1	Relation to previous work	76
3.6.2	General trends in the simulated data	76
3.6.3	Trade-offs and comparing radial and circumferential strains	77
3.6.4	Performance of tracking	78
3.6.5	Imaging considerations	79
3.6.6	Minor (avoidable) sources of errors	80
3.7	Summary and Recommendations	80
3.8	Forward Pointers: What is coming up next?	82
4	Communications Theory Framework	84
4.1	AM-FM Signals	84
4.2	Instantaneous Frequency and Fourier Frequency	88
4.3	Monocomponent signals	88
5	Dynamic Range of HARP-MRI	90
5.1	Introduction	90
5.2	Dynamic Range of Tissue Point Tracking	92
5.3	Dynamic Range of Eulerian Strain	93
5.3.1	A Key Approximation	93
5.3.2	Dynamic Range of Eulerian Strain: Impulse In or Out	94
5.4	Results and Discussion	95
5.4.1	Feasible region in “strain-rotation” space	95
5.4.2	Computer Simulated Phantom	97
5.4.3	Cardiac MR data	98
5.4.4	Loss of Dynamic Range: Extreme case of IVPD	100
5.5	Conclusion	100
6	Spatial Resolution of HARP-MRI	102
6.1	Introduction	102
6.2	Traditional MR Resolution	103
6.3	An Alternate Definition of Resolution	104
6.3.1	Breakdown of Assumptions	105
6.3.2	Clinical Perspective of Resolution	105
6.4	Strain Resolution	107

6.4.1	Edge Model Simulation	107
6.4.2	Filtering	109
6.4.3	Results and Discussion	109
6.5	Tracking Resolution	112
6.5.1	Methods	114
6.5.2	Results	114
6.5.3	Discussion	116
6.6	Clinical Impact of the Resolution findings	117
6.6.1	Subendocardial Abnormalities	117
6.6.2	Functional Border Zone	117
6.6.3	Reconstruction of Smooth Strain Transitions	119
6.7	Summary	119
7	Detectability of HARP-MRI	121
7.1	Introduction	121
7.2	Theory	122
7.2.1	Contrast–Detail Analysis	122
7.2.2	System description of HARP-MRI	123
7.2.3	Detectability: Limited by Noise	123
7.2.4	Interplay between different sources of error	125
7.3	Methods	125
7.3.1	Contrast–Detail Simulations	125
7.3.2	Quantification of Noise	128
7.4	Results	130
7.4.1	Reconstructed Contrast	130
7.4.2	Noise Quantification	130
7.4.3	Detectability Results	130
7.5	Discussion	132
7.5.1	Clinical Studies	132
7.5.2	Assumptions and Simplifications	132
7.6	Conclusion	133
8	Artifacts in HARP-MRI Strain Maps	134
8.1	Introduction	134
8.2	Hypothesis	136
8.3	Mechanism of Production of Artifacts	137
8.3.1	Computation of Eulerian Strain	137
8.3.2	Errors in HARP phase and phase gradients	139
8.3.3	Combination of phase gradient and directional vectors	141
8.3.4	Why is RS worse than CS?	142
8.4	Artifact reduction	143
8.4.1	Previous work	143

8.4.2	Weighted Phase Unwrapping and Smoothing	144
8.4.3	Results	146
8.5	Discussion	147
8.6	Summary	148
9	Tracking Tongue Motion using HARP-MRI	149
9.1	Introduction	150
9.1.1	Background	151
9.1.2	Why HARP-MRI on the Tongue?	152
9.2	Stretching the Envelope	153
9.2.1	Dynamic range	154
9.2.2	Spatial resolution	155
9.2.3	Artifacts and detectability	156
9.2.4	Tongue, heart, and gold standards	156
9.3	Methods	157
9.3.1	MR imaging methods	157
9.3.2	HARP methods	162
9.4	HARP-MRI Results and Visualization	165
9.4.1	Principal strains and velocities	165
9.4.2	Strain in the lines of action of muscles	167
9.5	Discussion	169
9.5.1	Temporal resolution	169
9.5.2	Robustness of tracking	169
9.5.3	Corroboration of motivations	170
9.6	Summary	170
10	Conclusions and Future Work	172
10.1	Optimal performance of HARP-MRI	172
10.1.1	Key results	173
10.1.2	Future research	173
10.2	Peak Performance of HARP-MRI	174
10.2.1	Key Results	174
10.2.2	Future research	176
10.3	Artifacts in HARP	177
10.3.1	Key results	177
10.3.2	Future research	178
10.4	Tracking tongue motion using HARP-MRI	178
10.4.1	Key results	179
10.4.2	Future research	179
10.5	Publications	181
10.6	Software contributions	181
10.7	Closing Remarks	182

A Spatiotemporal Visualization of the Tongue Surface using Ultrasound and Kriging	183
A.1 Introduction	183
A.2 Methods	189
A.2.1 Data acquisition	189
A.2.2 Automatic contour extraction and tracking	189
A.2.3 Introduction to Kriging	189
A.2.4 Derivation of Kriging solution	190
A.2.5 Kriging algorithm	192
A.2.6 Connection to thin-plate splines	193
A.2.7 SURFACES software	194
A.3 Results and Applications	197
A.3.1 Application to speech data	197
A.3.2 Application to swallowing data	197
A.4 Validation of contour extension	199
A.4.1 Validation materials and methods	199
A.4.2 Validation results	199
A.4.3 Discussion	202
A.5 Conclusion	203
Bibliography	205
Vita	223

List of Tables

1.1	Description of different types of heart disease	4
3.1	Methods ‘at-a-glance’	52
3.2	True (simulated) strains and displacements for LV size of {27 39} for different values of ε . The value of ε determines the strain at different stages in the cardiac cycle.	57
3.3	Sources of error and their contributions to overall error. ‘0’ and ‘1’ represents the absence and presence of the respective sources of error.	59
3.4	Results organization at-a-glance. Key: V: Variable, OV: Optimizing variable,	62

List of Figures

1.1	Six leading causes of death in high-mortality developing countries, 2001. <i>Source: Data reproduced from a report titled “2003 World Health Report” produced by the World Health Organization</i>	2
1.2	Leading causes of death for all ages in the United States. <i>Source: Data reproduced from a report titled “Health, United States 2005” produced by the National Center for Health Statistics (Key: CLRD is Chronic Lower Respiratory Disease)</i>	2
1.3	(a) Schematic showing heart anatomy (source:www.zygote.com), (b) Detailed schematic of the short axis cross section.	3
1.4	Time series of cine MR images showing the motion of the heart during systole. Note the difference in the myocardial wall thickness between (a) end-diastole and (b)end-systole.	7
1.5	Time series of tagged MR images showing the motion of the heart during systole. Notice the bending of tag lines as the myocardial wall expands radially.	8
2.1	Overview of the background chapter. The right panel show representative results at each stage.	15
2.2	Microscopic magnetic moments align themselves either in the parallel or in the anti-parallel orientation, with a slight preference towards the parallel orientation, thereby resulting in a small magnetization M	17
2.3	Precession of bulk magnetization and orthogonal components of magnetization	19
2.4	MRI scanner showing the fixed or laboratory frame of reference	21
2.5	RF excitation: In the fixed frame, M follows a helical path towards the transverse plane. In the rotating frame, the effect of B_0 is not felt, and excitation is seen as direct tipping towards the transverse plane.	22
2.6	1-1 SPAMM tagging pulse sequence and behavior of five spins spaced equally apart on the x' axis.	24

2.7	1-1 SPAMM tag pattern (a) right after application of tags , and (b) during relaxation	27
2.8	CSPAMM tag pattern (a) right after application of tags , and (b) during relaxation	29
2.9	(a) Gradient echo pulse sequence and (b) corresponding k-space trajectory .	31
2.10	Tagged images in two orthogonal tag directions at two different time frames in systole. Note the increased radial thickening and circumferential shortening in the mid-systolic time frame.	35
2.11	Top right: Vertically tagged CSPAMM image. Top right: Spectrum with the HARP-MRI bandpass filter as white circle. Bottom left: HARP Magnitude image, $D(\mathbf{x}, t)$, Bottom right: HARP phase $\phi(\mathbf{x}, t)$ masked using the magnitude image.	37
2.12	Left: Trajectories of tissue points on the myocardium overlayed on HARP phase image. Right: A track zoomed in; Progression of colors from violet-blue-green-yellow-orange-red indicates the motion through different time frames.	38
2.13	Radial and circumferential directions	41
2.14	Radial and Circumferential Strains	41
2.15	Cartesian k-space sampling pattern	43
3.1	Intra-voxel phase dispersion: (a) Phases dispersed within a voxel (b) Net magnitude and HARP value	48
3.2	Partial Volume Effect: (a) Pixel partly occupied by tissue and blood, showing the individual HARP vectors, (b) the net HARP vector	49
3.3	Spectrum of a CSPAMM tagged image showing the HARP-MRI bandpass filter. Arrows indicate regions of the harmonic peak most corrupted by spectral interference	51
3.4	(a) Simulated image of the underlying magnetization. The central donut shaped is simulated and background is obtained from an in-vivo image, (b) Image of the underlying magnetization horizontally tagged using CSPAMM protocol.	53
3.5	Cost functions for (a) circumferential strain and radial strain, (b) HARP angle and tracking displacement for $\text{CNR} = 5$, $\varepsilon = -15\%$, LV size of {27 39}, and a tag separation of 7mm.	60
3.6	Optimal filter diameters for (a) circumferential strain, (b) radial strain, and (c) tracking displacement for LV size 27,39, tag separation of 7mm, and for 2 CNRs 5 (circle) and 20 (square). Note that the tracking displacements are plotted on the radial strain axis to facilitate comparison between strain and tracking, and also to indicate the position of the heart in the cardiac cycle. .	63

3.7	Minimum pixel-wise RMS errors corresponding to the optimal filter sizes are given in (a)–(c) for three layers of the myocardium. The corresponding signed errors are given in (d)–(f). The errors are calculated for CNR 5, LV size of {27 39}, and a tag separation of 7 mm.	65
3.8	Data acquisition sizes plotted as a function of tag separation for (a) circumferential strain, (b) radial strain, and (c) tracking displacement, for LV size of {27 39} as function of tag separation. The data acquisition size of radial strain is more than circumferential strain and tracking.	67
3.9	A comparison of minimum errors in radial strain across (a) hearts with different wall thickness, but the same inner radii and (b) hearts with different inner radii, but the same wall thickness. Corresponding optimal filter diameters are shown in (c) and (d). While hearts with the same wall thickness have similar optimal values, the hearts with different wall thickness have markedly different optimal filter sizes and minimum errors.	69
3.10	Optimal tag separations as a function of CNR for hearts with different wall thicknesses.	70
3.11	Schematic showing the three layers and eight octants of the myocardium . .	72
3.12	Top row shows the ratio of minimum RMS error calculated region-wise and pixel-wise. The bottom row shows a ratio of the optimal filter sizes calculated in the two cases. The errors in the region-wise measurements are always less than pixel-wise. And the optimal filter sizes in region-wise are always greater than or equal to their pixel-wise counterparts.	73
3.13	The first column shows the corresponding strains using a filter sizes that is smaller than optimal. The second column shows the strains using a filter size that is larger than optimal. The third column are the estimates of circumferential strain (top row) and radial strain (bottom row) using the optimal filter. The third column offers a compromise between the blurring and loss of accuracy in column 1, and spoke-like artifacts and loss of precision in column 2. All strain maps are plotted on the same color scale. .	74
4.1	An example of an AM-FM signal.	85
4.2	(a) Three parts of the object have different amplitudes but same IF. (b) shows a horizontal profile across the image in (a). (c) Three parts of the object have different amplitudes and different IF as well. (d) shows a horizontal profile across image in (c)	87
5.1	FastHARP k-space acquisition.	91
5.2	Top left figure shows a tag pattern at time t_n . Bottom left figure shows the tag pattern translated to the left by half the tag separation. Right panel shows the corresponding HARP phase. The star represents the initialization point at time t_{n+1} and shaded circle represent two equally close probable solutions to HARP tracking.	92

5.3	Schematic of the bandpass filter in frequency domain	94
5.4	Feasible region in strain-rotation space. White regions represent IFs that are within the dynamic range of HARP	96
5.5	(a) Tagged image (b) Feasible regions in space domain: white regions indicate regions where IF inside the bandpass filter. (c) Reconstructed tagged image; note the blurring in regions where the tags bend a lot (d) Reconstructed magnitude image (e) Phase estimate; Note the phase cuts in regions corresponding to regions of blurred tags.	97
5.6	(a) Actual tagged image (b) White region denote feasibility regions predicted by theory (c) reconstructed real image; Note the loss in contrast in the regions blacked out in (b), (d) reconstructed HARP magnitude (e) phase image; Note the inaccurate estimates of harmonic phase in regions blacked out in (b)	99
5.7	Phases dispersed within a voxel such that the net signal from the voxel is zero as shown in (b). This is the limit of dynamic range	100
6.1	(a,b) Single delta function input and Impulse response showing the FWHM (c,d) Two delta functions more than FWHM apart and the delta functions resolved in the output (e,f) Two delta function inputs exactly FWHM apart; only one lobe is seen since the system cannot resolve the two delta functions.	104
6.2	Myocardial showing transmural defect and subendocardial defect. Notice how the transitions in strain are in one case along the direction of tags (transmural) and in the other case, orthogonal to the directions of tags (subendocardial)	106
6.3	Top row: Vertically tagged image with (a) edge in strain in the direction of tags, (b) edge in strain orthogonal to the tags. Bottom row: Magnitude image with corresponding edges in magnitude	108
6.4	(a) strain responses,(b) magnitude responses, (c) profiles along the lines marked.	110
6.5	Top row: Real part of the complex harmonic images. Bottom row: The behavior of HARP vectors within a interface voxel. The dispersion of vectors causes an error due to IVPD.	111
6.6	Top row shows the HARP magnitude images for the edges along the tags and the edges across the tags. Note the loss of signal at a few regions along the interface, where the dispersion of IF within a voxel results in zero net signal in the voxel. The corresponding HARP values shown in the bottom row are erroneous as well.	113
6.7	Tracking error for different displacement conditions. Note the very steep interface between the areas of zero error and non-zero error. This implies that the resolution of tracking is not limited by the bandpass filer. The profiles are shown in the bottom row.	115

6.8	Top: Transmural and subendocardial injuries shown with respective functional border zones. Bottom: Strain reconstruction of smooth edge.	118
7.1	Input/Output diagrams: Top block diagram models the no noise case. The sources of output noise in this case are the systematic noise sources like spectral interference and Gibbs ringing. The bottom block diagram shows the noise case, where input noise affects the estimates as well.	123
7.2	(a) True strain profile with infarcted region with 0% strain, with the background compression with -15% strain; (b) Reconstructed strain using HARP-MRI with no input noise. (c) Reconstructed strain with CNR = 5; (d) Reconstructed strain with CNR = 2. Note how the noise overwhelms the contrast in (c) and (d).	124
7.3	(a) Input strain pattern in the left right direction. The background tissue is under a state of -15% compression and the infarcted tissue has 0% strain. The encoding of this left-to-right compression is shown in the vertically tagged image in (c). (b) Strain pattern in the up down direction, with the similar strain pattern except that the tissue is stretched by +15% in the vertical direction. The encoding of this vertical expansion is shown in the horizontally tagged image in (d). Figs. (e) and (f) show the resulting strain maps produced using HARP-MRI	126
7.4	(a) and (b) show the noise tagged images without the infarcted region. (c) and (d) show the corresponding strain maps. A 1 cm × 1 cm square is selected to compute the error to derive the noise threshold. The bottom figure shows the histogram of the noise in strain.	129
7.5	Plots (a) and (b) show the results from the contrast-detail experiment, plot (c) show the result from the noise quantification experiment. Plots (a), (b), and (c) are used to derive detectability limits for horizontal and vertical tags as shown in plots (d) and (e)	131
8.1	Example of circumferential strain map showing accentuated zebra artifacts.	135
8.2	(a) True circumferential strain map (b) Reconstructed HARP strain map with coverage ratio 0.5 and no noise (c) Reconstructed HARP strain map with a bigger filter of coverage ratio 0.9 (d) Reconstructed strain map with noise added with CNR 10	136
8.3	(a) True radial strain map (b) Reconstructed HARP strain map with coverage ratio 0.5 and no noise (c) Reconstructed HARP strain map with a bigger filter of coverage ratio 0.9 (d) Reconstructed strain map with noise added with CNR 10. Note the gross errors that occurs due to IVPD and PVE	137
8.4	(a,b) Vertical and horizontal tagged images, (c,d) Corresponding HARP phases, (e,f) circumferential and radial strain maps	138

8.5	Left panel: (La, Lb) Errors in HARP phase. (Lc, Ld, Le, Lf) Errors in HARP phase derivatives. Right panel: (Ra, Rb) shows quiver plots of the circumferential and radial strains in a sector of the myocardium. (Rc, Rd, Re, Rf) show the x and y components of the directionality vectors. Bottom: Errors in computed strain	140
8.6	Regions 1 and 2 encode radial motion. In Regions 3 and 4 the radial motion is orthogonal to the tagging direction and hence not encoded. Regions 1 and 2 have high error due to IVPD and PVE, Regions 3 and 4 have negligible IVPD and PVE errors.	142
8.7	(a) HARP Magnitude image (b) HARP phase unmasked (c) Binary mask generated by thresholding the magnitude image (d) masked HARP image (e) demodulated HARP image (f) unwrapped HARP phase	145
8.8	First column shows the strain maps from the no-smoothing case. Second and third columns show the strain maps from the 1-D smoothing and the proposed methods respectively. The two row represent two different time frames. The second row is later in systole and hence has more strain than strain maps in the first row.	146
8.9	Comparison of preservation of transmural gradient.	147
9.1	(a) Schematic of anatomy of the midsagittal cross section (b) static MRI of midsagittal slice with coronal and axial slice marked.	150
9.2	cine-MRI series for utterance of /i/-/u/	151
9.3	Left: Tagged MRI image of a retroflex ‘r’, especially made speakers of Tamil, a south Indian language. (Image courtesy: Dr. Maureen Stone, Univ. of Maryland, Dental school). Right: Schematic of how the dynamic range of HARP is exceeded due to this extreme motion.	154
9.4	Left is a picture of a tongue model showing the muscles in the midsagittal slice. While the genioglossus muscle is homogenous in the midsagittal slice, the off-sagittal slice (right) shows a high degree of muscle interdigitation.	155
9.5	Images (a) and (b) form a pair of vertically tagged CSPAMM images with phase shifted tags, and (c) is the MICSР combination of images (a) and (b). Images (d) and (e) form a pair of horizontally tagged CSPAMM images and (f) is the MICSР combination of images (d) and (e). Intensity of MICSР images (c) and (f) have been thresholded for better visualization of the tags.	158
9.6	(a, b, c) show one time frame from cine-MRI acquisition of midsagittal, and coronal, and axial slices respectively. The region of interest around the tongue is marked.	160
9.7	(a) MICSР trinary display (b) Overlay of MICSР checkerboard and untagged image; Note the better edge definition near the tongue tip in the overlay image	161

9.8	(a) Horizontally tagged image produced by MICSР combination, (b) magnitude of its Fourier spectrum with the HARP bandpass filter, (c) harmonic magnitude image, and (d) harmonic phase image	162
9.9	(a,b) show the principal strains in the midsagittal slice from time frame 9 and 10 respectively. Blue denotes compression, red denotes expansion. (d,e) shows the principal strains for the same two time frames for a coronal slice. (c,f) show the velocities of tissue points between time frames 9 and 10. Note the inhomogeneity of strains and velocities corresponding to actions of a muscles or a combination of a set of muscles	166
9.10	Tracking of the lines, hypothesized as a parts of genioglossus. All time frames from 12-frame cine-series set of utterance of /disuk/ are shown.	168
10.1	Finite element meshes manually superimposed on checkerboard images. Figs. (a) and (b) show initial and deformed time frame, respectively.	180
A.1	(a) Midsagittal tongue schematic with superimposed surface contours points. (tip of tongue on the right). (b) Midsagittal ultrasound image with tracked surface contour points (c) Sequence of tongue contours in time overlaid on each other. (d) Waterfall display of contours for the word ‘golly’.	185
A.2	Comparison of Kriging with inverse square distance weighting and cubic splines: (a) Extrapolation using cubic splines and inverse square distance weighting; note the swing in the case of cubic spline(cross) and the unsmooth contour produced by inverse square distance weighting methods. (b) Extrapolation using Kriging; note the improved performance of Kriging at the back of the tongue.	187
A.3	(a) A snapshot of the SURFACES software and (b) a spatiotemporal surface of the word ‘golly’.	195
A.4	Applications of SURFACES: (a) Overlay of 2 spatiotemporal tongue surfaces of the word ‘golly’. Mesh surface was spoken in ‘upright’ position and the filled surface in ‘supine’ surface. (b) Difference between the two spatiotemporal surfaces in form of an image. (c) Spatiotemporal surface of a swallow. The water is contained in front of tongue, then propelled backwards, followed by tongue surface elevation after the water’s passage. (d) Visualization of the swallow as an image with colors denoting height. Note in (c) and (d) the black lines separate the regions that contain real data from the regions that contain extrapolated data.	198
A.5	Validation experiment: The center line along with the lower lines (gray) on either side is the actual tongue contour. The edges are artificially cut in order to see how Kriging performs in extrapolation. The last data points on the edge of the contour are represented as black circles. The extrapolated lines (blue) are the contours that Kriging estimated. The difference between the blue and green regions is measured as error.	200

A.6 Validation Results: Mean errors in estimation when the length of tongue contour cut is (a) 1 mm (b) 3 mm (c) 5 mm and (d) 10 mm. The error bars represent standard deviation. The x-axis denotes distance along the surface of the tongue, not the distance along the spatial axis (x-axis). The red curves denote the errors in the front of the tongue and blue denotes the errors in the back of the tongue.	201
A.7 Maximum Errors: Maximum expected errors in estimation as a function of the length of tongue cut.	202

Abbreviations

2-D Two-dimensional

3-D Three-dimensional

AM-FM Amplitude Modulation-Frequency Modulation

CAD Coronary Artery Disease

CNR Contrast to Noise Ratio

CS Circumferential Strain

CSPAMM Complementary Spatial Modulation of Magnetization

DENSE Displacement Encoded Stimulated Echo

ECG Electrocardiogram

FastHARP Fast Harmonic Phase

FBZ Functional Border Zone

FFT Fast Fourier Transform

FOV Field of View

FWHM Full Width at Half Maximum

HARP Harmonic Phase

IF Instantaneous Frequency

IVPD Intra Voxel Phase Dispersion

LV Left Ventricle

MICSR Magnitude Image CSPAMM Reconstruction

MRI Magnetic Resonance Imaging

PC Phase Contrast

PVE Partial Volume Effect

RF Radio Frequency

RMS Root Mean Square

RS Radial Strain

SPAMM Spatial Modulation of Magnetization

VENC Velocity Encoding

Chapter 1

Introduction

“[We] cannot afford to lose sight of the growing social and economic threats posed by cardiovascular diseases. The population-wide application of existing knowledge has the potential to make a major, rapid, and cost-effective contribution to the prevention and control of cardiovascular disease.”

— From the 2003 World Health Report published by the World Health Organization

1.1 Clinical and Economical Significance

In 2003, the World Health Organization listed cardiovascular diseases as one of the three neglected global epidemics [Fig. 1.1]. In the United States, the Centers for Disease Control and Prevention report that over 927,000 Americans die of cardiovascular diseases each year; amounting to 1 death every 34 seconds [1]. Heart disease is a major component of cardiovascular diseases accounting for nearly 40% of all deaths in the United States [Fig. 1.2], more than 70 million Americans (over 25% of the population) live with cardiovascular disease. The cost of cardiovascular diseases in the United States is estimated to be \$394 billion in 2005, which includes health care expenditures and lost productivity from death and disability [1].

The focus of this dissertation is Harmonic Phase Magnetic Resonance Imaging (HARP-MRI), a medical imaging technique used for the diagnosis of heart disease. In recent years, HARP-MRI has shown great promise for accurate and reliable detection of precursors for heart attacks. In this dissertation, we will address some of the technical challenges for HARP-MRI to become a part of routine clinical use. We begin this dissertation with a

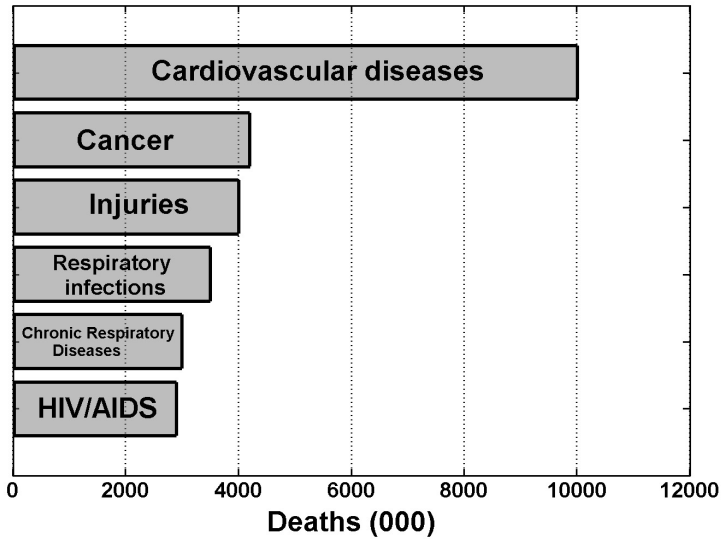
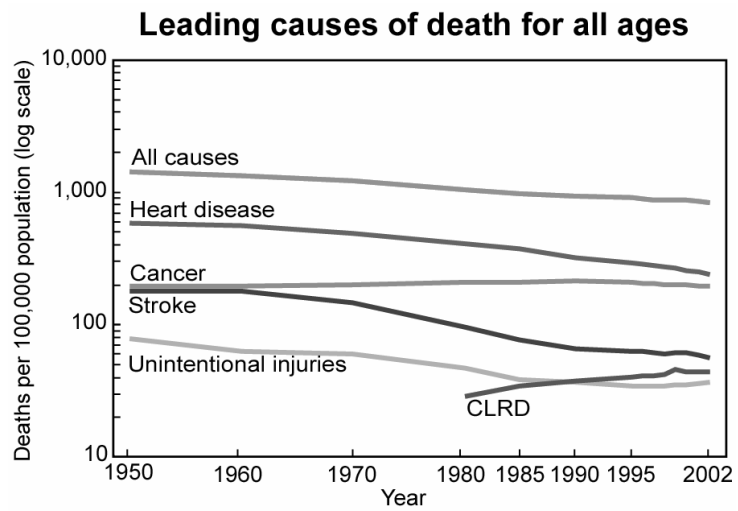


Figure 1.1: Six leading causes of death in high-mortality developing countries, 2001.

Source: Data reproduced from a report titled “2003 World Health Report” produced by the World Health Organization



SOURCE: Centers for Disease Control and Prevention, National Center for Health Statistics, *Health, United States, 2005*, figure 29.

Figure 1.2: Leading causes of death for all ages in the United States.

Source: Data reproduced from a report titled “Health, United States 2005” produced by the National Center for Health Statistics (Key: CLRD is Chronic Lower Respiratory Disease)

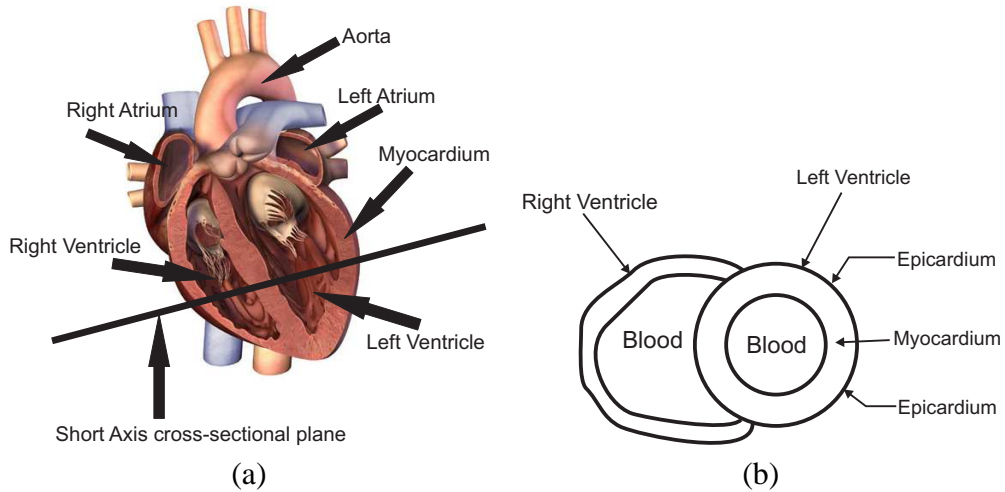


Figure 1.3: (a) Schematic showing heart anatomy (source:www.zygote.com), (b) Detailed schematic of the short axis cross section.

brief explanation of the physiology and diseases of the heart. We will discuss different diagnostic techniques that are currently used to detect heart disease, and explain the role of HARP-MRI among these diagnostic procedures. Finally, we will explain the challenges and contributions of this dissertation.

1.2 The Human Heart

The human heart is slightly larger than a human fist and it beats about 80,000 to 100,000 times a day, pumping approximately 2,000 gallons of blood per day. The human heart is made of specialized muscle fibers capable of sustaining continuous beating. It consists of four chambers: right atrium, right ventricle (RV), left atrium, and left ventricle (LV) [see Fig. 1.3(a)]. For the heart to function properly, the four chambers must beat in a synchronized manner during a heartbeat. A heartbeat consists of two stages: diastole and systole. During diastole, the two ventricles get filled with blood from the respective atria. While the RV gets filled with oxygen-depleted blood from the right atrium, the LV gets filled with oxygen-rich blood from the left atrium. During systole, the muscles of the ventricle contract to push the blood out. The oxygen-depleted blood from the RV is pumped out into the lungs for re-oxygenation, and the oxygen-rich blood in the LV is pumped out

Table 1.1: Description of different types of heart disease

Name	Description
Coronary artery disease	Blocking of arteries supplying blood to the heart
Cardiomyopathy	Disease of the heart muscle
Pericardial disease	Disease of the sac that encases the heart
Valvular heart disease	Diseases of the valves between heart chambers
Heart failure	Inability of heart to pump enough blood to organs

to the entire body through the aorta [54]. Because of its crucial role to supply blood to the entire body, the left ventricle is the largest cavity in the heart with a thick muscular wall called the myocardium [see Fig. 1.3(a)].

Imaging the heart can be done in several different ways in many different cross-sectional views. The black line in Fig. 1.3(a) shows one such cross-section called the short-axis cross-section. In this cross-section, the left ventricle appears like a donut [Fig. 1.3(b)]. The myocardium is sandwiched between two boundary layers on either side; the inner layer is called endocardium and the outer layer is called the epicardium. The right ventricle appears as a semicircular ring, and the myocardial wall corresponding to the right ventricle is much thinner than that of the left ventricle. This schematic of a short axis slice in Fig. 1.3(b) will be useful while correlating the anatomy of the heart with features in the MRI images.

1.3 Cardiovascular disease

Cardiovascular disease refers to any disorder in the cardiovascular system. The cardiovascular system consists of the heart (*cardio*) and the blood vessels (*vascular*). Heart disease specifically refers to the disorders of the heart. Table 1.1 shows the different types of heart diseases and a brief description of each of them.

Coronary artery disease (CAD) is the most common type of heart disease [75]. The coronary arteries are responsible for providing oxygen and nutrients to the muscles of the heart. In CAD, the coronary arteries get progressively narrower due to a build up of plaque, which is a deposit of fat, cholesterol, calcium, and other cellular sludge from the blood. This gradual build-up of plaque is called atherosclerosis and sometimes referred to as hard-

ening of the arteries. This results in reduced supply of blood and oxygen to the heart, resulting in a condition called cardiac ischemia. If ischemia is severe or lasts too long, it can cause heart attack (myocardial infarction), which can eventually lead to death of the heart tissue.

1.4 Methods for diagnosing CAD

1.4.1 Gold standard in CAD diagnosis

The first set of diagnostic tests for CAD include physical examination, blood tests, and electrocardiogram tests (ECG) with and without tread-mill stress [24]. Depending on the initial diagnosis, one or more diagnostic tests might be prescribed for a more detailed analysis of the symptoms. These diagnostic tests include several non-invasive techniques based on medical imaging and an invasive technique called catheterization. Catheterization, also called coronary angiography or angiogram, is the gold standard in the diagnosis of CAD. During catheterization, a small tube called the catheter is inserted into the artery and a dye is injected into it. As the dye flows through the coronary arteries, X-rays images are acquired, which clearly show the narrowing and blockage of the arteries. Depending on the severity of the blockage, the cardiologist recommends either medications with changes in diet and life style or surgical procedures to improve the flow of blood. These surgical procedures, known as re-vascularization procedures, include bypass surgery and angioplasty. Both catheterization and revascularization are expensive procedures.

1.4.2 Imaging techniques

There are a suite of non-invasive imaging techniques that can be used to detect and characterize CAD. Broadly speaking, there are three approaches to detect CAD non-invasively. The first approach is to directly image the anatomy of the coronary arteries and to look for blockages. Computed tomography (CT) and MR-based angiography are examples of this approach. The second approach is called the perfusion test. This test detects the amount of blood flow in the heart muscle. The premise of the perfusion test is that narrowing of

the coronary artery causes a reduction in blood flow in the heart, which can be detected. Thallium-based nuclear imaging and MR-based perfusion tests are examples of this approach. The third approach is based on measuring the motion of the heart. This approach is based on the fact that the lack of blood supply to the heart muscle deprives it of much-needed oxygen. This in turn affects its ability to contract efficiently, and hence affects its motion. Ultrasound-based echocardiography and MRI provide direct measurements of the motion of the heart. Since the motion of the heart directly correlates to its functioning of the LV as a pump, heart motion is also called ventricular function.

In this research, we contribute to the third approach. Left ventricular function is known to be a sensitive indicator of ischemia and infarction [100, 99, 87, 123]. The measures of ventricular function can be of two types: global measures and regional measures. Global measures of ventricular function include ejection fraction (blood pumped / blood contained) and left ventricular volume. These global measures provide useful information about overall ability of the heart to pump blood. They, however, do not localize the specific regions of the heart affected by CAD [55]. Ischemia and infarction caused by CAD are known to be localized to certain regions of the heart, depending on the coronary artery that is affected. Therefore, regional ventricular functional measures are better than the global measures in the detection and characterization of certain heart diseases [77]. In this research, we focus on measuring regional ventricular function.

1.4.3 Regional ventricular function

Regional ventricular function can be measured using two modalities: ultrasound-based echocardiography (called “echo” for short) and MRI. Currently, echocardiography is the most widely used modality to measure regional ventricular function. Images from echo, however, do not contain detailed motion of the myocardium and are noisy. In spite of these drawbacks, echocardiography is the most popular among cardiologists. This is because echo is affordable, portable, simple to learn and use, and provides instant images — all hallmarks of a successful diagnostic imaging system in clinical cardiology. These hallmarks will be revisited when we discuss the clinical usability of HARP-MRI.

MRI has become a gold standard for the measuring ventricular function [32, 25, 34].

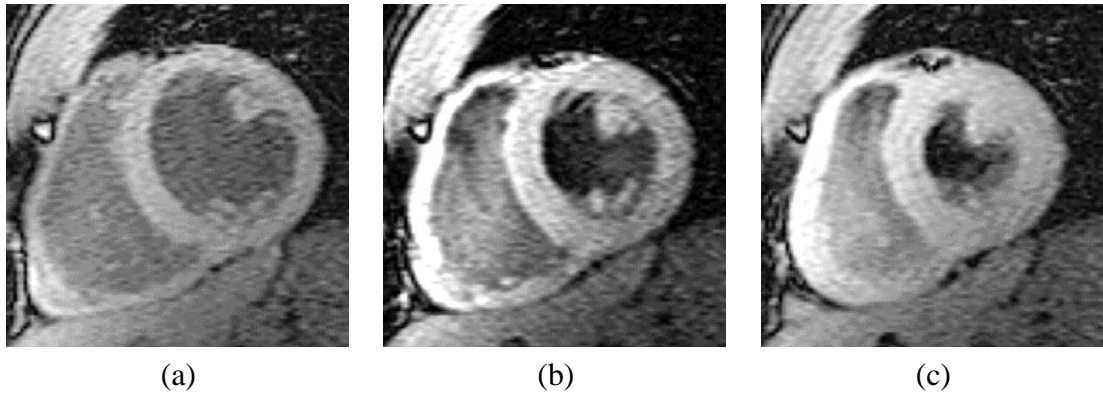


Figure 1.4: Time series of cine MR images showing the motion of the heart during systole. Note the difference in the myocardial wall thickness between (a) end-diastole and (b) end-systole.

Regional ventricular function can be measured using different MR techniques, which can again be split into two categories: 1) techniques that measure the motion of only the boundaries of the myocardium and 2) methods that measure the motion of tissue within the boundaries of the myocardium.

Cine-MRI falls within the first category. Fig. 1.4 shows a series of cine-MR images of a short axis slice. The images show the progression of the heart's motion during systole. The donut-shaped object in the middle of the image is the left ventricle [compare with Fig. 1.3(b)]. In Fig. 1.4(a), the LV is filled with blood and the myocardial wall is thin. As systole progresses [Fig. 1.4(b) and Fig. 1.4(c)] and as the heart pumps out blood, the myocardium becomes thicker and the blood pool becomes smaller. Using cine-MRI, the boundaries of the myocardium can be tracked and regional ventricular function can be measured as the wall thicknesses all along the circumference of the heart [139]. These measurements, however, do not take into account the variation in heart's motion in between the endocardium and the epicardium. These variations can be important to visualize in CAD [84, 49].

The second category of MR based methods, providing ventricular function measurement within the two boundaries of the myocardium, include velocity-encoded (VENC) imaging [125, 124, 159], displacement-encoded stimulated echo imaging(DENSE) [8, 72], and MR tagging [14, 13, 165]. Each of these three methods — VENC, DENSE, and MR

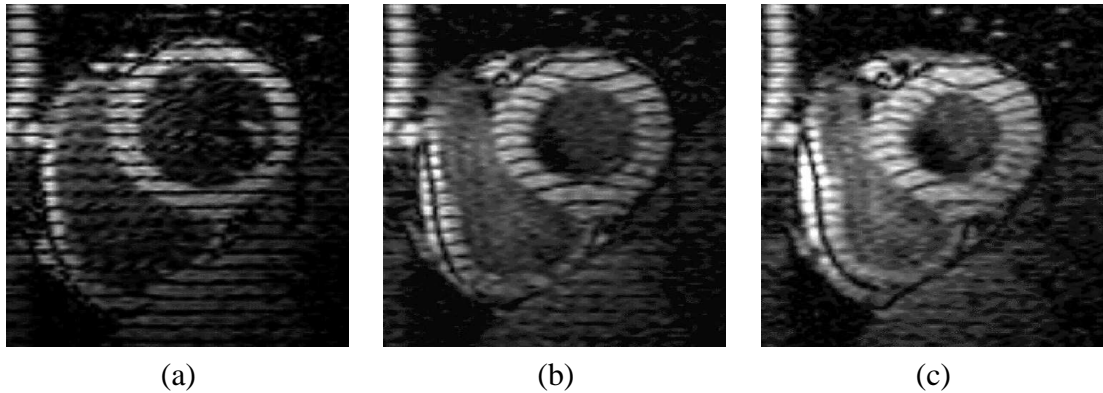


Figure 1.5: Time series of tagged MR images showing the motion of the heart during systole. Notice the bending of tag lines as the myocardial wall expands radially.

tagging — encode and image tissue motion. VENC encodes tissue velocity while DENSE and MR tagging encode tissue displacement. All three approaches convert motion information into measurements of mechanical strain, which serves as an indicator of ventricular function. These three approaches are explained in detail in Chapter 2, after aspects of MR physics are provided for reference.

1.5 MR Tagging

This dissertation concerns MR tagging. In MR tagging, tissue magnetization is spatially modulated in a periodic fashion just before the heart tissue begins to contract. This modulation appears as tag lines on the image, and these tag lines move along with the tissue. Fig. 1.5 shows a series of tagged MR images with horizontal tags. The motion corresponds to the same systolic motion of the heart as seen in cine-MRI in Fig. 1.4. In Fig. 1.5(a), the tag lines are straight and the myocardium is thin. As the heart tissue moves, the tag lines move along with it, thereby tracking the motion of the heart. These tag lines can be automatically tracked using a variety of image processing techniques and displacement and strain of the tissue can be calculated [69, 56, 129, 70, 164, 114, 37]. A detailed review of tagged MRI and related processing techniques can be found in a recent review article in [15] (see also Chapter 2).

MR tagging has evolved as a gold standard in diagnosis and characterization of CAD [41, 97, 91, 35]. However, in comparison to echocardiography, the use of tagging has been very limited in the clinical setting [26]. One of the outstanding issues has been long imaging times and even longer post-processing times. Long imaging times are often accompanied with patient discomfort and can yield motion corrupted images. The discovery of Harmonic phase (HARP) MRI has changed this situation [110, 111]. HARP-MRI is a tagged image analysis method that can measure myocardial motion and strain in near real-time and is seen as a potential candidate to make MR tagging clinically viable.

1.6 HARP-MRI and Clinical Challenges

In this thesis, we focus on measuring regional ventricular function using HARP-MRI. The unique selling points of a HARP-MRI exam are its non-invasiveness, speed, and the high density of functional measurements in the myocardium. Apart from these advantages, there are several other criteria that need to be satisfied to warrant HARP-MRI's use in a clinical setting. First, the results of the HARP-MRI exam should be clinically significant and reliable. Second, the HARP-MRI exam should be fast (near real-time) and comprehensive. Third, the exam should not only provide as much information as the commonly used techniques, but should also provide diagnostically relevant information that is unique.

In response to the first criterion, several patient and normal volunteer studies have been conducted in order to validate HARP-MRI. Preliminary clinical studies have used HARP-MRI to evaluate the reperfusion of stunned myocardium in dogs [51] and to image myocardial infarction and ischemia in patients with CAD [50]. More recently, HARP-MRI has been used in the quantification of regional cardiac function in rat hearts [88, 57]. In response to the second criterion, fast imaging protocols have been developed and are currently being tested. FastHARP, a fast image acquisition protocol based on the HARP concept, has proved the feasibility of real-time imaging and detection of ischemia in MR stress tests [76, 135, 4]. Recent advances in HARP-MRI technology has led to comprehensive 3-D evaluation of myocardial motion [133, 115, 138, 136, 5]. The contributions of this dissertation are in response to the third criterion — the ability of HARP-MRI to provide

diagnostically significant information.

1.7 Thesis Contributions

The ability of HARP-MRI to provide diagnostically significant information depends on the accuracy of its measurements and its ability to differentiate between healthy and diseased heart tissues. One of the main goals of this dissertation is to translate these clinical aims into engineering problems and to solve them. In addressing this goal, we have made three contributions.

1.7.1 Optimal parameter selection for HARP-MRI

Optimal performance of HARP-MRI depends on fine-tuning of two key parameters, tag frequency and filter size, which are explained in Chapter 2. Currently, these two parameters are selected in a heuristic way. We propose a systematic way to select these two parameters for optimal performance under a wide variety of imaging scenarios. We systematically identify the different sources of error in HARP and their respective contributions in reducing accuracy. We then simulate a variety of different imaging scenarios that could occur during a clinical study, and in each case derive optimal parameters such that the errors in measurement are minimized. As a supplement to this research, we have developed a publicly distributable *HARP-MRI Parameter Optimization Toolbox* intended to be used by users of HARP to generate custom-made optimal parameters for any given clinical setting.

1.7.2 Performance limits of HARP-MRI

Preliminary clinical studies have shown that HARP-MRI is capable of reliable detection of heart abnormalities. In order to completely understand the significance of such results, it is important to understand the limits of HARP-MRI’s performance. We define and derive three quantities that quantify the performance limits of HARP — dynamic range, resolution, and detectability.

The dynamic range answers the question, “What is the limit of motion (strain and rotation) that can be detected using HARP-MRI?” In order to answer this question, we develop

an analogy between HARP-MRI and phase demodulation in communications theory. Using this analogy, we derive an approximate analytic expression for the dynamic range of HARP-MRI and validate our expression using real and simulated data.

The resolution of HARP-MRI captures the diagnostic utility of HARP-MRI in one number. It is a very important quantity that defines the ability of HARP-MRI to differentiate between healthy and diseased tissue. Deriving HARP-MRI’s resolution was challenging because the traditional definitions of resolution are based on linear systems theory, while HARP-MRI is a nonlinear technique. We redefined the concept of resolution so that we can answer certain key clinical questions pertaining to heart disease diagnosis. We validated this new definition using computer simulations.

Finally, we discuss the ability of HARP-MRI to detect abnormalities. We ask the question, “What is the smallest abnormality that can be detected using HARP-MRI?” In answering this question, we define the concept of detectability and validate the concept using a simple motion model. We illustrate the differences and similarities between the concept of resolution and detectability.

1.7.3 Artifact reduction in HARP-MRI strain maps

The tissue in the myocardium stretches and contracts in order for the LV to pump blood. In order to visualize these deformations, maps of mechanical strains are computed and visualized. Strain maps produced using HARP-MRI are corrupted with noisy artifacts, however, which obscures the real measurements and reduces their diagnostic utility.

Using our knowledge of the sources of errors from our earlier contribution, we studied how these errors manifest in the strain maps. We propose an algorithm to improve these strain maps using postprocessing. Our method is based on phase unwrapping the HARP phase, and smoothing the strain maps while respecting the resolution we derived previously. The performance of this method is compared to other existing artifact smoothing methods using *in vivo* real data.

1.7.4 Pushing the envelope of HARP-MRI: tracking the tongue during speech

So far, we have summarized three contributions of this dissertation in cardiac MR imaging. Our knowledge of the performance limits of HARP have helped us to push the envelope and apply HARP-MRI to an application other than cardiac motion. This leads us to the fourth contribution of this dissertation — tracking the motion of the human tongue during speech. While the clinical use of tracking tongue motion is to study speech pathology, its scientific use is to understand the dynamics of the tongue muscles and how they deform to produce normal speech.

Tracking the motion of the tongue using HARP-MRI is challenging for several reasons. The motion of the tongue is much faster than the heart, thereby making the imaging more challenging. The tongue has higher degrees of freedom in motion, both spatially and temporally, and does not repeat in a systematic way. We addressed all these challenges and present a study on tracking and visualizing the motion of the tongue using HARP-MRI. We devised unique ways of collecting MR data and developed post-processing algorithms to extract motion indices relevant to the tongue. We also showed how imaging the tongue stretches the performance limits of HARP-MRI and offers new challenges.

1.8 Organization

This dissertation begins in Chapter 2, where we give a background on MR imaging, MR tagging, and HARP-MRI. In Chapter 3, we discuss the sources of error in HARP-MRI and use simulations to derive optimal parameters for the operation of HARP-MRI. Chapter 4 sets HARP-MRI in a communications theory framework, which will serve as a theoretical framework which links the observations made in Chapter 3 to the characterization of HARP-MRI in Chapters 5, 6, and 7. In Chapter 5 we discuss the dynamic range of HARP-MRI. In Chapter 6 we redefine the concept of spatial resolution to derive the resolution of HARP-MRI. In Chapter 7, we investigate the detectability of HARP-MRI, and answer the question of how small an abnormality HARP-MRI can detect. In Chapter 8, we discuss artifacts in HARP-MRI strain maps and propose an algorithm to reduce them. This

chapter concludes the characterization of HARP-MRI for its use in cardiac imaging. In the next chapter, we explain how to adapt HARP-MRI to track the motion of the tongue during speech. We discuss the challenges in this new application of HARP-MRI. Finally we conclude our dissertation in Chapter 10 with a summary of the research and future work.

Chapter 2

Background

2.1 Introduction

The previous chapter gave the clinical motivations and explained the significance of this dissertation. In this chapter, we lay the foundation on which the entire thesis rests: MR tagging and HARP-MRI. Fig. 2.1 gives a broad overview of this chapter showing different topics that are covered. Representative results after each step are shown on the right. We begin the understanding of MR tagging with a detailed description of MR physics. We then move on to use the concepts of MR physics to understand the production of tags. Following tagging, we briefly explain the image acquisition process, known as MR imaging. Finally, we describe in detail HARP-MRI and the algorithms used to measure different motion indices.

An MR tagged image can be understood as a combination of two components. The first component is the anatomy component, and the second is the tagging component that is overlayed on the anatomy. We will understand the anatomy component using MR physics and tagging component using the physics of tagging.

2.2 MR Physics

MR physics can be understood from two different perspectives: microscopic and macroscopic. The microscopic perspective uses quantum physics to explain the fundamental be-

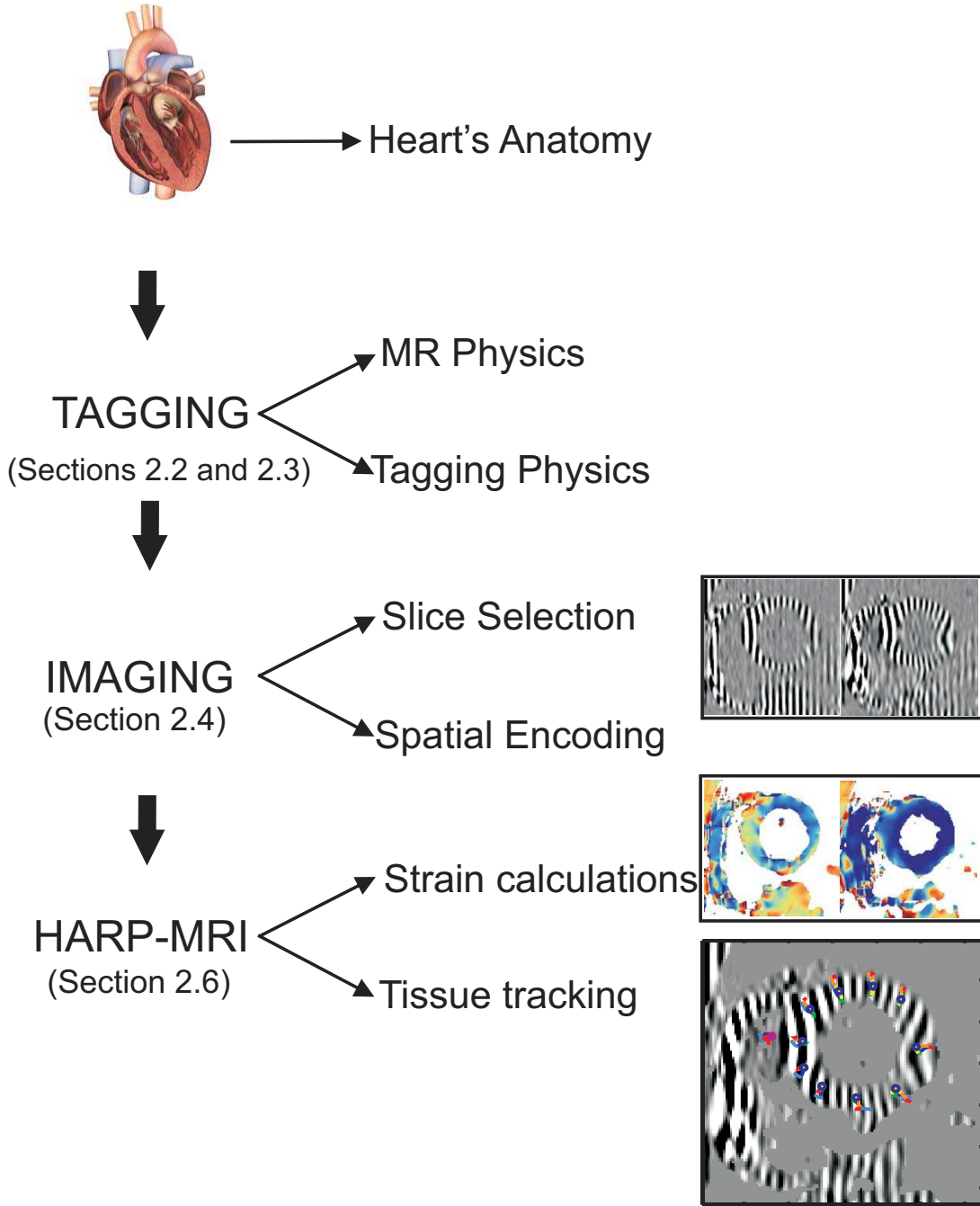


Figure 2.1: Overview of the background chapter. The right panel show representative results at each stage.

havior of magnetization. Once the fundamentals are understood, the formation of the MR signal and the MR image is more easily described using the macroscopic model, which uses the laws of classical physics. More details about the theory and principles of MRI can be found in [128, 108, 86].

2.2.1 Microscopic perspective

Nuclear Magnetic Resonance or NMR forms the core physics of MRI. NMR is concerned with the behavior of the nuclei of atoms in the presence of external magnetic fields. All nuclei have a positive charge because they contain positively charged protons and neutral neutrons. In addition to this charge, nuclei with odd mass number or odd atomic number have an angular momentum Φ . Such nuclei are called spins, and they act like a magnet with a microscopic magnetic moment μ associated with it,

$$\mu = \gamma\Phi ,$$

where γ is the gyromagnetic ratio that is unique to each NMR-active nucleus. ^1H is one such NMR active nuclei whose gyromagnetic ratio is $(2\pi \times 42.58) \frac{\text{radians/sec}}{\text{Tesla}}$. ^1H nuclei, also known as protons, are the main source of NMR signal in the body because our body contains a very high density of water.

In the absence of a strong external magnetic field, all the ^1H nuclei in our body are oriented in random directions. Therefore, the microscopic magnetic moments cancel each other out resulting in zero net magnetization. But this situation changes in the presence of a strong magnetic field $\mathbf{B}_0 = B_0\hat{z}$, where B_0 is the magnitude of the magnetic field and \hat{z} denotes the direction of the magnetic field. Our intuition from classical physics tell us that under the influence of this external magnetic field, all the small microscopic magnetic moments will align themselves in the direction of this external magnetic field. But the laws of quantum mechanics predict otherwise. Each magnetic moment μ has two choices: either to align itself 54° off \hat{z} (parallel orientation) or 54° off $-\hat{z}$ (anti-parallel orientation) (see Fig. 2.2). The parallel orientation corresponds to a lower energy state than the anti-parallel configuration. Therefore, the number of microscopic moments in the parallel configuration is a fraction more than in the anti-parallel configuration. This difference in the number

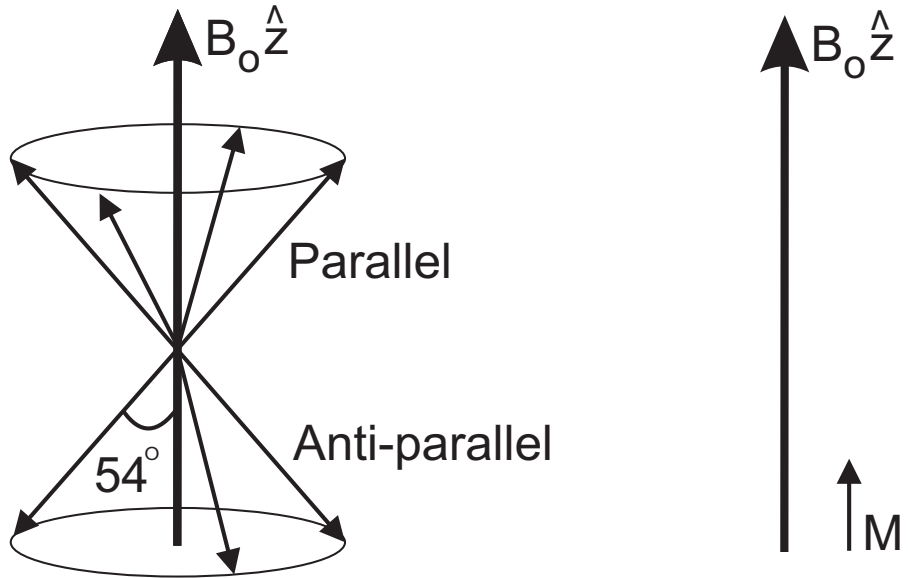


Figure 2.2: Microscopic magnetic moments align themselves either in the parallel or in the anti-parallel orientation, with a slight preference towards the parallel orientation, thereby resulting in a small magnetization M

of moments generates a small, yet observable, magnetization $M = M\hat{z}$, oriented in the direction of the main external magnetic field. M is called the bulk magnetization vector and is the source of the NMR signal. While understanding the generation of M requires knowledge of quantum physics, understanding its behavior in the presence of other external fields can be done using the macroscopic perspective.

2.2.2 Macroscopic perspective

Classical physics takes a macroscopic view of the bulk magnetization vector M , which is a function of both space $\mathbf{p} \in \mathbb{R}^3$ and time t . The density of ${}^1\text{H}$ nuclei is different at different spatial positions, and this produces contrast between different tissues in the body. This type of contrast is called proton density contrast. The other sources of contrast in a MR image comes from the behavior of $M(\mathbf{p}, t)$ under the influence of time varying and spatially varying external magnetic fields. These varying magnetic fields are used to manipulate the behavior of $M(\mathbf{p}, t)$ in a variety of ways, and a MR image is essentially a map of $M(\mathbf{p}, t)$ under the influence of these fields.

2.2.3 Precession and Larmor frequency

In MRI, $\mathbf{M}(\mathbf{p}, t)$ experiences two kinds of magnetic fields: a constant main magnetic field \mathbf{B}_0 that is always turned on and a varying magnetic field $\mathbf{B}^{\text{varying}}(\mathbf{p}, t)$. Let, $\mathbf{B}(\mathbf{p}, t)$ be the sum of these two magnetic fields. The effect of $\mathbf{B}(\mathbf{p}, t)$ on $\mathbf{M}(\mathbf{p}, t)$ is given by the Bloch equation,

$$\frac{d\mathbf{M}(\mathbf{p}, t)}{dt} = \gamma \mathbf{M}(\mathbf{p}, t) \times \mathbf{B}(\mathbf{p}, t). \quad (2.1)$$

In the presence of a time-varying and spatially varying magnetic field, the bulk magnetic moment experiences a torque. The above equation is of fundamental importance in the study of nuclear magnetization, which was part of the pioneering work done by Felix Bloch and Edward Mills Purcell, who were jointly awarded the Nobel Prize in Physics in 1952.

The effect of the torque on $\mathbf{M}(\mathbf{p}, t)$ can be rigorously explained using rotation matrices (see [108]). In this dissertation, however, we take a more intuitive approach to understand Eq. (2.1), which can be summarized in three practical steps. In the presence of a net magnetic field $\mathbf{B}(\mathbf{p}, t)$:

1. $\mathbf{M}(\mathbf{p}, t)$ precesses about $\mathbf{B}(\mathbf{p}, t)$ with the direction of $\mathbf{B}(\mathbf{p}, t)$ as the axis of rotation.
2. $\mathbf{M}(\mathbf{p}, t)$ precesses with a frequency of $\gamma B(\mathbf{p}, t)$, where B is the magnitude of \mathbf{B} .
3. Direction of precession is clockwise when viewing $\mathbf{B}(\mathbf{p}, t)$ head-on (left hand rule).

It is seen from Eq. (2.1) that, because of the cross product, the precession will occur only when \mathbf{M} and \mathbf{B} vectors are not in the same direction. But in the state of equilibrium, these two vectors are in the same \hat{z} direction (Fig. 2.2). Therefore in order for precession to occur, the vector \mathbf{M} needs to be disturbed from equilibrium. This act of disturbing \mathbf{M} is called excitation, and is performed using time-varying magnetic fields. Before going into the discussion of excitation, we need to develop four more concepts in order to understand why inducing precession is essential to generate a NMR signal. The four concepts are the two orthogonal components of magnetization, generation of the FID signal, relaxation, and the concept of a rotating frame.

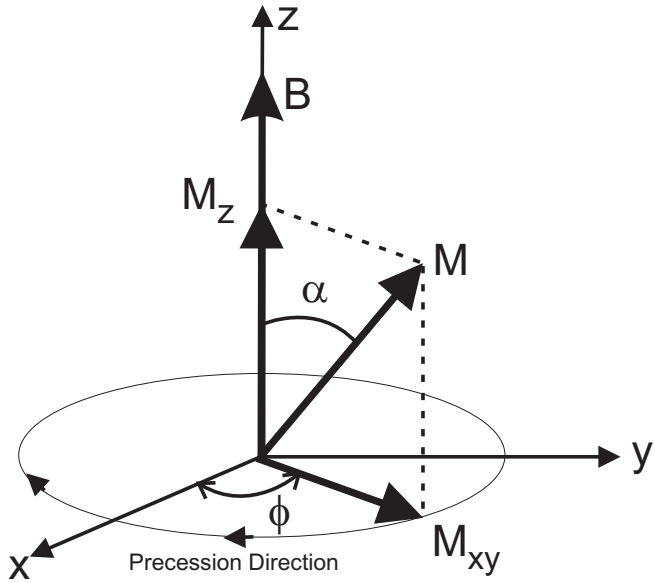


Figure 2.3: Precession of bulk magnetization and orthogonal components of magnetization

2.2.4 Transverse and longitudinal magnetization

Consider a magnetization vector $\mathbf{M}(\mathbf{p}, t)$ that has been distributed from its equilibrium making an angle α with the z axis (see Fig. 2.3). Let the external magnetic field be $\mathbf{B}(\mathbf{p}, t) = B(\mathbf{p}, t)\hat{z}$. In this state of non-equilibrium, the behavior of $\mathbf{M}(\mathbf{p}, t)$ is better understood by considering its two components: longitudinal and transverse. The longitudinal component M_z is oriented along the z axis, which is conventionally the direction of the constant main magnetic field \mathbf{B}_0 . The magnitude of M_z is $M(\mathbf{p}, t) \cos \alpha$, where $M = |\mathbf{M}|$. The transverse magnetization M_{xy} is the component of \mathbf{M} on a plane that is orthogonal to the z direction (see Fig. 2.3). The magnitude of the transverse magnetization is given by $M(\mathbf{p}, t) \sin \alpha$. The transverse magnetization can be further split into M_x and M_y .

Using the three rules of thumb, we can see that $\mathbf{M}(\mathbf{p}, t)$ will precess about $\mathbf{B}(\mathbf{p}, t)$ in the clockwise direction with a frequency of $\gamma B(\mathbf{p}, t)$. Mathematically, this can be written in terms of the components of magnetization as,

$$M_z(\mathbf{p}, t) = M(\mathbf{p}, t) \cos \alpha, \quad (2.2)$$

$$M_x(\mathbf{p}, t) = M(\mathbf{p}, t) \sin \alpha \cos(-\gamma B(\mathbf{p}, t)t + \phi), \quad (2.3)$$

$$M_y(\mathbf{p}, t) = M(\mathbf{p}, t) \sin \alpha \sin(-\gamma B(\mathbf{p}, t)t + \phi).$$

For simplicity, the two transverse components can be combined in one complex number as,

$$M_{xy}(\mathbf{p}, t) = M_x(\mathbf{p}, t) + jM_y(\mathbf{p}, t), \quad (2.4)$$

$$= M \sin \alpha e^{j(-\gamma B(\mathbf{p}, t)t + \phi)}. \quad (2.5)$$

The exponential term in Eq. (2.5) completely describes the precession. At any given spatial position \mathbf{p} , the precession starts with a random initial phase of ϕ , and continues with a frequency of $-\gamma B(\mathbf{p}, t)$ in the clockwise direction (hence the negative sign). Over a period of time τ this precessing vector will accrue a phase of $\int_0^\tau -\gamma B(\mathbf{p}, t) dt$ radians.

2.2.5 Free induction decay

The precessing transverse magnetization is an example of a moving magnetic field. Hence, by Faraday's law of induction should induce a current in a nearby coil. This current is the NMR signal, which is also known as the free induction decay (FID), and can be measured using a RF antenna. The magnitude of the FID signal in any given voxel is given by

$$|V| = \gamma B_0 \times |M_{xy}| \times (\text{voxel volume}) \times (\text{sensitivity of RF antenna}),$$

where a voxel is collection of spatial positions in a 3-D volume, analogous to the image pixel in 2-D.

2.2.6 Relaxation

The precession of the magnetization spins does not go on for forever. In order for the spins to stop precessing and return to the state of equilibrium, there are two independent relaxation processes: longitudinal (T_1) relaxation and transversal relaxation (T_2) relaxation. While the longitudinal relaxation causes the longitudinal component M_z to grow, the transverse magnetization is responsible for the transverse magnetization M_{xy} to diminish. Because they are caused by different physical processes, these two relaxation phenomenon occur at two different rates [86]. T_2 is much smaller than T_1 , implying that M_{xy} disappears at a faster rate than the growth of M_z . Eventually, when $t = \infty$, the magnetization will come back to equilibrium $M_z(t) = M$ and $M_{xy} = 0$. Mathematically, relaxation can be

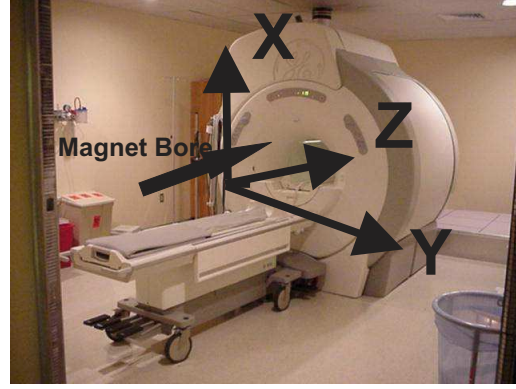


Figure 2.4: MRI scanner showing the fixed or laboratory frame of reference

appended to the expressions of the two components of magnetization in Eqs. 2.2 and 2.5.

$$M_z(t) = M(1 - e^{-t/T_1(\mathbf{p})}) + M \cos \alpha e^{-t/T_1(\mathbf{p})}, \quad (2.6)$$

$$M_{xy}(t) = M \sin \alpha e^{j(-\gamma B(\mathbf{p}, t)t + \phi)} e^{-t/T_2(\mathbf{p})}. \quad (2.7)$$

2.2.7 Rotating frame of reference

At any given time t , the total external magnetic field that magnetization \mathbf{M} experiences is $\mathbf{B}_0 + \mathbf{B}^{\text{varying}}(\mathbf{p}, t)$. Accordingly, the precession frequencies corresponding to these two fields also add up linearly. In an MR scanner, the main magnetic field \mathbf{B}_0 is always turned on, and is both spatially and temporally invariant within the bore of the magnet (see Fig. 2.4). Therefore, irrespective of whether $\mathbf{B}^{\text{varying}}(\mathbf{p}, t)$ is turned on or not, an excited \mathbf{M} will always precess about $\mathbf{B}_0 \hat{z}$ at a frequency of γB_0 . Since, this precession happens all the time and enters into all expressions of magnetization, it is easier to neglect it by considering a rotating frame of reference that precesses at a angular velocity of γB_0 in the clockwise direction. In the rotating frame the transverse magnetization becomes,

$$M_{x'y'}(t) = M \sin \alpha e^{j\phi} e^{-t/T_2(\mathbf{p})} \quad (2.8)$$

where primes over the x and y denote that the rotating frame is being considered. In the rotating frame, the magnetization \mathbf{M} does not feel the effect of the \mathbf{B}_0 field and hence does not precess about \mathbf{B}_0 .

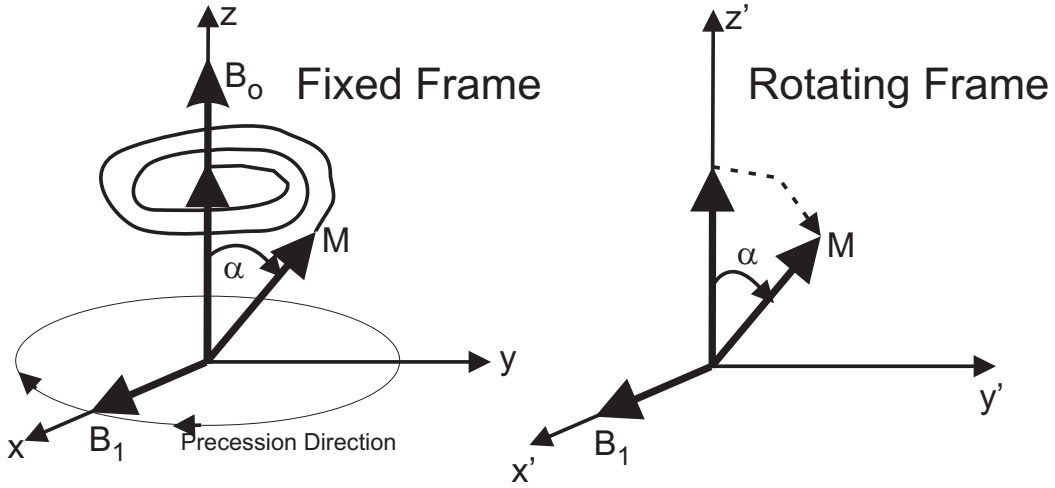


Figure 2.5: RF excitation: In the fixed frame, \mathbf{M} follows a helical path towards the transverse plane. In the rotating frame, the effect of \mathbf{B}_0 is not felt, and excitation is seen as direct tipping towards the transverse plane.

2.2.8 Excitation

The precession of \mathbf{M} occurs only when \mathbf{M} and \mathbf{B} are not aligned with each other; i.e., \mathbf{M} is not in equilibrium. The process of exciting \mathbf{M} from its equilibrium is achieved using a radio frequency (RF) pulse, which is a very short burst of rotating magnetic field. A RF pulse is conventionally denoted as $\mathbf{B}_1(\mathbf{p}, t) = B_1^e(\mathbf{p}, t)e^{-j\gamma B_0 t} \hat{\mathbf{r}}$, where $B_1^e(\mathbf{p}, t)$ is time-varying envelope function which limits the duration of the RF pulse to a very short time, say τ . It rotates with a frequency of γB_0 in the clockwise direction, and it is oriented in the particular direction $\hat{\mathbf{r}}$.

Fig. 2.5 shows the effect of a RF field applied along the \hat{x} direction. For a brief time τ during which the RF pulse is turned on, the \mathbf{M} experiences the combined effect of two fields, $B_0 \hat{z} + B_1^e(t)e^{-j\gamma B_0 t} \hat{x}$ in the fixed frame. Invoking the three rules of thumb, the precession of \mathbf{M} will be a combination of precessing about the \hat{x} axis and precession about the \hat{z} axis. The combination of these two precessions will be a helical path as shown in the left panel of Fig. 2.5. It is very interesting to note that, in order for a RF pulse to have the tipping effect, the rotating magnetic field should be rotating at the same Larmor frequency of the spins, which is $\gamma B_0 t$ in this case.

In the rotating frame, however, the effect of \mathbf{B}_0 is non-existent, and the spins feels only the effect of $B_1^e(t)\hat{x}'$. Note that, in the rotating frame, the rotating component of the RF pulse also disappears and x' is used instead of x . Again using the three rules of thumb, the magnetization \mathbf{M} will precess about x' axis with a frequency of $\gamma|B_1^e|$ in the clockwise direction. Using this, we see that the magnetization will bend towards the $x'y'$ plane (see right panel in Fig. 2.5). This bending of the magnetization is called tipping and the tipping angle is dependent on pulse duration τ . Mathematically the tipping angle α is given by,

$$\alpha = \int_0^\tau \gamma|B_1^e|dt \quad \text{radians.} \quad (2.9)$$

2.3 Physics of Tagging

The intensities that appear on an MR image depend on both the type and timing of the variable magnetic fields used. Both the type and timing of the variable magnetic fields can be controlled using a set of instructions called a pulse sequence. A pulse sequence is a timed set of instructions that determines the total variable magnetic field at any given time. A pulse sequence is usually drawn in the form of a timing diagram as shown in Fig. 2.6(a). Fig. 2.6(a) shows the pulse sequence to produce a tagging pattern called 1-1 SPAMM (Spatial Modulation of Magnetization) [14, 13]. The research in this dissertation is based on tagged images obtained using 1-1 SPAMM tagging.

1-1 SPAMM tagging is only one of many ways to produce tag lines in a MR image. Details of other methods of tag production can be found in [15, 165, 98]. The unique aspect of 1-1 SPAMM is that it produces a sinusoidal pattern of tags, which we will later see is ideally suited for HARP-MRI. In the following sections we will explain in detail how this sinusoidal tag pattern is produced.

2.3.1 1-1 SPAMM pulse sequence

The 1-1 SPAMM tagging pulse sequence is timed with respect to the ECG signal. The QRS complex of the ECG signal [shown as a peak in Fig. 2.6(a)] denotes that the heart's position is in end-diastole; the point at which the tagging pulse sequence is triggered. The

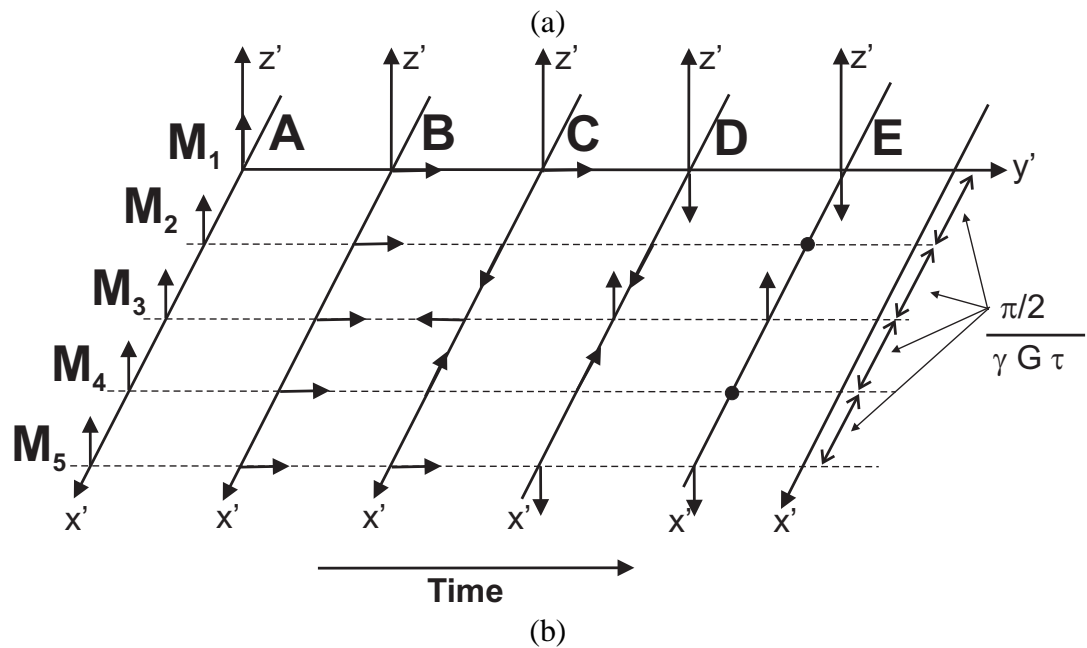
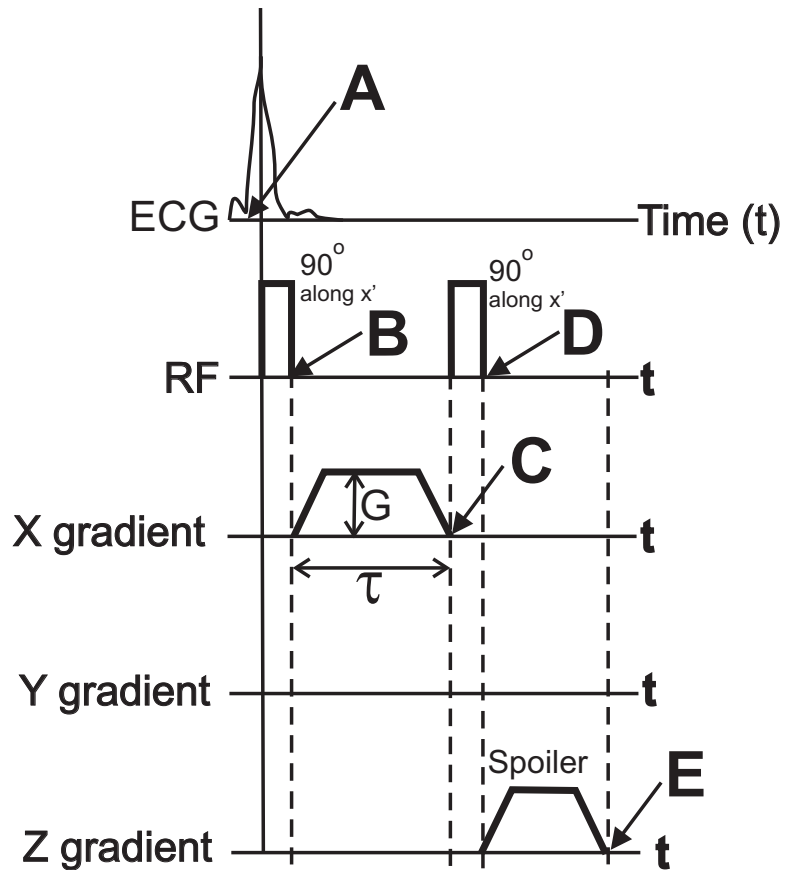


Figure 2.6: 1-1 SPAMM tagging pulse sequence and behavior of five spins spaced equally apart on the x' axis.

triggering of tagging is done at end-diastole because the heart is full of blood and is undergoing least amount of motion [96]. The actual application of tags consists of four time-varying magnetic fields called pulses. There are two RF pulses that are separated by a linear gradient pulse in between. The second RF pulse is followed by a spoiler gradient pulse [see Fig. 2.6(a)].

Gradient pulses A linear gradient pulse is special type of MR instruction that creates a spatially varying magnetic field that varies linearly with distance. For example, an x -gradient of amplitude $G(t)$, means that there is spatially varying magnetic field of $G(t) \times x$ oriented toward the \hat{z} direction¹. Generalizing this, if $\mathbf{G}(t) = [G_x(t) \ G_y(t) \ G_z(t)]^T$, then the magnetic field created by the gradient at a spatial point \mathbf{p} is $[\mathbf{G}(t)^T \mathbf{p} \ \hat{z}]$ and $\mathbf{M}(\mathbf{p}, t)$ will precess at a frequency of $\gamma \mathbf{G}(t)^T \mathbf{p}$ about the \hat{z} axis. In this particular example, we use a x -gradient of magnitude $G(t)$ and keep it switched on for τ milliseconds. Depending on their x position, different magnetization vectors will precess at different frequencies, and will accrue different phases at the end of τ seconds. This phase difference deliberately creates a small, yet useful, incoherence in the magnetizations. The spoiler gradient pulse is a extreme form of linear gradient pulse. It creates a strong incoherence such that the phases cancels each other and the signal coming from the precessing spins is zeroed out.

2.3.2 Sinusoidal modulation of magnetization

The production of a sinusoidal modulation using the 1-1 SPAMM can be understood by carefully studying the behavior of five magnetization vectors M_1 through M_5 that are placed equidistantly on the x axis with the following co-ordinates: $x = 0$, $x = \frac{\pi}{2}/\gamma G_x \tau$, $x = \pi/\gamma G_x \tau$, $x = \frac{3\pi}{2}/\gamma G_x \tau$, $x = 2\pi/\gamma G_x \tau$. We will study the behavior of these vectors at five different time-points A through E [see Fig. 2.6(a)]. In the following narrative, the analyses will be done in the rotating frame. Recall that in the rotating frame, \mathbf{M} does not feel the effect of main $\mathbf{B}_0 \hat{z}$ field and hence precession about \mathbf{B}_0 field is a not relevant. Also, in order to simplify the analysis, we will assume that all the magnetization vectors have unit magnitude.

¹A spatial varying field created by a gradient always faces the \hat{z} direction. This is irrespective of whether the gradient is applied in the x , y , or z directions.

Before the application of any pulses (time A), all the spins are aligned in \hat{z}' direction. Immediately after the ‘QRS’ complex in the ECG, the first 90° RF pulse is applied along the x' direction. This RF pulse tips all the magnetization vectors onto the $x'y'$ plane, aligning them along the y' axis (time B). (The phase shift ϕ in Eq. 2.8 is assumed to be zero.) The linear x gradient of amplitude G is switched on at time B for a period of τ milliseconds. Due to this gradient, each vector experiences a different external field depending on its x' position, and hence precesses at different frequencies. M_1 at $x = 0$ experiences zero magnetic field in the rotating frame and does not precess. M_2 precesses at a frequency of $\gamma G_x \left(\frac{\pi}{2} / \gamma G_x \tau \right) = \frac{\pi}{2\tau}$. Similarly, M_3 , M_4 , and M_5 precess with a frequency of $\frac{\pi}{\tau}$, $\frac{3\pi}{2\tau}$, and $\frac{2\pi}{\tau}$ respectively.

Differential phase accrual In τ milliseconds, each magnetization vector accrues different phases. M_1 accrues zero phase. M_2 accrues a phase of $\int_0^\tau \frac{\pi}{2\tau} dt = \frac{\pi}{2}$ radians, and thus aligns itself along x' -axis. Similarly, M_3 , M_4 , and M_5 accrue phase of π , $3\pi/2$, and 2π aligning themselves along $-y'$, $-x'$, and y' axis respectively (time C). In this state of incoherence, a second 90° RF pulse is applied along the x' direction, the same direction as the first RF pulse.

Storing information in M_z We again use the three rules of thumb to study the effect of the second RF pulse. M_1 and M_5 precess clockwise for 90° about the x' axis and end up in $-z'$ direction. Similarly, M_3 ends up in z' direction. M_2 and M_4 are unaffected because they are aligned along the axis of the RF pulse, and hence do not feel the torque (time D). This is a very interesting configuration of magnetization. Out of the five vectors, three are aligned in the z' direction and two of them, M_2 and M_4 are in the transverse plane. Therefore, by definition, in the fixed frame, only M_2 and M_4 are actually precessing. The spoiler gradient is applied so that it makes all precessing vectors out-of-phase with each other, thereby killing all the transverse magnetization. Now, at time E, all the magnetization information is stored in the longitudinal magnetization M_z .

In order to understand how the magnetizations along the x' axis look like in-between these five example vectors, we look more closely into the effect of the linear gradient and the second RF pulse. The gradient provides the required phase dispersion to M_{xy} which

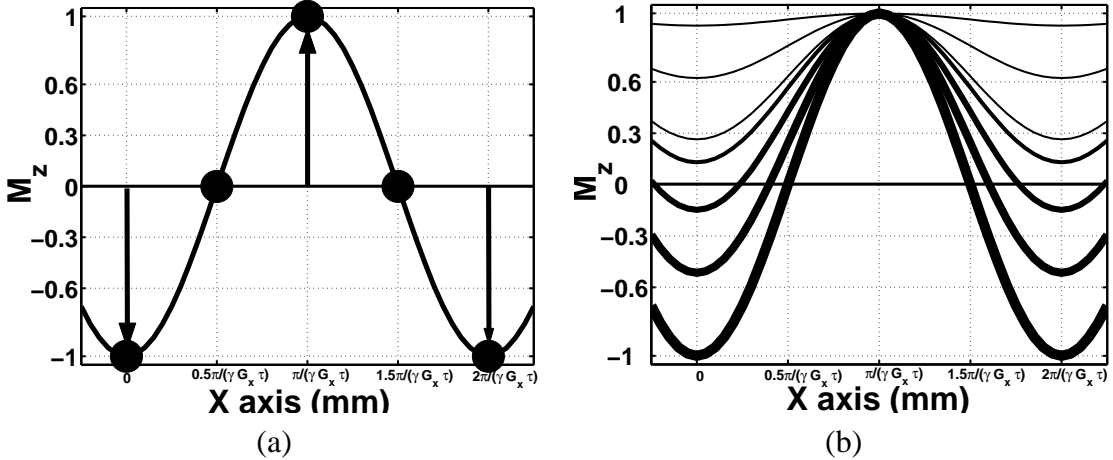


Figure 2.7: 1-1 SPAMM tag pattern (a) right after application of tags , and (b) during relaxation

varies with x' position. Very interestingly, the second RF pulse stores only the y' component of this phase dispersion. In other words, the second RF pulse preferentially selects the component of M_{xy} that are orthogonal to the direction of the gradient. The orthogonal x' component of M_{xy} is left to precess in the $x'y'$ plane, only to be later annihilated by the spoiler gradient. The y' component is precisely the cosine of the phase dispersion $\gamma G_x x \tau$ and is stored in M_z in the form of a sinusoid as shown in Fig. 2.7(a).

In this manner, a tagging pulse sequence ‘tags’ or modulates the magnetization in a sinusoidal manner. Relaxing the condition that the magnetizations should be of magnitude 1, the final map of M_z magnetization will look like, $M(\mathbf{p}, t) \cos((\gamma G_x \tau)x)$, where the frequency of the sinusoid is determined by the gradient (both amplitude and direction) and the time for which it is turned on. In general, the gradient vector \mathbf{G} can be in any direction and the final map of longitudinal magnetization can be written as,

$$M_z(\mathbf{p}, t) = \mathbf{M}(\mathbf{p}, t) \cos \left(\gamma \int_0^\tau \mathbf{G}^T \mathbf{p} dt \right) \quad (2.10)$$

In the case described above, $\mathbf{G} = [G_x \ 0 \ 0]$ and M_z is modulated along the x' axis. This type of tag pattern is called a 1-D tag. An orthogonal direction of tag can be formed using $\mathbf{G} = [0 \ G_y \ 0]$, where M_z will be modulated along y' . On the other hand, if $[G_x \ 0 \ 0]$ is followed by $[0 \ G_y \ 0]$ in the same tagging pulse sequence, then the sinusoids in both

directions multiply each other to produce a crisscross pattern called *grid tags*.

2.3.3 Tag Fading

The sinusoidal modulation of M_z lasts only for a period of time comparable to the T_1 of the tissue, after which the magnetization recovers and settles into equilibrium. This process is called tag fading. Fig. 2.7(b) shows the phenomenon of fading. The thickest line corresponds to the initial tag modulation, which is the same as one on the left panel. Progressively thinner sinusoids represent the fading of the sinusoid. The tag modulation starts off as a zero mean sinusoid, and subsequently as the tags fade, a constant bias develops and continues to increase. Tag fading can be represented by expressing M_z as a function of time

$$M_z(\mathbf{p}, t) = M(\mathbf{p}, t) \cos(\gamma G_x \tau x) e^{-t/T_1} + M(\mathbf{p}, t)(1 - e^{-t/T_1}). \quad (2.11)$$

Eq. (2.11) shows how the tagging component fades at the rate of T_1 and the bias component increases at the rate of T_1 . The bias component, also known as the DC component, reduces the contrast of the tags, which is defined as peak-to-peak amplitude. This reduction of contrast makes the tagged images in the later time frames, namely the end-systolic and diastolic time frames noisier.

2.3.4 CSPAMM

Complementary SPAMM (CSPAMM) is an improved form of 1-1 SPAMM [46]. CSPAMM provides improved tag contrast and addresses the problem of tag fading. It consists of two separate 1-1 SPAMM acquisition with two different set of RF pulses. The first acquisition, usually called the ‘A’ acquisition uses two 90° RF pulses as described above. The second acquisition, called the ‘B’ acquisition, uses a $+90^\circ$ for the first RF pulse and -90° for the second RF pulse. A similar analysis like the one above yields,

$$\begin{aligned} M_z^A(\mathbf{p}, t) &= M(\mathbf{p}, t) \cos(\gamma G_x \tau x) e^{-t/T_1} + M(\mathbf{p}, t)(1 - e^{-t/T_1}), \\ M_z^B(\mathbf{p}, t) &= -M(\mathbf{p}, t) \cos(\gamma G_x \tau x) e^{-t/T_1} + M(\mathbf{p}, t)(1 - e^{-t/T_1}) \end{aligned}$$

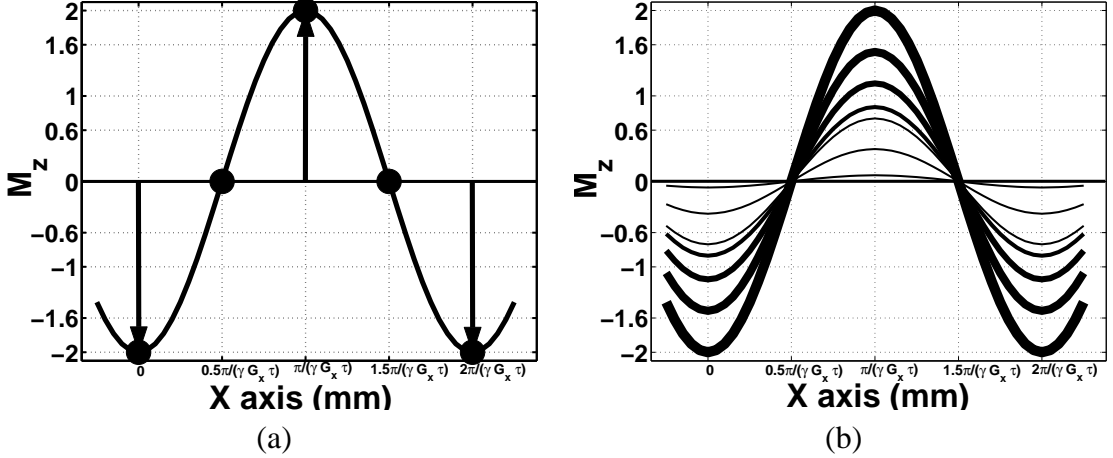


Figure 2.8: CSPAMM tag pattern (a) right after application of tags , and (b) during relaxation

The two sinusoidal modulations are π radians out of phase, which accounts for the negative sign in the B acquisition. A simple subtraction of $(A - B)$ yields

$$M_z^{\text{CSPAMM}}(\mathbf{p}, t) = 2 \times M(\mathbf{p}, t) \cos(\gamma G_x \tau x) e^{-t/T_1}. \quad (2.12)$$

Eq. (2.12) shows that the contrast of the sinusoid is twice than that of the original [see Fig. 2.8(a)]. Another interesting aspect is that the DC component gets subtracted out even as the tags fade; and hence, CSPAMM tags fade out as zero mean sinusoids [see Fig. 2.8(b)]. Because of its improved tag contrast and fading properties, we use CSPAMM tagging extensively in this research.

MICSR Eq. (2.12) is an ideal representation of the longitudinal magnetization. For a variety of reasons, there are minor phase errors that enter the measurements. One of the main reasons is the non-uniformity of the main \mathbf{B}_0 field in the bore of the magnet. Since it is desirable to form real images, the Magnitude Image CSPAMM reconstruction (MICSR) method can be used. MICSR uses the magnitudes of A and B , thereby eliminating the phases completely. Instead of $A - B$, MICSR uses the formula, $|A|^2 - |B|^2$, which also yields a pure sinusoid without the DC bias having different tag fading properties, as follows.

$$M_z^{\text{MICSR}}(\mathbf{p}, t) = 4 \times [M(\mathbf{p}, t)]^2 (1 - e^{-t/T_1}) (e^{-t/T_1}) \cos(\gamma G_x \tau x) \quad (2.13)$$

The MICSР reconstruction has been shown to provide good contrast and its fading properties are comparable to that of CSPAMM [105, 104]. In this dissertation, we use the MICSР reconstruction of CSPAMM acquisitions.

2.4 Image Acquisition

In the previous section, we explained the sinusoidal modulation of the longitudinal magnetization of the tissue. In this section, we will describe how this longitudinal magnetization is imaged using a pulse sequence. Developing faster and better image acquisition pulse sequences is integral to overcome the clinical challenges of MR tagging and HARP-MRI [134]. In this dissertation, however, we do not pursue this direction and hence we do not explain image acquisition in great detail. In the following paragraphs, we will briefly describe a simple pulse sequence for image acquisition.

Spin echo and gradient echo pulse sequences are two broad categories of image acquisition schemes. Here, we explain the gradient echo pulse sequence. Fig. 2.9 shows a simple version of the gradient echo pulse sequence. There are two main parts of the pulse sequence that warrant attention: slice selection and spatial encoding.

Slice selection The modulation of M_z , as described in the preceding section, was not restricted to any particular cross-sectional slice of the body. This type of tagging is called non-selective tagging. To form an 2-D image, however, we need to restrict the FID signal to be generated only from the cross-sectional slice that we are interested in. The slice selection part of the pulse sequence does precisely this — to excite only those spins that lie on the interested slice. Slice selection consists of an RF pulse in presence of the z gradient. The z gradient creates an incoherence in spins linearly along the z direction, thereby making different z slices precess at different Larmor frequencies. The frequency of the RF pulse is designed in such a way that it coincides with the Larmor frequencies of the spins in the interested slice. By doing this, only the spins in the interested slice will be excited and will contribute to the FID.

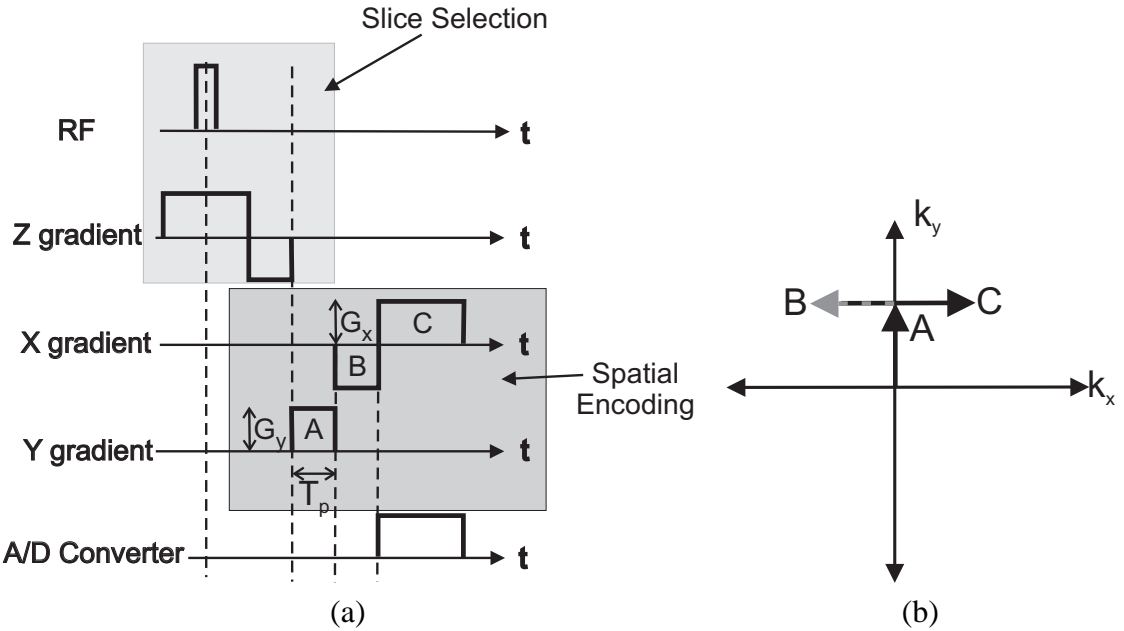


Figure 2.9: (a) Gradient echo pulse sequence and (b) corresponding k-space trajectory

Spatial encoding The FID signal that the RF antenna measures is a 1-D signal [Eq.(2.6)]. In order for this 1-D signal to convey image about a 2-D cross-section, the magnetizations in a slice are encoded in two different directions using two spatial gradients called the phase encoding and readout gradient. The two gradients are used to manipulate the Larmor frequencies in such a way that every voxel is encoded with a unique precession frequency. The right portion of Fig. 2.9 shows the spatial encoding gradients.

Let G_x and G_y be the x (readout) and y (phase encode) gradients respectively. Let T_p be the time for which the G_y gradient is switched on. Using the rules of thumb, we can see that at any time t during which the analog to digital converter is switched on, the signal $s(t)$ is given as the summation of all spins on that slice

$$s(t) = \int_{-\infty}^{\infty} \int_{-\infty}^{\infty} M(x, y) e^{-j\gamma(G_x x t)} e^{-j\gamma(G_y y T_p)} dx dy, \quad (2.14)$$

where $\mathbf{x} = [x \ y]$ are the 2-D spatial coordinates.

K-space sampling If $M(x, y)$ is a 2-D image, its Fourier transform is given as

$$M(u, v) = \int_{-\infty}^{\infty} \int_{-\infty}^{\infty} M(x, y) e^{-jux} e^{-jvy} dx dy. \quad (2.15)$$

Comparing Eqs. 2.14 and 2.15, we see that samples of the FID are actual samples of the Fourier transform of $M(x, y)$ with

$$\begin{aligned} u &= \gamma G_x t, \\ v &= \gamma G_y T_p. \end{aligned}$$

In the above expressions, the frequency variable u and v are expressed as continuous variables. But in reality, they are sampled using an analog to digital converter that samples the continuous Fourier spectrum, which is more commonly known as k-space in the MR literature. Mathematically, samples of the Fourier spectrum can be seen a Fourier series and the final MR image can be reconstructed using an inverse Fourier series reconstruction.

$$M(x, y) = \Delta k_x \Delta k_y \sum_{m=-\infty}^{\infty} \sum_{n=-\infty}^{\infty} M(m \Delta k_x, n \Delta k_y) e^{j2\pi(m \Delta k_x x + n \Delta k_y y)},$$

where Δk_x and Δk_y are the sampling intervals in k-space. If we collect infinite samples in k-space, we can reconstruct $M(x, y)$ perfectly. Practically, we collect only finite samples and the reconstruction is done using a truncated inverse Fourier series reconstruction.

$$M(x, y) = \Delta k_x \Delta k_y \sum_{m=-N_x/2}^{N_x/2} \sum_{n=-N_y/2}^{N_y/2} M(m \Delta k_x, n \Delta k_y) e^{j2\pi(m \Delta k_x x + n \Delta k_y y)}, \quad (2.16)$$

where N_x and N_y are the number of samples acquired in the k_x and k_y directions respectively. The extent of k-space collected defines the spatial resolution of the image. A brief explanation about spatial resolution is given in Sec. 2.7.3 of this chapter and a more detailed version will be given in Chapter 6 on HARP-MRI resolution.

2.5 Encoding tissue motion using tagging

A tagged image is created by applying the imaging pulse sequence soon after the tagging is done. While the tagging is applied only once in one heart beat cycle, the imaging

pulse sequence is repeatedly applied in order to capture different time frames of the tagged heart. The difference in time between two time frames is called the temporal resolution of the image series. In this section, we understand how a tagged image series encodes tissue motion.

M_z in terms of tissue displacement. The value of M_z immediately after the tags are applied is given as

$$M_z(\mathbf{p}, t_{\text{ref}}) = M(\mathbf{p}) \cos(\gamma\tau\mathbf{G}^T \mathbf{p}), \quad (2.17)$$

$$= M(\mathbf{p}) \cos(\boldsymbol{\omega}_0^T \mathbf{p}), \quad (2.18)$$

where $\boldsymbol{\omega}_0$ is the frequency of the tagging sinusoid and t_{ref} is the time at which tags are applied (time E in Fig. 2.6). A tagged image can be written as $I(x, y, t; z_0)$ where z_0 is the z coordinate specified by slice selection and spatial encoding. Since heart tissue is moving, the magnetization residing at $\mathbf{x}_{z_0} = [x \ y \ z_0]^T$ at current time t , must have moved from its original location $\mathbf{p}(\mathbf{x}_{z_0})$ at time t_{ref} ; $\mathbf{p}(\mathbf{x}_{z_0})$ is known as the reference map. The tagged image $I(x, y, t; z_0)$ is the map of the longitudinal magnetization of $M_z(\mathbf{x}_{z_0}, t)$. Longitudinal magnetization is a material property of the tissue, i.e. when the tissue moves, the longitudinal magnetization moves along with it. Therefore the longitudinal magnetization,

$$M_z(\mathbf{x}_{z_0}, t) = M_z(\mathbf{p}(\mathbf{x}_{z_0}, t), t), \quad (2.19)$$

$$= M(\mathbf{p}(\mathbf{x}_{z_0}, t)) \cos(\boldsymbol{\omega}_0^T \mathbf{p}(\mathbf{x}_{z_0}, t)). \quad (2.20)$$

This magnetization can be expressed in terms of the displacement of the tissue which is given as the vector difference between the current position and its reference position.

$$\mathbf{u}(\mathbf{x}_{z_0}, t) = \mathbf{x}_{z_0} - \mathbf{p}(\mathbf{x}_{z_0}, t) \quad (2.21)$$

Therefore, using Eqs.(2.20) and (2.21) the map of longitudinal magnetization on the imaging slice can be rewritten in terms of its displacement.

$$M_z(\mathbf{x}_{z_0}, t) = M(\mathbf{p}(\mathbf{x}_{z_0}, t)) \cos(\boldsymbol{\omega}_0^T (\mathbf{x}_{z_0} - \mathbf{u}(\mathbf{x}_{z_0}, t))). \quad (2.22)$$

Tagged image in terms of tissue displacement. In order to convert the above equation into an expression for the image, we substitute $\mathbf{G} = [G_x \ 0 \ 0]$, and neglect z_0 to get an expression for a vertically tagged image.

$$I^{ver}(\mathbf{x}, t) = M(\mathbf{x}, t) \cos(\omega_x x - \omega_x u_x(\mathbf{x}, t)), \quad (2.23)$$

where $\omega_x = \gamma\tau G_x$ is the tag frequency and u_x is x component of displacement \mathbf{u} . The vertically tagged can track only one component of motion, namely u_x . In order to track in 2-D, we need both the components of displacement, for which we need another tagging gradient that is linearly independent $[G_x \ 0 \ 0]$. In the simplest case, we can select $\mathbf{G} = [0 \ G_y \ 0]$ to get a horizontally tagged image

$$I^{hor}(\mathbf{x}, t) = M(\mathbf{x}, t) \cos(\omega_y y - \omega_y u_y(\mathbf{x}, t)).$$

Tagged Image Visualization. Figure 2.10 shows horizontally and vertically tagged images of the short-axis cross-section of the heart. The images in the first column correspond to early systolic time frame, while the images in the second column correspond to mid-systole. Note that the myocardial wall in the figures in the mid-systolic time frames are much thicker than the early systolic time frames. This thickening of the wall is caused by its stretching in the radial direction, and a consequent contraction in the orthogonal circumferential direction. Consider, for example, the region marked using arrows in Fig. 2.10. While the circumferential shortening in this region is captured by the vertical tags, the radial expansion is encoded by the horizontal tags. The bending of the tags caused by the wall thickening can also be clearly seen in the images in the second column. The vertical tags bend according to the lateral left-right motion, and the horizontal tags bend according to the up-down motion.

All images in Fig. 2.10 are the result of CSPAMM acquisitions with MICSIR reconstruction. Therefore the black and white modulations actually represent pure sinusoidal modulations. Both the extreme positive and negative values in the images have been clipped so that the tags appear with better clarity. This clipping is, however, only for visualization purposes [105].

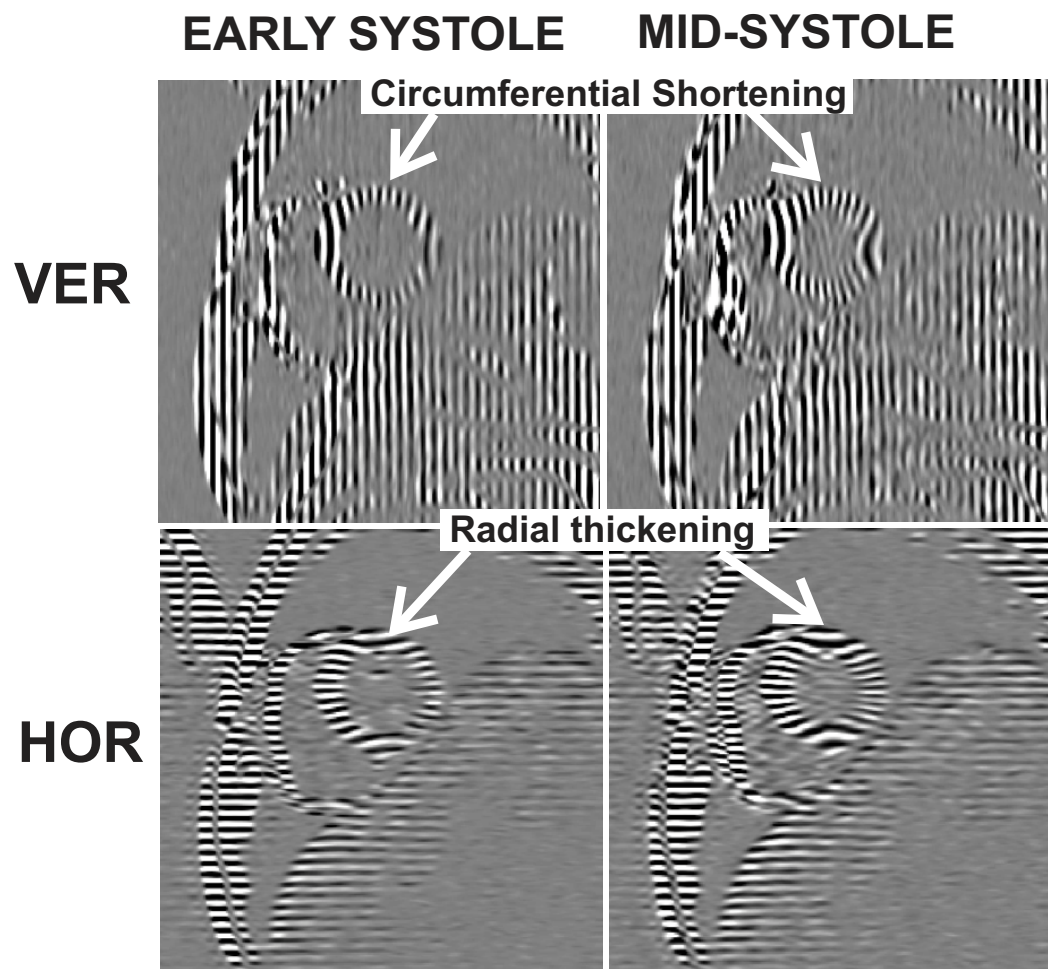


Figure 2.10: Tagged images in two orthogonal tag directions at two different time frames in systole. Note the increased radial thickening and circumferential shortening in the mid-systolic time frame.

2.6 Harmonic Phase (HARP) MRI

A vertically tagged CSPAMM image can be considered a product of two spatial signals: the anatomy signal $M(\mathbf{x}, t)$ and the tagging signal $\cos(\gamma G_x \tau x)$ [see Eq.(2.23)]. The multiplication of these two signals in the spatial domain is analogous to the convolution of their Fourier transforms. Fig. 2.11(b) shows the spectrum of vertically tagged image. It consists of two harmonic spectral peaks, whose centers are located at the first harmonic frequencies of the tagging sinusoid. The premise of HARP-MRI is that most of the spectral energy corresponding to the motion of the tissue is localized around one of the harmonic spectral peak. A bandpass filter [see circle in Fig. 2.11(b)] is used to filter one of the harmonic peaks and the rest of the spectrum is zero padded. The zero padded spectrum is an asymmetric spectrum, and hence the inverse Fourier transform of this one-sided spectrum results in a complex image called the harmonic image, which can be expressed as

$$I_{\text{Har}}^{\text{ver}}(\mathbf{x}, t) = D^{\text{ver}}(\mathbf{x}, t)e^{j\phi^{\text{ver}}(\mathbf{x}, t)}. \quad (2.24)$$

The magnitude of this harmonic image $D^{\text{ver}}(\mathbf{x}, t)$ is shown in Fig. 2.11(c) and the phase of this complex image $\phi^{\text{ver}}(\mathbf{x}, t)$ is called the *Harmonic Phase* or HARP and is shown in Fig. 2.11(d).

Drawing parallels between Eqs.(2.24) and (2.23), we can see that harmonic image is the exponential analog of the tagging signal. Therefore, the harmonic magnitude is proportional to the transverse magnetization $M(\mathbf{x}, t)$, and the HARP phase can be expressed as

$$\phi^{\text{ver}}(\mathbf{x}, t) = \omega_x x - \omega_x u_x. \quad (2.25)$$

A similar equation can be written for the horizontally tagged images.

$$\phi^{\text{hor}}(\mathbf{x}, t) = \omega_y y - \omega_y u_y.$$

These two equations represent the basic concept of HARP-MRI — the harmonic phase is linearly related to 2-D tissue displacement. This concept can be visually corroborated by comparing the tagged image and the HARP image. Note how the phase wraps in the HARP image exactly coincide with the troughs of the tagging pattern. (The phase wrap

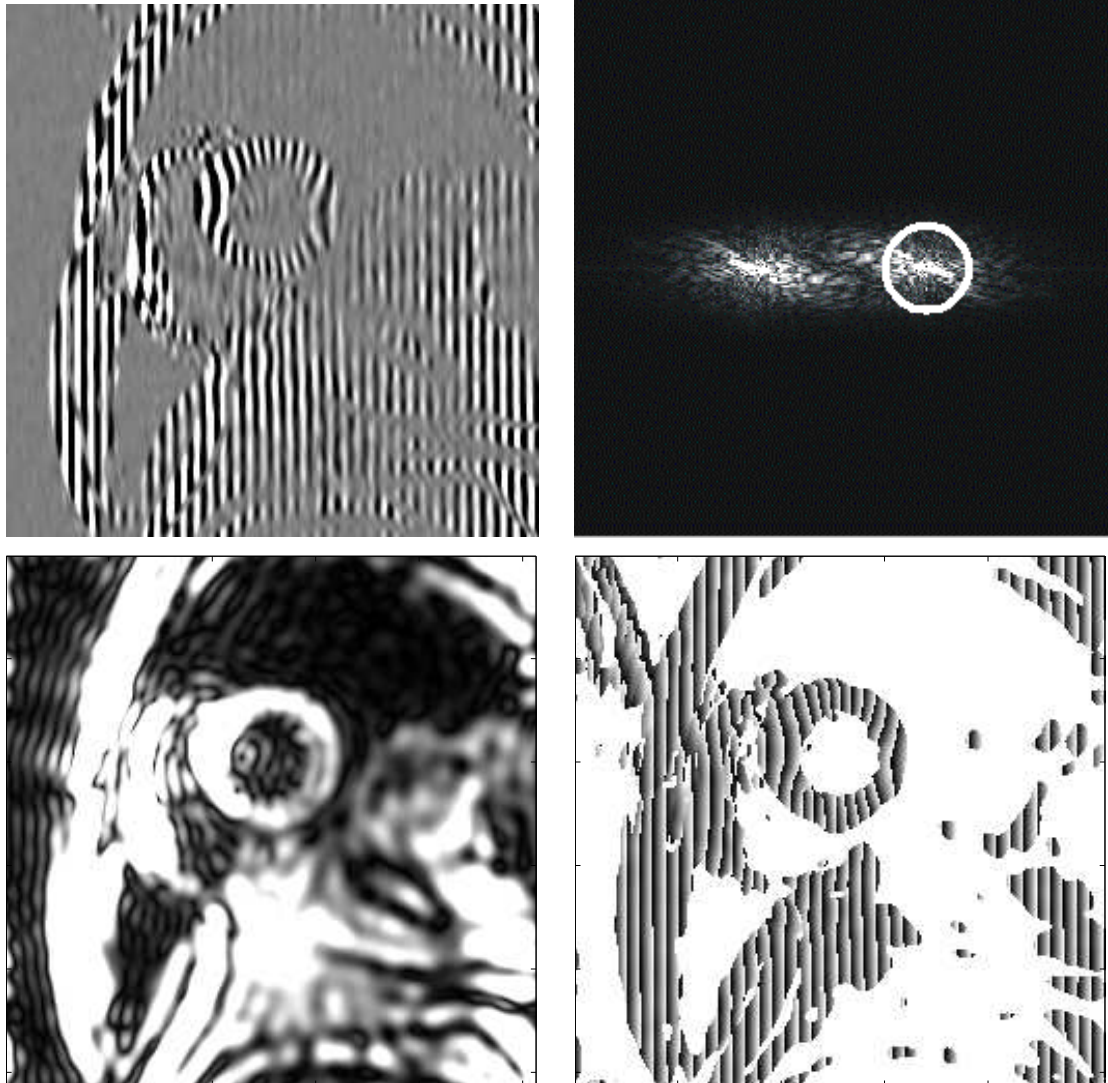


Figure 2.11: Top right: Vertically tagged CSPAMM image. Top right: Spectrum with the HARP-MRI bandpass filter as white circle. Bottom left: HARP Magnitude image, $D(\mathbf{x}, t)$, Bottom right: HARP phase $\phi(\mathbf{x}, t)$ masked using the magnitude image.

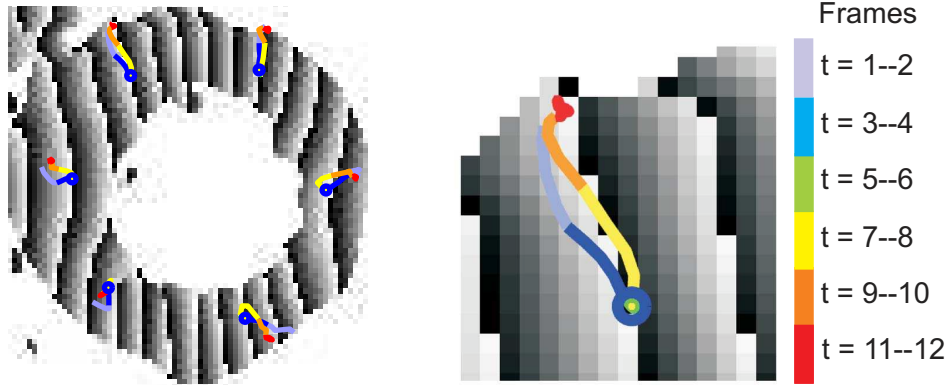


Figure 2.12: Left: Trajectories of tissue points on the myocardium overlaid on HARP phase image. Right: A track zoomed in; Progression of colors from violet-blue-green-yellow-orange-red indicates the motion through different time frames.

occur because the phase of a complex image is computed between $-\pi$ and π .) Writing Eq.(2.25) in more general form for any tag direction.

$$\phi(\mathbf{x}, t) = -\boldsymbol{\omega}_0^T \mathbf{u}(\mathbf{x}, t) + \boldsymbol{\omega}_0^T \mathbf{x} , \quad (2.26)$$

The displacement $\mathbf{u}(\mathbf{x}, t)$ can be used for various indices of motion like, trajectories of tissue point, Eulerian strain, velocities, and Lagrangian strains [112]. In this dissertation, we focus on the properties of the algorithms that compute the trajectories of tissue points and Eulerian strain, which are explained in more detail below.

2.6.1 HARP Tracking

The motion of individual tissue points can be tracked and displayed as trajectories. A tagged tissue point has two HARP values, one from the horizontal tags and another from the vertical tags. Let the horizontal HARP value be ϕ^{hor} and the vertical HARP value be ϕ^{ver} . Let the overall HARP vector be $\phi = [\phi^{ver} \ \phi^{hor}]^T$. The HARP vector, like longitudinal magnetization, is a material property of the tissue while the tag pattern lasts. Therefore, as a tissue point moves, its HARP value moves along with it. Hence, by tracking the HARP value through a cine series of images, the trajectory of a tissue point can be estimated [110]. Consider a material point located at \mathbf{x}_n at time t_n . If \mathbf{x}_{n+1} is the position of this point at

time t_{n+1} , then since HARP is a material property, we must have

$$\phi(\mathbf{x}_{n+1}, t_{n+1}) = \phi(\mathbf{x}_n, t_n).$$

This relationship provides the basis for tracking \mathbf{x}_n from time t_n to time t_{n+1} . Our goal is to find \mathbf{x} that satisfies

$$\phi(\mathbf{x}, t_{n+1}) - \phi(\mathbf{x}_n, t_n) = 0,$$

and then set $\mathbf{x}_{n+1} = \mathbf{x}$. This *HARP tracking* algorithm is repeated for consecutive time frames to track a particular point through the entire cine series and the trajectory is visualized as a path line.

Fig. 2.12 shows the path lines of individual tissue points in the myocardium. A zoomed version of a track is shown on the right. The progression of colors from violet-blue-green-yellow-orange-red indicates the progression of motion through different time frames. It is important to note that, since each pixel in the image has a unique HARP vector associated with it, every pixel in the image can be tracked. This is unlike many other tag tracking methods, which compute complete 2-D motion only on pixels where the horizontal and vertical tags intersect. The ability to track arbitrary points in the image make HARP-MRI unique among other tag tracking methods.

2.6.2 Eulerian Strain Calculation

When a body deforms from one configuration to another, the deformation gradient tensor completely characterizes the local deformation of the tissue [79]. If $d\mathbf{X}$ is size of infinitesimally small piece of tissue in the reference configuration, and it deforms to $d\mathbf{x}$ at a later time, then

$$d\mathbf{X} = F^{-1} d\mathbf{x}. \quad (2.27)$$

The deformation gradient tensor F can be calculated using the gradient of displacement as,

$$F^{-1} = I - \nabla \mathbf{u},$$

where I is the identity tensor. Combing the horizontal and vertical HARP values into ϕ and using Eq. (2.26), F^{-1} can written in terms of the HARP values as

$$\begin{aligned}\Omega \mathbf{u} &= \Omega \mathbf{x} - \phi, \text{ where} \\ \Omega &= \begin{bmatrix} \omega_x & 0 \\ 0 & \omega_y \end{bmatrix}.\end{aligned}$$

Therefore,

$$F^{-1} = \Omega^{-T} \nabla \phi(\mathbf{x}, t). \quad (2.28)$$

The gradient of the ϕ is not defined at the phase wrap points, where the phase is discontinuous. So in such points, a modified gradient operator is used to implement the forward difference. This operator uses an inherent difference property² of the wrapped phase to circumvent the problem.

Eulerian strain in any local direction \mathbf{r} at time frame t_n can be computed by selecting $d\mathbf{x} = d\mathbf{r}$, and then using the HARP values to calculate

$$d\mathbf{R} = F^{-1} d\mathbf{r} \quad (2.29)$$

$$= \Omega^{-T} \nabla \phi(\mathbf{x}, t) d\mathbf{r}. \quad (2.30)$$

The Eulerian strain in the direction of $d\mathbf{r}$ in the final configuration is given as,

$$S_{\mathbf{r}} = \frac{\|d\mathbf{r}\| - \|d\mathbf{R}\|}{\|d\mathbf{r}\|} \quad (2.31)$$

This calculation of strain is a Eulerian measure because the strain is being calculation on the deformed grid at time t_N .

Circumferential and radial directions are the two most relevant directions for measuring heart regional deformation (see Fig. 2.13). The circumferential shortening and radial thickening of the myocardial wall have been shown to be good indices of heart's motion. Therefore, by selecting $d\mathbf{r}$ in the circumferential and radial directions, we can calculate local deformations in the circumferential and radial directions. Fig. 2.14 corresponds to

²If $a = \mathcal{W}(\phi)$, then $\nabla \phi = \mathcal{W}(\nabla a)$, where \mathcal{W} is the wrapping operator that wraps any value between $-\infty$ and ∞ to lie between $-\pi$ and π

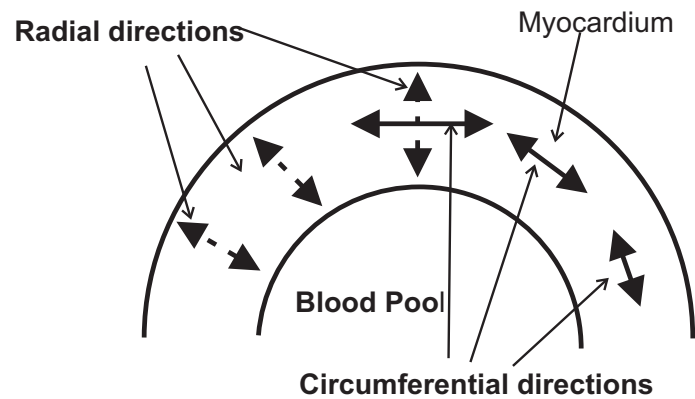


Figure 2.13: Radial and circumferential directions

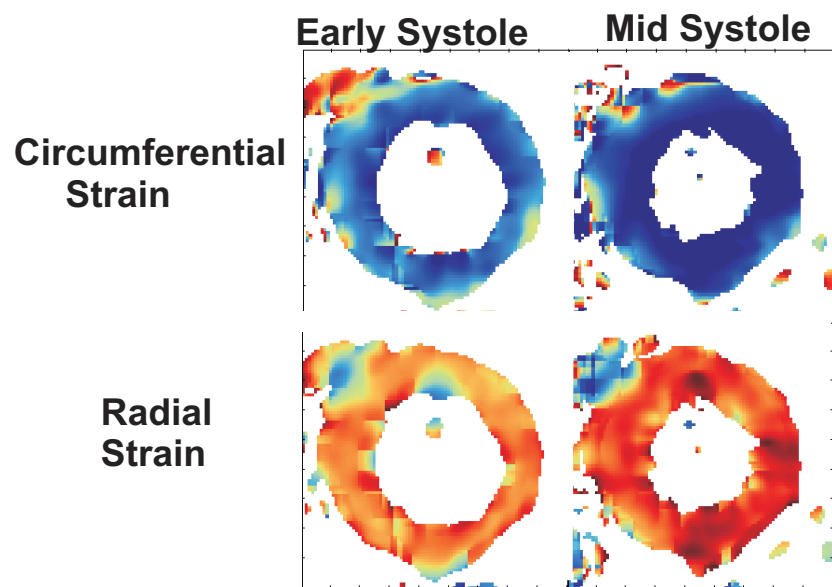


Figure 2.14: Radial and Circumferential Strains

strain the early systolic time frame, while the right panel corresponds to a mid-systolic time frame. Blue corresponds to negative strain or compression, while red corresponds to positive strain or expansion. In the circumferential strain maps, we can see more compression in the mid-systolic time when compared to the early systolic time frame. A similar pattern can be seen in the radial strain, where there is brighter red in the mid-systolic time frames.

2.7 Miscellaneous Background Material

2.7.1 VENC and DENSE

VENC and DENSE are two other methods used for measuring regional deformation of the heart. A key difference between MR tagging and these two methods is that MR tagging uses longitudinal magnetization in order to encode the position of the particle, while VENC and DENSE use the transverse magnetization. VENC-based methods use velocity-sensitive pulse sequences to encode the velocity of each particle in the transverse magnetization [125, 124, 159]. The velocity is then integrated to obtain the displacement. The derivative of displacement gives strain [166]. 1-D strain rates can also be directly obtained from velocities.

DENSE, on the other hand, encodes the tissue displacement directly into the phase of the transverse magnetization. The DENSE pulse sequence looks very similar to that of tagging, and the algorithms used to extract motion bear similarity to HARP-MRI methods. Recent methods have introduced DENSE with parallel imaging techniques, with better temporal resolution, and also with CSPAMM-like techniques[9, 10, 73, 7, 72]

2.7.2 Nyquist Sampling

Fig. 2.15 shows the simplest sampling pattern known as the cartesian sampling. According to sampling theory, sampling of a continuous function in Fourier space creates replicates of the continuous object in space. If the sampling is not fine enough the replica overlap with each other, i.e. spatial aliasing. The Nyquist criterion gives the optimal value for Δk such that an object with a spatial extent of FOV (field of view) mm will not alias in

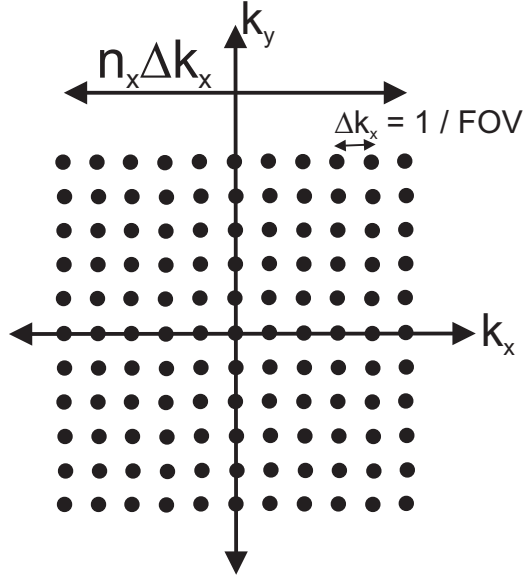


Figure 2.15: Cartesian k-space sampling pattern

the spatial domain

$$\Delta k_{\text{Nyquist}} = \frac{1}{\text{FOV}} \text{ mm}^{-1} \quad (2.32)$$

2.7.3 Spatial resolution

The spatial resolution of the resulting MR image is defined by the extent of k-space acquired. As mentioned earlier in this chapter, only a finite amount of k-space samples are acquired, and the extent of k-space acquired defines the highest frequencies in the MR image. The higher the Fourier frequencies acquired, the more details that can be seen in the MR image, and hence the higher the spatial resolution. In the cartesian sampling shown in Fig. 2.15, the extent of k-space is determined by the number of samples n_x and n_y with sampling intervals Δk_x and Δk_y , respectively. The spatial resolution is defined as the inverse of the extent of k-space acquired. In other words, spatial resolution Δx and Δy are defined as

$$\begin{aligned} \Delta x &= \frac{1}{n_x \Delta k_x} \text{ mm}^{-1}, \\ \Delta y &= \frac{1}{n_y \Delta k_y} \text{ mm}^{-1}. \end{aligned}$$

For a simple cartesian imaging pattern shown in Fig. 2.15, $\Delta x = \Delta y$. These two quantities define the pixel size in an MR image.

The above understanding of spatial resolution as the pixel size is a very practical one, and is also called the intrinsic Fourier resolution. This understanding will be helpful to understand the concepts presented in next chapter. In Chapter 6, however, we expand on this concept in greater detail in order to study the resolution of HARP-MRI. We will model the MR imaging system as a linear system and discuss resolution in terms of the point spread function of this linear system.

Chapter 3

Optimizing HARP-MRI using Simulations

Preface

HARP-MRI uses bandpass filters to extract harmonic spectral peaks that are then used to estimate the motion of the heart. In this chapter, we use simulations to study the effect of the bandpass filter on the accuracy of the estimated motion. A computational cardiac motion simulator is used to simulate the motion of the heart. A variety of different imaging conditions are simulated by varying the parameters of the simulator, namely the size of left ventricular, myocardial strain, and the noise level. For each imaging condition, optimal values of tag separation and bandpass filter size are calculated. The behavior of the optimal values is studied for different imaging conditions, which is then used to form guidelines on how to select optimal HARP-MRI parameters for any given cardiac motion study.

3.1 Introduction

The core idea behind HARP-MRI is that the spectral information required to reconstruct two-dimensional motion is contained around two off-centered harmonic peaks, each containing information about one component of the 2-D displacement. HARP-MRI selectively filters these harmonic peaks for the reconstruction of motion and strain. The filtering operation can be done using three different techniques. First one can acquire the entire k-

space data and then filter out the harmonic peak using a bandpass filter (as explained in the background chapter). The second method is to apply Hilbert transformation on the tagged images, which amounts to acquiring the entire k-space data, zeroing out the negative frequencies, and then take the inverse Fourier transform of the one-sided spectrum [78]. The third method is to avoid acquiring the entire k-space, but only acquire data around the harmonic peak that is finally useful for HARP-MRI. The third method requires a specialized pulse sequence called FastHARP [135].

In all these three cases, the effect of the filter is the same. If the filter is too small, then there is no ability to measure large deformations; and if the filter is too large, then noise and unnecessary patterns called artifacts overwhelm the measurements. Currently, in most HARP-MRI studies the choice of the filter size is based on visual inspection of the spread of the harmonic peak in the spectrum. This heuristic approach depends on the arbitrary scaling of the computer display.

In this chapter, we propose a technique to optimally select the filter size for HARP-MRI. In addition, we will also propose a method to pick the optimal tag separation. Our analysis is based on simulations done using a computational cardiac motion simulator, which uses an analytical model of the heart's motion. We simulate a variety of conditions to mimic the many possible clinical and imaging scenarios that can occur during a HARP-MRI study. We simulate the possible conditions by varying the model parameters of the simulator, namely the left ventricular (LV) size, myocardium strain level, noise level, tag separation, and bandpass filter size. In each case, the error in the strain estimation and tissue point tracking is computed. These errors are used to propose a technique to select optimal values of tag separation and filter size such that the overall error is minimized. Further, we discuss the trade-offs in this approach and provide additional guidelines to optimally use HARP-MRI.

3.2 HARP Vector Field

Recall that a tagged image $I(\mathbf{x}, t)$ is a two-dimensional representation of the sinusoidal modulation of the longitudinal magnetization $M_z(\mathbf{x}, t)$ (see Sec. 2.5 of Chapter 2).

The process of HARP-MRI converts this tagged image into a complex harmonic image $I_{\text{har}}(\mathbf{x}, t) = D(\mathbf{x}, t)e^{j\phi(\mathbf{x}, t)}$. It is useful to see this complex harmonic image as continuous field of 2-D HARP vectors with magnitude $D(\mathbf{x}, t)$ and HARP phase $\phi(\mathbf{x}, t)$, which contains information about the displacement of the tissue.

This perspective of HARP-MRI helps to bridge the gap between VENC and DENSE, and MR tagging. The fundamental difference between VENC/DENSE and MR tagging is that, in the case of VENC/DENSE, motion is encoded in the transverse magnetization M_{xy} , whereas in tagging tissue motion is encoded in M_z . But, when viewed from the vector field perspective, HARP-MRI looks very similar to VENC/DENSE methods, especially DENSE. This is because the HARP vector field lies in the imaging plane, which is the plane of transverse magnetization. Based on this concept, Derbyshire et al. [38] argued that, even though HARP-MRI and DENSE employ very different data acquisition strategies, eventually their motion encoding schemes are the same. The vector field perspective is very useful in studying the errors in HARP-MRI because some sources of error are common to VENC based methods, and VENC errors have been well studied in the literature [163, 154, 27, 160].

Discrete HARP vector field In real MR imaging, the HARP vector field is computed in discrete domain both spatially and temporally. The temporal coordinates are grouped into time frames t_n , $n = 1 \dots N$, where N is the number of time frames in the cine data set. The k-space samples collected in a span of $\Delta t = t_n - t_{n-1}$ are used to form one MR image at time t_n . The quantity Δt defines the temporal resolution of the image series. The spatial coordinates are grouped into voxels, which is cube of size $\Delta x = \frac{1}{N\Delta k}$. The size of the voxel defines the spatial resolution of the MR image (see Section 2.7 in Chapter 2)¹ We will see in this chapter that the spatial resolution dictates the behavior of two major sources of errors.

¹In MR imaging, pixel is commonly referred to as voxel, which is the 3-D analog of a pixel. The third dimension comes from the fact that the imaged 2-D slice is not wafer-thin, but has a thickness that usually in the order of around 5 – 7 mm.

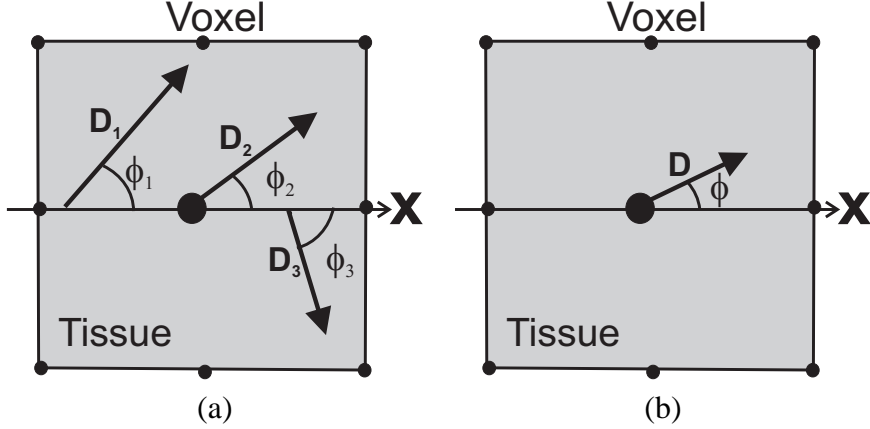


Figure 3.1: Intra-voxel phase dispersion: (a) Phases dispersed within a voxel (b) Net magnitude and HARP value

3.3 Sources of Error in HARP-MRI

There are three major sources of error in HARP-MRI: 1) voxel-based errors: intra-voxel phase dispersion (IVPD) and partial volume effect (PVE), 2) spectral interference, and 3) image noise. We will explore each source in the following.

3.3.1 Voxel-based Errors

Intra-voxel phase dispersion (IVPD). Fig. 3.1(a) shows three HARP vectors within a voxel of a harmonic image. The three vectors have magnitudes D_1 , D_2 , and D_3 and corresponding HARP phases ϕ_1 , ϕ_2 , and ϕ_3 . The averaging of these three complex numbers results in complex number with net magnitude D and net HARP value ϕ at the center of the voxel [see Fig. 3.1(b)]

$$D = \left| \frac{1}{3} (D_1 e^{j\phi_1} + D_2 e^{j\phi_2} + D_3 e^{j\phi_3}) \right|, \quad (3.1)$$

$$\phi = \angle \left\{ \frac{1}{3} (D_1 e^{j\phi_1} + D_2 e^{j\phi_2} + D_3 e^{j\phi_3}) \right\}. \quad (3.2)$$

Since the phase is a nonlinear function, the averaged net HARP phase ϕ is not equal to the average of three component phases. Because of this, there is an error in net HARP

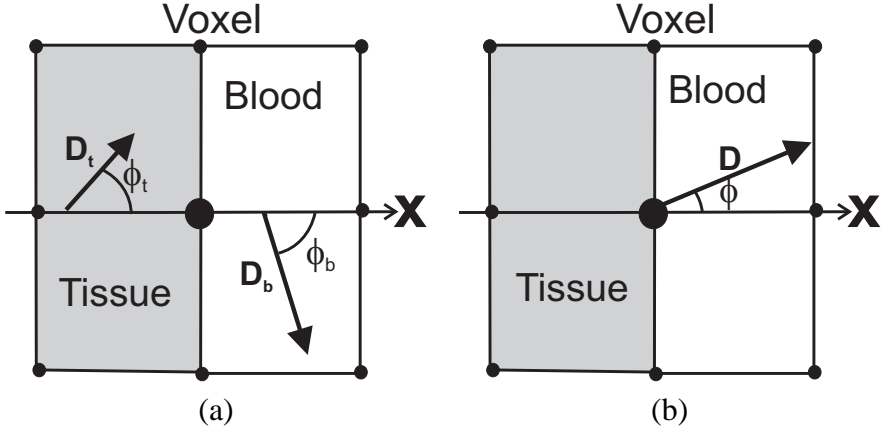


Figure 3.2: Partial Volume Effect: (a) Pixel partly occupied by tissue and blood, showing the individual HARP vectors, (b) the net HARP vector

measurement ϕ at a given voxel and the IVPD error at any given voxel is given as

$$\text{IVPD Error} = \phi - \left(\frac{1}{3}(\phi_1 + \phi_2 + \phi_3) \right). \quad (3.3)$$

IVPD error is caused because of the dispersion of the HARP vectors within an voxel. This dispersion is caused due to the stretching and contracting of the heart muscle, which results in adjacent tissue points having different displacements. This dispersion can be quantified using strain, which is defined as the spatial rate of change of displacement. Since strain occurs at all tissue points, IVPD error occurs all around the myocardium. While the presence of IVPD cannot be eliminated, its effect can be controlled by picking an appropriate voxel size, which is in turn decided by the size of the bandpass filter.

In cases of large strains, the vectors can disperse such that they are completely out of phase and thus can cancel each other out. This causes a signal void within the voxel. On the other extreme, if all the tissue points within a voxel have the same direction of displacement, then IVPD error will be zero. This situation is, however, impossible in the heart.

Partial Volume Effect (PVE). Fig. 3.2 describes another voxel-based error called the partial volume effect. PVE usually occurs at the edges of the myocardium, where a part of the voxel is occupied by the heart tissue and the other part is occupied by a different

tissue or by blood. Ideally, if the signal corresponding to the other tissue is zero, then the signal from the voxel will contain the true motion of the heart. This is not possible since the surrounding tissue has a finite magnitude and HARP phase, which consequently corrupts the net HARP vector. The net HARP vector in a partially occupied voxel is

$$\phi = \angle \left\{ \frac{1}{2} (D_t e^{j\phi_t} + D_b e^{j\phi_b}) \right\}$$

and the PVE error is

$$\text{PVE Error} = \phi - \phi_t.$$

Simulation parameters While the effect of PVE depends solely on the size of the voxel, the effect of IVPD depends on three factors: size of the voxel, strain in the tissue, and tag separation. For the same strain, a smaller tag separation will cause more dispersion in phase than a larger tag separation. This can be seen from Eq. (2.26) of Chapter 2, where the displacement \mathbf{u} is linearly scaled by tag frequency ω_0 . Therefore, in order to study the effects of IVPD and PVE, we need to simulate different tag separations, various levels of strains, and different sizes filters. Both IVPD and PVE lead to a loss of accuracy in the motion estimates.

3.3.2 Spectral Interference

Tagging patterns generated using CSPAMM produce two spectral peaks in k-space: the harmonic peak and the conjugate harmonic peak. Even though most of the spectral energy is concentrated around the two harmonic peaks, the tails of the peak extend much farther than the center of the peak and hence interfere with the other peak. This mutual spectral interference can be seen in Fig. 3.3, where the arrows show the regions of the filtered harmonic peak that are most corrupted by the conjugate peak.

There are two main reasons for the spreading of harmonic peaks. First, the harmonic image is an example of a phase modulated signal. It is well known from the theory of communications that a phase modulated signal has infinite bandwidth, or in other words, has a spread spectrum [82]. The second reason for spectral spreading is the presence of edges in the underlying anatomy, which leads to high frequency components in the spectrum.

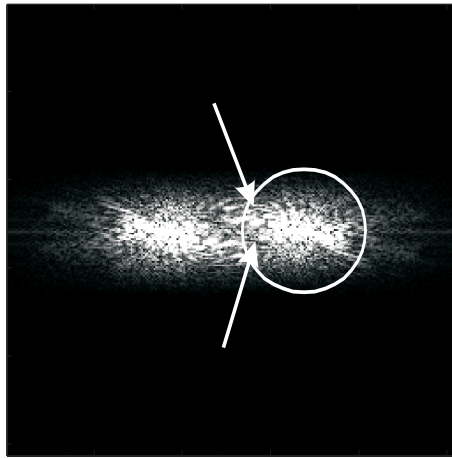


Figure 3.3: Spectrum of a CSPAMM tagged image showing the HARP-MRI bandpass filter. Arrows indicate regions of the harmonic peak most corrupted by spectral interference

Simulation parameters. It is difficult to model spectral interference because the spreading is dependent on the tissue motion, which is the quantity that we want to measure. Moreover, in case of a phase modulated signal, there is no analytical relation between the modulating phase (tissue motion) and its spectrum [93]. Nevertheless, since we understand the reasons behind spectral spreading, we can investigate its effect by simulating different levels of strains, different tag separations, and by varying the position of edges in the image by changing the LV size. Spectral interference primarily affects the smoothness of the measurements and leads to arbitrary patterns called artifacts.

3.3.3 Image Noise

Image noise primarily affects the smoothness of the measurements. It is difficult to model the behavior of noise analytically because the noise in the tagged image undergoes a nonlinear transformation when the phase is computed. Therefore, there is no simple linear relationship between the noise statistics in the image and the noise statistics in the final motion estimates. Moreover, the effect of noise is accentuated during the computation of derivatives for strain calculations.

Table 3.1: Methods ‘at-a-glance’

Simulation type	Model parameters	Model parameter values	Relevant error sources
Anatomy	Left ventricular size	$\{R_i R_o\} = [\{27 34\}, \{27 39\}, \{27 45\}, \dots \{22 34\}, \{32 44\}]$	Spectral interference
	Endocardial strain	$\varepsilon = \{-5\%, -10\%, -15\%, -19\%, \dots -22.5\%\}$ (ε controls strain)	Spectral interference, IVPD/PVE
Tagging	Tag separation	Tag sep (mm) = {14, 10, 7, 5}	Spectral interference, IVPD/PVE
	Contrast to noise ratio (CNR)	CNR = {5, 10, 15, 20}	Noise
HARP-MRI	Filter size (coverage ratio)	Coverage ratio = {0.2, 0.3, ..., 1} (coverage ratio = filter radius/tag frequency)	Spectral interference, IVPD/PVE, and noise

Simulation parameters. The effect of image noise is studied by considering different values of contrast-to-noise ratio (CNR) of the tagged image. The contrast is defined as the peak-to-peak intensity difference of the tagging sinusoid, and noise quantified by its standard deviation.

3.4 Methods

We start this section by describing the simulation methodology. We use the simulations to study the relative magnitudes of the three different sources of error. We then describe the optimization methodology, where we describe the different simulation model parameters that are considered to mimic different imaging scenarios. Finally, we describe the details of real MR data acquisition, which will be used to corroborate the simulation results.

Table 3.1 gives an “at-a-glance” description of the essential details of simulation and optimization methodologies. The first column shows the different parts of the simulation methodology: anatomy simulation, tagging simulation, and HARP-MRI processing. The second column lists the model parameters in the respective parts. The third column shows the different model parameters that are simulated in the optimization methodology. The last column shows the sources of error that the respective model parameters control. Table 3.1 serves as a guide in both the methods and results sections.

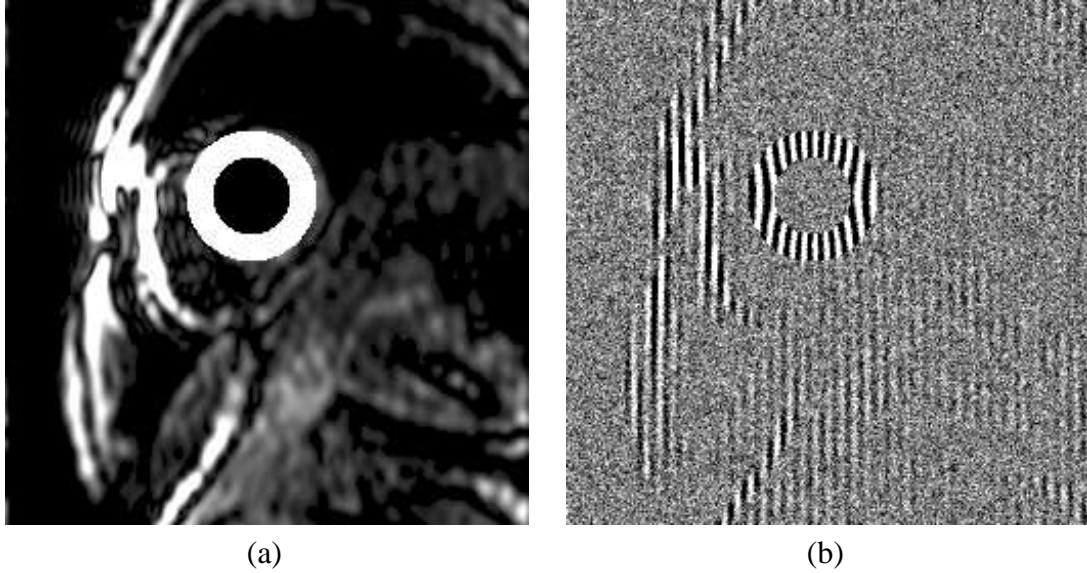


Figure 3.4: (a) Simulated image of the underlying magnetization. The central donut shaped is simulated and background is obtained from an in-vivo image, (b) Image of the underlying magnetization horizontally tagged using CSPAMM protocol.

3.4.1 Simulation Methodology

Anatomy simulation. A computational cardiac motion simulator was used to simulate the motion of the left ventricle of the heart. The simulated contracting left ventricle is incompressible and is shaped like a annulus with a inner radius R_o^i and outer radius R_o^o at end diastole. During systole, the annulus deforms under radial contraction, where an intermediate layer with radius R_o shrinks to a smaller circle of radius $R_n(R_o)$ at time frame t_n .

$$R_n(R_o) = \sqrt{(R_o)^2 + (2\varepsilon_n - \varepsilon_n^2)(R_o^i)^2} ,$$

where ε_n is parameter controlling the strain in the left ventricle at time frame t_n and ‘n’ denotes the n^{th} time frame in a cine image series. The end diastole is considered to be the reference time ($\varepsilon_o = 0$) and the tags are assumed to have been applied at end-diastole.

Figure 3.4(a) shows an example of a short axis image with a simulated left ventricle (see the annulus in the center). All images were generated with field of view of 280 mm and image size of 256×256 pixels. The background is simulated so that the image looks realistic and has spectral components that are comparable to an actual in-vivo image. To simulate

in this realistic background, we performed HARP-MRI on an in-vivo short axis image, and extracted the harmonic magnitude image $D(\mathbf{x}, t)$. The magnitude image was scaled and thresholded in order to regain the sharp edges that were blurred during the HARP-MRI filtering. The left ventricle in the in-vivo magnitude image is replaced by the simulated annulus by making sure that the center of the simulated annulus coincides with the left ventricle in the in-vivo image.

In this chapter, we study the estimation of both Eulerian strain and tissue point tracking. While one set of horizontally and vertically tagged image is sufficient to calculate Eulerian strain at any given time frame t_n , tracking of material points requires a matching set of tagged images that will correspond to the previous time frame. Such a set is simulated by selecting a value of ε_{n-1} so that the strain in time frame t_{n-1} is smaller than that in the current time frame t_n . It is important to select an appropriate value of ε_{n-1} because it controls the amount of displacement between the two time frames. A very large displacement between two consecutive frames causes ambiguity in HARP tracking and may cause tag jumping and erroneous tracks [110]. Recall from Sec. 2.6.1 in Chapter 2, that the basic goal of HARP tracking is to find \mathbf{x} that satisfies:

$$\phi(\mathbf{x}, t_{n+1}) - \phi(\mathbf{x}_n, t_n) = 0. \quad (3.4)$$

Eq.(3.4) always has multiple solutions due to the wrapping of the HARP phase. The HARP tracking algorithm is design to select the solution that is nearest to \mathbf{x}_n . But if the displacement of the tissue point \mathbf{x}_n exceeds half the tag separation between time frames t_n and t_{n+1} , then nearest solution might be the wrong one; and this is known as tag jumping. Therefore one half the tag separation can be regarded as the limit of tracking displacements using HARP-MRI. This quantity, however, is approximate because the exact limit will vary pixel-wise depending on the local strain in the tissue. (A detailed explanation of the dynamic range of tracking is given in Chapter 5).

In this chapter, the tagged images for time frame t_{n-1} are simulated with the constraint that the displacement between two frames be within the limit of tracking at all material points in the myocardium. Mathematically, ε_{n-1} is selected such that the inter-frame radial displacement of the endocardial layer is less than or equal to one half the tag separation, i.e., $[R_{n-1}(R_o^i) - R_n(R_o^i)] \leq \frac{\text{tag separation}}{2}$. In addition to enforcing this condition, we impose

an additional constraint that the endocardial radius of time frame t_{n-1} cannot be bigger than the original end-diastolic endocardial radius, i.e., $R_{n-1}(R_o^i) \leq R_o^i$. This constraint is imposed so that the endocardial radius at t_{n-1} is not bigger than its size at end-diastole, which corresponds to time frame t_o .

It is worth noting that all constraints are solely based on the endocardial radius, R^i , because it undergoes the maximum displacement in the myocardium. In a practical setting, the constraints imposed to avoid tag jumping translates into having adequate temporal resolution.

Tagging simulation. The simulated image of the underlying magnetization is tagged using a CSPAMM protocol. The CSPAMM protocol has been shown to reduce errors in HARP-MRI strain maps when compared to traditional 1-1 SPAMM tagging protocol [78]. We simulated a black blood pool, i.e., all the signal in the blood was zeroed out. This is typical of CSPAMM images. We also ensured that remnants of the in-vivo background are not present in the blood pool [Fig. 3.4(a)]. Also, use of flip angle compensation was assumed to preserve tag contrast [46]. Flip angle compensation is an imaging technique where the fading of tags is largely minimized. White Gaussian² noise is added to the tagged images at a specified CNR level to produce a simulated tagged image as shown in Fig. 3.4(b). For each set of model parameters, a set of two tagged images are simulated, one horizontal and the other vertical.

HARP-MRI processing. Each set of horizontal and vertical tagged images is processed using HARP-MRI and three motion measures are computed: Eulerian circumferential strain, Eulerian radial strain, and tissue point tracking. The HARP-MRI bandpass filter size is measured in terms of the *coverage ratio*, which is defined as the ratio of the filter radius to the tag frequency, i.e.,

$$\text{Coverage ratio} = \frac{\text{filter radius (cycles)}}{\text{tag frequency (cycles)}} = \frac{\text{filter radius}}{\text{field of view/tag separation}} \quad (3.5)$$

The filter size and coverage ratio are directly proportional to each other. For a fixed tag separation, the two terms are interchangeable. The tag separation is embedded in the measurement of the filter radius because it strongly influences the spreading of the spectrum.

²Rician noise is approximated as Gaussian noise because we consider CNR values of 5 or higher.

In Eq.(3.5), both filter radius and tag frequency are measured in discrete k-space units of number of sinusoidal cycles. K-space is assumed to be sampled at the Nyquist sampling rate of $\frac{1}{\text{FOV}} \text{ mm}^{-1}$. Unlike its continuous domain definition $\left(\frac{2\pi \text{ (rads)}}{\text{tag separation (mm)}} \right)$, the tag frequency is discretely measured as the number of sinusoidal cycles in the field of view (FOV).

3.4.2 Relative Magnitude of Error Sources

A four stage experiment was designed to study the relative magnitudes of the different sources of error. In the first stage, a set of tagged images (horizontal and vertical) were simulated in which the left ventricle underwent pure translation with no strain ($\epsilon_n = 0$), no spectral interference, and no image noise. Spectral interference was zeroed out by simulating complex tagging sinusoid $e^{j\phi(\mathbf{x}, t)}$, which has only one peak, instead of a real tagging sinusoid $\cos(\phi(\mathbf{x}, t))$. This first stage is hypothesized to have no sources of error. In the second stage, a strain corresponding to a maximum circumferential strain of -30% was applied ($\epsilon = -19\%$), with other known sources of error remaining zero. The errors due to IVPD and PVE were studied in this stage. In the third stage, in addition to the strain, interference was introduced by simulating a real tagging sinusoid, but still keeping image noise at zero. In the final stage, white Gaussian noise with a CNR of 10 was added to the tagged images. The tag separation in all cases was 7 mm, and a circular HARP bandpass filter of diameter 64 was applied. The root mean squared (RMS) error in circumferential strain, radial strain, and tracking were calculated at all pixel in the myocardium and averaged.

3.4.3 Optimization Methodology

Varying model parameters The steps outlined in the simulation methodology are performed for one set of model parameters. In order to analyze the different possible conditions that could occur during a HARP-MRI study, we simulate different values of the model parameters (see Table 3.1). The details are given below.

Five different sizes of the left ventricle were simulated. The LV size is represented as $\{R_o^i R_o^o\}$, where R_o^i and R_o^o are the inner and outer radii of the left ventricle at end diastole, respectively. The five ventricular sizes were split into two groups. The first group

Table 3.2: True (simulated) strains and displacements for LV size of {27 39} for different values of ε . The value of ε determines the strain at different stages in the cardiac cycle.

ε (%)	Endocardial circumferential strain (% strain)	Endocardial radial strain (% strain)	Endocardial displacement for tracking (mm) [tag sep = 7mm]
-5 (begin systole)	-5.5	5.3	1.4
-10	-12.5	11.1	3.0
-15 (mid-systole)	-21.3	17.6	3.3
-19	-30.9	23.6	3.1
-22.5 (end systole)	-41.4	29.3	2.9

was composed of left ventricles of sizes {27 34}, {27 39}, and {27 45}, sharing the same inner radius, but having varying myocardial wall thickness of 7 mm, 12 mm, and 18 mm, respectively, at end diastole. The second group has left ventricles of sizes {22 34}, {27 39}, and {32 44}, which share the same diastolic myocardial thickness of 12 mm, but have different inner radii. The LV size of {27 39}, which is in common to the two groups coincided with the size of the heart in the in-vivo data set. Analyzing hearts with different myocardial thickness is important in the case of a thinned or enlarged left ventricle, and in the case of the right ventricle, which is much thinner than the left ventricle. Analyzing heart with different inner radii is important in cases of small animal hearts.

Five progressively increasing levels of strain were simulated to mimic the variation of strain from end-diastole to end-systole. The increasing levels of strain were simulated by progressively decreasing the value of ε_n , thereby simulating a cine series during systole. The following values of ε_n were tested: -5% , -10% , -15% , -19% , and -22.5% . Table 3.2 shows the maximum (endocardial) strain values and displacements corresponding to each value of ε_n . The maximum displacements are given for a tag separation of 7 mm. Unlike the maximum strains, the values of maximum displacements do not monotonically increase with ε_n ; most of them are approximately 3 mm. This is because the displacements are bounded above by the dynamic range of tracking, which is $7/2 = 3.5$ mm in this case. The displacements are also bounded from below by R_o^i , which determines the minimum value of endocardial displacement.

The level of noise was changed by varying the CNR values between 5, 10, 15, and 20. These values of CNR are typical for cardiac tagging [132, 58, 152]. For each CNR, 50 Monte Carlo realizations of random noise were performed and the results were averaged.

The number of Monte Carlo trials was decided depending on the convergence properties of the errors in strain and tracking. The convergence of error for p Monte Carlo trials implies that $\frac{\sigma_p}{\sqrt{p}} \leq \frac{1}{100}\mu_p$, where σ_p and μ_p are standard deviation and mean of error after p trials. Fifty Monte Carlo trials were observed to be sufficient for the convergence of the errors in both strain and tracking.

Four typical tag separations of 14 mm, 10 mm, 7 mm, and 5 mm were studied. For each value of tag separation, bandpass filter sizes corresponding to coverage ratios of 0.2, 0.3, ..., 1.0 were considered. For each set of model parameters, HARP-MRI was performed and three motion indices were computed: material point tracking, Eulerian circumferential strain, and Eulerian radial strain. Both the material point tracks and strains were computed on all pixels in the myocardium.

Error computations For each of the three measures, the root mean squared (RMS) error is calculated and averaged over all the pixels in the myocardium. We call this type of error the *pixel-wise RMS error*. Mathematically,

$$[\text{R.M.S. Error}]_{\text{pixel-wise}} = \sqrt{\frac{1}{NK} \sum_{k=1}^K \sum_{(x,y) \in \mathcal{M}} \left(\hat{X}(x, y, \xi_k) - X_{\text{truth}}(x, y) \right)^2}, \quad (3.6)$$

where, \hat{X} is an estimate of motion, X_{truth} is the true motion, \mathcal{M} is the myocardium, N is the number of pixels in the myocardium, ξ_k is the k^{th} realization of random noise, K is the number Monte Carlo realizations of noise, and (x, y) are spatial coordinates of the pixel.

Optimal operating parameters Out of five model parameters, only two of them — tag separation and bandpass filter size — can be selected by the user in a HARP-MRI cardiac motion study. We call these two parameters the *operating parameters*. The overarching aim of these simulations is to learn how to best select the operating parameters for a given study. While the optimal filter size could be selected based on all the model parameters, the optimal tag separation can only depend on LV size and image CNR. Therefore the two questions of optimality are: 1) given an LV size, image CNR, tag separation, and myocardial strain, what is the optimal filter size to use? and 2) given an LV size and image CNR what is the optimal tag separation to use?

Table 3.3: Sources of error and their contributions to overall error. ‘0’ and ‘1’ represents the absence and presence of the respective sources of error.

Sources of error			Magnitude of Error		
IVPD/PVE	Interference	Noise	Circumferential strain (% strain)	Radial strain (% strain)	Tracking (mm)
0	0	0	0	0	0
1	0	0	0.62	6.8	0.42
1	1	0	0.81	7.5	0.42
1	1	1	2.43	7.97	0.43

3.4.4 Invivo Data

We collected in vivo data from a human volunteer to corroborate the optimal values of filter sizes. One healthy volunteer was imaged using a 1.5 T Marconi Eclipse scanner. Informed consent was obtained from the volunteer. A short axis slice was imaged with $\text{FOV} = 280 \text{ mm}$ and tag separation of 7 mm. A CSPAMM data set was obtained for horizontal and vertical tag directions and combined using MICSIR. This data set was also used for creating the background image in the simulations. A set of tagged images from a mid-systolic time frame was picked and CNR was estimated to be approximately 15. The data set was processed with three different sizes of filters: optimal size, less than the optimal size, and more than the optimal size, where the optimal size was calculated using the simulation results given below.

3.5 Results

3.5.1 Relative Magnitude of Error Sources

Table 3.3 shows the contribution of each source of error to the overall RMS error. The ‘0’ and ‘1’ indicate the absence and presence of a particular source of error, respectively. In the absence of any of the sources of error (row 1), the estimation of motion (pure translation in this case), as hypothesized, is perfect. But as soon as strain is introduced, the effects of IVPD and PVE start to affect the motion estimates. The second row shows the contribution of IVPD and PVE to the error in radial and circumferential strains. This effect is especially severe in the case of radial strain, where the loss of accuracy is 6.8%. The effect of spectral

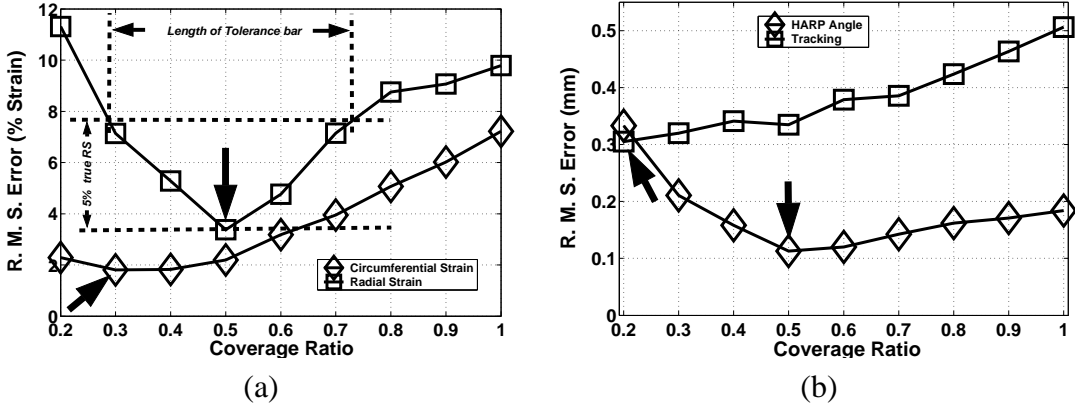


Figure 3.5: Cost functions for (a) circumferential strain and radial strain, (b) HARP angle and tracking displacement for CNR = 5, $\varepsilon = -15\%$, LV size of {27 39}, and a tag separation of 7mm.

interference (row 3) is small and leads to only a slight increase in error in both strains. The addition of image noise (row 4) leads to a three-fold increase in error in circumferential strain, implying that noise is the major source of error in the estimation of circumferential strain. Radial strain is quite robust to the addition of noise and the bulk of the error in radial strain is due to the loss of accuracy due to IVPD and PVE. In contrast to the strains, tracking is very robust to the addition of noise and spectral interference. The error remains almost the same, around 0.4 mm in all rows, which is less than half the original pixel size.

3.5.2 A typical optimality analysis

In this section, we describe a typical optimality analysis. As an example, we use the coverage ratio as the operating parameter to optimize. All other model parameters are fixed. The LV size is {27 39}, strain is fixed at a mid-systolic value ($\varepsilon = -15\%$), CNR is 5, and tag separation is 7 mm. Figs. 3.5(a) and (b) show a set of pixel-wise RMS errors plotted as function of coverage ratio for four different measurements: radial strain, circumferential strain, material point tracking, and HARP angle measurement ϕ . These curves are cost functions for our optimality analysis. The differences in the shape of the four different cost functions are striking. In particular, even though HARP angle is the basic measurement from which the strains and tracking displacements are computed, the error in HARP angle

is not directly predictive of the errors in strain or tracking. This is the main reason why we optimize on strains and material point tracking separately.

Consider the question: Given a set of LV size, strain, CNR, and tag separation, what is the optimal coverage ratio? Among all the coverage ratios, the optimal coverage ratio is the one for which the RMS error is minimum. The optimal coverage ratios for the different measurements are marked using thick arrows in Figs. 3.5(a) and (b). A characteristic minimum is seen in Fig. 3.5(a) in the cost function of radial strain. When the coverage ratios are small, the voxel sizes are large, and the error is dominated by the loss of resolution due to IVPD and PVE. On the other hand, when the coverage ratios are close to 1, interference from the conjugate peak is maximum. Spectral interference and noise dominate the error and reduce the smoothness of the strain maps. A coverage ratio of 0.5 balances out these two sources of errors in the case of radial strain. For tracking performance [Fig. 3.5(b)] we see that the coverage ratios for optimal tracking are very small, unlike those of strains. Smaller coverage ratio means lower resolution. This implies that tracking can perform better with low resolution data than with high resolution data — a counterintuitive result.

Tolerance bars. The optimal operating point is only one descriptor of a cost function. We also need to consider the behavior of the cost function near the optimum. For example, for a very narrow cost function, a small deviation from the optimal parameter will result in large deviation from optimal performance. On the other hand, for a broad cost function, large deviations from the optimal parameter can still be tolerated to achieve near optimal performance. In order to display this property, tolerance bars will be plotted above and below the minimum, where the lengths of the tolerance bars specify the range of filter sizes within which the errors will be the minimum error $\pm 5\%$ of the true motion quantity (see Table 3.2 for true motion quantities). Fig. 3.5(a) gives a pictorial representation of the length of the tolerance bar for the radial strain, which has a narrow optimum compared to the circumferential strain. If the cost function is narrow, then the tolerance bar is small, implying that the measurement is not robust to changes in the optimum operating parameter [Fig. 3.6(b)]. On the other hand, if the cost function is broad, the tolerance bars are large, and suggests that the measurement is robust to changes in optimum [Fig. 3.6(a)]. In a few cases, the cost function has an oscillatory behavior within the tolerance limit of error. In

Table 3.4: Results organization at-a-glance. Key: V: Variable, OV: Optimizing variable,

Analysis #	Section index	Figure index	LV size	strain (ε_n)	CNR	tag sep (mm)	filter size
Analysis 1.1	Sec. 3.5.4	Figs. 3.6, 3.7, 3.8	{27 39}	V	V	7	OV
Analysis 1.2	Sec. 3.5.5	Fig. 3.9	V	V	5	7	OV
Analysis 2	Sec. 3.5.6	Fig. 3.10	V	-19%	V	OV	already optimized

such cases, a symbol ‘NM’ is printed next to the optimal value. Practically, this symbol means that the optimal values are inconclusive and should be seen with less confidence.

3.5.3 Organization of Results

In the remainder of the results section, we study how the optimal operating parameters vary with other model parameters. We have streamlined the entire analysis into two smaller analyses, each corresponding to the one question of optimality (see Table 3.4). Analysis 1 addresses the first question: how to select the optimal filter size? The optimal filter size could depend on all model parameters, and the analysis can get complicated. Hence, we have further split this analysis into 2 parts (analysis 1.1 and 1.2). In each part, two model parameters are fixed, and the optimal filter size is studied as functions of the two variable parameters. Analysis 2 addresses the second question: how to select an optimal tag separation? The strain is fixed to a mid-systolic value and the optimal tag separation is studied for different LV sizes and different values of CNR.

3.5.4 Analysis 1.1: Selection of Optimal Filter Size for {27 39} and 7 mm tag separation

This analysis shows how to select the optimal filter diameter for a LV size of {27 39}, a tag separation of 7 mm, and two extreme CNR values of 5 and 20. Figure 3.6 shows plots of optimal filter diameters for circumferential strain, radial strain, and tracking. Note that the optimal coverage ratios have been converted to actual filter diameters. The optimal filter diameters are plotted as function of increasing strain. In all three cases, the optimal filter size for CNR 20 is greater than or equal to that of CNR 5. As CNR improves, the image noise decreases, and more of k-space can be included without losing smoothness due to noise. In the case of circumferential strain [Fig. 3.6(a)], the filter sizes are distinctly

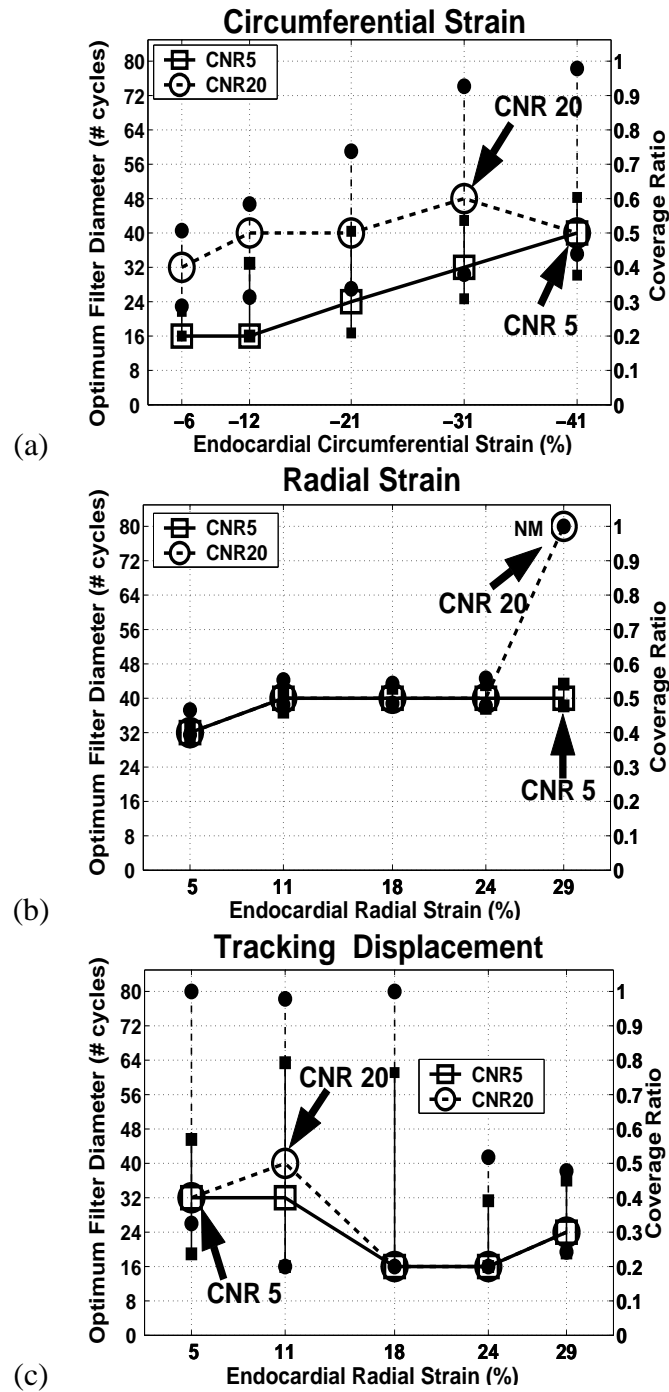


Figure 3.6: Optimal filter diameters for (a) circumferential strain, (b) radial strain, and (c) tracking displacement for LV size 27,39, tag separation of 7mm, and for 2 CNRs 5 (circle) and 20 (square). Note that the tracking displacements are plotted on the radial strain axis to facilitate comparison between strain and tracking, and also to indicate the position of the heart in the cardiac cycle.

greater for CNR 20. This corroborates an earlier finding that image noise is one of the major sources of errors in circumferential strain. In the cases of radial strain [Fig. 3.6(b)] and tracking [Fig. 3.6(c)], the difference between CNR 5 and CNR 20 is not very distinct, implying that noise is not a main contributor to the errors in radial strain and tracking.

The tolerance bars for tracking and strain have very different lengths. In particular, the bars for radial strain are much shorter than those of tracking, indicating a lack of robustness in the radial strain estimates. Another example of this lack of robustness is the abrupt increase in the filter size for the largest value of strain [Fig. 3.6(b)]. The ‘NM’ sign beside it confirms that this is an inconclusive optimum. On the other hand, the tolerance bars for circumferential strains, like that of tracking, are long, showing that both are quite robust to change in filter sizes.

In terms of coverage ratios (right hand axis in Fig. 3.6), the optimum for radial and circumferential strains range between 0.4 and 0.7. The ratios are even smaller (0.5–0.3) in the case of tracking displacement. These ratios correspond to optimum filter sizes of 40 ± 10 samples in k-space, which explains the feasibility of acquisition protocols like FastHARP, which acquires only 32×32 samples around the harmonic peak [135].

The minimum pixel-wise RMS errors corresponding to the optimal filter sizes are shown in Figs. 3.7(a)–(c). The errors in endocardium, mid-wall, and epicardium are plotted separately as functions of increasing strain. In both strain plots, the errors in all three layers increase with increasing strain. The reason for this is that spectral spreading increases with strain, which in turn leads to increased IVPD, PVE, and spectral interference. Furthermore, the error in the radial strain is around 1.5 to 2.5 times that of CS. In both strains, the mid-wall has the least error and endocardium has the maximum error. While the higher strain in the endocardium leads to more IVPD, PVE affects the endocardium and epicardium more than the mid-wall. Even though no such consistent pattern can be seen in tracking, tracking errors for all ranges of strains are bounded by an error of 0.45 mm, which is less than half the original pixel size.

A consistent pattern is seen in tracking in the case of signed error [Fig. 3.7(f)], which gives a measure of bias of the estimate. The signed error still considers the errors pixel wise, but unlike the RMS error [Eq.(3.6)], it averages them directly without the squaring. The sign of the error gives a measure of bias of the estimate. While the tracking displacements

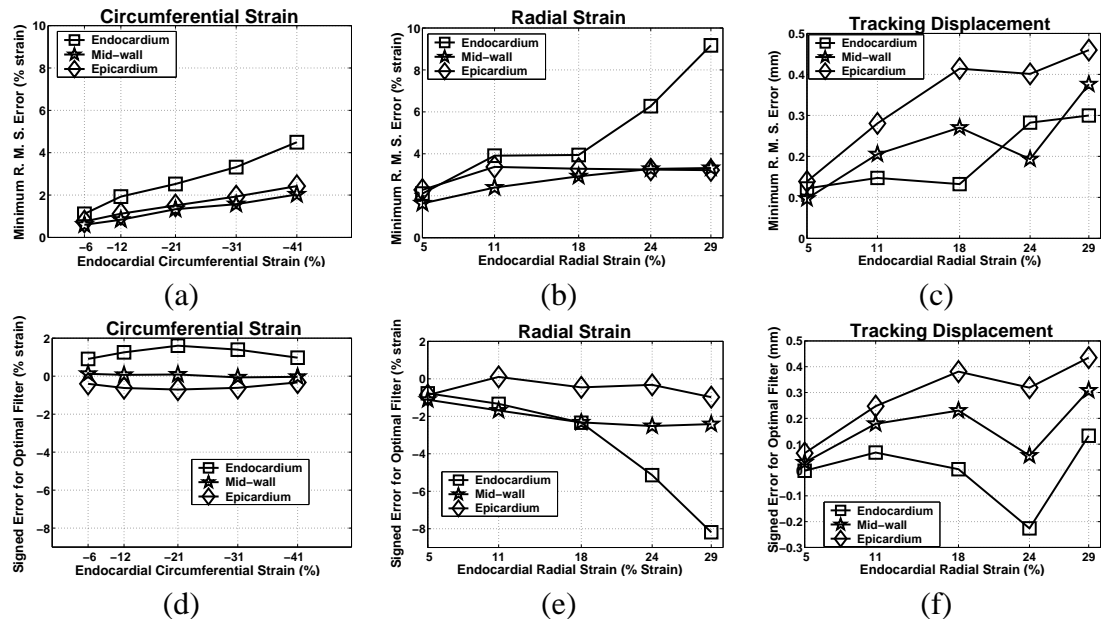


Figure 3.7: Minimum pixel-wise RMS errors corresponding to the optimal filter sizes are given in (a)–(c) for three layers of the myocardium. The corresponding signed errors are given in (d)–(f). The errors are calculated for CNR 5, LV size of {27 39}, and a tag separation of 7 mm.

are underestimated (signed error < 0) in the endocardium, the displacement in the mid-wall and epicardium are overestimated (signed error > 0). A exact opposite pattern is seen in the circumferential strain [Fig. 3.7(a)] where the endocardial strain is overestimated, and the epicardial strain is underestimated; albeit only by $\sim 1\%$ percent. (Care should be taken in interpreting the bias of the circumferential strain, since it is a negative number). The estimates of radial strain are always underestimated, in some cases as high as 8% for maximum strain [Fig. 3.7(e)]. While the mid-wall and epicardium have relatively low errors ($\sim 2\%$), the endocardium is the most severely affected due to the increased effect of IVPD.

After analyzing the optimal filter sizes, we now ask the question, how many k-space samples should be acquired in the first place? This is a more basic question. Unlike the optimal filter sizes, the amount of data acquired cannot generally be a function of the strain in the tissue. Therefore, the data acquisition size should correspond to the maximum filter size for each set of model parameters. The maximum filter sizes are marked with arrows in Fig. 3.6 for the two values of CNRs. The data acquisition size is usually equal (though not necessary) to the optimal filter size corresponding to the maximum strain value. In Fig. 3.8, the data acquisition sizes are shown as a functions of tag separation. As the tag separation decreases, the spectral spreading increases and the data acquisition size also increases. Also, the data acquisition values increase with increase in CNR. The data acquisition sizes for radial strain are much larger than that of circumferential strain and tracking. So, the decision to pick the data acquisition size should be based on the maximum radial strain expected in the entire cardiac cycle.

The discussion about the amount of data acquisition size is not only pertinent to limited k-space pulse sequences like FastHARP, but also to traditional tagging acquisitions where both the harmonic peaks are acquired. This analysis can help reduce the number of phase encode lines acquired, thus considerably speeding up image acquisition for cardiac motion estimation.

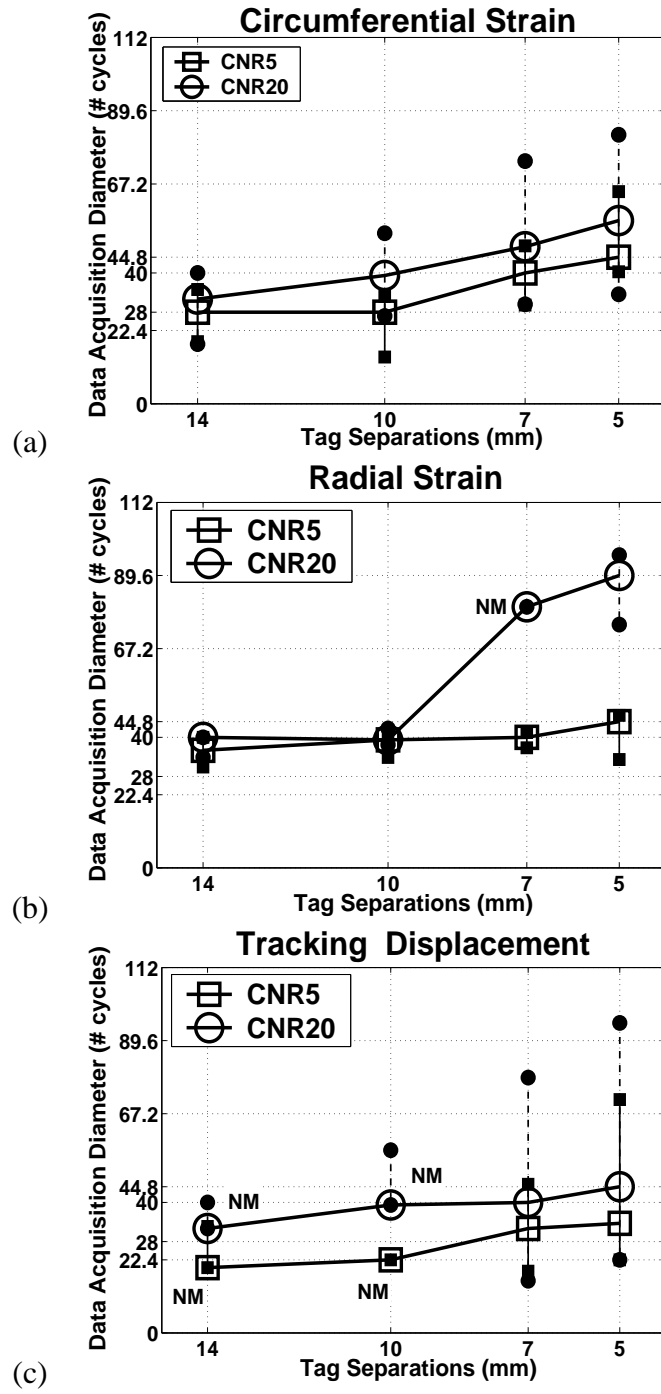


Figure 3.8: Data acquisition sizes plotted as a function of tag separation for (a) circumferential strain, (b) radial strain, and (c) tracking displacement, for LV size of {27 39} as function of tag separation. The data acquisition size of radial strain is more than circumferential strain and tracking.

3.5.5 Analysis 1.2: Variation of Optimal Filter Sizes with LV size for 7 mm tag separation

The difference in optimal filter sizes between the two sets of LV sizes is shown in Figs. 3.9(a) and (b). Unlike our earlier analyses, where all the three motion measures were analyzed, in this analysis only the results for radial strain are considered. From our observations, we have seen that circumferential strain and tracking are quite robust to changes in LV size, and therefore these results not presented here. Also, as a representative case, only the lowest CNR of 5 is considered.

Myocardium with thinner walls (for example {27 34}) have a larger spread in the spectrum, which leads to more RMS errors [Fig. 3.9(a)]. In contrast, the corresponding comparison of minimum RMS errors for myocardium of same thickness but with varying inner radius shows that the errors are not very different [Fig. 3.9(b)]. The variation of optimal filter sizes between these two groups of LV sizes are shown in Figs. 3.9(c) and (d). Among the hearts with same thickness, the difference in optimal filter sizes is small [Fig. 3.9(d)]. Among hearts with different wall thicknesses, there is no consistent pattern that can be seen [see higher strains in Fig. 3.9(c)]. This is because the errors due to wall thickness enter as spectral interference, whose behavior cannot be modelled completely. Nevertheless, the key observation from this analysis is that the myocardial wall thickness is an important factor to be considered while deciding the optimal parameters for HARP-MRI.

3.5.6 Analysis 2: Selection of Optimal Tag Separation for a mid-systolic strain

In this analysis, we discuss the selection of the optimal tag separation for a mid-systolic strain ($\varepsilon = -19\%$). The optimization of tag separation is not independent from the optimization of filter size; in fact, they are nested, with the filter size optimization as the inner core, and the tag separation optimization as the outer core. In optimizing for tag separation, we use only the optimal values of filter size that were derived from the previous two analyses. Therefore, the actual question we will be addressing in this analysis is: Given an LV size, an image CNR, a strain value, and optimal filter sizes, which tag separation produces

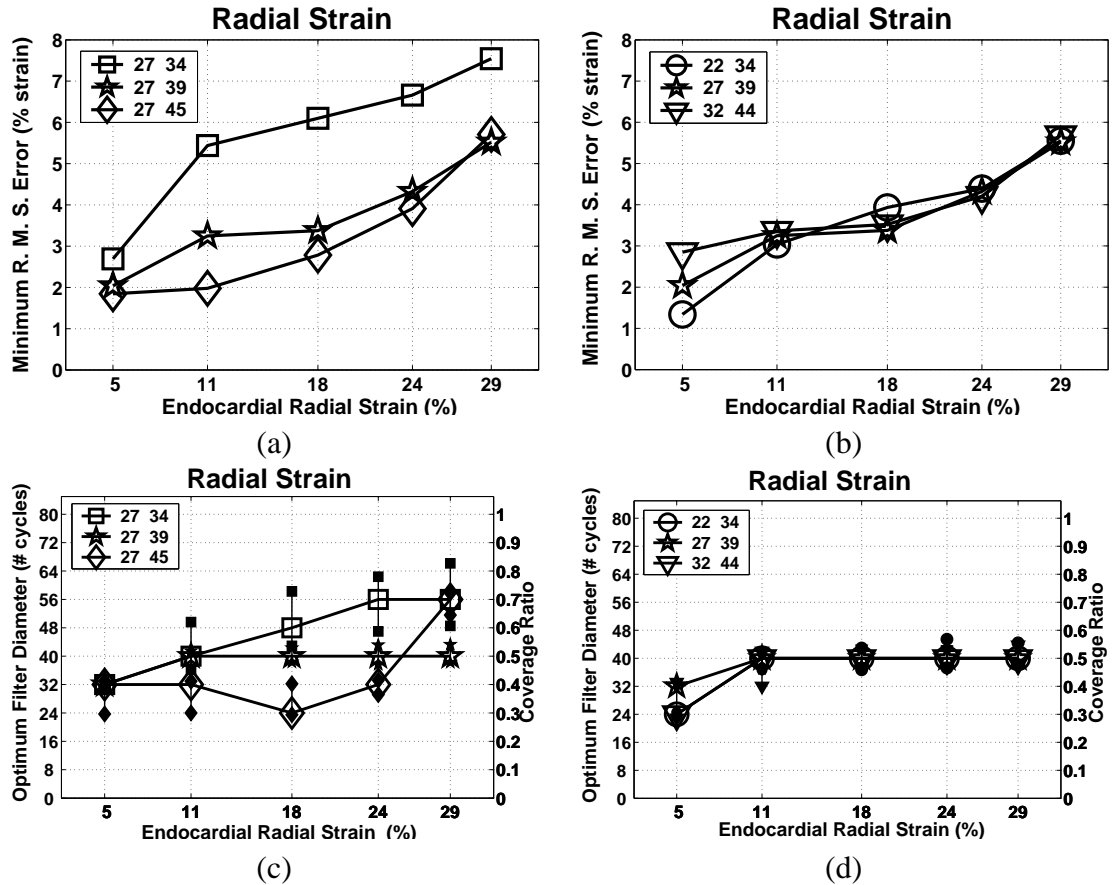


Figure 3.9: A comparison of minimum errors in radial strain across (a) hearts with different wall thickness, but the same inner radii and (b) hearts with different inner radii, but the same wall thickness. Corresponding optimal filter diameters are shown in (c) and (d). While hearts with the same wall thickness have similar optimal values, the hearts with different wall thickness have markedly different optimal filter sizes and minimum errors.

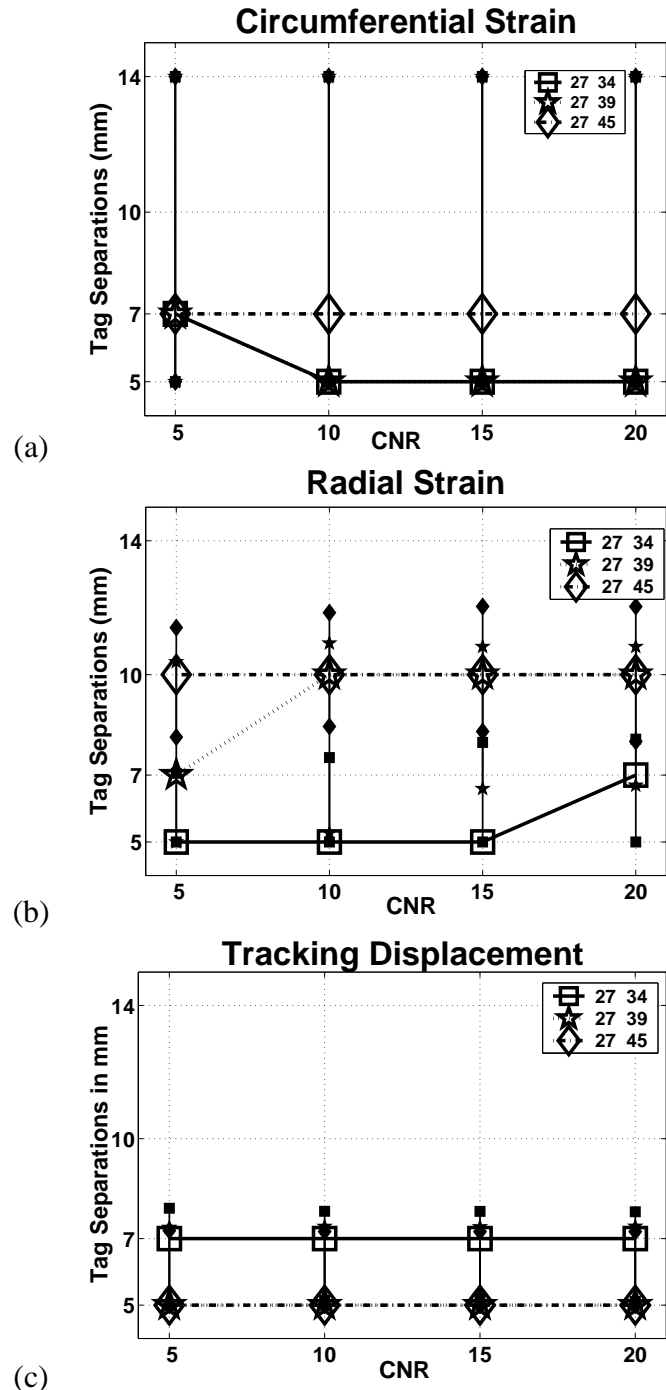


Figure 3.10: Optimal tag separations as a function of CNR for hearts with different wall thicknesses.

the minimal RMS error?

Fig. 3.10 shows the optimal tags separations for the strains and tracking as function of CNR for 3 different LV sizes with varying heart thickness. Figs. 3.10(a) and (c) indicate that smaller tag separations of 5 and 7 mm are better for both circumferential strain and tracking, and they are quite robust to changes in wall thickness as well. For radial strain, however, tag separation should increase with increasing wall thickness [Fig. 3.10(b)]. This implies that the optimal number of tag lines across the myocardial wall is approximately the same for different wall thicknesses. Interestingly, in all three cases the optimal tag separation does not change dramatically with CNR, and also the tolerance bars are long. This implies that the tag separations are quite robust to changes in both CNR and wall thickness.

3.5.7 Comparison with Region-based Cost Function

In the previous analyses, the pixel-wise RMS error was used in the cost functions. This was done in order to explicitly analyze the error at every pixel. In most clinical applications, however, the measures are averaged over regions of interest (ROI) like in the case of bulls-eye plots. In order to study such ROI measures, we define the region-wise RMS error based on dividing the myocardium into N_o octants along the circumference and $N_{\mathcal{L}}$ layers along the radii of the myocardium (see Fig. 3.11) as follows

$$[\text{R.M.S. Error}]_{\text{region-wise}} = \dots$$

$$\sqrt{\frac{1}{N_o N_{\mathcal{L}} K} \sum_{k=1}^K \sum_{i=1}^{N_o N_{\mathcal{L}}} \left(\frac{1}{N_i} \sum_{(x,y) \in S_i} \hat{X}(x, y, \xi_k) - \frac{1}{N_i} \sum_{(x,y) \in S_i} X_{\text{truth}}(x, y) \right)^2},$$

where $i = 1, \dots, (N_o \times N_{\mathcal{L}})$, S_i is i^{th} ROI, and N_i is the number of pixels in S_i . In this work, we use $N_o = 8$ octants, and $N_{\mathcal{L}} = 3$ layers (endocardium, mid-wall , and epicardium).

Fig. 3.12(a)–(c) plots the ratio between minimum errors of region-wise and pixel-wise cost functions. In all the three cases of circumferential strain, radial strain, and tracking, the ratio is less than one. This implies that the minimum error in the region-wise measure

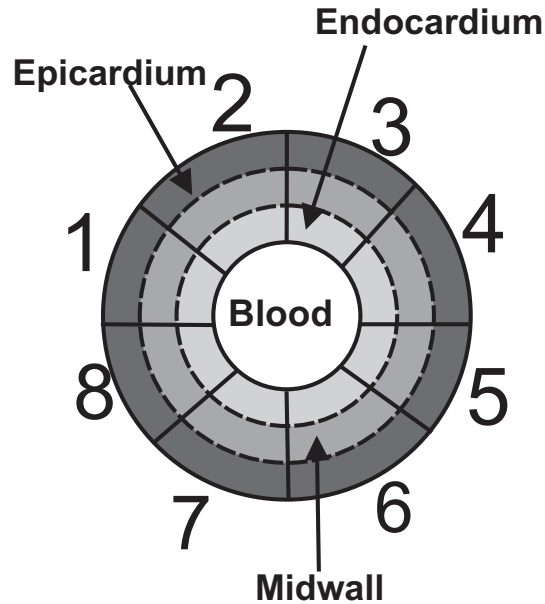


Figure 3.11: Schematic showing the three layers and eight octants of the myocardium

is always less than the minimum error in the pixel-wise case. This is because the region based approach averages out small perturbations in the estimates caused by noise and interference. Since noise and interference are the main error sources in circumferential strain, region-wise averaging has the most dramatic effect on circumferential strain. Errors are reduced by more than half in the region-wise case when compared to the pixel-wise case. For radial strains, the decrease in strain is not very pronounced because radial strain is affected more by IVPD and PVE. The reduction in errors in tracking is neither very dramatic nor consistent.

The bottom row of Fig. 3.12 shows the ratio of optimal filter sizes for the two error measures. In all three cases, the ratio is greater than or equal to one. This implies that the optimal filter sizes derived using the region-wise approach are larger than those derived using the pixel-wise approach. This is because the smoothing of local perturbations in the region-wise approach increases the robustness and smoothness of the estimates, thereby leading to larger filters. Optimal filter sizes for tracking are least affected by the choice of error measure, with the ratios near one, whereas the circumferential strain filter sizes are 1.5–2 times larger than their pixel-wise counterparts. The ratios for radial strain are also

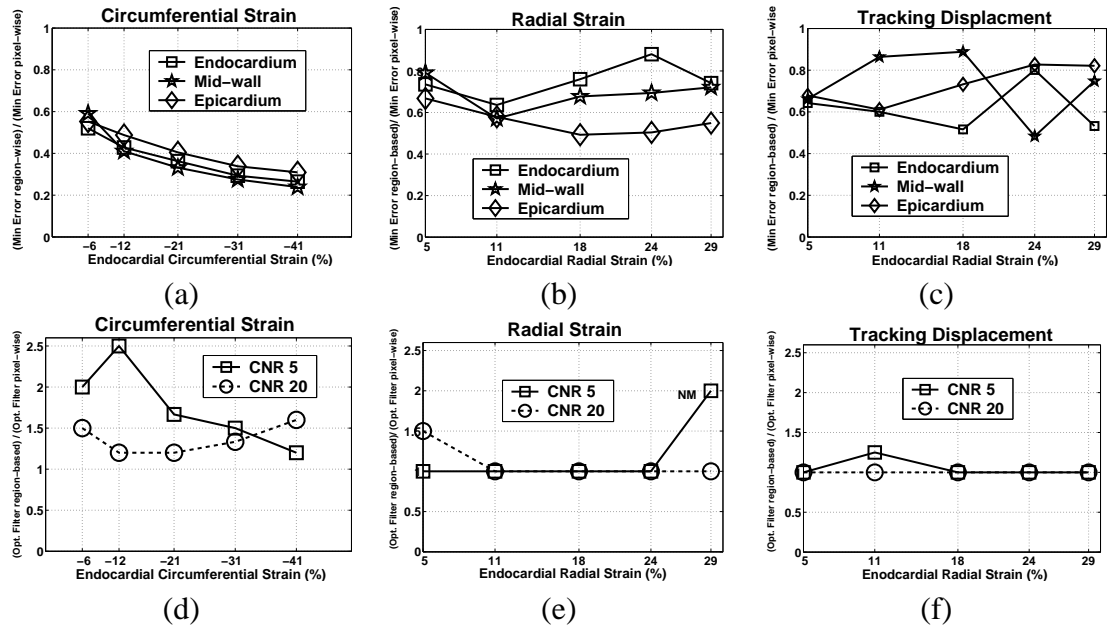


Figure 3.12: Top row shows the ratio of minimum RMS error calculated region-wise and pixel-wise. The bottom row shows a ratio of the optimal filter sizes calculated in the two cases. The errors in the region-wise measurements are always less than pixel-wise. And the optimal filter sizes in region-wise are always greater than or equal to their pixel-wise counterparts.

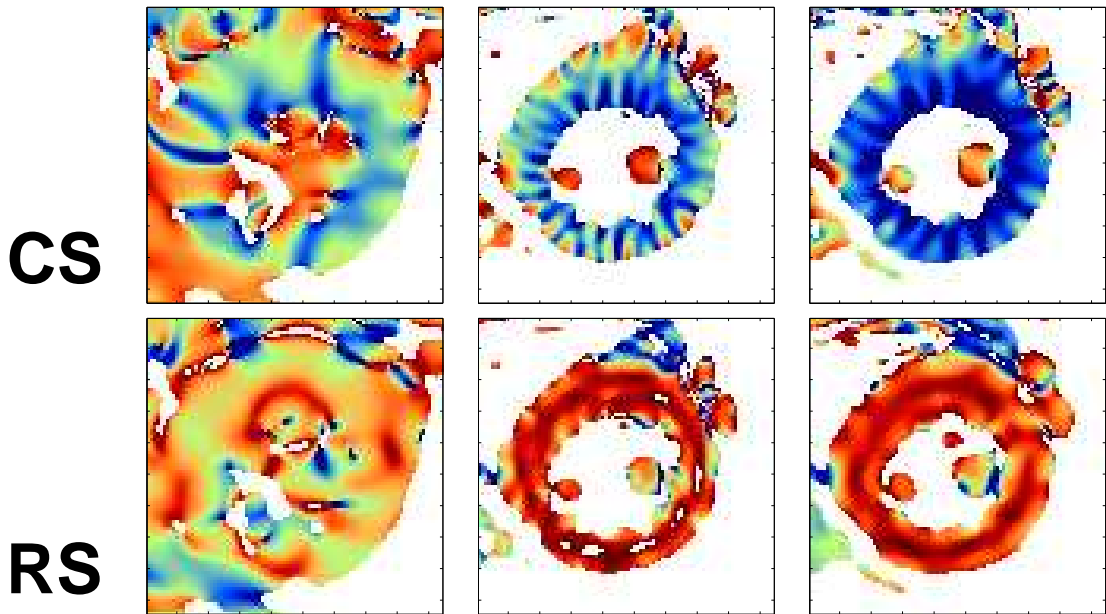


Figure 3.13: The first column shows the corresponding strains using a filter size that is smaller than optimal. The second column shows the strains using a filter size that is larger than optimal. The third column are the estimates of circumferential strain (top row) and radial strain (bottom row) using the optimal filter. The third column offers a compromise between the blurring and loss of accuracy in column 1, and spoke-like artifacts and loss of precision in column 2. All strain maps are plotted on the same color scale.

around one.

3.5.8 In vivo Results

Figure 3.13 demonstrates an application of the optimization analysis on a mid-systolic time frame from our in vivo data set. The heart size was {27 39}, FOV was 280 mm, and the tag separation was 7 mm. The image CNR was estimated to be 15. Using a preliminary HARP filter having coverage ratio 0.5, the endocardial strain was estimated to be -35% in the circumferential direction and 25% in the radial direction. These strain estimates were obtained by manually picking pixels corresponding to the endocardium and averaging the strains at these pixels. With these strain inputs, the optimization toolbox was used to calculate the optimum filter diameters for circumferential strain and radial strain. The coverage ratio of 0.6 was found optimal for circumferential strain, which corresponds

to a filter diameter of 48 ($2 \times 0.6 \times \frac{280}{7}$) cycles. A filter diameter of 40 cycles was found optimal for radial strain.

The first column shows the results using a filter of diameter 20 cycles, and the second column shows the corresponding results using a filter of diameter 70 cycles. All images are multiplied using a mask generated by applying a threshold on the harmonic magnitude image. While the strain maps in the first column are grossly smoothed out by the loss of resolution, the second column is affected by noise and spectral interference, which manifests as spoke-like ‘zebra’ artifacts. The white patches in the middle of the heart wall in the radial strain estimates (Fig. 3.13 second column second row) indicate that the radial strain has been so excessively overestimated that it is out of range of display. The last column shows the map of circumferential strain and radial strain estimated using optimal filter sizes. Even though the effect of IVPD and PVE can still be seen in these optimal strain maps [see for example the difference in red coloration between the mid-wall and endocardium in radial strain in Fig. 3.13(c)], the results show a dramatic improvement over strain maps in column 1, in terms of resolution and accuracy. When compared to column 2, the circumferential strain in column 3 has reduced zebra artifacts, and the radial strain looks better. Thus, use of the optimal filter size is a trade-off between the lack of accuracy in column 1 and the lack of smoothness in column 2.

3.5.9 HARP-MRI Optimization Toolbox

The entire analysis performed in this chapter can be reproduced with user-defined model parameters using the ‘HARP-MRI optimization toolbox’. This toolbox is a supplement to this chapter and can be downloaded from

<http://iacl.ece.jhu.edu/projects/optimHARP/>. All the figures in the results section of this chapter are outputs of this toolbox. This tool box was created using MATLAB 6.5 (Mathworks, Natick MA, USA).

3.6 Discussion

3.6.1 Relation to previous work

The effect of the bandpass filter on HARP-MRI measurements has been previously studied in different contexts. Osman et al. [111] made the first attempt to select an optimal filter, where the optimality was based on the error in the HARP angle. Kuijer et al. [78] calculated the errors in principal strain maps for showing that the use of CSPAMM is more desirable for HARP-MRI. Sampath et al. [137] used a gel motion phantom to validate the FastHARP pulse sequence in terms of tracking errors. Each of these previous works concentrated on only specific aspects of the optimality problem, whereas the present chapter is more comprehensive because it considers the effects of different sources of error on the estimation of Eulerian strain and tracking.

3.6.2 General trends in the simulated data

A few general trends can be discerned from the plots in the results section. These trends are not only consistent across the plots presented in this chapter, but also across the remainder of the data as well. (The simulated data for cases other than the representative ones can be accessed using the toolbox.) The progression of error in strain across the myocardial wall (endocardial error > epicardial error > mid-wall error) is consistent across all values of CNR, tag separations, and LV sizes. This phenomenon can be attributed to the increased effect of IVPD and PVE in the endocardium. With respect to image noise, an increase in CNR increases the robustness of the estimates, and thereby leading to larger filters. This effect is most noticeable in the estimation of circumferential strain. The effects of changes in tag separation are also consistent across different model parameters. A decrease in tag separation leads to an increase in filter sizes. As the tag separation decreases, the tag frequency increases pushing the harmonic peak farther away from the center of k-space. An increase in tag frequency also increases the spectral spread of the harmonic peak, thus requiring larger filters to capture the spread. An increase in tag separation, however, has quite a different effect. As the tag separation increases, the spectral peaks come closer to the center of k-space and also to each other. In such cases, there is an increased oscillation in the

cost functions, which leads to inconclusive minima and ‘NM’ symbols [see Fig. 3.8(c)]. A probable reason for this behavior is that, as the coverage ratio is progressively increased from 0.2 to 1, the amount spectral information added at each step is small. Moreover, this small amount of spectral information is corrupted by increasing spectral interference because the peaks are close to each other.

Unlike strain, it is difficult to describe general trends in the estimation of tissue point tracking. The overall performance of tracking can be judged by a worst case analysis. With a tag separation of 14 mm (maximum spectral interference) and with a CNR of 5 (maximum noise) the error in tracking was still bounded by 0.7 mm, which is 3/4 the size of the original pixel.

3.6.3 Trade-offs and comparing radial and circumferential strains

In order to systematically analyze the effects of different sources of error, it is important to understand the trade-offs between sources that reduce the resolution of the estimates (IVPD and PVE) and the sources that affect their smoothness (noise and interference). This trade-off, which can be clearly seen in Fig. 3.5, is one of the over-arching themes of this chapter. It is striking to see the marked difference in the effects of this tradeoff in the estimation of radial and circumferential strains. The estimation of circumferential strain is always more accurate and more robust than the estimation of radial strain. This difference is akin to the difference in estimation resolution of the principal stretch ratios reported by Kuijer et al. [78]. (The principal stretch ratios λ_1 and λ_2 are oriented along the radial and circumferential directions respectively.) Two reasons can be attributed to this difference. First, the degrading effect of IVPD and PVE are more pronounced than the effects of noise and interference. Since, radial strain is primarily affected by IVPD and PVE, their estimation suffers from a huge loss of resolution. Second, the part of the harmonic peak corresponding to radial expansion is closer to the conjugate spectral peak than the part corresponding to circumferential compression. Therefore the radial strain is more prone to interference errors as well. This difference between the patterns in radial and circumferential strains will be revisited in the chapter on smoothing artifacts.

3.6.4 Performance of tracking

Another important finding in this chapter is the difference in HARP-MRI’s performance in estimating Eulerian strain versus tracking. Contrary to previous understanding [78], the effect of the bandpass filter on tracking is dramatically different than its effect on strain. The optimal filter sizes for tracking are much smaller compared to those of strains, implying that IVPD, PVE and the subsequent loss of resolution does not affect tracking resolution. This suggests that the motion tracking spectrum — i.e. the spectral information that is needed to track a tissue point accurately — is contained within a very small region in k-space. The apparent difference in the performance of tracking and Eulerian strain stems from the fact that while estimation of Eulerian strain uses only the current frame, tracking uses two images of consecutive frames to track tissue points. So, even though both the images are smoothed out by the filter, they are smoothed out to the same extent. Hence, the uniqueness of the HARP phase — the basic premise of HARP tracking — is preserved, and the loss of spatial resolution does not affect HARP tracking. This robustness of phase information in tracking is not surprising, given that phase has been widely used in measuring image velocity and optical flow [47]. As an important corollary to the robustness of tracking, the Lagrangian strains, which are computed using tracked points, can also be estimated accurately.

The main source of tracking errors in practice is fast motion between frames. As long the motion between the two frames is not too large, the resolution of tracking is preserved at small filter sizes. This limit of motion, which is defined was the dynamic range of tracking, is approximately one half the tag separation. The selection of optimal tag separation, therefore, is crucial to the performance of tracking. Although Fig. 3.10 shows that smaller tag separations are better, it is not advisable to use the smallest possible tag separation because the smaller the tag separation, the higher temporal resolution that is required in order to maintain the dynamic range of tracking. Also, smaller tag separations cause more spectral spreading and hence need larger amounts of k-space to be collected. Moreover, the chance of annihilation of the tag signal due to heart rotation is higher for smaller tag separations. Therefore, selecting an mid-range tag separation (like 7 mm) instead of the smallest possible one, is a good way to balance the demands of temporal resolution, the

amount of k-space data to be acquired, and the problem of heart rotation. This was the reason why a tag separation of 7 mm was used in both Analyses 1.1 and 1.2.

3.6.5 Imaging considerations

We recommend the use of CSPAMM for use with HARP-MRI, and all our simulations herein were based on CSPAMM. CSPAMM produces pure sinusoidal tags with no peak at the center of k-space. This improves the smoothness by reducing the spectral interference, thereby improving the visual appeal of the strain maps. Also, the absence of the central peak allows the use of larger filter, which increases the resolution as well. But, in the event that 1-1 SPAMM is used, a switch in the toolbox can be used to generate the corresponding optimal filter sizes. Further, the effect of tag fading is not considered in this chapter since use of flip angle compensation is assumed. The absence of flip angle compensation can be folded into the optimization analysis as a decrease in CNR, which can be set using the HARP-MRI optimization toolbox.

Even though there is a trade off between the sources of error affecting the resolution and smoothness, the improvement of both resolution and smoothness go hand-in-hand. Imaging protocols that inherently reduce spectral interference not only improve the smoothness, but also improve the resolution by allowing the use of larger filters. CSPAMM is one example. In this respect, the use of grid tags is undesirable for HARP-MRI since the spectrum of sinusoidal grid tags consists of four or more spectral peaks, each of them having their own spectral spread. Compared to acquiring horizontal and vertical tags separately, the spectral interference in the case of grid tags is four-fold. Because of this increased spectral interference the size of the optimal filter also needs to be small, which in turns reduces the resolution as well. Therefore, the use of grid tags is a lose-lose situation, with respect to resolution and smoothness. The acquisition of grid tags, however, requires only half the time as compared to acquiring horizontal and vertical tags separately, and may nevertheless be required in some applications.

3.6.6 Minor (avoidable) sources of errors

Apart from the major sources of error, there are a few minor sources that are avoidable with little extra care during the imaging and processing steps. First, the tag separation and the FOV should be selected such that there are integer number of tag cycles in the FOV. The Fourier transform of an unmodulated 2-D sinusoid with integer number of cycles consists of two delta peaks at the tag frequency on either side of the origin. In the case where there are non-integer number of cycles, the spectrum of the 2-D sinusoid are no longer delta peaks, but are small peaks spread out around the tag frequency. This non-ideal spectrum corrupts the underlying modulating spectrum by a small amount. Second, while positioning the bandpass filter, it is important to position it exactly at the tag frequency and not at the center of mass of the harmonic peak. Wrong centering of the peak leads to errors in the strain values. Finally, in the calculation of the HARP phase derivatives, it is better to use a symmetric finite difference rather than a one-sided finite difference. The symmetric difference produces more accurate estimates of strain compared to one-sided finite difference [19]. Finally, the Gibbs ringing effect due to the bandpass filter also leads to loss of visual quality. The ringing effect can be minimized by appropriate roll-off of the filter. The filter used in this chapter has a flat pass band, with a Gaussian roll-off on the sides as described in [111].

3.7 Summary and Recommendations

This chapter used simulations to identify the sources of error in HARP-MRI and to derive optimal operating parameters for using HARP-MRI in different clinical scenarios. The key results of this chapter are as follows:

- Circumferential strain is sensitive to noise and interference; radial strain is sensitive to IVPD and PVE; and tracking is robust to all sources of error. Tracking is mainly affected by inadequate temporal resolution.
- Noise and interference lead to a loss in smoothness in the estimates, whereas IVPD and PVE lead to a loss in spatial resolution.

- Selection of optimal parameters is a trade-off between resolution and smoothness of the measurements.
- Estimation of strain and tissue point tracking require different optimal parameters.

Based on these key results and the other analyses in this chapter, we have the following recommendations for the optimal imaging and analysis of HARP-MRI data. The recommendations have been split into three categories: before, during, and after k-space acquisition.

1. Before k-space acquisition

- (a) The use of the CSPAMM with flip angle compensation is recommended.
- (b) Separate acquisitions of horizontal and vertical tags is recommended instead of a combined grid tag acquisition.
- (c) A preliminary scan should be used to roughly estimate the LV size and the CNR of the tagged image. Then the parameter optimization toolbox can be used to run the simulations for different values of tag separations, strain levels, and filter sizes.
- (d) Simulated data should be used to find the optimal tag separation for an expected mid-systolic value. The choice of the optimal tag separation will depend on whether the aim of the study is to estimate Eulerian strain or to perform tissue tracking. When both need to be done, select tag separation based on the strains, especially the radial strain.
- (e) Tag separation should be divisible by the FOV.

2. During k-space acquisition

- (a) Selection of the data acquisition size should be based on the maximum strain that is expected during the cardiac cycle. Since radial strain requires the most k-space coverage, the data acquisition sizes should also be decided based on maximum optimal filter diameters for radial strain.

- (b) Selection of the optimal HARP filters should be based on two factors: image CNR and an initial estimate of the strain in the tissue. A coverage ratio of 0.5 gives a good initial estimate of endocardial strain at each time frame, which can then be used to select optimal filters.

3. After k-space acquisition and during HARP-MRI analysis

- (a) Place the bandpass filter exactly at the tag frequency and not on the center-of-mass of the harmonic peak spectrum. If the filter is required to placed off the tag frequency, care should be taken to note down the exact position of the filter and use it appropriately in the HARP calculations.
- (b) The use of region-wise (octant-based) measures is recommended over pixel-wise strain maps. The region-wise measurements are twice as accurate as pixel-wise measurements.

3.8 Forward Pointers: What is coming up next?

This chapter used a brute-force approach to simulate different imaging conditions in order to better understand HARP-MRI. Consideration of all the different conditions led to a very high-dimensional (around 400 dimensional) optimization space. Hence, the main challenge in this chapter was to systematic organize the methods and the results so that the analyses did not degenerate into a group of mere simulated plots. This resulting systematic organization resulted in a stepwise recipe (in typical ‘cook-book’ style) for the optimal use of HARP-MRI.

The brute-force approach raises a very interesting question: ‘Why are simulations necessary to select the optimal filter?’ The answer to this question lies in the fact that HARP-MRI is a nonlinear system, because computation of phase is a nonlinear operation. This nonlinear system has five inputs (tag separation, filter size, LV size, CNR, and strain) and two outputs (strain and tracking), and the principles of convolution and superposition do not hold for this system. Hence, the effect of the bandpass filter on the HARP phase cannot be studied under a customary and familiar linear mathematical framework. Using a linear

approximation does not capture the true effects of the system. As a result, each case had to be studied separately, which required simulations.

The above answer raises another question: ‘Is there a more elegant way to pick the optimal filter?’. The short answer is ‘approximately’. In the next few chapters, we set HARP-MRI in a communications theory framework, which allows us to make some key simplifying approximations. These approximations help us derive analytical expressions to study the effect of the bandpass on the motion estimation. The analogy with communication theory sets the stage for a series of smaller chapters, each studying a different aspect of HARP. In Chapter 5, we analyze the maximum motion that can be measured for a given filter size, also known as the dynamic range of HARP-MRI. In Chapter 6, we re-define the concept of strain resolution and use the communication theory to explain observations in this chapter. In Chapter 7, we will study the ability of HARP-MRI to detect small abnormalities, even in cases of reduced strain resolution. Finally in Chapter 8, we devise an algorithm to reduce the artifacts produced by noise and interference. The observations made in this chapter underly the strategies explored in these subsequent chapters.

Chapter 4

Communications Theory Framework

Preface

The selection of an optimal HARP bandpass filter requires understanding the effect the filter has on the HARP phase. Although the actual process of filtering is linear, the computation of HARP phase makes the entire system nonlinear. Therefore, the effect of the filter on the HARP phase cannot be analytically expressed in closed form. In this chapter, we circumvent this problem by setting HARP-MRI in a communications theory framework. We interpret the tagged image as a signal that is modulated in both magnitude and frequency, i.e. an AM-FM signal. The tissue strain is interpreted as the instantaneous frequency (IF) of the AM-FM signal. The theory of AM-FM signals is used to derive two key approximations that relate tissue strain to the filtered Fourier data.

This chapter is relatively short and sets HARP-MRI in a communication theory framework. The purpose of this chapter is to facilitate the formal characterization of HARP-MRI in light of the observations made in the previous chapter. The communications theory framework is seen as the bridge between Chapter 3 and the subsequent chapters.

4.1 AM-FM Signals

The signal

$$s(t) = a(t) \cos(\phi(t)) \quad (4.1)$$

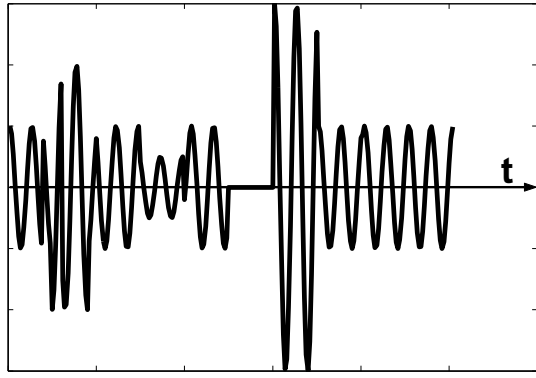


Figure 4.1: An example of an AM-FM signal.

represents an AM-FM signal, where $a(t)$ and $\phi(t)$ modulates the amplitude and the frequency of the sinusoid, respectively. An example of an AM-FM signal is shown in Fig. 4.1. The frequency modulation $\phi(t)$ is expressed in terms of the carrier frequency of the sinusoid,

$$\phi(t) = \omega_c t + k_p m(t),$$

where ω_c is the carrier frequency, k_p is a constant, and $m(t)$ is the “message” encoded in the phase of the carrier. Since the message varies with t , the frequency content of the AM-FM signal varies as well. This variation in the frequency of the AM-FM signal is captured by the *instantaneous frequency* (IF) $\omega_i(t)$ which is defined as the derivative of the phase of the AM-FM signal [18, 19]

$$\omega_i(t) = \frac{d}{dt}\phi(t) = \omega_c + k_p \frac{d}{dt}m(t).$$

Practically, IF is computed using the analytic form of the AM-FM signal.

$$\omega_i(t) = \frac{d}{dt}[\angle z(t)], \text{ where} \quad (4.2)$$

$$z(t) = s(t) + j\mathcal{H}[s(t)] \quad (4.3)$$

$$= a(t)e^{j\phi(t)}, \quad (4.4)$$

where \mathcal{H} is the Hilbert transformation operator and $z(t)$ is the complex-valued analytic signal uniquely associated with $s(t)$.

Analogy with tagged images. Recall the expressions of a vertical tagged image and the corresponding harmonic image (Eqs.(24) and (25) in Chapter 2).

$$I^{ver}(\mathbf{x}, t) = M(\mathbf{x}, t) \cos(\omega_x x - \omega_x u_x(\mathbf{x}, t)) \quad (4.5)$$

$$I_{\text{Har}}^{ver}(\mathbf{x}, t) = D^{ver}(\mathbf{x}, t) e^{j\phi^{ver}(\mathbf{x}, t)}, \quad (4.6)$$

Comparing Eqs.(4.1) and (4.4) with Eqs.(4.5) and (4.6) respectively, we see that a tagged image is an AM-FM signal, and the complex harmonic image is analogous to the corresponding analytic image, with the only difference that the sinusoid is in two-dimensional space rather than time. By analogy, the two-dimensional instantaneous frequency of the harmonic image is a vector which is equal to the spatial gradient of the HARP phase.

$$\boldsymbol{\omega}_i^{ver}(\mathbf{x}, t) = \nabla \phi^{ver}(\mathbf{x}, t) = \left[\frac{\partial}{\partial x} \phi^{ver}(\mathbf{x}, t) \quad \frac{\partial}{\partial y} \phi^{ver}(\mathbf{x}, t) \right]^T \quad (4.7)$$

Similarly, the horizontal component can also be computed using horizontally tagged images. The two IF vectors can be combined into one matrix

$$\nabla \phi(\mathbf{x}, t) = [\nabla \phi^{ver}(\mathbf{x}, t) \quad \nabla \phi^{hor}(\mathbf{x}, t)]. \quad (4.8)$$

This IF matrix is equal to the derivative of the HARP vector field and is used directly to calculate the Eulerian strain (Eqs.(33) and (34) in Chapter 2)

The relation between IF and Eulerian strain can be easily understood pictorially. Fig. 4.2(a) shows a vertically tagged image of an rectangular object split into three parts with different amplitudes in each part. A horizontal profile is shown in Fig. 4.2(b). Even though the amplitudes of the sinusoid are different in the three parts, their frequency is the same in all three parts. The bottom row shows a horizontally tagged image where the left one third is compressed (negative Eulerian strain), the right one third is stretched (positive Eulerian strain). The middle portion is neither stretched nor compressed (zero Eulerian strain). The corresponding profile in Fig. 4.2(d) clearly shows a increase in frequency of the local sinusoid in the compressed part and a corresponding decrease in frequency in the expanded part.

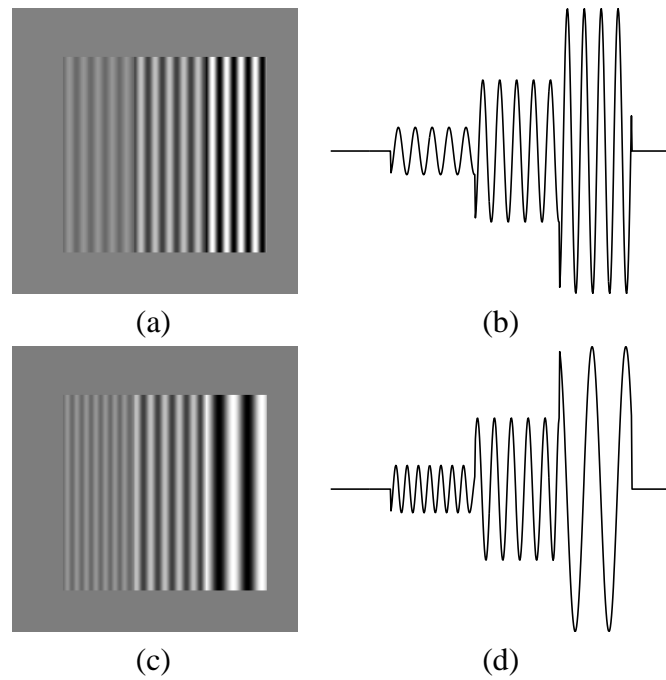


Figure 4.2: (a) Three parts of the object have different amplitudes but same IF. (b) shows a horizontal profile across the image in (a). (c) Three parts of the object have different amplitudes and different IF as well. (d) shows a horizontal profile across image in (c)

4.2 Instantaneous Frequency and Fourier Frequency

HARP-MRI is as a phase demodulation process, in which the estimation of Eulerian strain is essentially the estimation of instantaneous frequency. Therefore, the aim of this chapter can be restated as: to understand the effect of a linear filter on the estimation of instantaneous frequency. Since the filtering is done in the Fourier domain, it is necessary that we understand the relation between instantaneous frequencies and Fourier frequencies.

The above pictorial explanation intuitively suggests that there is direct relation between the instantaneous frequency of the sinusoid and the sinusoidal Fourier frequency. Unfortunately, this intuition is not supported by theory. The relation between IF and Fourier frequencies has been a subject of much research and discussion over several decades [93, 45, 18, 33]. In 1974, Mandel gave two specific examples where the instantaneous frequency present in the AM-FM signal was completely absent in the Fourier spectrum of the signal [93]. He argued that they are fundamentally different quantities with very different physical meanings, and that there is no one-to-one relationship between the two frequencies. Theoretically, the Fourier frequencies are defined over the entire time domain, whereas the instantaneous frequencies are defined at a particular instant in time.

In 1966, Fink that argued this apparent contradiction is usually overlooked by the engineering community [45]. This is because, for the simplest harmonic signal $s(t) = a \cos(\omega_c t + \phi)$, the constant instantaneous frequency and the position of the impulse in the spectrum coincide. So, he concluded that there must be some connection between IF and Fourier frequencies, but the connection cannot be expressed simply. This lack of this direct relation makes the study of the effects of the filter on the HARP phase even harder. In the 1990s, however, a few simplifying approximations were introduced for a special class of AM-FM signals called *monocomponent signals*.

4.3 Monocomponent signals

Monocomponent signals are AM-FM signals that have a single spectral component, with a narrow range of Fourier frequencies varying as a function of time or space [64]. The intuitive relation between the IF and Fourier frequencies were proved to be true for

monocomponent signals. This intuitive relation can be summed up in two statements.

1. The instantaneous frequency at each time is the frequency of the local sinusoid that fits the signal at that time.
2. The instantaneous frequency is the average of Fourier frequencies at each time.

A detailed explanation of this idea requires a background in time-frequency analysis and is beyond the scope of this dissertation. Details can be found in [161, 90, 106, 33].

A cine series of one-dimensional CSPAMM tagged MR images is an example of a monocomponent signal because it has only one spectral component at the tag frequency, with the majority of the energy lying around the harmonic peak. Therefore the above two statements apply to tagged MR images, and will be used to explain the behavior of HARP-MRI in the next two chapters on dynamic range and resolution.

Chapter 5

Dynamic Range of HARP-MRI

Preface

In using simulations to optimize HARP-MRI in Chapter 3, we analyzed an inverse problem: ‘Given values of the output (tissue displacement and strain), how to select the optimal inputs (filter size and tag separation)?’ In this chapter, we study a corresponding forward problem: ‘Given a set of filter size and tag separation, what are the limits of displacement and strain that HARP-MRI can measure?’ The limits of displacement and strain are collectively called the *dynamic range* of HARP-MRI. We will use an approximate relation between IF and Fourier frequencies to derive analytical expressions for dynamic range. These expressions are validated using simulated and real MR data.

5.1 Introduction

Dynamic range of a medical imaging system is its ability to observe the organs of interest with good level of contrast. Most medical imaging systems have adjustable parameters that are used to control their dynamic range. For example, in X-ray projection radiography, image contrast can be controlled by changing the H&D curve of the X-ray film [128]. The H&D curve adjusts the exposure parameters of the film so that the organs of interest fall in the linear part of the film’s response, thereby producing better contrast. The length of the linear part of the H&D curve defines the dynamic range of the X-ray detector.

All imaging and related image processing methods that measure cardiac motion have either an implicit or an explicit limit on their ability to measure heart’s motion. In echocar-

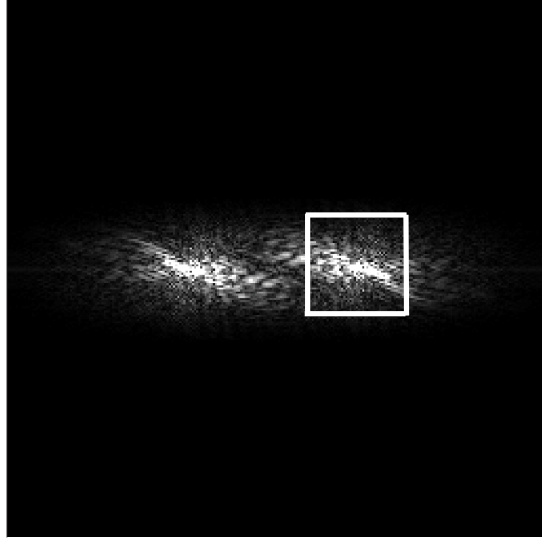


Figure 5.1: FastHARP k-space acquisition.

diography, the frequency of the ultrasound waves can change the limits of wall motion that can be observed. In the case of MR phase contrast methods, the velocity encoding parameter controls the maximum and minimum velocity that can be measured [126]. Tagged image processing methods, which track tag lines, use models of heart motion in order to reconstruct strain from tag displacements [69]. The parameters of the model control the smoothness of the results and indirectly control the amount of motion that these methods can measure.

In this chapter, we will determine the limits of tissue displacement and strain that HARP-MRI can measure. In HARP-MRI, the two controllable parameters are tag frequency and filter size. Figure 5.1 shows the size and position of a typical bandpass filter. Note that the shape of the filter is square rather than circular. This is because, in this chapter, we study the dynamic range of the FastHARP pulse sequence [135], wherein only a limited number of k-space samples are acquired around the harmonic peak. The results in this chapter is easily adapted for other filtering approaches.

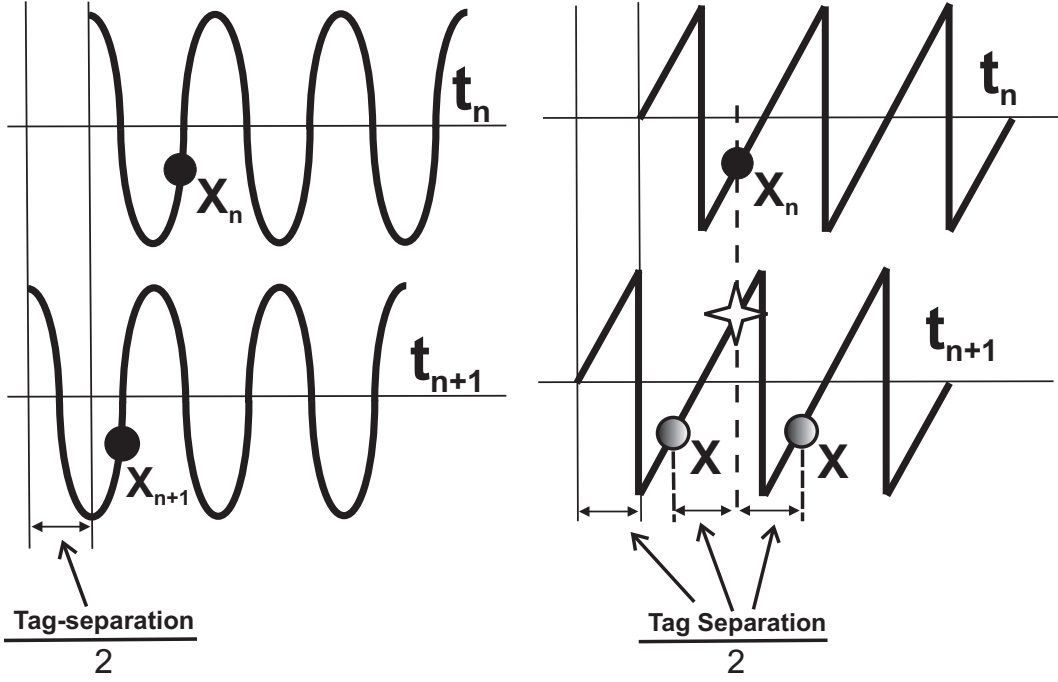


Figure 5.2: Top left figure shows a tag pattern at time t_n . Bottom left figure shows the tag pattern translated to the left by half the tag separation. Right panel shows the corresponding HARP phase. The star represents the initialization point at time t_{n+1} and shaded circle represent two equally close probable solutions to HARP tracking.

5.2 Dynamic Range of Tissue Point Tracking

In Chapter 3, we concluded that the main cause of error in tracking was tag jumping due to insufficient temporal resolution. Fig. 5.2 explains this phenomenon in detail. The top row shows the position of point x_n on a tagging sinusoid at time t_n . Let us suppose that in time frame t_{n+1} , the entire tissue moved to its left by half the tag separation under pure translation (bottom row). Assume, for simplicity, that the tissue doesn't undergo any compression or elongation. In order to track the point x_n , HARP tracking algorithm solves for \mathbf{x} in t_{n+1} such that,

$$\phi(\mathbf{x}, t_{n+1}) - \phi(\mathbf{x}_n, t_n) = 0, \quad (5.1)$$

This is pictorially shown in the right side of Fig. 5.2. Equation 5.1 is solved iteratively with \mathbf{x}_n as the initial point for the iteration (denoted as a star in Fig. 5.2). Due to the wrapping of the phase, there are multiple points with the same HARP phase, implying that Eq. 5.1

has multiple solutions. For a lack of better criterion, the algorithm is designed to converge to the closest solution.

When the motion is exactly equal to half the tag separation, there are two solutions (shaded circles in Fig. 5.2) that are equally close to the initial point, and this causes ambiguity. The correct solution is to the left of the initial point. If the displacement is more than half the tag separation, the point on the right will be the closest solution, and hence the solution will converge to the wrong position. Therefore, half the tag separation defines the dynamic range of tracking, the limit up to which HARP tracking algorithm can measure displacement correctly.

This limit is, however, is approximate because it assumes that the tissue underwent pure translation, without any strain. In the case of compression, when tags come closer together, the dynamic range of tracking reduces further. On the other hand, during expansion, the tags go farther apart and the dynamic range of tracking increases. Generally, the actual dynamic range of tracking depends on the local strain in the tissue.

5.3 Dynamic Range of Eulerian Strain

In this section, we study the dynamic range of Eulerian strain, which is bit more involved than the dynamic range of tracking. First, we describe a key approximation that links the IF with the Fourier frequency.

5.3.1 A Key Approximation

The dynamic range of Eulerian strain can be seen as the dynamic range of instantaneous frequencies. Recall that the IF is defined as the spatial gradient of the HARP phase.

$$\boldsymbol{\omega}_i(\mathbf{x}, t) = \nabla\phi(\mathbf{x}, t) = \left[\frac{\partial}{\partial x}\phi(\mathbf{x}, t) \quad \frac{\partial}{\partial y}\phi(\mathbf{x}, t) \right]^T, \quad (5.2)$$

$$= \Omega(\mathbf{x}, t)\angle\theta(\mathbf{x}, t). \quad (5.3)$$

(The superscript has been omitted because the analysis is common to both horizontal and vertical tags.) From communications theory, we understand that for monocomponent AM-FM signals, an instantaneous frequency of value ω_i at a particular point \mathbf{x} means that

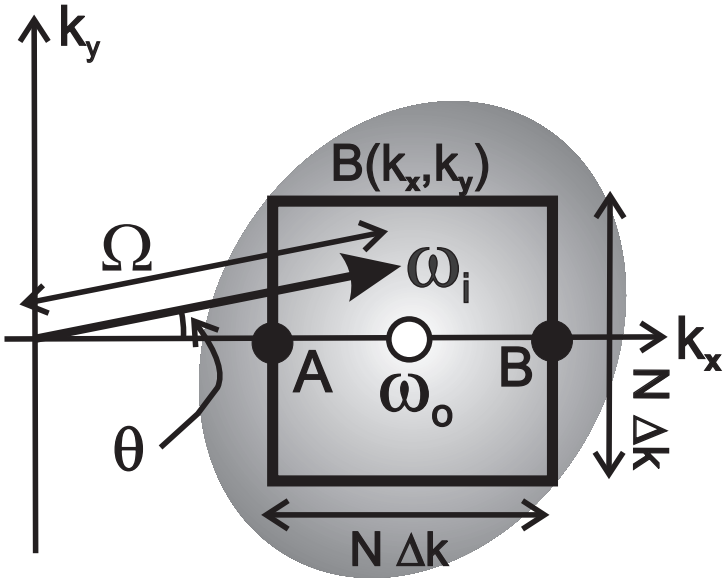


Figure 5.3: Schematic of the bandpass filter in frequency domain

there exists a local sinusoid of frequency Ω in the direction of $\angle\theta$ at that point. In order to relate this local sinusoid to the Fourier spectrum of the AM-FM signal, we make a key approximation. We know that an eternal sinusoid with frequency ω_i will have two impulses in the spectrum placed at $\pm \omega_i$ in Fourier space. Now, even though the sinusoid in this consideration are very localized, we make an approximation that the spectrum associated with the local sinusoid of frequency ω will also be impulses in the Fourier domain. In other words, a small region around x with IF ω_i will correspond to impulses in the Fourier domain at $\pm \omega_i$. This is rather a drastic approximation; nevertheless, we make it in order to make the mathematics tractable. We will validate this approximation using simulated and real MR data.

5.3.2 Dynamic Range of Eulerian Strain: Impulse In or Out

Fig. 5.3 shows a diagram of the filtering process. The gray blob represents the spectrum of the tagged image (only one side of the spectrum is shown). The bandpass filter $B(k_x, k_y)$ is a square of side $N \Delta k$, where N and Δk are the number of samples and sampling interval in k -space (in mm^{-1}) respectively. The filter is centered around the tag frequency $[\omega_0 \ 0]^T$.

We claim that the IF at a spatial point \mathbf{x} will be detected if the impulse corresponding to the IF lies within the bandpass filter $B(k_x, k_y)$. Mathematically, this claim can be written by placing simple bounds on the x and y components of the IF. Let $W = N\Delta k$ be size of the bandpass filter in mm^{-1} . Let $A = \omega_0 - \frac{W}{2}$ and $B = \omega_0 + \frac{W}{2}$, be the bounds of the filter along the k_x axis (Fig. 5.3). Given W , A , and B , the instantaneous frequency $\Omega\angle\theta$ will be reconstructed by HARP if the x and y components are fall within the horizontal and vertical extents of the filter, i.e.,

$$A \leq \Omega |\cos \theta| \leq B , \quad (5.4)$$

$$0 \leq \Omega |\sin \theta| \leq \frac{W}{2} . \quad (5.5)$$

The maximum and minimum value of Ω is the dynamic range of compression and elongation, respectively. The dynamic range of θ determines the dynamic range of the rotation of tags. The dynamic range of θ also determines the maximum tag bending that HARP-MRI can see.

Eqs.(5.4) and (5.5) are coupled inequalities i.e. the dynamic range of elongation and compression is a function of θ and vice versa. By decoupling the inequalities and plotting them on Ω - θ plane (or equivalently the strain-rotation space), we can visualize the dynamic ranges of elongation, compression, and rotation for given tagging and imaging parameters. By simple manipulations we can decouple Eqs.(5.4) and (5.5). The decoupled inequalities are given as follows

$$\begin{aligned} \max \left[\frac{A}{|\cos \theta|} , 0 \right] \leq \Omega &\leq \min \left[\frac{B}{|\cos \theta|} , \frac{W}{2|\sin \theta|} \right] , \\ \cos^{-1} \sqrt{\max \left[1 - \frac{W^2}{4\Omega^2} , \frac{A^2}{\Omega^2} \right]} &\leq \theta \leq \cos^{-1} \sqrt{\min \left[1 , \frac{B^2}{\Omega^2} \right]} . \end{aligned}$$

5.4 Results and Discussion

5.4.1 Feasible region in “strain-rotation” space

Consider the following tagging and imaging parameters: tag separation 7mm, FOV 280 mm, and a bandpass filter with 33 samples on each side centered about tag frequency (used

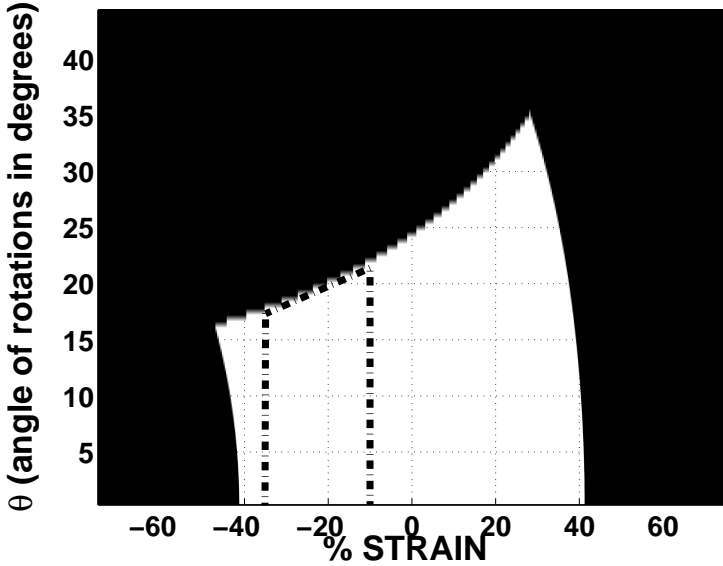


Figure 5.4: Feasible region in strain-rotation space. White regions represent IFs that are within the dynamic range of HARP

in FastHARP). Further assume Nyquist sampling of the image; $\Delta k = 1/\text{FOV mm}^{-1}$. These parameters will be consistently used throughout this section. The same analysis can be repeated for any choice of parameters.

The dynamic ranges can be visualized in the form of *feasible regions* plotted in strain-rotation space, as shown in Fig. 5.4. The feasible region is calculated using the decoupled inequalities. Now, let us interpret Fig. 5.4 in terms of cardiac imaging. With the above parameters, the dynamic range of strain of $\pm 41.25\%$ (negative is compression, positive is expansion) and maximum rotational angle range from 16° – 34° degrees depending of the magnitude of strain. The ranges are adequate for imaging both normal and diseased hearts [89]. Even during stress tests these ranges are adequate for measuring circumferential strains and tag rotations. Measuring radial strains during stress tests, however, will be difficult since radial strains can be as high as 50% with increasing doses of stress inducing agents that the used in cardiac stress tests.

We recommend using the “rule of thirds” when specifying the HARP-MRI imaging parameters. If the tag frequency is ω_0 then the size of box on each side should also be ω_0 . Assuming only one tag orientation, this rule splits up the frequency space into three

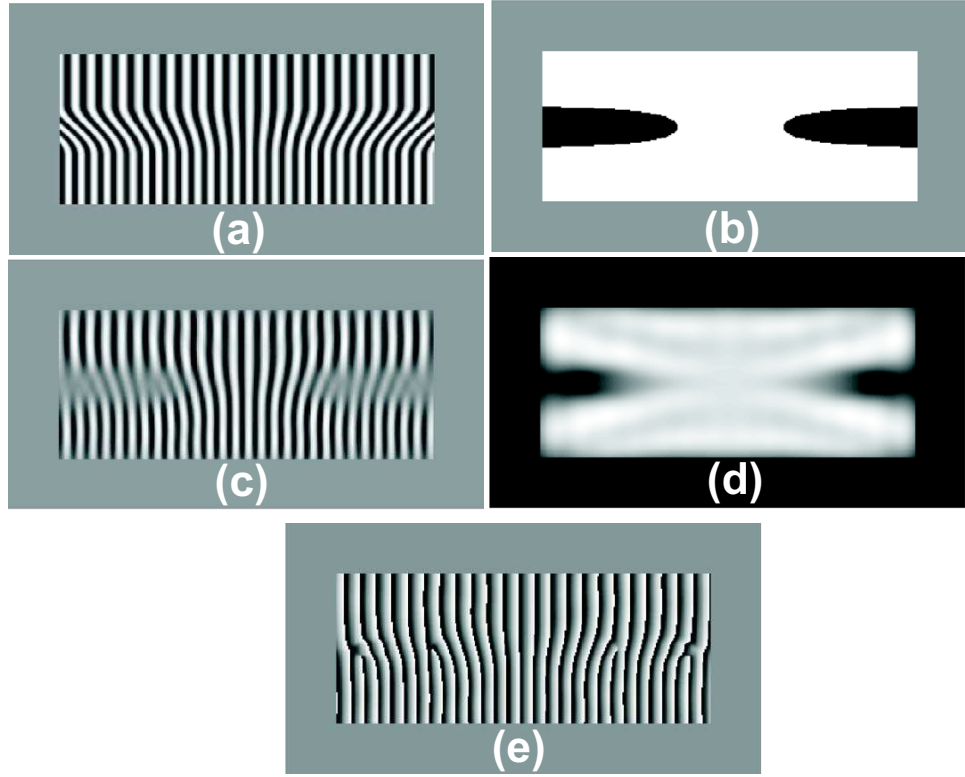


Figure 5.5: (a) Tagged image (b) Feasible regions in space domain: white regions indicate regions where IF inside the bandpass filter. (c) Reconstructed tagged image; note the blurring in regions where the tags bend a lot (d) Reconstructed magnitude image (e) Phase estimate; Note the phase cuts in regions corresponding to regions of blurred tags.

boxes of equal sizes: two around the harmonic peaks and one around the DC peak. With these parameters it is straightforward to show that $\pm 50\%$ strain and the maximum rotational angle of 18° – 46° degrees can be successfully imaged.

5.4.2 Computer Simulated Phantom

A computer simulation is shown in Fig. 5.5. Panel (a) shows three underlying tissue regions. The top region is under a horizontal strain of -10% and the bottom region is under a horizontal strain of -35% . In the middle region, the strain varies in a cosine fashion, yielding a continuous bending of tags. The tagging and imaging parameters are the same as in the previous section. Panel (b) shows the set of points (white) whose IF is contained

within the Fourier acquisition box implied by these parameters. Panel (c) shows the real part of the harmonic image after the filtering. There is a significant loss of tag contrast in object regions that are black in Panel (b). In fact, misalignments of the tags in those regions, faintly apparent in Panel (c), are quite evident in the magnitude of the harmonic image in Panel (d). This is because, as the tag contrast fails, this means that the magnitude of the HARP vectors are near zero. With the magnitude of the complex number close to zero, the HARP phase values are invariably artifactual as seen in Panel (e). HARP tracking and Eulerian strain computations are erroneous in those regions as a result.

We can use Fig. 5.4 to gain an intuitive appreciation of the results in Fig. 5.5. All object strains in this simulation lie in the range -35% to -10% , the range indicated by the vertical dash-dot lines in Fig. 5.4. The feasible domain in Fig. 5.4 indicates that the largest rotations that will be visible given this range of strains are in the range 18° – 22° , depending on the amount of strain. Those IFs in Fig. 5.5(a) disappearing after bandpass filtering are precisely those that have rotated beyond this visible range.

5.4.3 Cardiac MR data

Figs. 5.6(a)–(d) demonstrate the validity of this theory on real cardiac MR image that is obtained during mid-systole. All images in Fig. 5.6 have been cropped and masked for better visualization of the myocardium. The bandpass filter was set to very small size of 15×15 in order to clearly see the effect of dynamic range. Panel (a) shows the original tagged image. Panel (b) shows the set of points (white) whose IF is contained within the Fourier acquisition box implied by these parameters. Panel (c) shows the reconstructed tags after bandpass filtering; there is significant loss of tag fidelity in object regions that are black in Panel (b). In fact, misalignments of the tags in those regions, faintly apparent in Panel (c), are quite evident in the magnitude image in Panel (d) and the HARP phase image in Panel (e).

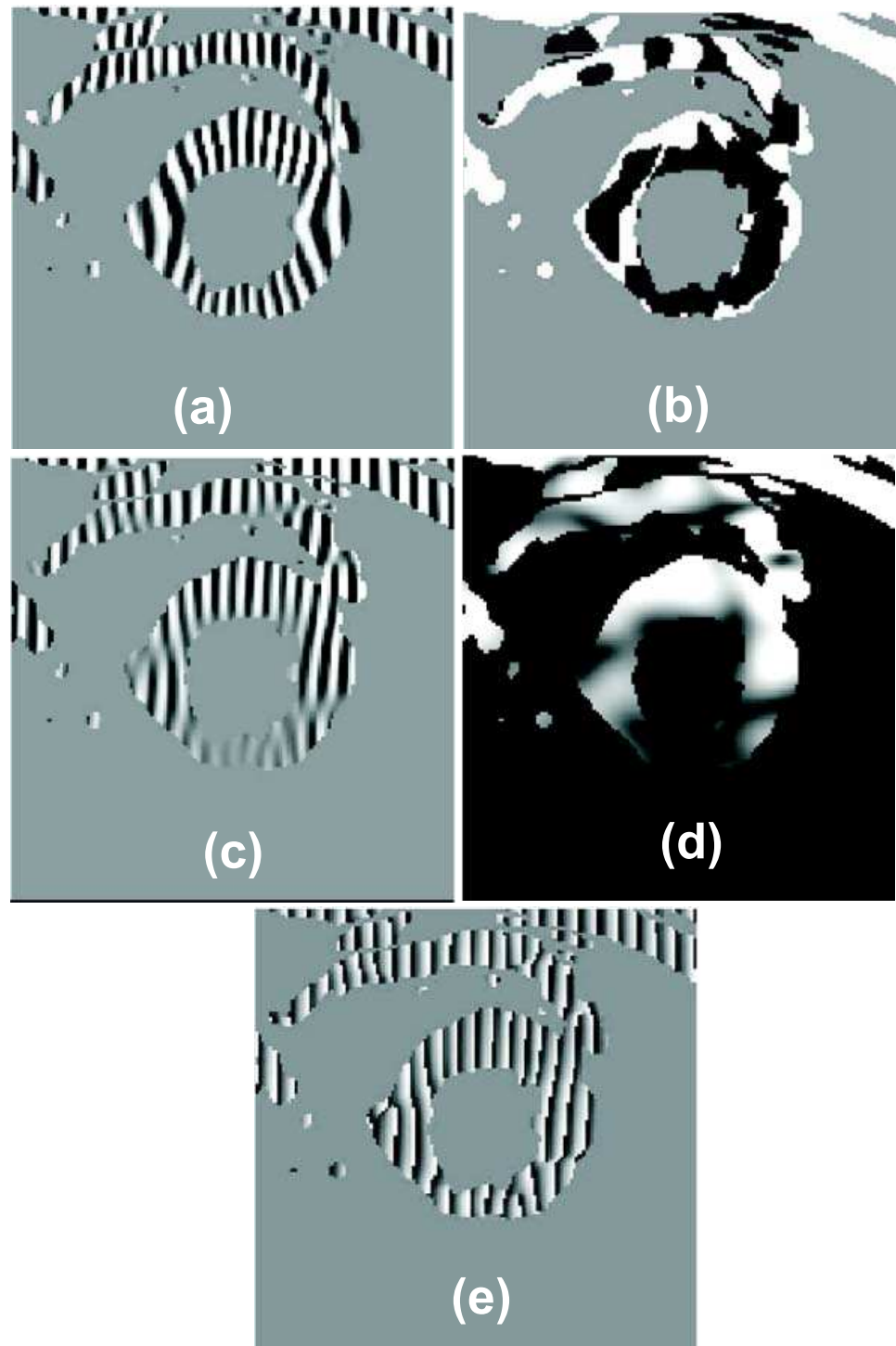


Figure 5.6: (a) Actual tagged image (b) White region denote feasibility regions predicted by theory (c) reconstructed real image; Note the loss in contrast in the regions blacked out in (b), (d) reconstructed HARP magnitude (e) phase image; Note the inaccurate estimates of harmonic phase in regions blacked out in (b)

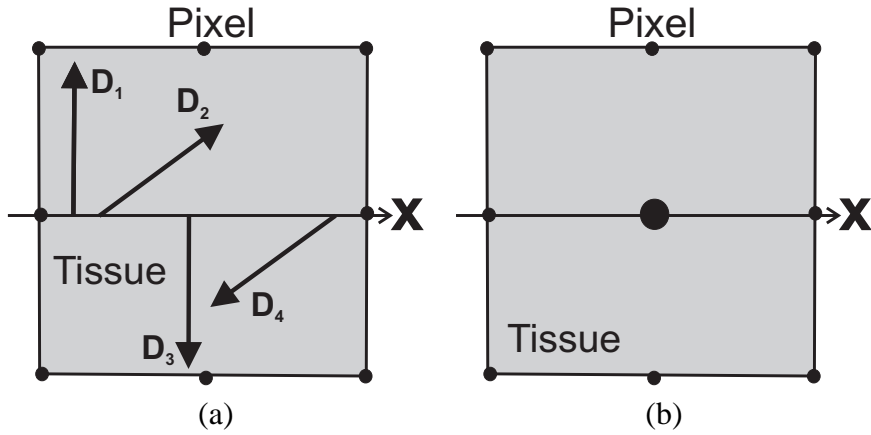


Figure 5.7: Phases dispersed within a voxel such that the net signal from the voxel is zero as shown in (b). This is the limit of dynamic range

5.4.4 Loss of Dynamic Range: Extreme case of IVPD

It is very interesting to see how the loss of dynamic range is related to the sources of errors introduced in Chapter 3. The reduction of contrast due to loss of dynamic range can be seen as an extreme case of IVPD. If the strain around a tissue point is so high with respect to the bandpass filter, the displacement vectors around that point are dispersed completely out of phase with each other, resulting in zero net signal from the voxel that is located around that point. This can be seen as the loss of dynamic range (see Fig. 5.7).

5.5 Conclusion

In this chapter, we addressed a forward problem: ‘Given a set of tagging and imaging parameters, what is the dynamic range of HARP-MRI?’ Using an approximate relation between the instantaneous frequencies and Fourier frequencies, we derived simple expressions for the dynamic range of elongation, compression, and rotation of tags, and expressed them in form a strain-rotation feasibility space. We concluded that the relatively small bandpass filter commonly used in current HARP applications is adequate for capturing the strains and rotations for both normal and diseased tissues. In a clinical setting, the strain-rotation feasible space can give an indication of areas in the image where the estimates

could be erroneous, thereby attaching a measure of confidence to the estimated motion.

In the next chapter, we will analyze another forward problem: ‘Given a set of tagging and imaging parameters, what is the resolution of HARP-MRI?’

Chapter 6

Spatial Resolution of HARP-MRI

Preface

The classical theory of spatial resolution is based on modelling the imaging system as a linear shift invariant system. Since HARP-MRI is a nonlinear system, the classical theory of resolution does not hold. In this chapter, we propose an alternate definition for resolution based on edge models in strain. The models are used to derive measures for resolution in both Eulerian strain and tissue tracking. The strain resolution is found to be comparable to the resolution predicted by the classical definition. The resolution of tracking, on the other hand, is observed to have a very different behavior. We discuss the reasons of these observations and their clinical implications.

6.1 Introduction

Image resolution is one of the important figures of merit of an observed image. The classical definition of resolution originated in the field of optics and is known as the *two point resolution* [23]. Two point resolution is the ability to distinguish two overlapping functions in a set of observations. When set of observations are functions of spatial variables, the resolution is called *spatial resolution*. Spatial resolution is defined as the amount of blurring that the system introduces to a single event in space. When there are two spatial events in the input, the overall output of a linear system will be a superposition of two blurred outputs. If the two inputs are close enough to each other, then the blurring causes the two outputs to merge into one. Therefore, resolution of the system is defined as the

least distance by which two inputs need to be separated, in order for them to be resolved in the output.

6.2 Traditional MR Resolution

In traditional MR resolution, the MR imaging system is modelled as a linear shift invariant system. A single event in space is represented by an impulse function, and the blurring of the system is studied using the system's impulse response. In MRI, k-space samples are acquired and the final MR image is reconstructed using a truncated inverse Fourier series reconstruction,

$$M(x, y) = \Delta k_x \Delta k_y \sum_{m=-N_x/2}^{N_x/2} \sum_{n=-N_y/2}^{N_y/2} M(m\Delta k_x, n\Delta k_y) e^{j2\pi(m\Delta k_x x + n\Delta k_y y)}. \quad (6.1)$$

Since the samples of the spectrum of a single impulse function consists of all ones, the point spread function $p(x, y)$ can be calculated as,

$$p(x, y) = \Delta k_x \Delta k_y \sum_{m=-N_x/2}^{N_x/2} \sum_{n=-N_y/2}^{N_y/2} 1 \times e^{j2\pi(m\Delta k_x x + n\Delta k_y y)}. \quad (6.2)$$

The sums can be separated and can be simplified as,

$$p(x, y) = \Delta k_x \frac{\sin(\pi N_x \Delta k_x x)}{\sin(\pi \Delta k_x x)} \times \Delta k_y \frac{\sin(\pi N_y \Delta k_y y)}{\sin(\pi \Delta k_y y)}. \quad (6.3)$$

Note that the PSF $p(x, y)$ is periodic with period $1/\Delta k_x$ and $1/\Delta k_y$ in each direction. Since the PSF is separable, we analyze only the x dimension of $p(x, y)$; call it $p(x)$. The amplitude part of one period of $p(x)$ is shown in Fig. 6.1(b). The single impulse input is shown on its left. The resolution of the system is measured as the width of the point spread function at half its maximum height. This width is called the *Full Width at Half Maximum (FWHM)*. By solving for $p(x) = 0.5$, it is easy to see that the FWHM is $1/N_x \Delta k_x$. In MRI, the full width at half maximum is also known as the *voxel size* or the *intrinsic Fourier resolution*. The significance of FWHM can be seen from Figs. 6.1(c)–(f). Fig. 6.1(c) shows two impulses that are separated by a distance greater than FWHM. The two impulses are resolved in the output [Fig. 6.1(d)]. In the limiting case, when the two impulse are separated exactly by FWHM, the system blurs the two inputs into one output response [Fig. 6.1(f)].

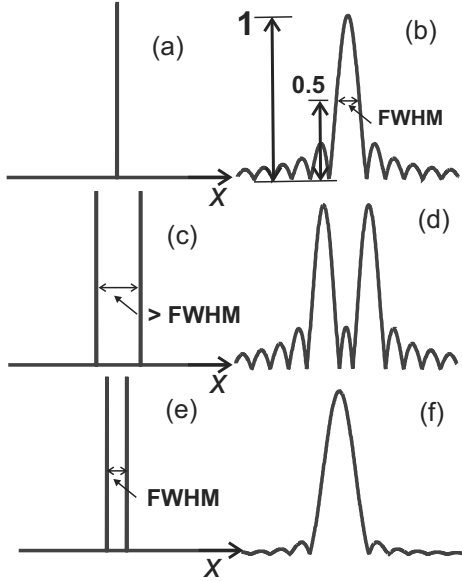


Figure 6.1: (a,b) Single delta function input and Impulse response showing the FWHM
 (c,d) Two delta functions more than FWHM apart and the delta functions resolved in the output
 (e,f) Two delta function inputs exactly FWHM apart; only one lobe is seen since the system cannot resolve the two delta functions.

Impulse responses completely characterize the behavior of a linear shift invariant system. Hence, the use of the impulse response to characterize resolution is justified. The superposition principle is automatically valid for such systems and the existence of impulse inputs are implicitly assumed.

6.3 An Alternate Definition of Resolution

The outputs of HARP-MRI are Eulerian strain maps and trajectories of tissue points. In order to investigate the resolution of HARP-MRI, we should study the responses of HARP-MRI to impulse inputs in Eulerian strain and tracking displacement. But unlike the classical case, impulses do not exist in strain and displacement, which renders the traditional definitions of resolution unusable.

6.3.1 Breakdown of Assumptions

Non-existence of impulses. The motion of the heart is modelled using continuum mechanics, where the heart is modelled as a continuous body undergoing motion and deformation [12, 62, 60, 61]. An impulse in Eulerian strain means that a piece of tissue with a finite length $d\mathbf{X}$ at a reference time, collapses into a single point $d\mathbf{x}$, where $|d\mathbf{x}| = 0$. This defies the principles of continuum mechanics. For a continuous body undergoing motion, the determinant of the deformation gradient F is always nonzero [79] (recall that the deformation gradient is defined as $F d\mathbf{X} = d\mathbf{x}$). Moreover, an impulse in Eulerian strain can model only tissue compression, but not tissue expansion. On a similar note, an impulse in displacement cannot exist in a continuous body. An impulse in displacement means that one single point undergoes infinite displacement, while the surrounding tissue remains stationary, which is impossible in a continuous body undergoing motion.

Nonlinearity of HARP-MRI. The nonlinearity of HARP-MRI is another hurdle in using the classical resolution definitions. Even in the case that the existence of impulses in strain and displacements are assumed [37], the principle of superposition does not apply for nonlinear systems like HARP-MRI. Further, nonlinear systems have been shown to be able to recover resolution in theory and are known to be the basis of many super-resolution methods [59, 22, 23].

6.3.2 Clinical Perspective of Resolution

The final goal of HARP-MRI is to provide measures to assess the regional function of the heart. One index of the heart’s regional function is given by the regional contractile function, which is the ability of the heart muscle to stretch and contract efficiently. The Eulerian strain is known to be a measure of regional contractile function, and variations in Eulerian strain are known to be good indicators of heart diseases like myocardial ischemia and infarction [77, 6]. The overall effectiveness of HARP-MRI in the diagnosis of ischemia or infarction can be studied by investigating its ability to 1) detect the abnormality, and 2) to estimate its extent. The first factor forms the basis for the next chapter, where we discuss the detectability properties of HARP-MRI. In this chapter, we focus on the second factor. We

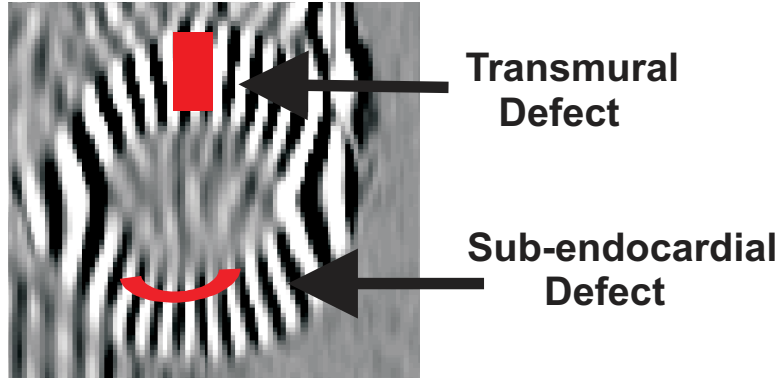


Figure 6.2: Myocardial showing transmural defect and subendocardial defect. Notice how the transitions in strain are in one case along the direction of tags (transmural) and in the other case, orthogonal to the directions of tags (subendocardial)

claim that the ability of HARP-MRI to estimate the extent of an abnormality is a measure of its resolution.

A myocardial infarction or ischemia can be classified either as subendocardial or transmural [16, 11, 53]. A subendocardial abnormality occurs in the beginning stages of heart disease and is restricted to the inner endocardial surface (see Fig. 6.2). A transmural abnormality, on the other hand, extends through the entire thickness of the myocardial wall. In both cases, the estimation of size of the abnormality is important for selection of treatment approaches and to predict the prognosis of the disease. From Fig. 6.2 it is easy to see that, an accurate estimate of the extent of the disease can be obtained by estimating the transitions between healthy and diseased tissues. These transitions occur in the regional contractile function and are reflected as transitions in Eulerian strain maps. Using this perspective, we define strain resolution as the ability of HARP-MRI to faithfully reconstruct transitions in strain. We model the transitions between healthy and diseased tissues as edges in strain. Simulations are used to understand how the bandpass filter affects edges in strain.

6.4 Strain Resolution

6.4.1 Edge Model Simulation

Edges in strain can occur in two different directions with respect to the tags: along the tags and across the tags. For example, in the type of subendocardial defect shown in Fig. 6.2, the strain edges are orthogonal to the tagging direction. On the other hand, for the transmural case, the edges are along the tagging direction. We simulate both type of edges in order to study the isotropy of HARP-MRI resolution.

The simulated images are shown in Fig. 6.3(a) and (b). The tagged image consists of a square object under a state of compression. The compression is restricted to be only in the left-right direction, since only vertical tags are considered. The object is 120 mm on each side, placed in a FOV of 280 mm, and tagged with a tag spacing of 7 mm. Fig. 6.3(a) shows an edge in strain along the direction of the tags. The edge in strain splits the object into two regions of equal size, but with different strains. The region on the left is under a strain of -10% , while the region on the right is compressed more with a strain of -35% . The difference in strain can be seen as an increase in instantaneous frequency (tags are closer) on the right region than on the left. It is interesting to note that even though there is step transition in strain, there is no tag discontinuity at the interface. This is because the phase of the tags is encoded by tissue displacement and not by tissue strain. The displacement, which is the integral of strain, remains continuous at the interface.

The difference between the two regions is more obvious in the case where the edges in strain are orthogonal to the direction of the tags [Fig. 6.3(b)]. In this case, there is shear between the top and bottom layers because of the differential displacement between the two layers. The top layer and bottom layer are under compression with strain -10% and -35% respectively.

In order to compare the strain edges to traditional MR resolution, we simulated two magnitude images with the same edge patterns [Figs. 6.3(c) and (d)]. The two regions have magnitudes -10 and -35 , respectively. The magnitude values were picked so as to match the strain values in the two regions.

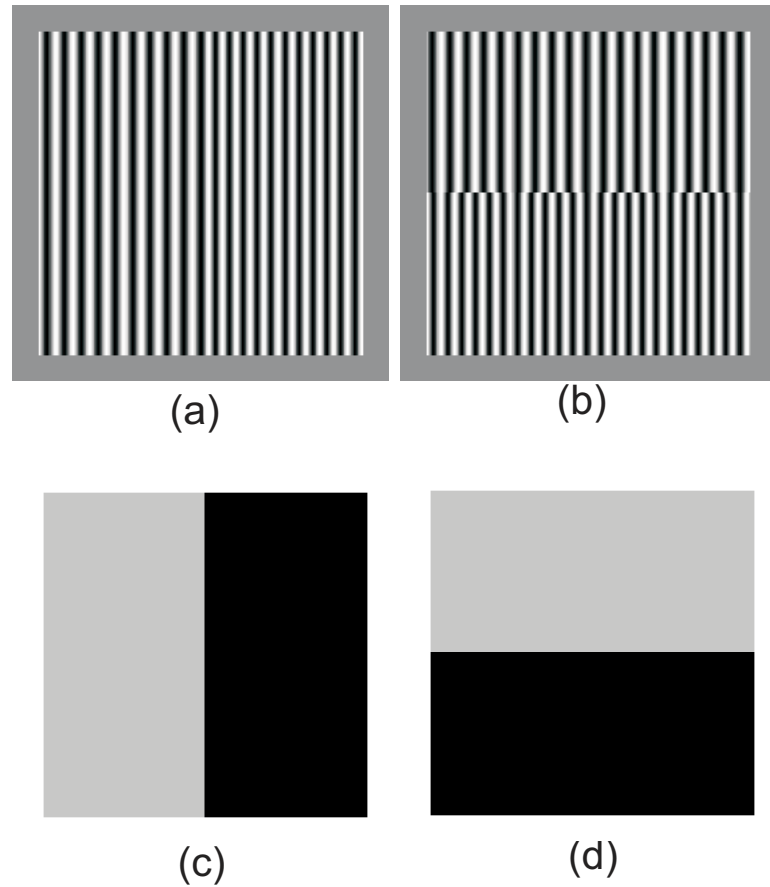


Figure 6.3: Top row: Vertically tagged image with (a) edge in strain in the direction of tags, (b) edge in strain orthogonal to the tags. Bottom row: Magnitude image with corresponding edges in magnitude

6.4.2 Filtering

The tagged images were processed using HARP-MRI with a bandpass filter size of 33×33 , the filter size that is used in the FastHARP imaging protocol. The Eulerian strains were calculated in each case. The same size filter was used to filter the magnitude images. In the magnitude case, the filter is centered around the origin, thereby simulating a truncated acquisition in k-space. In all the simulations, the FOV was 280 mm, and the images were cropped to show the object only. The classical MR resolution in this case was $1/(N\Delta k) = 1/(33 \times \frac{1}{280}) = 8.48$ mm.

6.4.3 Results and Discussion

Edge Responses. The top row of Fig. 6.4 shows the reconstructed strain maps. The middle row shows the reconstructed magnitudes and the corresponding horizontal and vertical profiles are plotted in the third row. The red, blue, and green curves denote the profiles of the true step function, magnitude response, and strain response, respectively.

Spatial resolution of strain is defined as the measure of blurring of the strain edge. The blur is measured as the distance between two points where the blurred function intersects the true step function on either side of the step (see arrows in Fig. 6.4). In the case of the magnitude (blue), the blur is about 10 mm. The blurring in strains is almost equal to the blurring in magnitude. Comparison between the ‘orthogonal-to-tags’ and ‘along-the-tags’ case shows that the blurring in the ‘orthogonal-to-tags’ case is lesser than the ‘along the tags’ case, revealing a small amount of anisotropy in the strain reconstruction.

Explanation using communications theory. This result clearly suggests that the resolution of Eulerian strain is approximately equal to the intrinsic Fourier resolution predicted by the classical resolution theory. The nonlinear phase operation does not recover resolution. The blur of the edge in the magnitude can be explained using the traditional MR resolution theory. Here, we explain the blurring in strain using the properties of monocomponent signals introduced in Chapter 4.

In this case, the monocomponent signals of interest are the real part of the complex harmonic images, namely $D(\mathbf{x}, t) \cos(\phi(\mathbf{x}, t))$. Fig. 6.5 shows the monocomponent signals

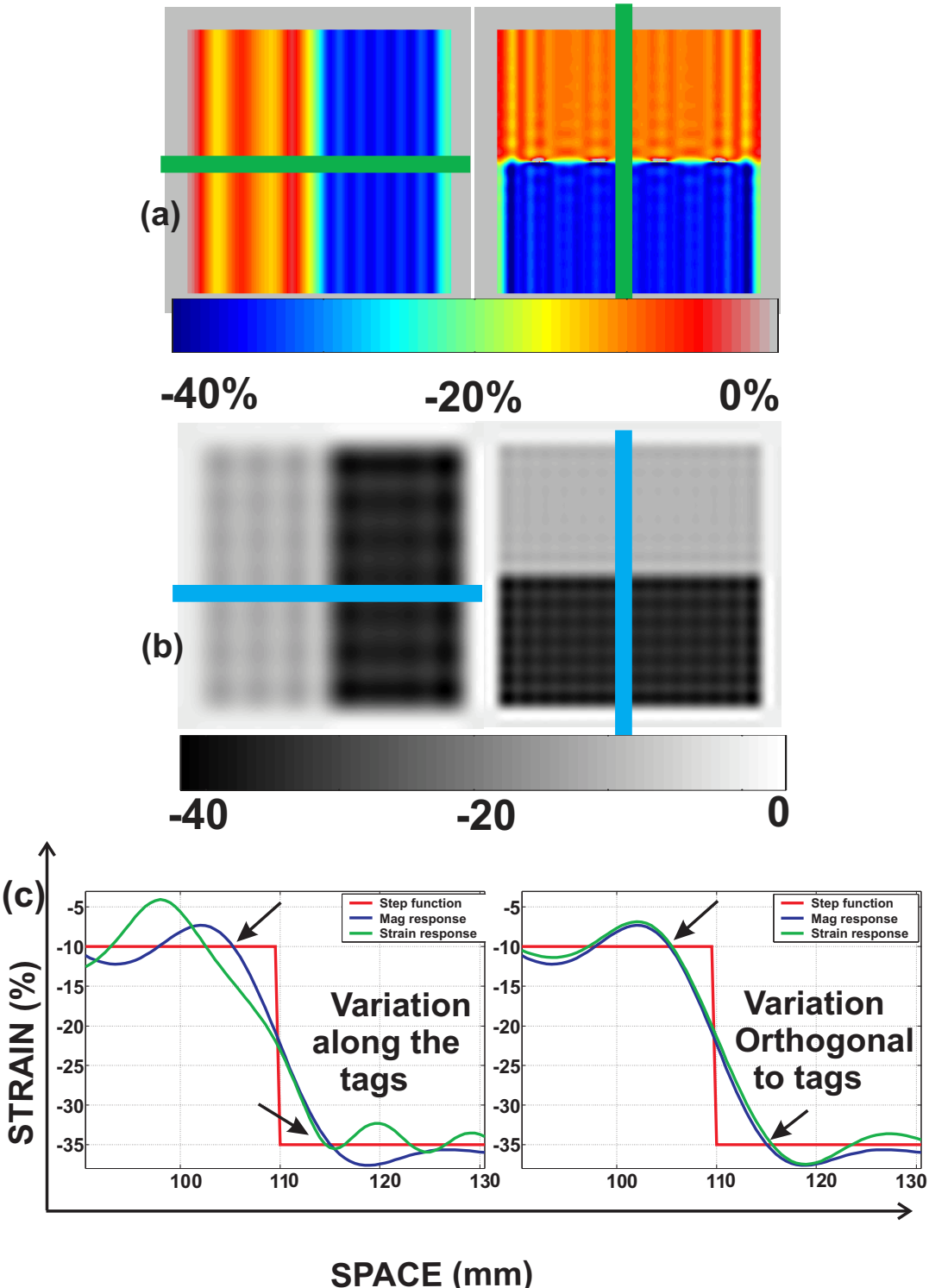


Figure 6.4: (a) strain responses,(b) magnitude responses, (c) profiles along the lines marked.

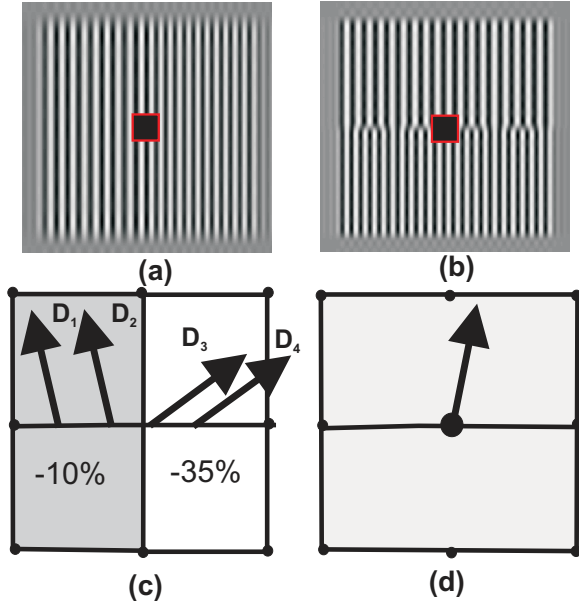


Figure 6.5: Top row: Real part of the complex harmonic images. Bottom row: The behavior of HARP vectors within a interface voxel. The dispersion of vectors causes an error due to IVPD.

for the two types of strain transitions. The reconstructed strains are the instantaneous frequencies of the monocomponent signals. Recall from Chapter 4, that for monocomponent signals the instantaneous frequency at each point is the average of the Fourier frequencies in a small region around that point. Consider such a small region at the interface shown as red squares in Fig. 6.5. The IF in that small region should be an average of Fourier frequencies around that point. Since the bandpass filter truncates all frequencies outside the pass band, the Fourier frequencies in the small red squares must be confined within the pass band of the bandpass filter. This implies that the average of these frequencies must also be within the pass band of the filter. Therefore, the highest achievable frequency in IF or strain is limited by the bandpass filter and hence the HARP strain resolution is equal to the resolution predicted by the classical theory.

Alternate explanation using IVPD. The blurring of strain at an edge interface can be viewed in terms of discrete voxels and can be explained using IVPD. Let the small square regions in Fig. 6.5(a) and (b) be voxels of size $8.48 \text{ mm} \times 8.48 \text{ mm}$, with the center of

the voxel exactly at the strain interface. An enlarged schematic of the voxel is shown in Fig. 6.5(c). In either case of strain transition, half the voxel consists of HARP vectors with phases corresponding to strain of -10% , whereas half the voxel will have phases corresponding to strain of -35% . The resulting IF [Fig. 6.5(d)] will have an error because of the phase dispersion within the voxel. The overall phase dispersion error will be a combination of all the phase errors incurred due to the blurring of HARP phase values along the edge.

Dynamic Range of Eulerian Strain. In the previous chapter, the loss of dynamic range of strain was interpreted as an extreme case of IVPD. The edge experiment sheds more light on this perspective. Fig. 6.6 shows the HARP magnitude and HARP phase images of the two edge patterns. In edges orthogonal to the tags [Fig. 6.6(b)], there is loss of signal in the HARP magnitude image at the interface. At these regions the HARP phase values are also erroneous. Now, consider a voxel at this interface. The shear in the tissue causes the IF vectors to disperse completely within the voxel such that the net signal is zero. This is precisely the loss in dynamic range of Eulerian strain. The loss of dynamic range happens all across the sheared interface except at the central vertical line shown in Fig. 6.4. On the vertical line, the phases of the tag patterns match up and there is no shear. At all other points on the interface, the HARP phase values are erroneous. This observation about dynamic range has important implications on the resolution of tissue tracking, which will be the topic of the next section.

6.5 Tracking Resolution

In Chapter 3, we noticed that the optimal filter sizes for tracking were much smaller than those for strain computations. The loss of resolution due to the small filter sizes did not affect the performance of HARP tracking. In this section, we use the edge models to investigate this phenomenon and understand how the resolution of HARP tracking is affected by filter size.

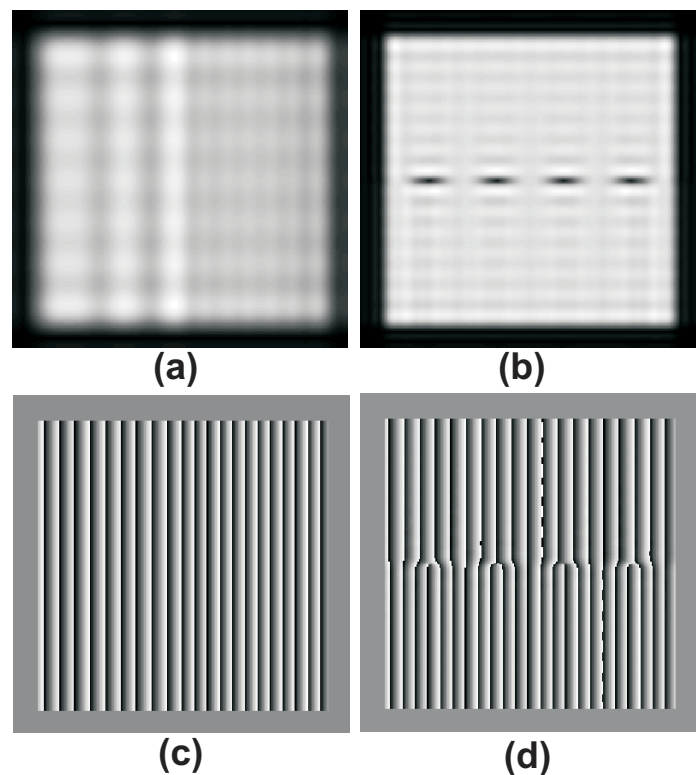


Figure 6.6: Top row shows the HARP magnitude images for the edges along the tags and the edges across the tags. Note the loss of signal at a few regions along the interface, where the dispersion of IF within a voxel results in zero net signal in the voxel. The corresponding HARP values shown in the bottom row are erroneous as well.

6.5.1 Methods

Let the images used in the previous section represent the position of the object at reference time t_0 . In order to analyze tracking resolution, the object was displaced from its reference position by three different amounts corresponding to three different time frames. HARP tracking was used to track this displacement. The three displacements were 2mm, 3mm, and 4mm in the left-right direction. The three displacements were selected based on the dynamic range of tracking for each portion of the image. The dynamic range of tracking depends on the initial tag separation of 7 mm and the current Eulerian strain that determines the current spacing between the tags. In the region with -10% strain, the dynamic range of tracking is 3.5 mm and in the region with -35% strain, the dynamic range of tracking is 2.5mm. The displacement of 2 mm is within the dynamic range of both regions, while the displacement of 4 mm is outside the dynamic range of both regions. The 3 mm displacement is within the dynamic range of the -10% region and outside the range of the -35% region. HARP tracking was used to track the position of the displaced object at each time, and the error in tracking displacement were calculated at each pixel within the object.

6.5.2 Results

Fig. 6.6 shows the error in tracking for three different displacements for the two edge models. In the ‘2 mm’ case along the tags [Fig. 6.7(a)], the tracking is nearly perfect; the tracking error approximately zero even at the interface between the two regions. Fig. 6.7(c) shows the tracking error for the ‘3 mm’ displacement; we can clearly see the effect of the dynamic range of tracking. The left portion, which is within the dynamic range of tracking has zero error, whereas the right portion has an error of around 5 mm, which corresponds to more than 150% error. In the ‘4 mm’ case, where both the regions are out of the dynamic range of tracking, the error is nonzero in both regions. Horizontal profiles of the error are shown in the bottom figure. We can see a very sharp transition in the ‘3 mm’ case (red curve), where the dynamic range of tracking is exceeded. In the ‘4mm case’ (green curve), when the entire object is out of dynamic range of tracking, the blurring of the edge is very similar to the blurring seen in the strain. These curves show that the error in tracking is not

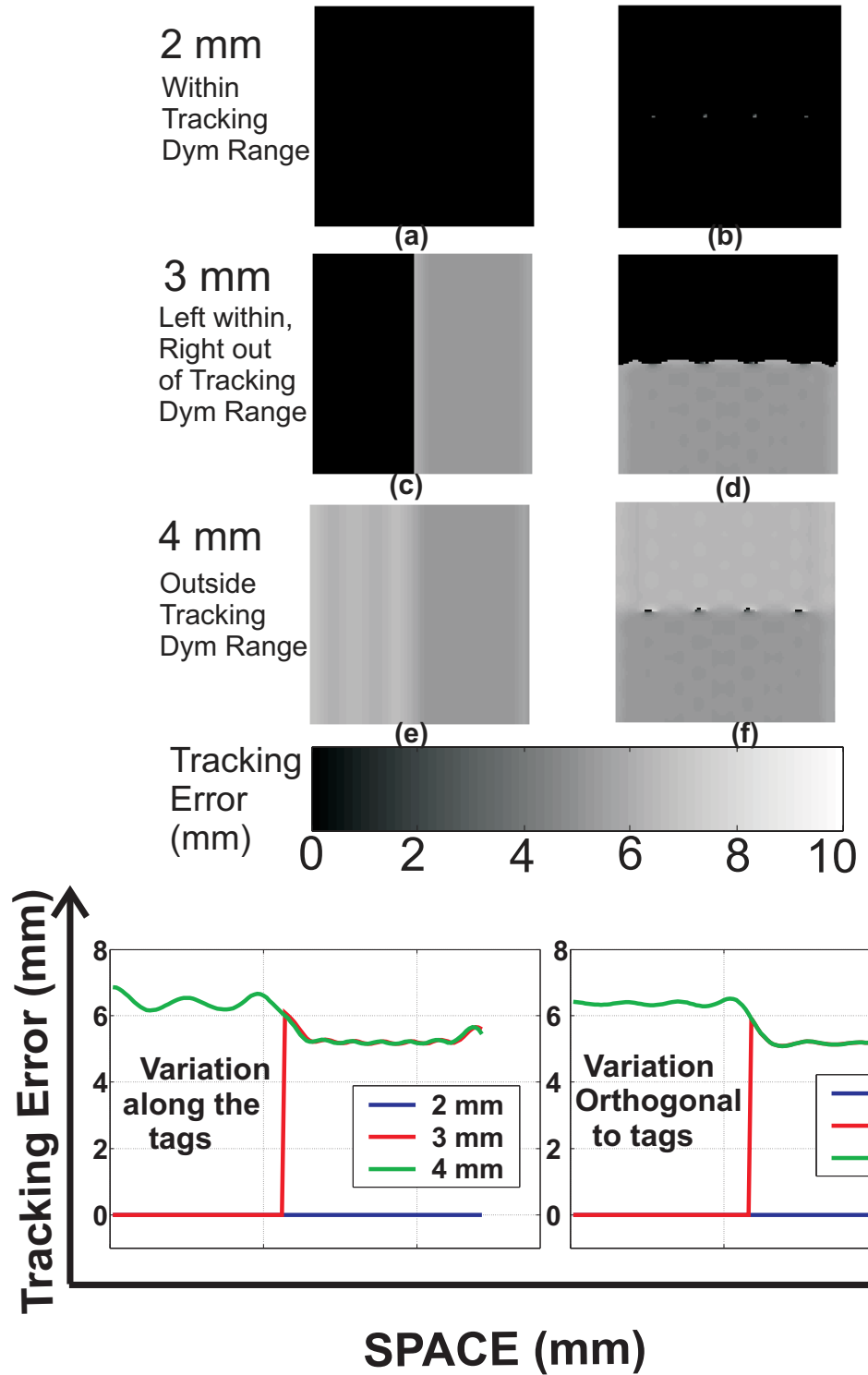


Figure 6.7: Tracking error for different displacement conditions. Note the very steep interface between the areas of zero error and non-zero error. This implies that the resolution of tracking is not limited by the bandpass filer. The profiles are shown in the bottom row.

affected by the filter size but dependent on the dynamic range of tracking. This implies that the tracking resolution is better than the intrinsic Fourier resolution.

The ‘orthogonal to the tags’ case shows a combined effect of the loss of dynamic range in both tracking and strain. Fig. 6.7(b) shows the tracking error for the ‘2 mm’ case. The tracking is perfect except for few isolated regions on the interface. On closer look, we see that these regions exactly coincide with regions that are outside the dynamic range of Eulerian strain [Fig. 6.6(b)]. A very similar effect is seen in two other cases as well. The strain profiles corresponding to a vertical line through the image is similar to ‘along the tags’ case.

6.5.3 Discussion

These results show that HARP tracking behaves very differently than strain. HARP tracking is not affected by the smoothing caused by the filter. The reason for this unique performance of tracking comes from the basic premise on which HARP tracking is based: “HARP value of a tissue point is a material property of a tissue point”. The HARP value moves along with the tissue point. This can be perceived as uniqueness condition of HARP tracking, which is satisfied as long as the motion is within the dynamic range of tracking. When the filter blurs the harmonic images, the blurring is common to both the time frames that are involved in HARP tracking. Because of this common blurring, the uniqueness of HARP phase is still maintained, thus making tracking robust to filtering. The performance of tracking can be seen as an ‘all-or-none’ phenomenon with respect to the dynamic range in tracking and strain. As long the movement of the point is within the dynamic range of tracking, and as long as the strain at that point is within the dynamic range of Eulerian strain, HARP tracking is perfect, up to the effects of spectral interference and noise. These tracking results corroborate our simulation results in Chapter 3. Among all the motion measures from HARP-MRI, HARP tracking provides the most robust measures of motion.

A very important corollary of this tracking performance is the robustness of Lagrangian strains. Lagrangian strain between two points is calculated by tracking the two points over time and calculating their relative change in length with respect to their original length. Since their computations are based on tracking, the robustness of Lagrangian strains is also

guaranteed.

6.6 Clinical Impact of the Resolution findings

In this section, we analyze the clinical impact of the resolution results. We see how these results affect the ability of HARP to estimate the extent of an ischemia or an infarction.

6.6.1 Subendocardial Abnormalities

The ability to localize the edge between healthy and diseased tissue is limited in a strain map by the bandpass filter. The biggest impact of this result is in the estimation of the extent of subendocardial abnormalities. Subendocardial abnormalities have a extent of around 3-5 mm across the wall, which is around one third of the thickness of heart wall. With a bandpass filter size of 33×33 and edge resolution of around 10 mm, a detailed analysis of the transmural distribution across the wall is not possible. In such cases, increasing the filter size is one option, but only at the expense of increased imaging time and artifacts.

6.6.2 Functional Border Zone

The edge model represents the worst case scenario in describing the transition between healthy and disease tissue. In actual clinical studies, the analysis of regional function is split into three coarse regions: Infarcted/ischemic regions, adjacent regions, and remote regions. The adjacent regions, also known as the functional border zone (FBZ), is known to act as a buffer between the epicenter of the abnormality and the remote regions [95, 20] (see Fig. 6.8). It has also been shown that the distribution of strain from the epicenter to the remote regions varies smoothly across the functional border zone [96]. The width of the functional border zone can extend anywhere from 2 mm to 30 mm depending on the direction of muscle fibers in the heart's wall. The existence of the functional border zone is attributed to a phenomenon called ‘tethering’. The epicenter of the diseased tissue is tethered to the adjacent regions and hence each region cannot deform independent of each

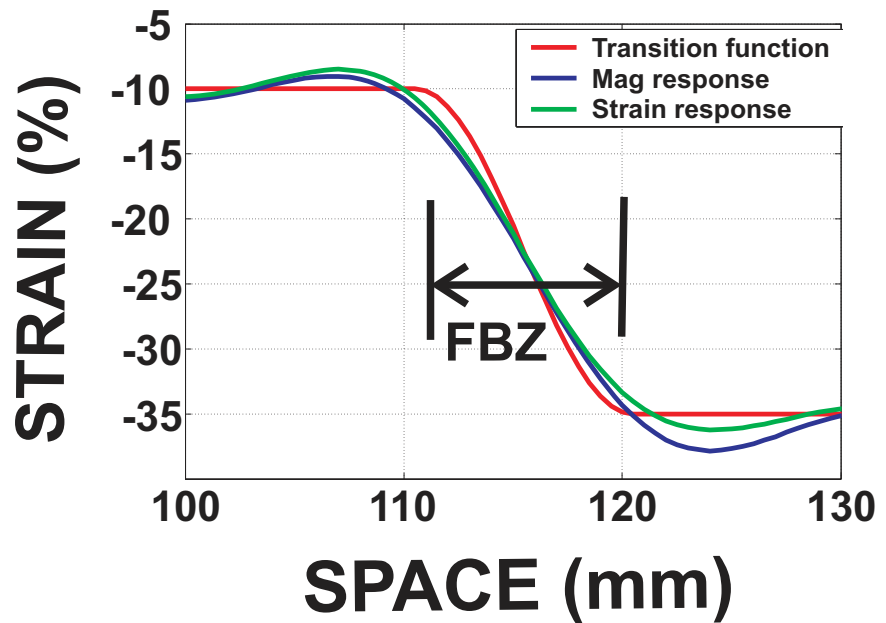
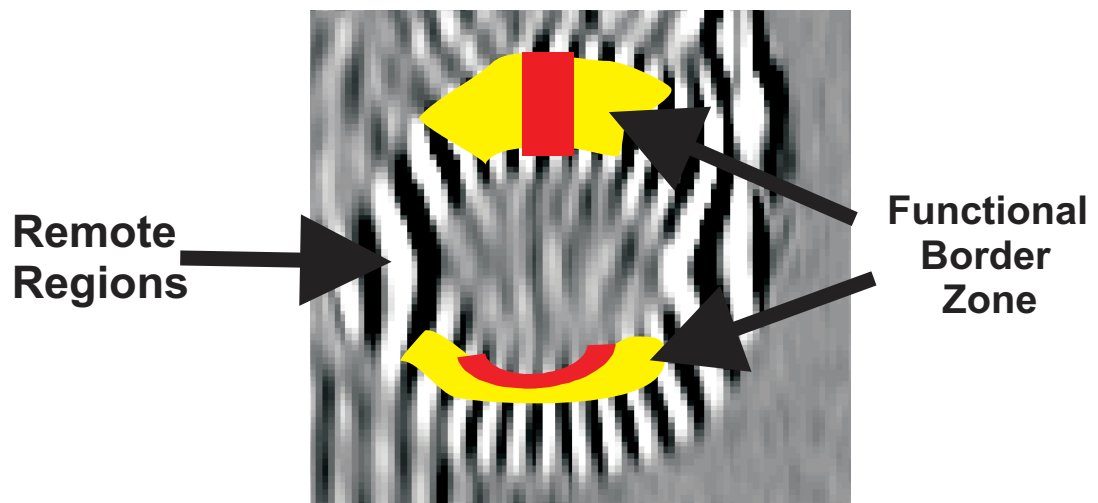


Figure 6.8: Top: Transmural and subendocardial injuries shown with respective functional border zones. Bottom: Strain reconstruction of smooth edge.

other. For example, in the case of subendocardial infarction, epicardial motion is tethered to the endocardial motion. Because of this phenomenon, in reality there are no sharp edges in the strain. Therefore, any analysis that is based on regional contractile function will overestimate the extent of the myocardial abnormality [96].

6.6.3 Reconstruction of Smooth Strain Transitions

The non-existence of sharp edges has a profound consequence on the resolution of HARP-MRI. If the width of the FBZ is greater than or equal to the edge resolution, then HARP-MRI can reconstruct the strain faithfully without blurring. This is shown in bottom plot in Fig. 6.8. The red curve, which was a sharp edge in the previous experiments, has been smoothed out to incorporate a FBZ of width 10 mm. The reconstructed strain curve shows the faithful reproduction of strain. The faithful reproduction of smooth transition in strain implies that the spectral energy that is associated with such smooth change in strain is contained within the HARP bandpass filter. This spectral energy produced by the strain can qualitatively viewed as the motion spectrum. The spreading of the motion spectrum depends on the frequencies components of the underlying strain pattern. So, as long as the spatial frequencies of the strain function is within the bandpass filter, then the strain can be reconstructed faithfully, up to the effect of noise and artifacts.

Perfect edges might not exist in strain, but edges do exist in the anatomy. For example, the transition between the heart tissue and the blood is abrupt. Therefore, even though smooth transitions can be reconstructed using small bandpass filters, the partial volume errors occurring at the endocardial edges cannot be recovered. These error will have an effect on the strain values in the endocardial regions.

6.7 Summary

The resolution of nonlinear imaging systems like HARP-MRI cannot be determined using classical resolution techniques. In this chapter, we defined resolution in terms of its clinical relevance by using edge models in strain. In theory, it was seen that the strain resolution is limited by the bandpass filter. In a practically setting, the transitions of strain

in the myocardium is not sharp and smoothness is controlled by the width of the functional border zone. If the width of the functional border zone is greater than or equal to the strain resolution, then the Eulerian strains are reproduced faithfully, up to the effects of noise and artifacts. Tracking resolution is not affected by the size of the filter, and is determined only by the temporal resolution of the image series. As a consequence, the resolution of Lagrangian strains are higher than the intrinsic Fourier resolution.

The resolution of HARP-MRI focussed on its ability to estimate the extent of heart disease. But another primary concern is the ability to reliably detect the myocardial injury. This will be the topic of the next chapter, which will focus on the detectability properties of HARP-MRI.

Chapter 7

Detectability of HARP-MRI

Preface

Detection of an abnormality is one of the most crucial traits of a diagnostic medical imaging system. In this chapter, we investigate the size of smallest abnormality that can be detected using HARP-MRI. We analyze how detectability is affected by the bandpass filter size. The work in this chapter presents a first step in understanding the differences and similarities between resolution and detectability of HARP-MRI.

7.1 Introduction

Objective image quality measures like resolution, contrast, and signal to noise ratio are important in determining the usefulness of a medical image. In linear imaging systems, the impulse response can be used to characterize all three measures. The spatial resolution is measured using the FWHM of the impulse response. The image contrast is characterized using the modulation transfer function, which is defined as the modulus of the normalized Fourier transform of the impulse response. The modulation transfer function can also be used to explain the noise characteristics of the image to obtain an estimate of signal-to-noise ratio [128]. In the case of nonlinear imaging systems, however, there is no single analytical expression that captures all the image quality measures objectively [127]. It is necessary to define each measures on a case-by-case basis. In the last chapter, we characterized the resolution of HARP-MRI using an edge model model in strain, and we concluded that the ability of HARP-MRI to localize an edge is limited by the FWHM defined by the bandpass

filter. In this chapter we ask a follow-up question, “How large should an abnormality be in order for it to be detected by HARP-MRI?”

Detectability is a crucial question that is probably as old as the field of diagnostic radiology itself. It is often regarded as a subjective measure because it is based on human perception. Nevertheless, many quality index measures have been proposed to capture the detectability of a system and to compare it with the efficiency of human observers [157, 28]. In the field of breast cancer detection using mammography, detectability is sometimes seen as a measure of spatial resolution [127]. Breast cancers are often revealed as cluster of micro-calcifications. The detectability of a mammography system is measured in terms of its ability to detect such small calcifications [39]. Objectively, detectability is measured as the diameter of the smallest perceptible spherical object. In this chapter, we adapt this definition to find the smallest perceptible infarction that can be detected in a Eulerian strain map computed using HARP-MRI.

7.2 Theory

7.2.1 Contrast–Detail Analysis

In HARP-MRI, the difference in regional contractile function helps to differentiate between healthy and diseased tissue. This difference is reflected as contrast in the Eulerian strain map. The more contrast there is between the two tissue types, the easier it is to detect the diseased tissue. Another aspect influencing the detectability is the size of the diseased tissue. Obviously, a larger abnormality is easier to detect than a smaller one. Therefore, the two factors – contrast and extent – are used as main control parameters for an image assessment tool called “contrast–detail analysis”. This tool is currently used to quantify detectability in mammography based techniques [127]. In this analysis, different sizes of abnormalities are simulated with differing levels of contrast, and are given as inputs to the imaging system. The system responses are then analyzed to answer two complementary questions: 1) Given a contrast level, what is the smallest infarction that can be detected?, 2) Given a size of infarction, what is the minimum contrast level required for the infarction to be detected?

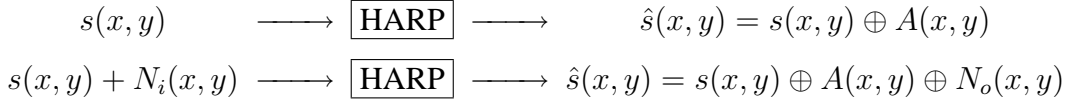


Figure 7.1: Input/Output diagrams: Top block diagram models the no noise case. The sources of output noise in this case are the systematic noise sources like spectral interference and Gibbs ringing. The bottom block diagram shows the noise case, where input noise affects the estimates as well.

7.2.2 System description of HARP-MRI

In this chapter, we will exclusively deal with detectability in Eulerian strain maps. In order to simplify notation, it is easier to model HARP-MRI as system whose input is a true strain pattern $s(x, y)$ and the output is an estimate of strain $\hat{s}(x, y)$. Fig. 7.1 shows the input-output diagrams for two scenarios. In the first case, the input noise is zero. The resulting estimate of the strain is affected by spectral interference and other systematic sources of error that cause errors in the strain maps. The overall magnitude of the error is $A(x, y)$. In the second case, input image noise $N_i(x, y)$ is added to the strain input. The input image noise manifests as an additional error of $N_o(x, y)$ in the final estimate of strain. The circled plus signs imply that the effects of these errors on the strain estimates are not linear.

7.2.3 Detectability: Limited by Noise

The detectability of a HARP-MRI system is not determined by resolution, but by noise. This can be seen using a simple 1-D schematic shown in Fig. 7.2. Consider a 1-D strain input as shown in Fig. 7.2(a). It consists of a piece of infarcted tissue in the center of a healthy background tissue. The infarcted tissue is a piece of inactive myocardium and is simulated to have 0% strain. The background tissue is healthy and simulated to have a strain of -15% compression. The difference in strain between the two regions is the ‘contrast’, and the width of the infarction is the ‘detail’. Figs. 7.2(b)–(d) show the output of HARP-MRI to such a strain input under three different conditions: (b) no input noise, (c) input noise

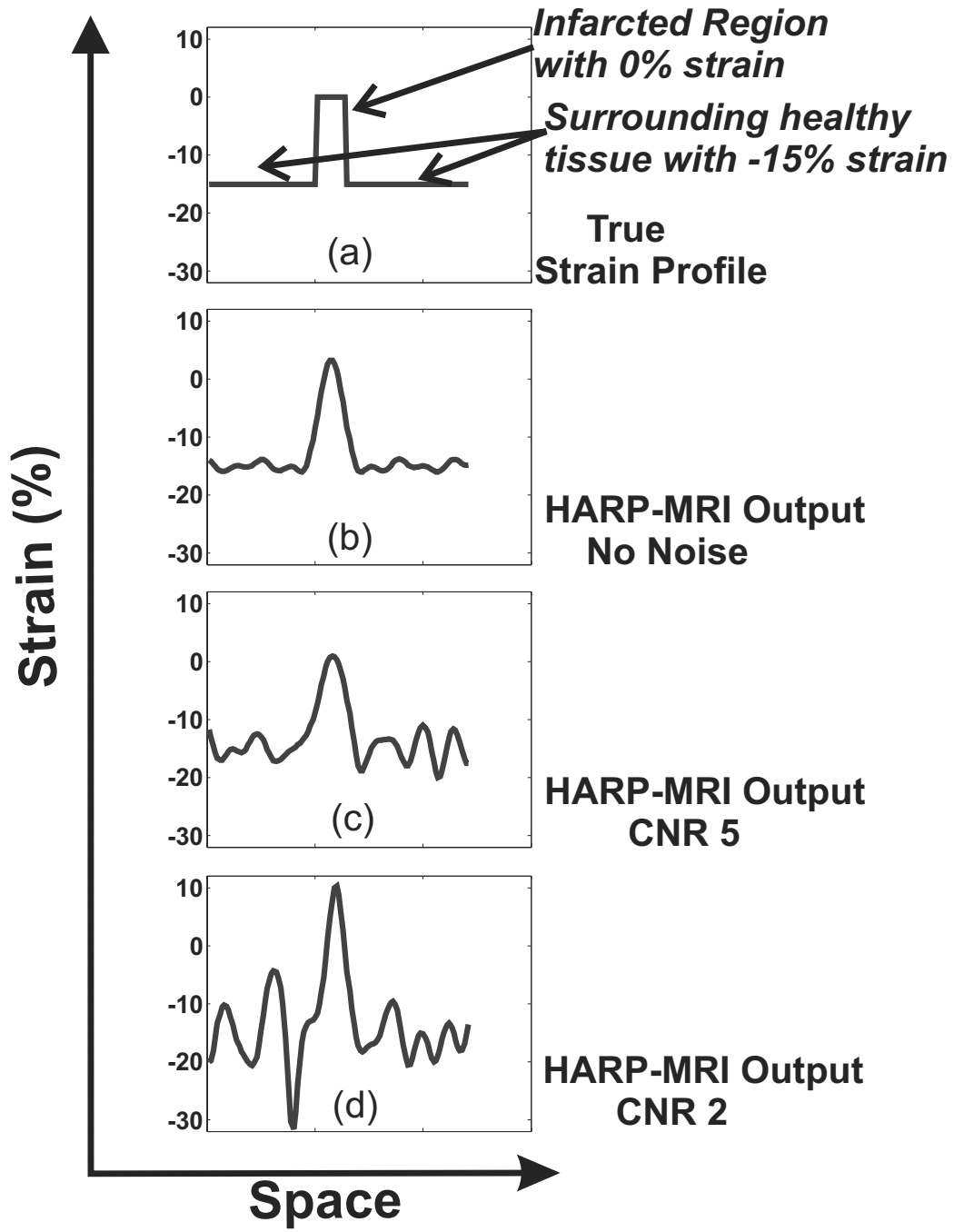


Figure 7.2: (a) True strain profile with infarcted region with 0% strain, with the background compression with -15% strain; (b) Reconstructed strain using HARP-MRI with no input noise. (c) Reconstructed strain with CNR = 5; (d) Reconstructed strain with CNR = 2. Note how the noise overwhelms the contrast in (c) and (d).

with image CNR = 5, and (d) input image noise with image CNR = 2¹.

The blurring of the infarcted region in Fig. 7.2(b) is a function of the size of the band-pass filter. The detection of this abnormal region, however, is dictated by the noise in the strain map, or in other words the output noise of the system. This can be seen from Figs. 7.2(c) and (d). As the input image CNR decreases, the output noise increases and it is increasingly difficult to differentiate the infarction from the background. Using this very simple idea, we define the detectability as the ability to see the contrast difference over the level of background noise in the Eulerian strain maps.

7.2.4 Interplay between different sources of error

In Chapter 3, we concluded that image noise and spectral interference were among the major sources of error in HARP-MRI. Here, we see that these two reduce the detectability of the HARP strain map. It is very interesting to see the interplay of all the sources of error that were introduced in Chapter 3. IVPD and PVE blur the edges of the infarcted region and thus reduce the contrast between the infarcted region and the background. While contrast is reduced by IVPD and PVE, noise is increased by image noise and spectral interference. Therefore, all sources of error contribute in reducing the detectability power of HARP-MRI.

7.3 Methods

The methods section consists of two parts. In the first part, we explain the contrast-detail simulations, and in the second, we describe the quantification of noise.

7.3.1 Contrast–Detail Simulations

In this section, we extend the 1-D input, explained above, to two 2-D strain inputs shown in Fig. 7.3(a) and (b). Fig. 7.3(a) represents the tissue strain in the horizontal direction, whereas Fig. 7.3(b) shows the input strain in the vertical direction. In either case, local

¹Image CNR means the contrast to noise ratio of the tagged pattern in the input image, and not the contrast in Eulerian strain

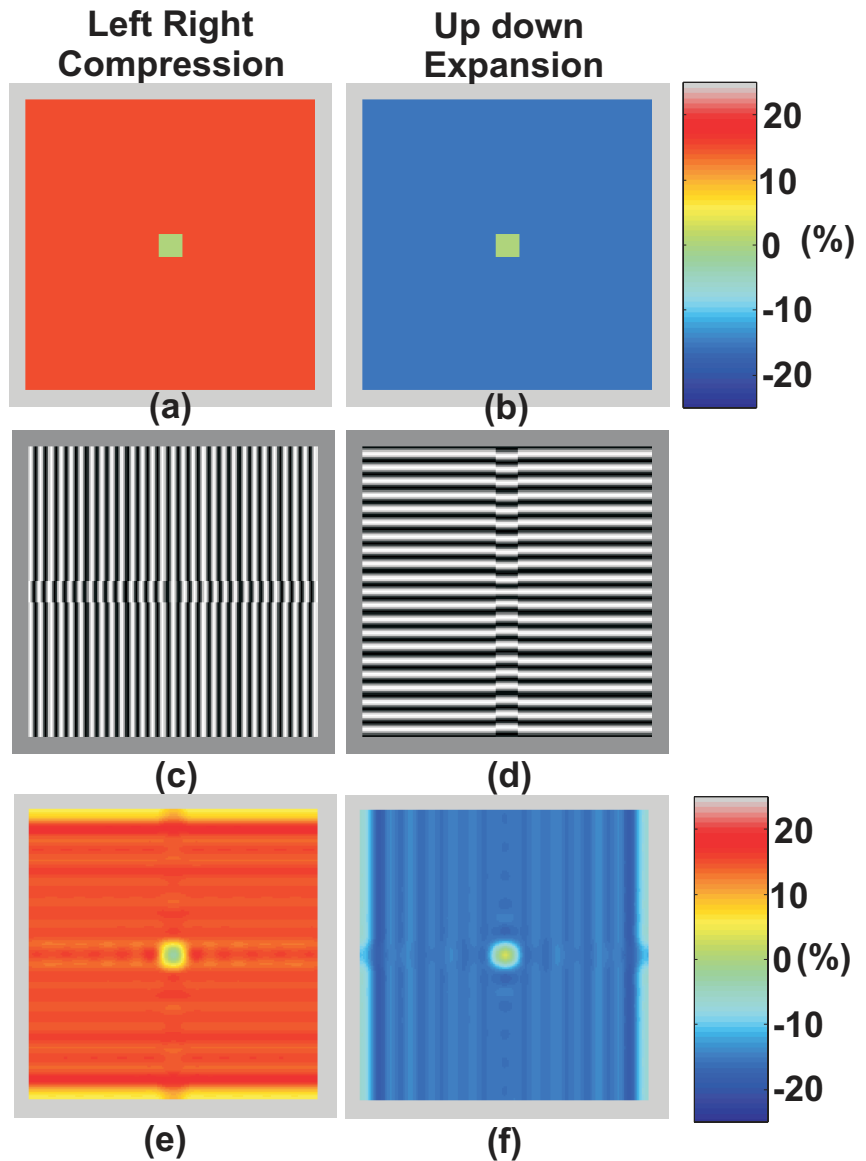


Figure 7.3: (a) Input strain pattern in the left right direction. The background tissue is under a state of -15% compression and the infarcted tissue has 0% strain. The encoding of this left-to-right compression is shown in the vertically tagged image in (c). (b) Strain pattern in the up down direction, with the similar strain pattern except that the tissue is stretched by +15% in the vertical direction. The encoding of this vertical expansion is shown in the horizontally tagged image in (d). Figs. (e) and (f) show the resulting strain maps produced using HARP-MRI

contrast in strain is produced by simulating an infarcted tissue with no compressibility in the center of a healthy background tissue. The difference between the two strain patterns is the sign of the background strain. The background tissue is compressed by $-S_b\%$ in the horizontal direction, while it is stretched by $+S_b\%$ in the vertical direction. This difference in sign of background strain is done to simulate an actual HARP-MRI study, where two strain maps are computed. One measures circumferential shortening and the other that measures radial thickening. The background tissue has different signs of strain in the two cases.

The tagged images that encode the strain patterns are shown in Figs. 7.3(c) and (d). The vertically tagged image encodes the horizontal displacement, while the horizontally tagged image encodes the vertical displacement. Since the edges of the infarcted region are steep, shearing is noticeable in both tagged images. The size of the background tissue is fixed at 8 cm on either side of the infarction. The tagged images were simulated with a tag separation of 0.7 cm and a FOV of 28 cm.

Contrast and Detail. Different levels of contrast are simulated by varying the background tissue strain, while fixing the strain in the infarction to be 0%. Six different values of background strain were tested: $\pm 5\%$, $\pm 15\%$ and $\pm 30\%$. Negative strains denote the strains in the horizontal direction and positive strains denote the strains in the vertical direction. Note that since the infarcted region has 0% strain, the term background strain and strain contrast mean the same thing. The shape of the infarcted region was fixed to be square and the size was varied from 1.1 cm to 0.1 cm on its side. A filter size of 33×33 was used in the HARP-MRI analysis of the tagged images. The estimated strain maps in the horizontal and vertical directions are shown in Figs. 7.3(e) and (f), respectively. The blurring of the infarcted region can be clearly seen. The detected contrast between the healthy and diseased regions is computed as follows.

$$\text{Detected contrast} = [\hat{s}(x, y)]_{\text{avg over infarction}} - [\hat{s}(x, y)]_{\text{avg over background}} \quad (7.1)$$

The averaging of strain over the infarction and the background region is useful for two reasons. First, in clinical studies, averaging is often done over octants and layers (see Chapter 3 Fig. 3.11), and the contrast is defined as the difference between the averaged

strain in the diseased and remote region. Second, the averaging smooths out the presence of $A(x, y)$ and gives a ‘clean’ measure of contrast. Note that the contrast-detail experiment was done for a noise-free case. Both measures of noise, $A(x, y)$ and $N_o(x, y)$, will be quantified in the next section.

7.3.2 Quantification of Noise

A piece of tissue in the myocardium is deemed infarcted if the average strain contrast between the infarcted and remote regions exceeds a noise threshold in the remote region. In order to derive this noise threshold, we perform the same simulation as above, but this time without the infarcted tissue. All geometric parameters like the size of the background tissue and the tag pattern remain the same. The tissue is simulated with six different values of uniform background strain: $\pm 5\%$, $\pm 15\%$ and $\pm 30\%$. The six values were selected so that they matched the background strains in the contrast–detail simulations. For each value of strain, Gaussian noise was added to yield CNR values of 5, 10, and 15. Figs. 7.4(a) and (b) show examples of the tagged images. Figs. 7.4(c) and (d) show the corresponding estimates of strain. For each strain map, noise was measured as the root mean squared (r.m.s) error in a $1 \text{ cm} \times 1 \text{ cm}$ square in the center of the object. The 1 cm size was picked because the size of the voxel in this simulation was around 1 cm.

For a given CNR value and background strain, 200 realizations of noise were added in Monte Carlo fashion and the r.m.s error was computed for every trial. An example of a histogram of the 200 value of r.m.s error is shown in bottom row of Fig. 7.4. The histogram shows the contribution of both the systematic and the random sources of error. The offset, or the mean of the histogram, quantifies the bias $A(x, y)$ due to systematic errors and the standard deviation $N_o(x, y)$ of the histogram quantifies the random errors. The noise threshold is computed as

$$\text{Noise threshold} = \mu_{\text{hist}} + 2 \sigma_{\text{hist}}, \quad (7.2)$$

where μ_{hist} and σ_{hist} are the mean and standard deviation of the histogram, respectively. An infarction is deemed detectable if the detected contrast [Eq.(7.1)] is greater than the noise threshold.

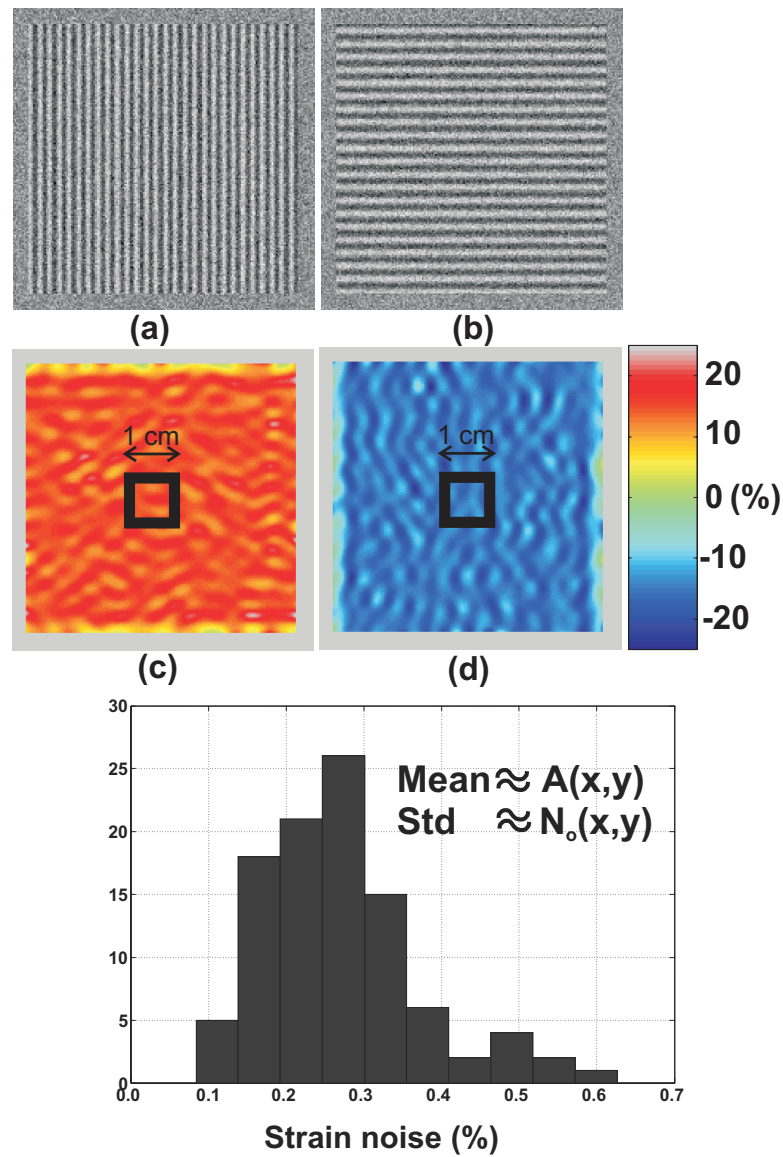


Figure 7.4: (a) and (b) show the noise tagged images without the infarcted region. (c) and (d) show the corresponding strain maps. A $1\text{ cm} \times 1\text{ cm}$ square is selected to compute the error to derive the noise threshold. The bottom figure shows the histogram of the noise in strain.

7.4 Results

7.4.1 Reconstructed Contrast

Plots (a) and (b) in Fig. 7.5 show the reconstructed contrasts plotted as function of infarction size for three different input contrasts. The output contrast is proportional to the input contrast, which is expected. The reduction of contrast is similar in both positive and negative background strains, implying that the effect of blurring is same irrespective of the sign of strain.

7.4.2 Noise Quantification

Plot (c) in Fig. 7.5 shows the noise thresholds as a function of background strain. The effect of random image noise on the errors can be seen from the variation of errors with CNR values. As CNR decreases, the noise threshold increases. The effect of systematic error is also observed to increase as magnitude of strain increases. As strain increases, the spreading of the spectral peak increases. Hence the errors due to spectral interference increase, thereby increasing the bias of the noise histogram.

7.4.3 Detectability Results

Plots (d) and (e) of Fig. 7.5 show the detectability limits for vertical and horizontal tagged images respectively. Apart from the detectability limits, two other sets of values are plotted. The black line with squares shows plots the intrinsic Fourier resolution of the system defined by the FWHM of the 33×33 bandpass filter, which is 0.84 cm. The black line with stars corresponds to the infarction sizes for which the output contrast is 50% of the input. In a previous work, this size has been used to define the resolution of an tag detection system [37]. It is interesting to see that the sizes that corresponds to 50% of the contrast are approximately equal to the value of the FWHM. This observation helps us understand the influence of the HARP bandpass filter on its detectability. If the size of the infarction is around the FWHM of the filter, the reconstructed contrast will be around 50% of its input contrast.

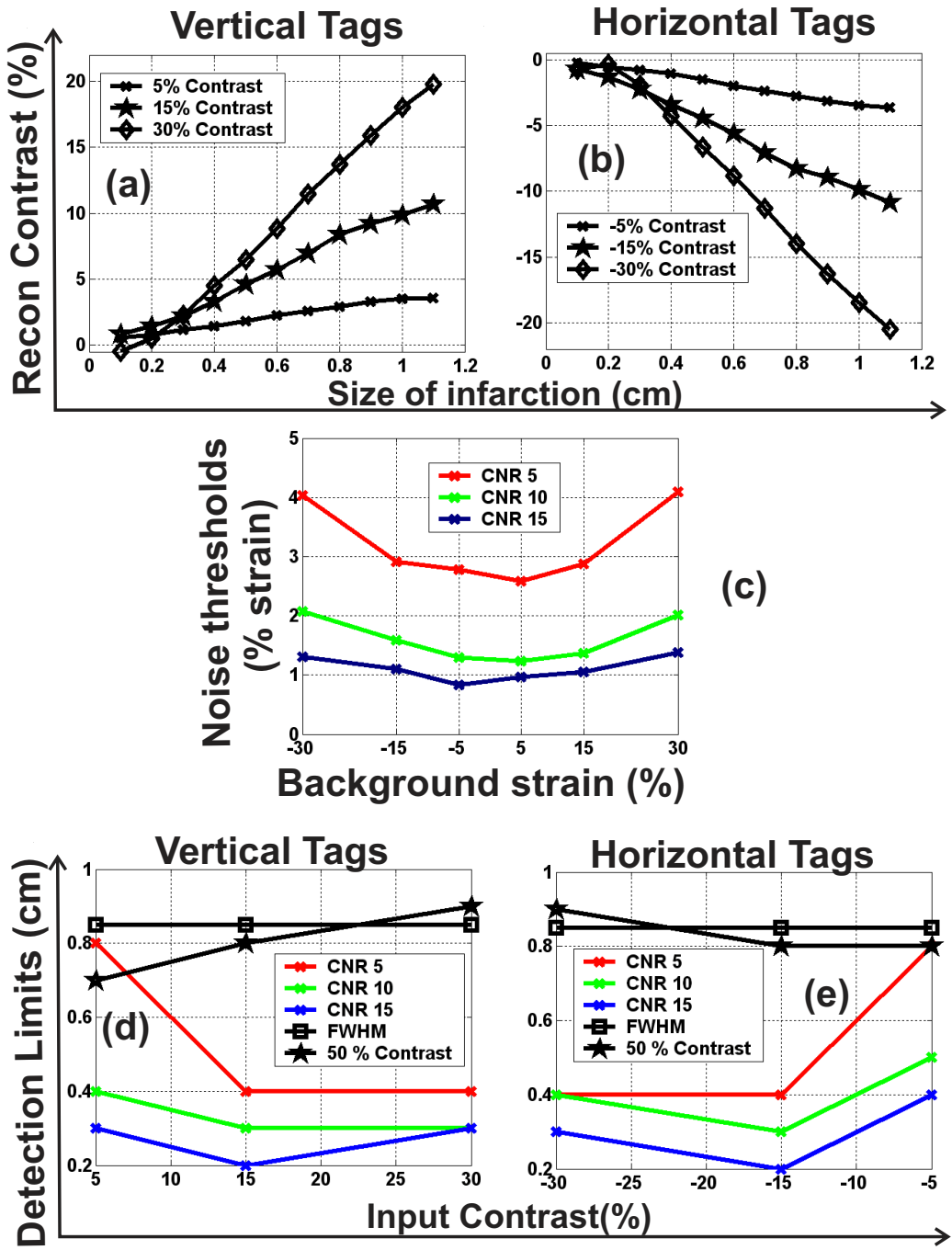


Figure 7.5: Plots (a) and (b) show the results from the contrast-detail experiment, plot (c) show the result from the noise quantification experiment. Plots (a), (b), and (c) are used to derive detectability limits for horizontal and vertical tags as shown in plots (d) and (e)

The detectability limits are plotted for three different CNR values as a function of background strain. The detectability measures are strikingly different than the FWHM. We observe that infarctions can generally be detected, even if they are much smaller than the FWHM. The variation in detectability limits are also quite intuitive. Detectability increases with increase in CNR of the image. A decrease in noise pushes the noise threshold down and hence increases the detectability. The increase of input contrast generally implies the increase of detectability. In the worst case for $\text{CNR} = 5$ and an input strain contrast of 5%, the detectable size of infarction is around 0.8 cm, which is close to the FWHM of the filter. In the best case, for $\text{CNR} = 15$, and an input contrast of 15%, infarction as small as 0.2 cm can be detected. Generally, for CNR typical of CSPAMM images, infarcts as small as 0.3–0.5 times the FWHM can be detected.

7.5 Discussion

7.5.1 Clinical Studies

This chapter makes an attempt to clear the confusion between the resolution of HARP-MRI and its ability to detect abnormalities in the heart. We showed that, even though both are related through 50% reduction in contrast, abnormal heart tissue can be detected even if they are much smaller than the FWHM of the filter. The results of the simulations in this chapter corroborates clinical studies, which have successfully used HARP-MRI to detect subendocardial ischemia and infarctions [76, 50].

7.5.2 Assumptions and Simplifications

The work in this chapter is only a first step in completing understanding detectability of HARP-MRI. This is because this work is based on simple simulations. These simplifications were done to illustrate the differences and connections between the concept of resolution and detectability. The following list illustrates the simplifications done.

1. The simulation had a very simple geometry of a square piece of tissue with a constant background size, and the object occupied a large portion of the FOV. Moreover the

regions of interest were far removed from the edges of the object. In reality, this is not the case. The subendocardial defects occur at the edges of the myocardium and blood, and the background tissue is only around 1.5 cm wide.

2. The shape of the infarction was assumed to be a square. In reality, sub-endocardial abnormalities start as thin layers and then grow. These shapes need to be incorporated in order to study the isotropic properties of detectability.
3. The edges of the infarcted region are assumed to be very sharp. As described in the previous chapter, there is functional border zone that acts as a buffer between the healthy and diseased tissue.

7.6 Conclusion

In this chapter, we studied the detectability properties of HARP-MRI. A simple motion model was simulated with a piece of infarcted tissue in the middle of healthy background tissue. The detectability was based on the ability to detect the output strain contrast in background noise. Our simulations suggest that regions of abnormal strain can be detected even though they are much smaller than the FWHM resolution of the system.

Chapter 8

Artifacts in HARP-MRI Strain Maps

Preface

So far in this dissertation, several approaches have been used to quantify and characterize the sources of error in HARP-MRI. In Chapter 3, errors were quantified using simulations. In Chapters 4 through 7, the errors were quantified and characterized in terms of image quality indices — dynamic range, resolution, and detectability. In this chapter, we shift the focus from the quantification of errors to their actual visual appearance. The understanding of how the errors visually appear in the final output is important for clinical diagnosis. However good an objective image quality index may be, a visually unappealing output renders the image diagnostically unusable.

In this chapter, we specifically focus on the effect of errors on Eulerian strain maps. The errors cause undesirable effects called *artifacts*, which reduces the diagnostic usability of strain maps. We investigate the mechanism through which these artifacts are produced. We will also propose an algorithm to reduce the artifacts. In short, this chapter is about the production and reduction of artifacts in HARP-MRI strain maps.

8.1 Introduction

Artifacts are unphysiological patterns that reduce the diagnostic usability of a medical image. Almost all medical imaging modalities suffer from the presence of artifacts in their images. Artifacts are caused by a variety of processes. For example, metal materials in a patient cause streak artifacts in computed tomographic (CT) images. In MRI, the so-called

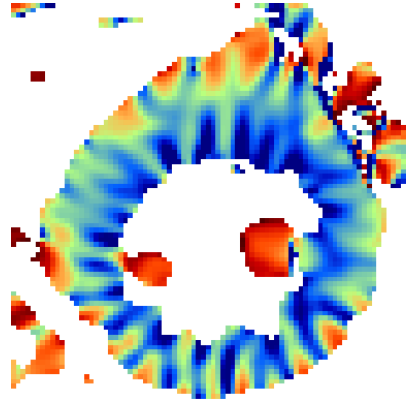


Figure 8.1: Example of circumferential strain map showing accentuated zebra artifacts.

ghost artifact occurs when the patient moves during the scanning. In most cases, artifacts impair proper visualization of the features of interest. Characterization, evaluation, and possible removal of the artifacts should be a part of any high quality medical imaging system [128].

The most commonly seen artifact in HARP-MRI strain maps are spoke-like artifacts. These artifacts are mainly seen in circumferential strain maps, an example of which is shown in Fig. 8.1. Because of its peculiar shape, this artifact has been called by different names in the literature: pin-wheel, stripe, spoke-like, and zebra. We call it the *zebra artifact* in this dissertation. The presence of this artifact was acknowledged as early as the first HARP-MRI publication in the year 2000 [111], and its presence has been reported by other groups that use HARP-MRI [131, 78]. The sources of error that contribute to this artifact are often claimed to be spectral interference and image noise. This can be seen using a simple simulation. Fig. 8.2(a) shows a circumferential strain (CS) map that given as an input to the HARP-MRI system. Fig. 8.2(b) shows the output CS map produced using a coverage ratio of 0.5¹. Mild spoke like patterns that seem to emanate from the center of the myocardium start to appear in these strain maps. Fig. 8.2(c) shows the output CS map reconstructed using a much bigger bandpass filter of coverage ratio 0.9. We can see a clear

¹Recall from chapter 3 that coverage ratio is defined as the ratio of the filter radius to the tag frequency

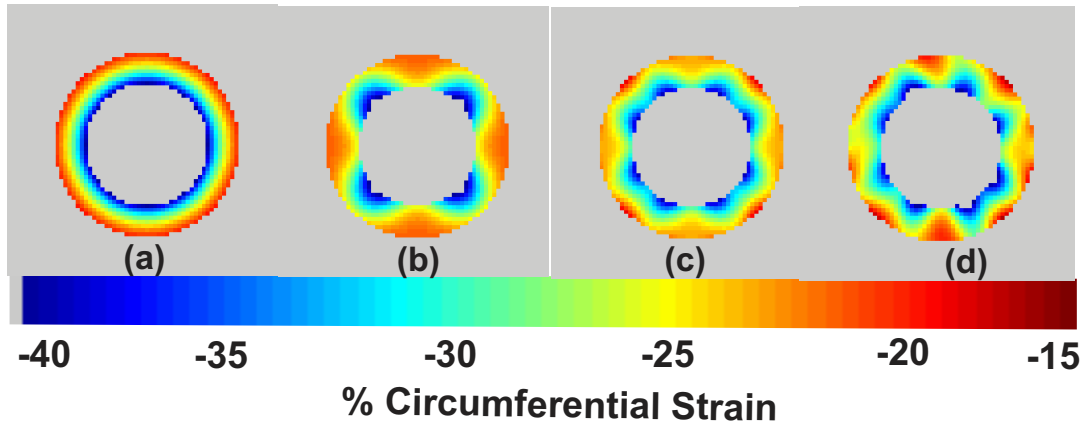


Figure 8.2: (a) True circumferential strain map (b) Reconstructed HARP strain map with coverage ratio 0.5 and no noise (c) Reconstructed HARP strain map with a bigger filter of coverage ratio 0.9 (d) Reconstructed strain map with noise added with CNR 10

increase in the zebra patterns. These patterns start to get distorted with the introduction of noise. Fig. 8.2(d) shows the reconstructed strain for input CNR of 10.

These observations corroborate the fact that spectral interference and noise are contributors to the artifact. As filter size increases, spectral interference from the conjugate harmonic peak becomes larger, thereby increasing the artifacts. The introduction of noise accentuates these artifacts.

8.2 Hypothesis

In spite of the identification of the sources of these artifacts, it is still not clear how the peculiar shape is formed. The zebra artifacts have strikingly regular spatial pattern around the myocardium. Our hypothesis is that the shape of the artifact is, in some way, dependent on the circumferential direction in which the strain is computed. In order to test this directionality hypothesis, we consider the estimation of the radial strain, which has been largely ignored in the discussion of artifacts. Fig. 8.3 shows reconstructed radial strain (RS) maps. The artifacts in the RS are not spoke-like, but have gross errors with a different pattern on directionality. The errors are seen mainly at the diametrically opposite parts of the myocardium. We hypothesize that the understanding of the directionality of these

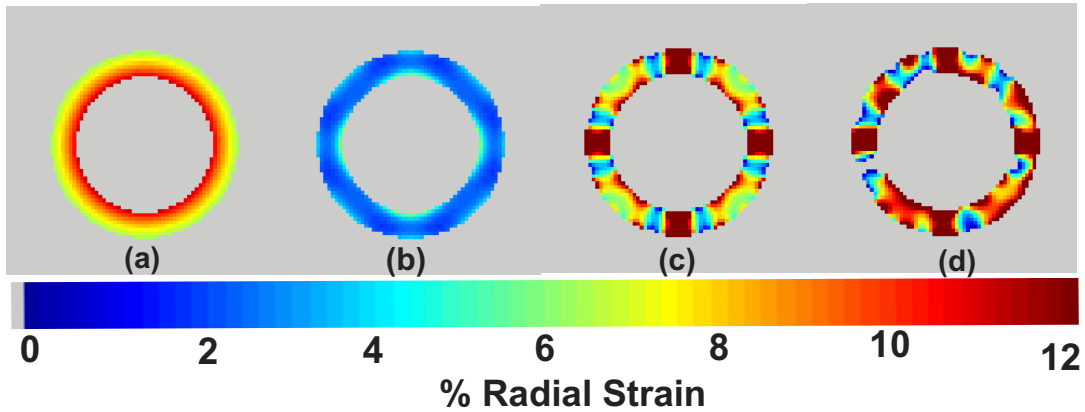


Figure 8.3: (a) True radial strain map (b) Reconstructed HARP strain map with coverage ratio 0.5 and no noise (c) Reconstructed HARP strain map with a bigger filter of coverage ratio 0.9 (d) Reconstructed strain map with noise added with CNR 10. Note the gross errors that occurs due to IVPD and PVE

errors is key to understand the mechanism of production of artifacts, both in the radial and circumferential strains. Therefore, in the first part of this chapter, we will go into the guts of the strain computation and understand the source of this directionality. In the second part, we will use this understanding to develop a method to reduce artifacts.

Artifacts and colormaps. Before judging the quality of a strain maps in terms of it artifacts, it is important to check the dynamic range of colors used to represent the strain maps. The visual effect of these artifacts look very different for different dynamic ranges. A tight colormap — one that covers the full range of strains with the entire dynamic range of available colors — often accentuates the artifacts. The colormaps used in this chapter have been carefully chosen to accentuate the effects of the artifacts so that their degrading effect is seen more clearly.

8.3 Mechanism of Production of Artifacts

8.3.1 Computation of Eulerian Strain

Consider two simulated tagged images as shown in Figs. 8.4(a) and (b). Note that

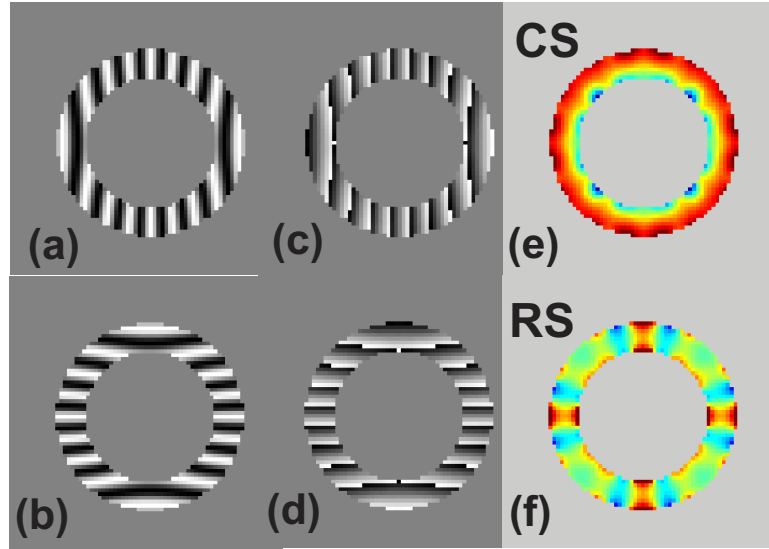


Figure 8.4: (a,b) Vertical and horizontal tagged images, (c,d) Corresponding HARP phases, (e,f) circumferential and radial strain maps

the tag patterns in this section are simulated without input noise. This is done so that the directionality can be studied better. The noise affects the measures throughout the myocardium, without any spatial directionality. The HARP phases corresponding to the tag images are shown in Figs. 8.4(c) and (d). The reconstructed strain maps are shown in Figs. 8.4(e) and (f).

The derivation of Eulerian strain was presented in Chapter 2, section 2.6.2. It is repeated here with more computational details. The Eulerian strain S in the direction of $d\mathbf{r}$ is given as

$$S_{d\mathbf{r}} = \frac{\|d\mathbf{r}\| - \|d\mathbf{R}\|}{\|d\mathbf{r}\|}, \quad (8.1)$$

where $d\mathbf{R}$ and $d\mathbf{r}$ are vectors that represent the reference and the deformed configurations of an infinitesimally small piece of tissue. In the computation of Eulerian strain, $d\mathbf{r}$ is selected so that $\|d\mathbf{r}\| = 1$, and the direction of $d\mathbf{r}$ corresponds to either the circumferential or the radial direction at any given point. Given $d\mathbf{r}$, the reference $d\mathbf{R}$ is computed as,

$$d\mathbf{R} = F^{-1}d\mathbf{r} \quad (8.2)$$

$$= \Omega^{-T} \nabla \phi(\mathbf{x}, t) d\mathbf{r}, \quad (8.3)$$

where

$$\Omega = \begin{bmatrix} \omega_x & 0 \\ 0 & \omega_y \end{bmatrix}, \quad (8.4)$$

where ω_x and ω_y are the frequencies of vertical and horizontal tags respectively. The gradient of HARP phase $\nabla\phi(\mathbf{x}, t)$ is computed using symmetric finite difference operator along the x (columns) and y (rows) directions. The gradient of HARP phase can be written as a matrix

$$\nabla\phi(\mathbf{x}, t) = \begin{bmatrix} \partial\phi^{ver}/\partial x & \partial\phi^{ver}/\partial y \\ \partial\phi^{hor}/\partial x & \partial\phi^{hor}/\partial y \end{bmatrix}. \quad (8.5)$$

The directional vector at a point can be either in the circumferential direction $d\mathbf{r}_C$ or in the radial direction $d\mathbf{r}_R$. Each directional vector can be decomposed in their x and y components as

$$d\mathbf{r}_C = [dr_C^x \ dr_C^y]^T, \quad (8.6)$$

$$d\mathbf{r}_R = [dr_R^x \ dr_R^y]^T. \quad (8.7)$$

From Eqs. 8.3, 8.5, and 8.6, the two components of $d\mathbf{R}$ in the circumferential direction can be calculated using simple matrix multiplications

$$\begin{bmatrix} d\mathbf{R}_C^x \\ d\mathbf{R}_C^y \end{bmatrix} = \Omega^{-T} \begin{bmatrix} \frac{\partial\phi^{ver}}{\partial x} dr_C^x + \frac{\partial\phi^{ver}}{\partial y} dr_C^y \\ \frac{\partial\phi^{hor}}{\partial x} dr_C^x + \frac{\partial\phi^{hor}}{\partial y} dr_C^y \end{bmatrix}. \quad (8.8)$$

Similarly, the components of $d\mathbf{R}$ in the radial direction can be calculated as

$$\begin{bmatrix} d\mathbf{R}_R^x \\ d\mathbf{R}_R^y \end{bmatrix} = \Omega^{-T} \begin{bmatrix} \frac{\partial\phi^{ver}}{\partial x} dr_R^x + \frac{\partial\phi^{ver}}{\partial y} dr_R^y \\ \frac{\partial\phi^{hor}}{\partial x} dr_R^x + \frac{\partial\phi^{hor}}{\partial y} dr_R^y \end{bmatrix}. \quad (8.9)$$

8.3.2 Errors in HARP phase and phase gradients

The frequency matrix Ω is a constant scaling matrix and hence cannot contribute to the directionality of the artifacts. Therefore, from Eq.(8.3), the source of the artifacts must be the result of the combination of HARP phase gradients and the directional vector $d\mathbf{r}$. We start by considering the errors in the HARP phases and their gradients.

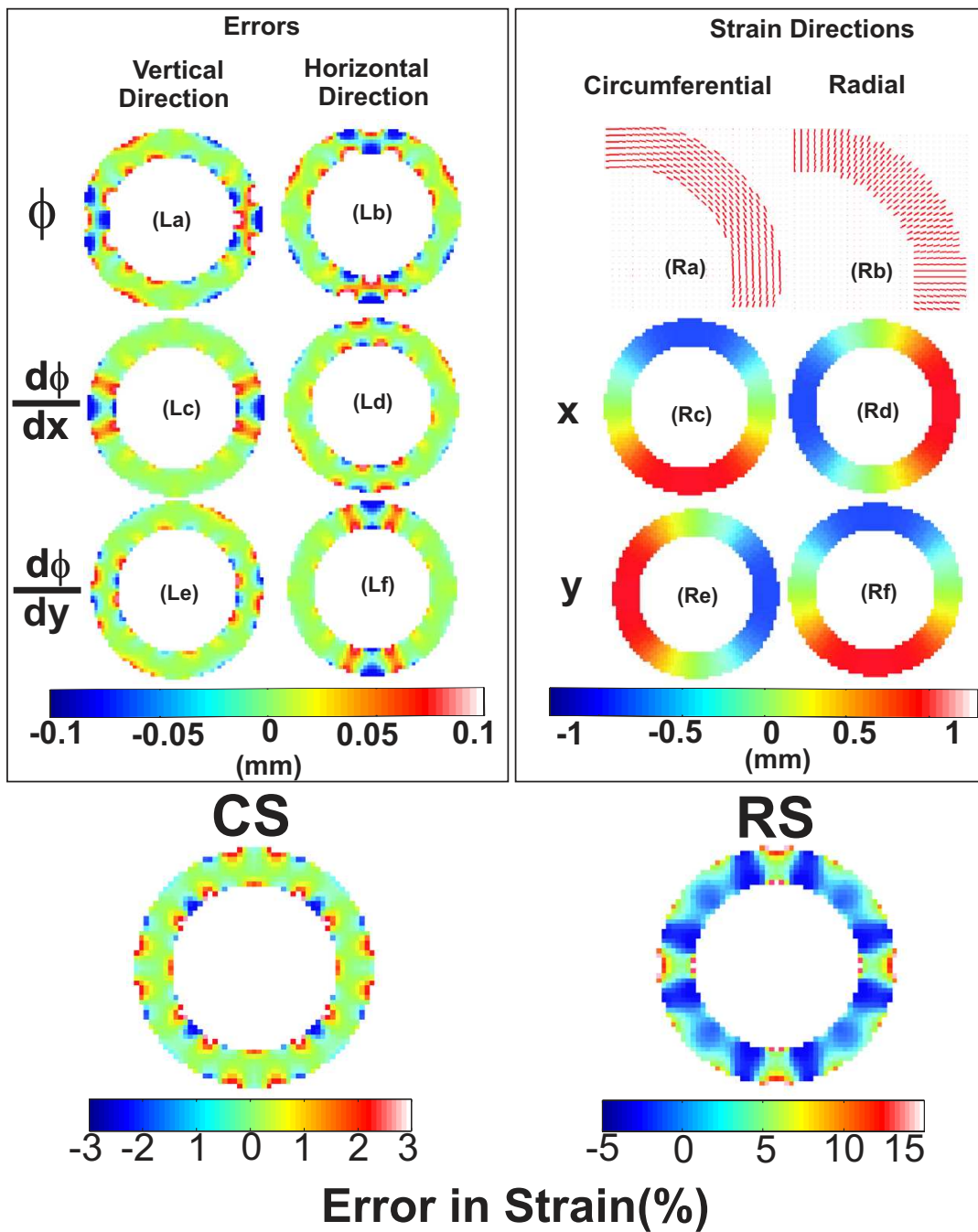


Figure 8.5: Left panel: (La, Lb) Errors in HARP phase. (Lc, Ld, Le, Lf) Errors in HARP phase derivatives. Right panel: (Ra, Rb) shows quiver plots of the circumferential and radial strains in a sector of the myocardium. (Rc, Rd, Re, Rf) show the x and y components of the directionality vectors. Bottom: Errors in computed strain

Figs. 8.5(La) and (Lb) show the errors in the HARP phases ϕ^{ver} and ϕ^{hor} . The error patterns have a very distinct directionality. The errors in the vertical HARP phase occur in the horizontal direction, whereas the errors in the horizontal HARP phase occur in the vertical direction. Figs. 8.5(Lc)–(Ld) show the errors in the different components of the HARP gradient tensor, which are precisely the x and y derivatives of error patterns shown in Fig. 8.5(La) and (Lb). The x -derivative of the vertical tags ($\partial\phi^{ver}/\partial x$ [Fig. 8.5(Lc)]) and the y -derivative of the horizontal tags ($\partial\phi^{hor}/\partial y$ [Fig. 8.5(Lf)]) have large errors. The two cross terms have low errors and are localized to the inner and outer edges of the myocardium. Both the derivative components of the vertical tags [Fig. 8.5(Lc,Le)] have errors oriented in the horizontal direction, whereas derivatives of the horizontal tags [Fig. 8.5(Ld,Lf)] have errors in the vertical direction. In all four gradient errors, the areas of large errors resemble errors in RS maps, while the area of low errors resemble the zebra pattern in CS maps.

8.3.3 Combination of phase gradient and directional vectors

All four derivative errors contribute to overall error in both radial and circumferential strain maps. Logically, the errors should be common to both strain maps; but observation does not support this. Therefore, the difference should come from the directions in which the strains are computed. The right panel of Fig. 8.5 show the components of the directional vectors $d\mathbf{r}_C$ and $d\mathbf{r}_R$. Figs. 8.5(Ra) and (Rb) show quiver plots of the circumferential and radial directions in one quadrant of the myocardial wall. Figs. 8.5(Rc) and (Re) show the images of the components dr_C^x and dr_C^y respectively. Similarly, Figs. 8.5(Rd) and (Rf) show the images of dr_R^x and dr_R^y . The errors in the RS and CS can be visualized by putting together the respective components from the left and the right panels using Eqs. 8.8 and 8.9.

It can be easily seen that, by the construction of circumferential direction, the CS zeros out all the high error regions and retains regions that have low error. On the other hand, RS zeros out all the low error regions and retain only the regions with high error. This explain, at least computationally, why the radial strain have higher errors than circumferential strain. The errors in the reconstructed CS and RS are plotted in the bottom row of Fig. 8.5. Also

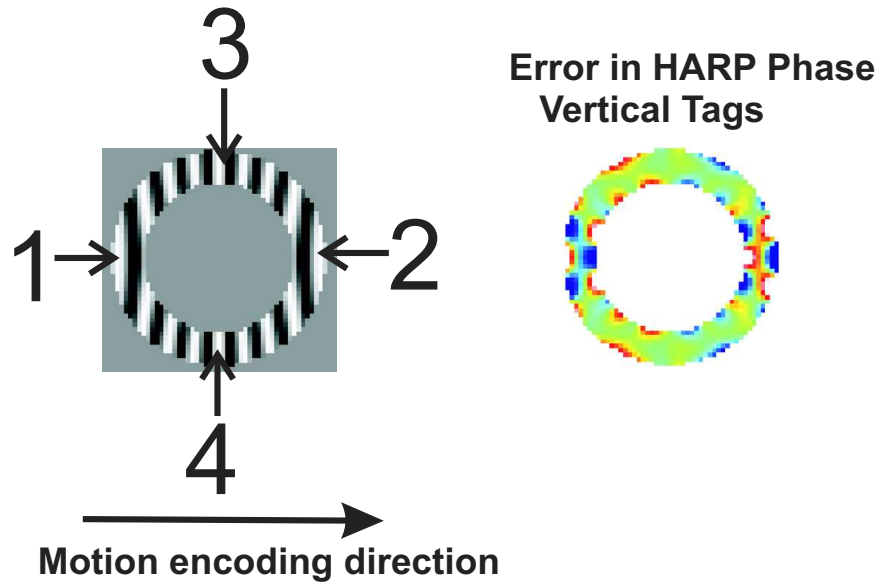


Figure 8.6: Regions 1 and 2 encode radial motion. In Regions 3 and 4 the radial motion is orthogonal to the tagging direction and hence not encoded. Regions 1 and 2 have high error due to IVPD and PVE, Regions 3 and 4 have negligible IVPD and PVE errors.

note that a seemingly small error of 0.1 mm in HARP phase and its gradients can cause large errors (3–15%) in strain calculations.

8.3.4 Why is RS worse than CS?

The differences between the estimation of RS and CS are very striking. This difference can be attributed to the fact that RS is affected more by voxel based errors IVPD and PVE, which cause more errors than spectral interference and noise. But, this begs the next question, “Why are radial measures affected more by IVPD and PVE?”

Short answer. The answer lies in the underlying motion of the tissue in the heart. The largest displacement of the myocardial tissue points is in the radial direction, and both radial thickening and circumferential shortening is caused by this radial motion. IVPD is present only in regions where the tags encode this radial displacement, irrespective of the direction of strain.

Long answer. Consider, for example, the case of vertical tags shown in Fig. 8.6. The

vertical tags encode radial displacement only in regions 1 and 2. In these regions, the tags encode radial thickening. In regions 3 and 4, although the vertical tags encode circumferential shortening, the radial displacement encoded by vertical tags is zero. In such regions, where there is no encoded displacement, the HARP phases do not undergo dispersion, and hence IVPD has zero effect. On the other hand, in regions 1 and 2, the tags encode the radial displacement directly, and hence the effect of IVPD is maximum. The key lies in understanding that, for IVPD to have effect, the motion should be in the direction of the tags; the strain direction is actually irrelevant. Since the motion of tissue points are always in the radial direction, the only displacements affected by IVPD are radial. Hence all the quantities dependent on radial displacement, like radial strains, have large errors.

Compounding this problem, radial thickening leads to a decrease in instantaneous frequency, which cause spectral spreading towards the other harmonic peak, thus increasing spectral interference. The effect of spectral interference, however, is small relative to the effect of IVPD.

8.4 Artifact reduction

In the previous section, we learned about the mechanism of the production of artifacts. While the effects of spectral interference and noise can be reduced, the errors due to IVPD and PVE are irrecoverable. Therefore, in this section we focus on artifacts in CS, which is affected only by spectral interference and noise. We propose an algorithm to reduce the artifacts and test the algorithm on an *in vivo* data set.

8.4.1 Previous work

The current approach to smooth the strain maps is based on one-dimensional filtering of HARP derivatives [113]. This approach takes into consideration the observations about the directionality of the errors in the HARP derivatives. For the derivatives in the x direction, it employs a 1-D weighted moving averaging filter in the x direction. For the derivatives in the y direction, the filtering is done along the y direction. The use of a 1-D filter was justified by the need to preserve transmural changes in strain, which is a crucial factor in

diagnosis. The size of the filter is fixed at 12 pixels in the spatial domain, and the weighting is done using the HARP magnitude image. The HARP magnitude provides the confidence as to whether the HARP phase value is good or not. The smoothed derivatives are then used to compute the strains.

This method has certain drawbacks. The size of the moving average filter is fixed; in other words, the size of the pass band of the corresponding low pass filter is fixed irrespective of the size of the bandpass filter used. Thus this method does not consider the spectral characteristics of the underlying strain. Also, since the filtering is in 1-D, new 1-D artifacts are sometimes introduced in the strain maps.

8.4.2 Weighted Phase Unwrapping and Smoothing

We propose to use a 2-D filter to smooth the HARP phase. A 2-D filter cannot be directly applied on HARP phase image because it is wrapped between $-\pi$ to π . Therefore, we use a weighted phase unwrapping algorithm [52]. The use of a weighting image during unwrapping causes the regions of high noise, like blood, to be excluded from the unwrapping process. Fig. 8.7(b) shows an unweighted HARP phase map. The magnitude image in Fig. 8.7(a) is thresholded to obtain a binary threshold image shown in Fig. 8.7(c). The weighted wrapped phase is shown in Fig. 8.7(d). This image is first demodulated so that phase of the carrier tagging signal is eliminated as shown in Fig. 8.7(e). The resulting demodulated phase image is then unwrapped to get the unwrapped HARP phase shown in Fig. 8.7(f).

The unwrapped phase is then smoothed with a 2-D linear low pass filter. Unlike the previous work, where the filter was designed in the spatial domain, here we design the low pass filter in the frequency domain. The selection of the size of the low pass filter was based on the lessons learned from the theory of resolution of HARP-MRI resolution in Chapter 6. We know that the highest frequency in the instantaneous frequency is limited by the size of the bandpass filter. Therefore the HARP phase, which is the integral of the IF, cannot have any frequencies outside the bandpass filter. Therefore, the size of the low pass filter is designed to be the same as that of the bandpass filter.

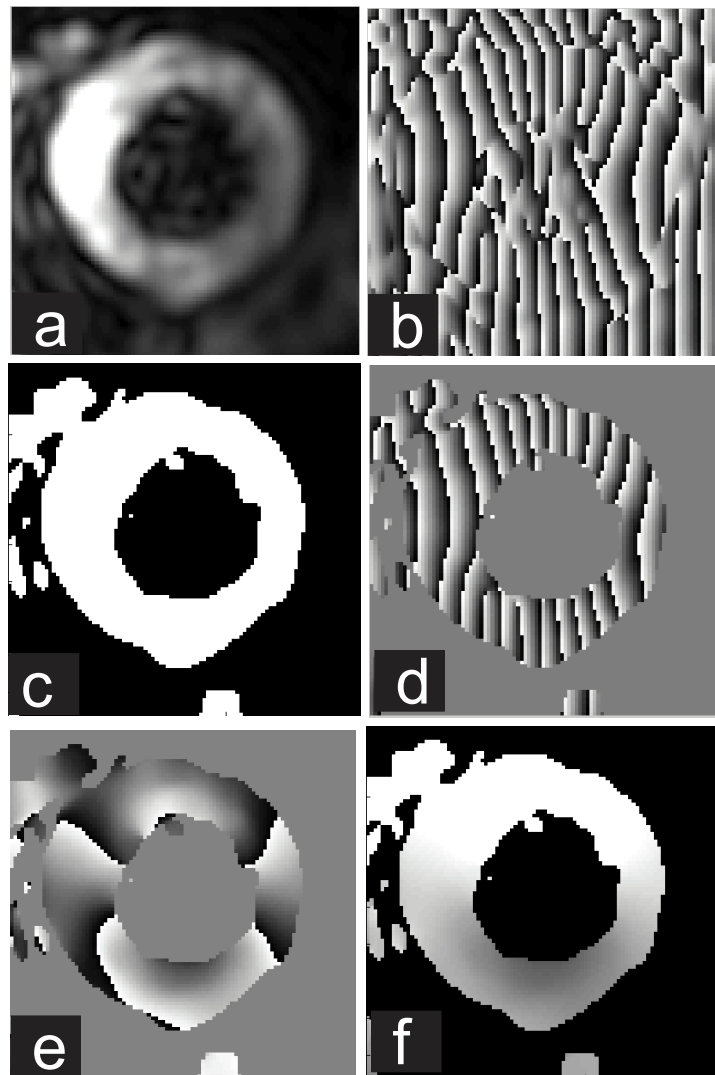


Figure 8.7: (a) HARP Magnitude image (b) HARP phase unmasked (c) Binary mask generated by thresholding the magnitude image (d) masked HARP image (e) demodulated HARP image (f) unwrapped HARP phase

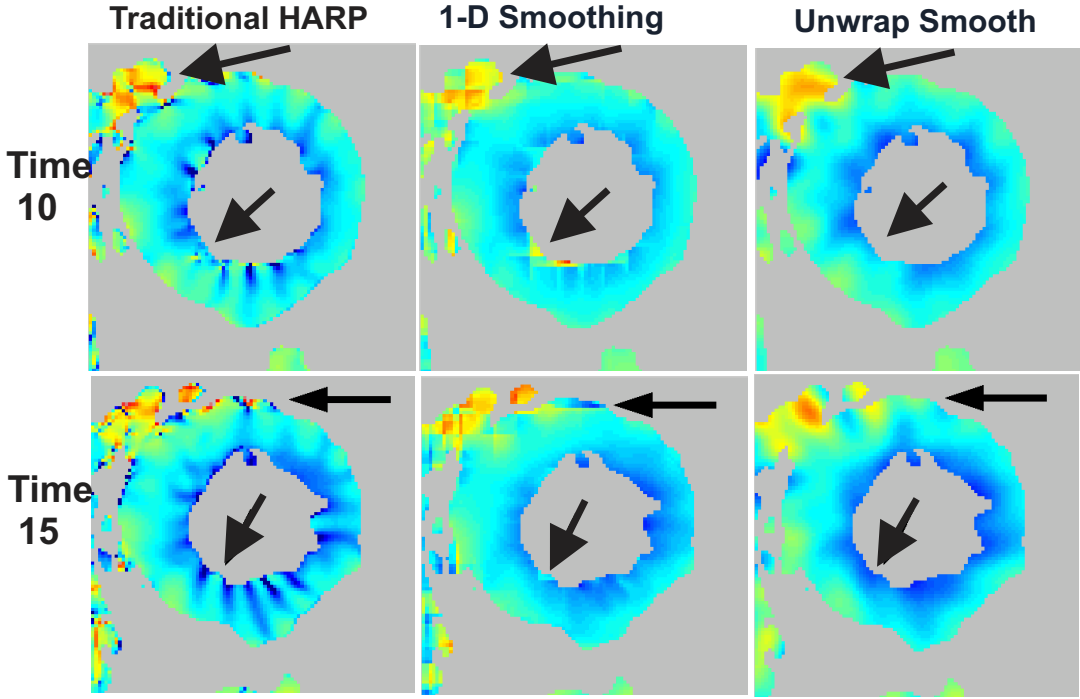


Figure 8.8: First column shows the strain maps from the no-smoothing case. Second and third columns show the strain maps from the 1-D smoothing and the proposed methods respectively. The two row represent two different time frames. The second row is later in systole and hence has more strain than strain maps in the first row.

8.4.3 Results

Fig. 8.8 shows the circumferential strain maps obtained using three methods. The first column shows the strain maps obtained using the traditional HARP without smoothing. The presence of the zebra pattern can be clearly seen in both the time frames 10 and 15 from an in vivo data set consisting of 28 time frames. It can also been observed that the zebra pattern in time frame 15 is more in time frame 10. This is because, as strain increases during systole, the spectral spreading become more, resulting in more interference. The 1-D smoothing methods reduce the artifacts, but introduces some additional artifacts (see the arrows). The 2-D filtering, on the other hand, uniformly smoothes the strain maps.

One key measure of performance of smoothing algorithms is their ability to preserve the gradient of strain between the three walls of the heart: endocardium, mid wall, and epicardium. In order to see this, the strains were averaged into eight octants and three

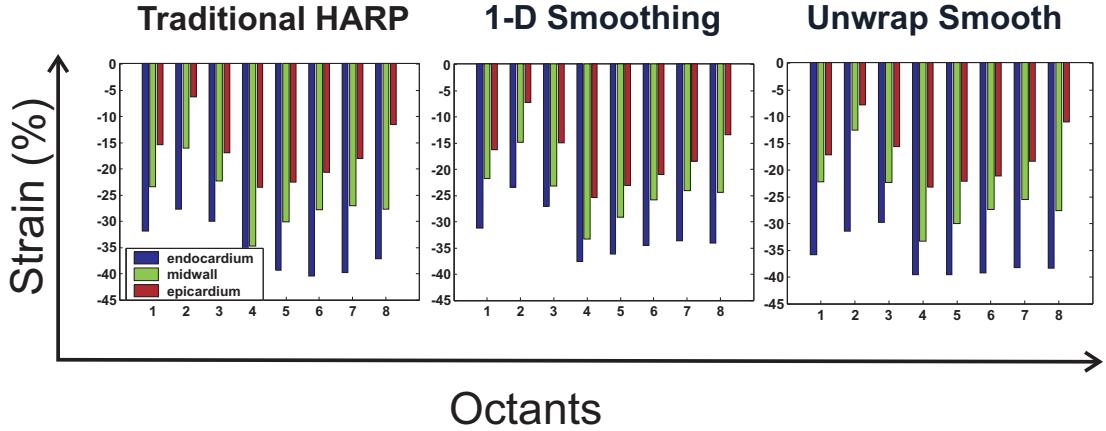


Figure 8.9: Comparison of preservation of transmural gradient.

layers (see chapter 3, Fig. 3.11) and are plotted in Fig. 8.9. The traditional HARP with no smoothing is considered the gold standard in this comparison. We see that the 1-D smoothing method slightly underestimates the strain and there is loss of transmural gradient. In case of the proposed method, the transmural gradient is preserved well. Finally, it needs to be noted that these results are preliminary. This work is a part of an ongoing research to find the optimal smoothing algorithm. Further research needs to be done to completely study the complete efficiency of the method. We plan to do this using simulations and more *in vivo* studies.

8.5 Discussion

The mechanism of the production of artifacts clearly indicate that spectral interference is one of two major sources of the zebra artifacts. Since spectral interference mainly comes from other spectral peaks, the use of CSPAMM acquisition is highly recommended for HARP-MRI computations. For the same reason, the use of grid tags is discouraged. Grid tags produce multiple peaks in k-space, thereby increasing artifacts in CS. Grid tags force the use of small filter size, which in turn increases IVPD effects in radial strains.

The best scenario is when both the central peak and the conjugate peak are suppressed, leaving us with only the harmonic peak in k-space. Recently developed imaging proto-

cols have been able to achieve that goal [44, 7, 156, 3]. But the elimination of the all peaks except the harmonic peak comes at the expense of imaging time, since these imaging protocols usually need usually twice the number of acquisitions that are needed with CSPAMM. One major challenge with such multiple acquisition protocols is the lack of registration between the different acquisitions, which might leads to further artifacts. More recently, nonlinear diffusion based image processing methods have been developed to reduce the artifacts [2], with promising initial results. Until these imaging and image processing methods are perfected, a optimal steps outlined in Chapter 3 will ensure minimal artifacts in both radial and circumferential strains.

8.6 Summary

The presence of the zebra artifacts affects the clinical usability of strain maps. This chapter explained the production of these artifacts from a computational viewpoint. We concluded that the zebra artifacts in circumferential strain map is caused by spectral interference and noise. We also studied IVPD affect RS more than CS. We proposed a method to reduce artifacts using a phase unwrapping approach and preliminary results were presented. We believe that the understanding of mechanism of production of artifacts will be useful in developing an optimal smoothing filter in the future.

Appendix: Properties of the Wrapping Operator

The following is a compilation of useful and interesting properties of the wrapping operator. If $\phi, \phi_1, \phi_2 \in \mathbb{R}$, then

1. $\mathcal{W}(\mathcal{W}(\phi_2) - \mathcal{W}(\phi_1)) = \phi_1 - \phi_2$, if $|\phi_1 - \phi_2| < \pi$
2. $\mathcal{W}(\mathcal{W}(\phi_2) + \mathcal{W}(\phi_1)) = \phi_1 + \phi_2$
3. $\mathcal{W}(a\phi) = \mathcal{W}(a\mathcal{W}(\phi))$
4. $\mathcal{W}(\mathcal{W}(\phi) + \phi_1) = \mathcal{W}(\phi + \phi_1)$

Chapter 9

Tracking Tongue Motion using HARP-MRI

Preface

In this chapter, we adapt HARP-MRI to a new application — to track the motion of a human tongue during speech. Tracking the tongue using HARP-MRI is challenging, because it stretches the performance envelope of HARP-MRI. Thus far in this dissertation, we have characterized the performance of HARP-MRI in two ways: optimal performance was characterized in Chapter 3, and peak performance was characterized in Chapters 5 through 7. In this chapter, we see how these performance measures hold up while tracking tongue motion during speech. The challenge in tracking the tongue comes from the fact that the motion of the tongue is both more variable and more complicated as compared to the heart. The tongue has more degrees of freedom of motion, both spatially and temporally.

In this chapter, we discuss the challenges in adapting HARP-MRI for tracking tongue motion. We use simple word utterances to test the feasibility of HARP-MRI in tracking tongue motion. We describe the imaging experiments in detail and explain the motion measures that have been developed exclusively for the tongue.

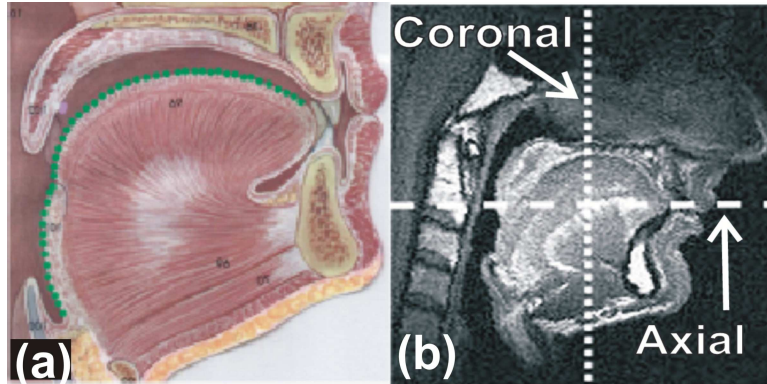


Figure 9.1: (a) Schematic of anatomy of the midsagittal cross section (b) static MRI of midsagittal slice with coronal and axial slice marked.

9.1 Introduction

Our interest in tracking the motion of the tongue is twofold: scientific and clinical. The scientific interest is to understand the role of the tongue in speech production. The related clinical interest is to understand how the speech production mechanism fails in disordered speech, as in deaf speakers. The motion of the tongue is critical not only to speaking, but also to swallowing and breathing. The human tongue has a complicated muscle structure, wherein different muscles intertwine and produce local compressions and expansions [92, 71]. The ensemble of these local deformations yields a change in shape of the tongue surface, which modulates the airway between the tongue surface and the palate. This modulation of the airway is partly responsible for producing different sounds during speech. Therefore, one of the goals of understanding speech production is to understand the relationship between the local deformations of the interior muscles and the movement of the tongue surface.

Fig. 9.1(a) shows a schematic of the anatomy of the midsagittal slice of the tongue (for reference, lips are to the right). It is easily seen that the tongue that is visible to the human eye forms only a small part of the tongue, namely the tongue tip. The body of the tongue is much larger, extending far below the tip of the tongue. Because of its location deep within the vocal tract, imaging the tongue has been quite challenging. Different imaging modalities are used both for measuring surface shape changes and for measuring

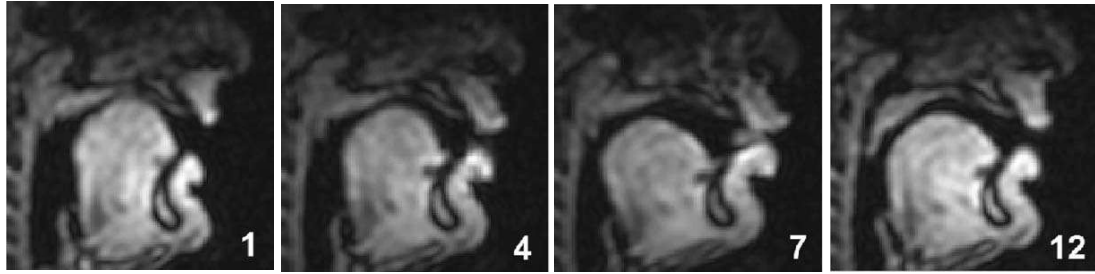


Figure 9.2: cine-MRI series for utterance of /i/-/u/

strain patterns in the interior of the tongue. Ultrasound, X-ray microbeam, electropalatography (EPG), and cine-MRI are examples of modalities that are used to measure surface movements. Electromyography (EMG) and MR tagging are used to quantify internal strain patterns [150, 143]. MRI is capable of measuring the tongue’s motion in both at its surface and in its interior.

9.1.1 Background

The use of MRI in speech research began with the recording of steady state vowels using a static MRI, where only one position of the tongue was imaged [17]. Fig. 9.1(b) shows a static MRI image of a midsagittal slice. The positions of coronal and axial slices are marked for reference. Static MRI is used to study the anatomy of various structures in the vocal tract, e.g., the tongue surface and the airway between the tongue and the palate. But, use of static MRI is limited to quantifying and modelling static features, and cannot be used to track tongue motion during speech [42, 150, 151]. The introduction of cine-MRI, which produces a time series of MR images, greatly enhanced the *in vivo* visualization of the tongue’s motion during speech. Fig. 9.2 shows four time frames out of a 12-frame cine-MRI data set. The utterance in this particular example is “ee-oo”, which is phonetically written as /i/-/u/. Notice the upward motion of the tongue for the /i/ in frame 1, and down and back motion for the /u/ in frame 7. The rounding of the lips in frame 7 clearly indicates the “oo” sound. In cine-MR k-space data is collected over multiple repetitions of the speech utterance and an ensemble combination of the data produces a cine series of images [140,

43, 103]. This ensemble combination is analogous to the acquisition of cardiac MR data from several heartbeats. Multiple repetitions are necessary so that rapid tongue motions can be imaged with adequate spatial and temporal resolution [94].

While cine-MRI has proven useful to study kinematics of the tongue surface, it is not rich enough to provide information about the deformation of muscles in the tongue's interior. This drawback was overcome with the introduction of MR tagging. The first use of MR tagging was done by Niitsu et al. [107], who first acquired two tagged images, one in the rest position and another in the deformed position. This work first demonstrated the ability to visualize internal tongue deformation using tagging. Subsequently, many research groups have used tagged MRI to extract strain in the interior of the tongue [101, 102, 147, 36, 63, 145].

The ability to acquire a cine series of tagged images was the next critical step forward. Being able to acquire a cine series of tagged images meant that the interior of the tongue could be tracked throughout the entire period of the speech utterance. This greatly enhanced the visualization of subtle spatiotemporal deformations of the tongue. The existing tissue tracking methods tracked only the oral surface of the tongue. MR tagging enabled tracking of the tongue surface from the tip to the root, including tissue points within the interior of the tongue.

The introduction of MR tagging in speech research parallels the use of tagging in cardiac imaging, where it was originally introduced. Naturally, the progress of processing the tagged images of the tongue also paralleled the development of algorithms for cardiac applications. Even though there are considerable differences in the motion of the heart and the tongue, some of these methods could be used for both organs. One such method was developed by Dick et al. [40], who adapted a 4D B-spline model to measure 3-D strains and motion tracks in the tongue. In the same vein, in this chapter we adapt HARP-MRI to track tongue motion.

9.1.2 Why HARP-MRI on the Tongue?

The primary motivation for using HARP-MRI in the tongue arises for two reasons: 1) to reduce the number of repetitions to collect MR tagging data, and 2) comprehensive

analysis of all aspects of the tongue.

One of biggest challenges in using tagged MRI for speech is the need for prohibitively large number of repetitions to image the entire cine series [94]. While it is true that similar protocols have been used in cardiac imaging, a human heart repeats quite regularly, while a human tongue does not. No two repetitions are exactly the same; they vary spatially and temporally, even between utterances by the same subject in the same imaging session. Moreover, the repetition time and style varies across speakers, accents, and ethnic backgrounds. This mindboggling degrees of variation is compounded by the fact that a patient with a speech disorder cannot repeat utterances properly. The need for many repetitions poses a very serious challenge to do high resolution tagged MRI in the tongue. In such cases, HARP-MRI is ideal. As we have seen in this dissertation, HARP-MRI uses a small amount of k-space to track motion. Hence, HARP-MRI needs less time to acquire data, which translates into faster imaging and fewer repetitions.

The goal of using tagged MRI in the tongue is to relate the dynamic forces of the muscles in the tongue’s interior to the kinematics of the tongue’s surface. Therefore, a comprehensive study of the tongue needs different types of motion measurements, which HARP-MRI is able to provide, namely displacements, strains, strain rates, velocities, and tissue point trajectories. The fact that all the different measurements come from the same modality alleviates the problems of data compatibility and registration. The comprehensive analysis helps in better data interpretation, and hence is a powerful motivation to adapt HARP-MRI to track tongue motion.

9.2 Stretching the Envelope

Before we adapt HARP-MRI to tagged tongue images, we ask the question, “Can HARP-MRI do it?” In other words, we want to understand the challenges in this adaptation. The answer(s) to this question come(s) from the performance measures that were investigated in this dissertation. The high degrees of variation in the tongue stretches the performance measures of HARP-MRI in several directions. The speed at which the tongue moves poses a challenge to the dynamic range of tracking. The degrees of freedom of

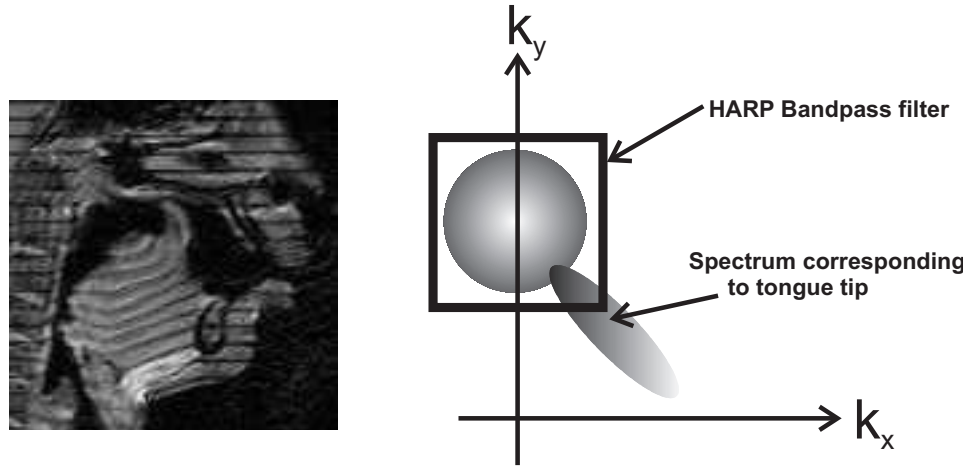


Figure 9.3: Left: Tagged MRI image of a retroflex ‘r’, especially made speakers of Tamil, a south Indian language. (Image courtesy: Dr. Maureen Stone, Univ. of Maryland, Dental school). Right: Schematic of how the dynamic range of HARP is exceeded due to this extreme motion.

tongue motion pushes the limits of dynamic range of strain and tag rotation. The intertwining of the muscles in the tongue’s interior is a challenge to spatial resolution. In this section, we understand how the envelope is stretched by understanding the behavior of the tongue in extreme cases. This analysis will not only help us understand what types of words can be studied using HARP-MRI, and also help us to interpret the results correctly.

9.2.1 Dynamic range

In Chapter 5 the dynamic range of tag rotation was derived to be around 16° – 34° degrees for a bandpass filter size of 33×33 . Fig. 9.3 shows an extreme example of tongue motion during the utterance of a retroflex ‘r’, during which the tip of tongue folds such that horizontal tags become vertical, i.e. the tag rotation is 90° degrees. The schematic on the right shows the energy corresponding to the tip goes outside the filter because the tags have rotated beyond the dynamic range of HARP-MRI. Obviously, conventional HARP-MRI cannot measure the tongue tip during the retroflex ‘r’. Thus the dynamic range of strain and rotation will help to select words that are feasible in a HARP-MRI study.

The speed at which the tongue moves pushes the limit of dynamic range of HARP

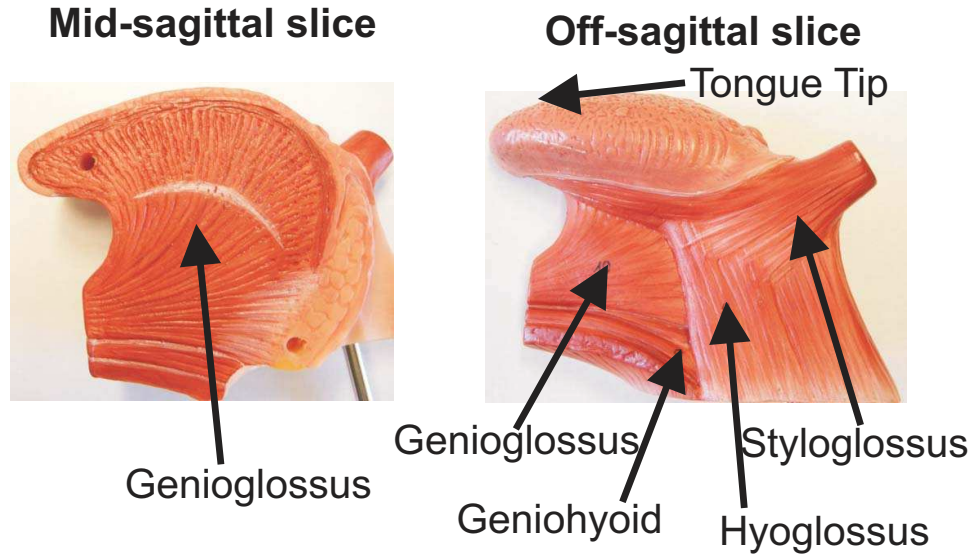


Figure 9.4: Left is a picture of a tongue model showing the muscles in the midsagittal slice. While the genioglossus muscle is homogenous in the midsagittal slice, the off-sagittal slice (right) shows a high degree of muscle interdigitation.

tracking. If the words are fast enough, tissue points in the tongue can move more than the dynamic range of tracking, thereby resulting in mistracking. Also, since the tongue surface and tongue tip moves much faster than the tongue body, tracking errors are more likely to occur at the tongue surface than in the interior.

9.2.2 Spatial resolution

In Chapter 6, spatial resolution of HARP-MRI was defined based on edges in strain. In the heart, the edges in strain were considered as exceptional cases of transitions between healthy and diseased tissue. In the tongue, however, edges in strain are the norm. The tongue is known to have a complicated muscle structure, which is often called a interdigitated musculature [153], examples of which are shown in Fig. 9.4. Fig. 9.4(a) shows a midsagittal slice, with the genioglossus muscle, which looks homogeneous. But, the interdigitation can be seen in an off-sagittal slice. Three muscles — genioglossus, styloglossus, and hyoglossus — are intertwined with sharp transitions from one to the other. Each muscle produces its own local deformations, which is measured using HARP strain maps. There-

fore, while inferring muscle activations using strain maps, it is important to keep in mind the edge resolution of HARP-MRI.

9.2.3 Artifacts and detectability

Artifacts Artifact characterization and correction is challenging in the tongue. In Chapter 8, the characterization of artifacts was based on the geometry of the heart and the directions in which strain was computed. But in the case of the tongue, the strains are calculated in no particular direction. Moreover, strain directions vary with words, subjects, and other factors. Hence, universal characterization of artifacts is difficult.

While errors due to spectral interference and noise are hard to characterize, the errors due to IVPD and PVE are common to the heart and the tongue. The edges of the tongue are bound to be affected more due to PVE than the interior of the tongue. Therefore, the strain measures near the edge of the tongue will have more error than those in the tongue's interior.

Detectability The use of HARP-MRI in the tongue is still in its beginning stages and is used strictly for scientific purposes. Therefore, the question of detectability is not applicable as of yet. With its use in clinical studies for speech disorders the question of detectability will become important.

9.2.4 Tongue, heart, and gold standards

The high degrees of variation implies that a construction of an universal analytical model of tongue motion is not possible. Therefore, establishment of a gold standard, which is necessary for deriving optimality criteria, becomes difficult as well. This is the primary reason why this dissertation focused on establishing limits in the heart first, and then using them to understand the performance of HARP-MRI on the tongue.

9.3 Methods

The methods section is split into two parts: MR imaging methods and HARP-MRI methods. MR imaging section provides a detailed description of the collection of in vivo tagging data in the tongue. The data collection was a collaborative effort with the dental and medical schools of University of Maryland at Baltimore. Although the author was an active participant in the data collection process, his primary contributions were in development of HARP-MRI methods to analyze the data. In the interest of completeness, the data collection process will be explained in detail.

9.3.1 MR imaging methods

Speakers and Speech Materials. We demonstrate the application of HARP-MRI on one normal speaker. The speaker was a 27 year old male, non-native speaker of Tamil accented English. The speaker did not have any dental fillings that might interfere with the MRI magnetic field. The speech material was the utterance “dee-suk”, phonetically written as /disuk/. This utterance was selected because it involves large movements of the tongue.

Tagging and imaging parameters. Tagged MR images were collected on a Marconi 1.5 Tesla Eclipse scanner. The speaker laid supine in the MR scanner with a TMJ (temporomandibular joint) phased array coil positioned to image the lower section of the face. Images in three different orientations were acquired: sagittal, coronal, and axial. Eight sagittal slices, nine coronal slices, and nine axial slices were collected with 5 mm slice thickness. On each slice, four sets tagged images were obtained. Two CSPAMM pairs were acquired, one each in horizontal and vertical directions. The field of view was 200 × 200 mm with a tag period of 10 mm. Imaging was done using a gradient echo imaging sequence. The data acquisition matrix was 64 × 22, zero filled to 128 × 128 sample points in Fourier space, which produces an interpolated voxel size of 1.56 mm × 1.56 mm × 5 mm. Figs. 9.5(a) and (b) show a CSPAMM pair of vertically tagged images in the sagittal orientation. Figs. 9.5(d) and (e) show a horizontally tagged CSPAMM image pair. In each case, only the magnitude of the tagged image is acquired and displayed. The CSPAMM images were combined using MICS (explained in Chapter 2), and displayed in Figs. 9.5(c)

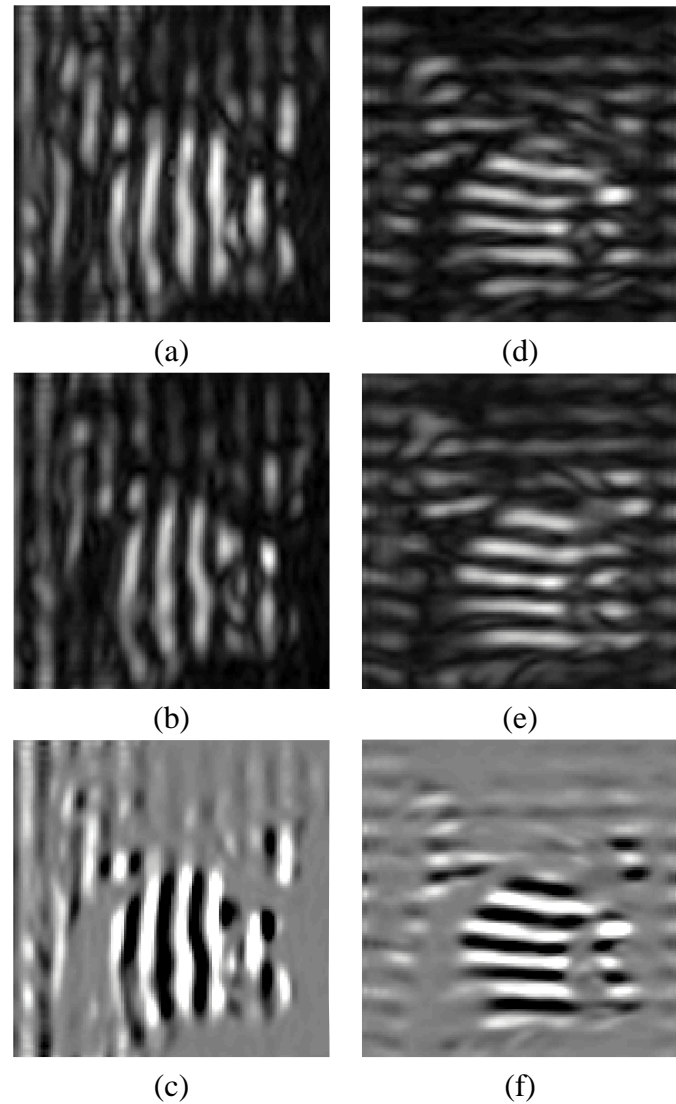


Figure 9.5: Images (a) and (b) form a pair of vertically tagged CSPAMM images with phase shifted tags, and (c) is the MICSR combination of images (a) and (b). Images (d) and (e) form a pair of horizontally tagged CSPAMM images and (f) is the MICSR combination of images (d) and (e). Intensity of MICSR images (c) and (f) have been thresholded for better visualization of the tags.

and (f).

Details of data acquisition matrix. Given the FOV and tag period, there are 20 (200/10) tag cycles across the field of view. This implies that the harmonic peaks will be centered at ± 20 in the tagging direction in Fourier space. Let us assume that HARP processing needs only ± 10 Fourier space samples on either side of the harmonic peak. Then all we need is 60 samples, i.e., from -30 to $+30$. We sample -32 to $+31$, a total of 64 points (a power of 2) to make the inverse fast Fourier transform (FFT) algorithm efficient. Essentially, we divide Fourier space into three parts along the tagging direction (recall the rule of thirds from Chapter 5). While the central third is centered around the center of Fourier space, the negative and positive thirds are centered around the negative and positive harmonic peaks respectively. Along the direction perpendicular to the tags, 22 (-11 to $+11$) Fourier samples are acquired.

Temporal resolution. The frame rate of the cine series is 18 Hz. Each cine series was collected over multiple repetitions, each repetition being one second long. The one second repetition time contains two parts: 667 ms recording time and 333 ms set up time for the next recording. With a frame rate of 18Hz and 667ms recording time, we collected 12 images for each cine series. This temporal resolution is high when compared to existing tagged imaging protocols in the tongue. This improvement is due to the necessity to collect only a small amount of data in k-space.

Acquisition of cine-MRI. In addition to tagged MR images, untagged cine-MRI images were also collected for the same speech task. The data acquisition matrix is 64×66 (three times the number of samples in the phase encode direction) over a rectangular field of view of $200 \text{ mm} \times 200 \text{ mm}$ and zero filled to 256×256 samples points in Fourier space. Thus interpolated voxel size is $0.75 \text{ mm} \times 0.75 \text{ mm} \times 5 \text{ mm}$. Figs. 9.6(a)–(c) show images of one particular time frame of the sagittal, coronal, and axial slices, respectively. The tongue surface is seen better on the untagged images than on the tagged images because more better spatial resolution.

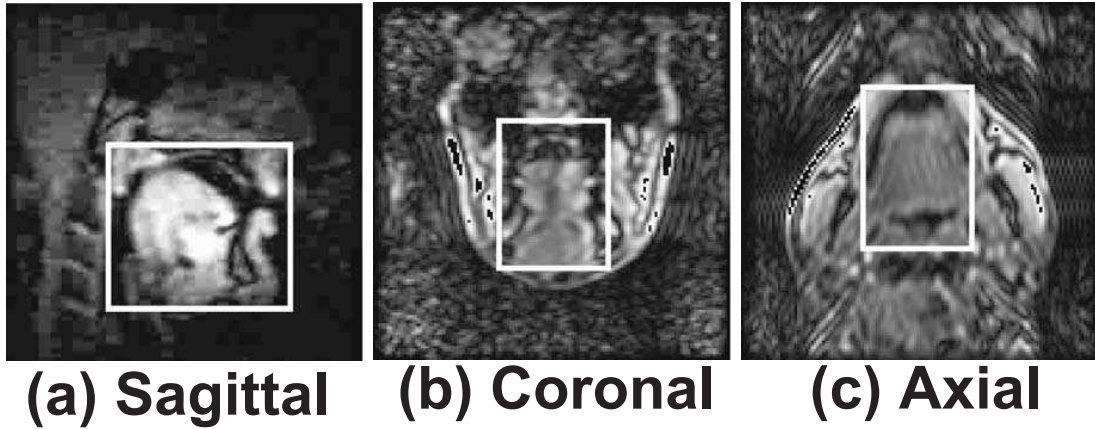


Figure 9.6: (a, b, c) show one time frame from cine-MRI acquisition of midsagittal, and coronal, and axial slices respectively. The region of interest around the tongue is marked.

Number of repetitions Four acquisitions are required for HARP-MRI — two CSPAMM acquisitions in two tag directions. We acquired each tagged cine series in four repetitions of the utterance. Therefore, we need 16 repetitions to track tongue motion on one slice. When compared to previous protocols that require 32 repetitions to acquire similar kind of data [145], this protocol represents a two fold improvement in speed of data acquisition.

Imprecision artifacts. Since each tagged MR image is a combination of four repetitions, the speaker’s ability to precisely repeat the utterance is critical to image quality. Variability across repetitions causes blurring of images and crisscrossing of tags after combination. Fig. 9.7(a) shows an example of this artifact in the tongue tip in a checkerboard visualization of the tagged images. In this visualization, the horizontal and vertical tagged MICS images are multiplied so that the internal muscle deformations can be seen as deformations of small checkerboard patterns [105]¹. Each checkerboard image is a combination of four tagged images, which were collected over 16 repetitions. Any imprecision during these 16 repetitions causes artifacts. These artifacts occur usually in the tongue tip or on its surface since their motion is faster than the tongue body.

These artifacts make the tongue surface visualization difficult. One way to circumvent

¹This checkerboard pattern is only for visualization purpose only and is not used for HARP processing. HARP-MRI is still separately done on vertical and horizontal tags separately.

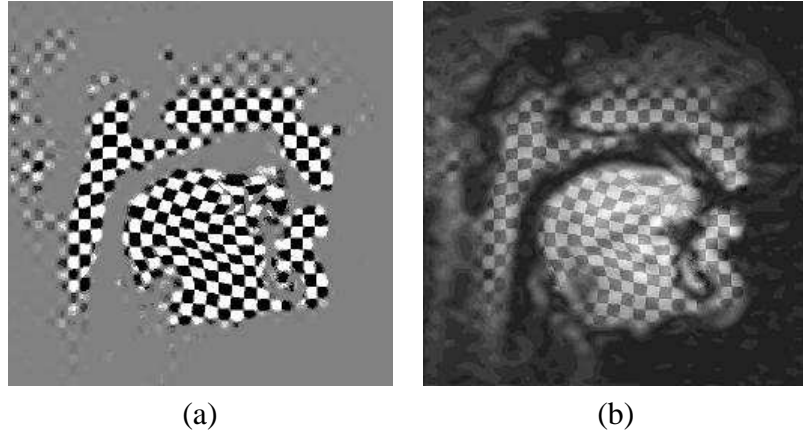


Figure 9.7: (a) MICSR trinary display (b) Overlay of MICSR checkerboard and untagged image; Note the better edge definition near the tongue tip in the overlay image

this problem is to overlay the checkerboard onto an untagged cine-MRI images after adjusting for the voxel sizes. One such overlayed image is shown in Fig. 9.7(b). The combined overlay is useful to see how the surface moves with respect to the internal deformations of the checkers. It is important to note, however, that this overlay is strictly for visualization and does not influence the HARP computations. HARP values in the tongue tip and surface will continue to be noisy.

Speaker training. In order to ensure least variability across repetitions, the speaker is pretested and trained before the MRI experiment. Subjects are selected based on this pretest, which consisted of repeating the proposed speech material (and others) to a metronome. The metronome is a combination of a repeating rhythmic tone [141] and MR gradient sound that was recorded during a previous imaging session. This pretest is virtually identical acoustically to the experience in the scanner during tagged image acquisition. The speech material is repeated at one second interval and the subject is asked to time his/her repetitions to this gradient sound cycle. The acoustic data are subsequently analyzed to measure the variability in repetition time. A variability threshold of 50 milliseconds is set, above which the speaker is not used. The speaker used in this chapter was very precise with a standard deviation of 20 milliseconds. Following the pretest, qualified subjects are trained by further synchronizing their utterance to the repeating rhythmic tone. The number of

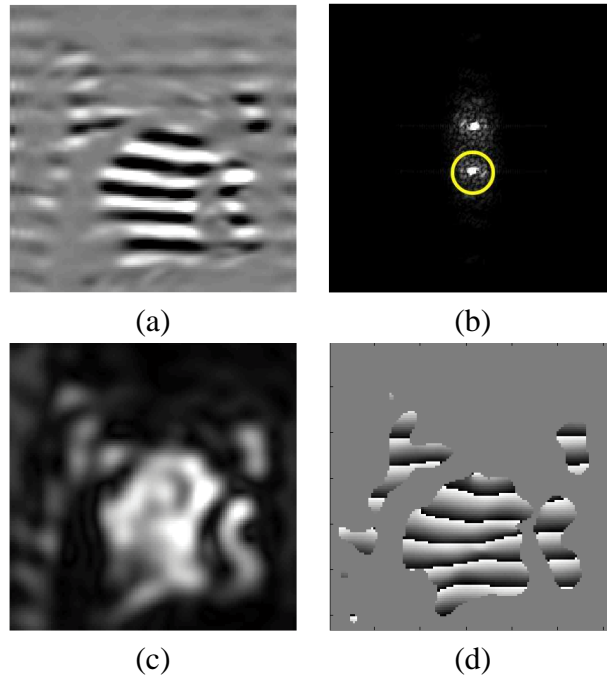


Figure 9.8: (a) Horizontally tagged image produced by MICSIR combination, (b) magnitude of its Fourier spectrum with the HARP bandpass filter, (c) harmonic magnitude image, and (d) harmonic phase image

repetitions for the subject to get into rhythm is determined and later incorporated into the MR imaging protocol. The subject presented in this chapter needed three repetitions to get into rhythm, and felt comfortable when the number of beats in the rhythmic tone was equal to number of syllables in the utterance, which is two in this case.

9.3.2 HARP methods

HARP-MRI processing was performed on the MICSIR tagged images. Fig. 9.8(b) shows the bandpass filter and Figs. 9.8(c) and (d) show the reconstructed magnitude and HARP phase respectively. This part of the processing is common to both heart and the tongue. The difference is how the HARP phases are used to compute measures of motion. Unlike the heart, the Eulerian strain is computed in the principal direction. HARP tracking is used to compute Lagrangian strains in the lines of action of certain muscles. These two measures were developed for the tongue and are explained in more detail in the following sections.

Principal strains in Eulerian framework. Local stretch and compression in the tongue can be objectively captured by the principal strains (also known as strains in the principal directions²). Principal strain has two components corresponding to the maximum and minimum strains at that point. The two component strains are oriented in directions in which the shear component of the strain is zero and the directions are always orthogonal to each other. Therefore, the principal strains quantify pure stretching and compression. The principal strains are derived from the Eulerian strain tensor

$$E^* = \frac{1}{2} (I - B^{-1}), \quad (9.1)$$

where, $B = FF^T$ is the left Cauchy-Green strain tensor and F is the deformation gradient. F can be decomposed as $F = VR$, where V is a symmetric tensor and R is a orthogonal tensor. Therefore, the left Cauchy-Green strain tensor $B = V^2$. Using these relations, the principal strains can be computed as follows.

Let λ_i , $i = [1, 2]$ be the i^{th} eigenvalue of V . Then, the eigenvalues of B^{-1} are,

$$\beta_i = \frac{1}{\lambda_i^2}. \quad (9.2)$$

Using the expression for E^* in Eq. (9.1), the eigenvalues of E^* can be written as $\frac{1}{2}(1 - \beta_i)$, $i = [1, 2]$. Since B is symmetric, E^* is also symmetric, and hence can be diagonalized when E^* is written with eigenvectors e_1 and e_2 as its basis. Given the definition of the diagonal terms in the E^* [80], we get,

$$\frac{\|ds_i\|^2 - \|dS_i\|^2}{\|ds_i\|^2} = (1 - \beta_i), \quad (9.3)$$

where dS_i is an infinitesimally small piece of tissue in the i^{th} direction when the tags were applied and ds_i is the same tissue at a later time after deformation. From the above relation, the unit Eulerian strain along the principal direction, S_i can be derived as,

$$S_i = \frac{\|ds_i\| - \|dS_i\|}{\|ds_i\|} = 1 - \sqrt{\beta_i}, \quad i = [1, 2]. \quad (9.4)$$

²In strict continuum mechanical sense, the term *principal strains* are not defined for finite deformations. Hence the topic of this paragraph reads “strain along the principal directions”. Nevertheless, this is minor technical issue and two terms are used interchangeably in this chapter.

In Eq. (9.4), β_i , $i = [1, 2]$ are the eigenvalues of B^{-1} , which can be computed using the deformation gradient tensor F . Recall from Chapter 2 that the deformation gradient tensor F can be written in terms of the HARP phase as $F = \nabla\phi(\mathbf{x}, t))^{-1}\Omega^T$, where Ω is the matrix whose columns are tag frequency vectors in the horizontal and vertical directions, and ϕ is the HARP vector. The matrix $\nabla\phi(\mathbf{x}, t)$ can be proven to be always invertible and from Eq.(9.1) E^* always exists; hence, the principal strains always exist.

Strain along the line of action of a muscle in Lagrangian framework. HARP-MRI is capable of calculating the change in length of any arbitrary line by simply tracking the endpoints of the line. By choosing a line on the tagged image where we expect a particular muscle to be, we can calculate the change in length of the line, and hence the strain along the line of action of a particular muscle. Since this line is attached to two specific tissue points, the resulting strain is a Lagrangian measure. The strain along this line is hypothesized to follow the compression and expansion patterns in the lines of action of the muscle.

Given the trajectory of each endpoint using HARP tracking, we can calculate the strain along the line segment joining the two end points. Consider 2 points with reference positions $\mathbf{x}_{\text{ref}}^1$ and $\mathbf{x}_{\text{ref}}^2$ at time t_{ref} . At time t_N , we can track the positions of these points using HARP tracking as \mathbf{x}_N^1 and \mathbf{x}_N^2 . The Lagrangian strain between these 2 points at time t_N with respect to the reference time can be calculated as

$$e = \frac{\|\mathbf{x}_N^2 - \mathbf{x}_N^1\|}{\|\mathbf{x}_{\text{ref}}^2 - \mathbf{x}_{\text{ref}}^1\|} - 1. \quad (9.5)$$

The strain is zero if the distance between the points remains unchanged, negative if there is shortening and positive if there is lengthening. The reference time, t_{ref} , can be set at any time frame. In particular, if t_{ref} is set as t_{N-1} , then strain evaluated using Eq. (9.5) will characterize the change in length of the line segment between t_{N-1} and t_N .

Velocities. The velocity of tissue points are also useful in tracking the tongue. The computation of tissue velocity use HARP was first presented in [112]. Velocity at time t can be calculated from the HARP vector as follows.

$$\mathbf{v}(\mathbf{x}, t) = -[\nabla\phi(\mathbf{x}, t)]^{-1} \frac{\partial\phi}{\partial t}. \quad (9.6)$$

The computation of velocity contributes to the comprehensive analysis of tongue motion. Principal strains and the velocity fields are complementary to each other. The principal strains indicate expansion and compression without indicating direction of motion. On the other hand, velocity fields indicate direction and extent of motion, but does not indicate whether the tissue point moved because of translation, expansion, or both.

HARP 2G software. As a final note on HARP-MRI methods, a new version of the HARP-MRI software was developed as a part of this dissertation. The new software, called “*HARP 2nd generation*”, integrates tools required for both the heart and the tongue.

9.4 HARP-MRI Results and Visualization

9.4.1 Principal strains and velocities

Fig. 9.9 shows the principal strains and velocities for the utterance */disuk/* for time frame 9 and 10. Between time frames 9 and 10 the tongue is hypothesized to move from */u/* to */k/*. The two rows correspond to the sagittal and coronal slices. The principal strains are plotted in the form of a cross, with blue denoting compression and red denoting expansion. The length of the cross lines denotes the amount of strain and the direction of the lines point to the directions of maximal and minimal strain. Although the strains are calculated at all pixels, strain is downsampled in the display to improve clarity.

In the midsagittal strains shown in row 1, there is a distinct difference in the local strain pattern in the front and back parts of the tongue. In the front and central parts, vertical compression is accompanied by either horizontal or oblique expansion. In contrast, in the back there is expansion in both principal directions. The second row of Fig. 9.9 shows the principal strains in the coronal slice. In both the coronal images, especially in time frame 10, one can see a vertical compression in the middle surrounded by a bilateral expansion. This pattern follows the anatomical distribution of the genioglossus muscle sandwiched between two bilateral muscles. All the strain maps in Fig. 9.9 show the inhomogeneity of the tongue musculature.

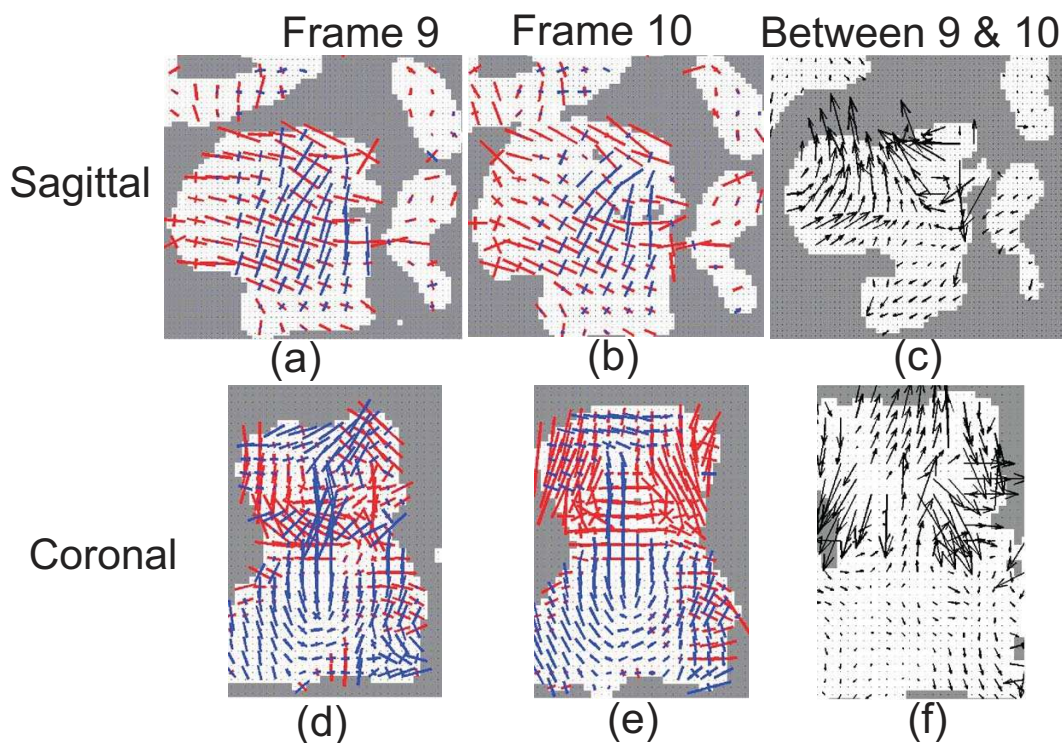


Figure 9.9: (a,b) show the principal strains in the midsagittal slice from time frame 9 and 10 respectively. Blue denotes compression, red denotes expansion. (d,e) shows the principal strains for the same two time frames for a coronal slice. (c,f) show the velocities of tissue points between time frames 9 and 10. Note the inhomogeneity of strains and velocities corresponding to actions of a muscles or a combination of a set of muscles

Velocities. Figs. 9.9(c) and (f) show the velocity vectors between time frame 9 and 10, in the sagittal slice and coronal slice, respectively. These are the same slices that were considered for the strain computations. The length and direction of the arrow heads denote the magnitude and the direction of the velocity. Like the display of the principal strains, the vectors are also displayed only on every other pixel for the sake of clarity. Examination of the sagittal velocity field in Fig. 9.9(c) shows that the upper tongue moves up, the back part of the tongue moves forward. The coronal image in Fig. 9.9(f) indicates that the upward motion occurs in the middle and that the sides of the tongue move laterally and downward.

Complementary analysis between principal strains and velocities. Comparison of the velocity fields with the principal strains reveal interesting relationships between translation, stretching, and the action of specific muscles. In case of the sagittal slice, the strain directions rotate from being vertical and horizontal in Fig. 9.9(a) to oblique in Fig. 9.9(b). Further, the upper surface of the tongue expands considerably between Figs. 9.9(a) and (b). These two strain patterns result in the velocity pattern Fig 9.9(c), where at least three zones of surface motion can be seen. The front, middle, and back portions of the tongue moves backward, inward, and upward respectively. Further, the coronal images add additional information. The upper surface moves upward in the middle part. The sideways lowering of the tongue in the velocity field can be seen as a consequence of expansion of bilateral muscles. These observations illustrate how different regions of the tongue move differently in order to create the overall surface pattern, which in turn partially determine the sound.

9.4.2 Strain in the lines of action of muscles

Fig. 9.10 shows five lines hypothesized to be the lines of action of the genioglossus muscle. The top row shows the tracking of these lines in three out of the total 12 frames. The bottom row shows the strains calculated along these lines. All strains start at zero because the first time frame is taken as the reference for the Lagrangian strains. Since there is no movement at the base point, the Lagrangian strains are entirely due to the surface motion of tissue points.

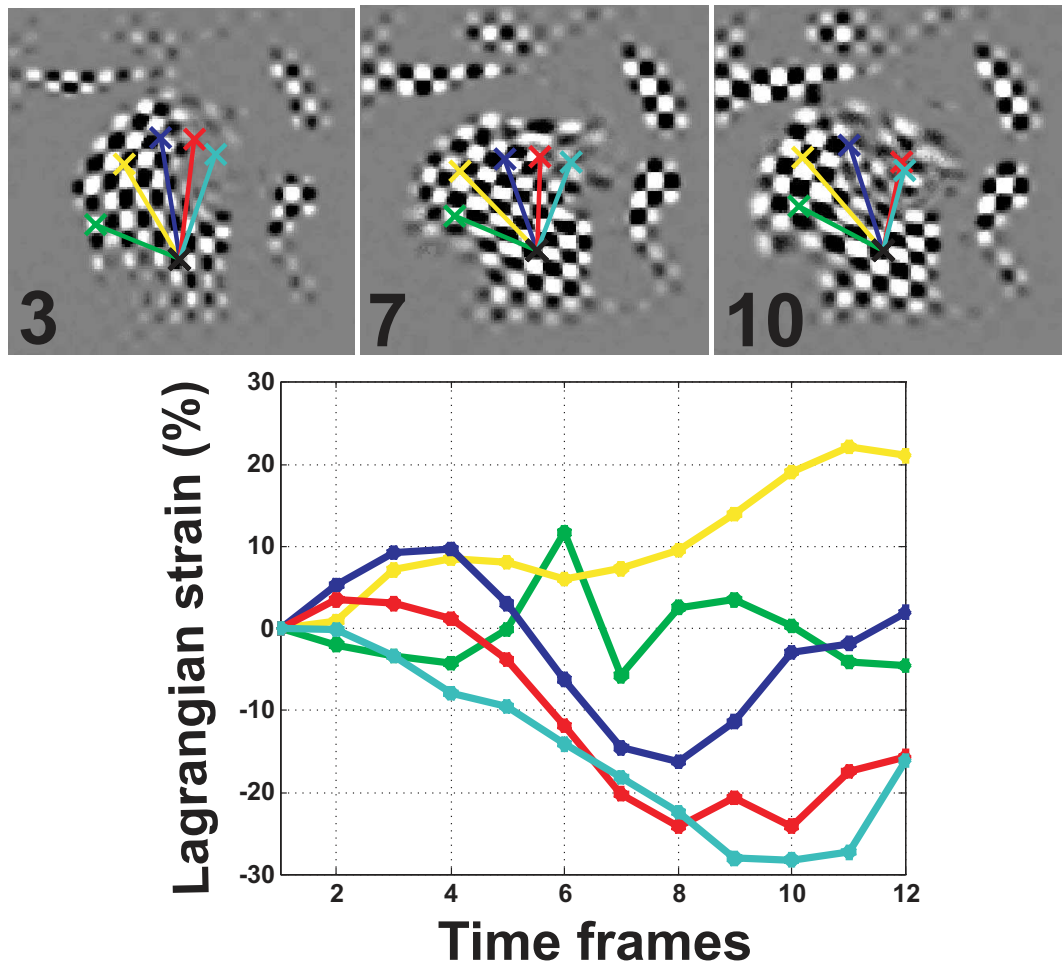


Figure 9.10: Tracking of the lines, hypothesized as parts of genioglossus. All time frames from 12-frame cine-series set of utterance of /disuk/ are shown.

Effect of tracking errors. Measuring the motion of points near the surface has limitations due to dynamic range of tracking and imprecision artifacts. The green line shows an example of tag jumping, which is the consequence of exceeding the dynamic range of tracking. The endpoint of the green line is a surface point in frame 3. But in frame 7, the HARP tracking has converged to the interior point. This jumping leads to the kink in the green curve at time frame 6. This error is propagated to frame 10 as well. The blue line shows the effects of the imprecision artifacts. Since the HARP values are noisy at the tongue tip, HARP tracking has errors and this can be seen from the behavior of the blue line. The blue line and red line are separated in frames 3 and 7. But, due to the tag blurring in the tongue tip, the blue line coincides with the red line in frame 10, thereby causing a error in the strains.

9.5 Discussion

9.5.1 Temporal resolution

The time resolution of 18 Hz, which is used in this study, is low when compared to the rate of normal speech. Even though there was potential to collect data at twice the rate (30 Hz), the speaker's temporal imprecision resulted in poor image quality and faded tags. At higher rates of data collection, even the slightest of speaker imprecision between repetitions tends to cause improper ensemble combination. By slowing down the frame rate, we were effectively averaging over larger time units thereby reducing the variability.

9.5.2 Robustness of tracking

As seen from previous chapters, tracking is least affected by noise, spectral interference, loss of spatial resolution. Therefore, the strain in line of action of muscle are very robust measures. Take for example the blue line. Even though the tag signal is very blurry, the tracking from frame 3 to 7 is quite good — in fact, it is very good considering the image quality. Moreover, given that all points were near the tongue surface, the tracking performs exceedingly well in spite of the loss of resolution due to the partial volume effect.

9.5.3 Corroboration of motivations

We now revisit our motivations for using HARP-MRI in the tongue. Our observations in this chapter justify our motivation.

1. The collection of small amount of k-space, not only reduced the number of repetitions, but also helped in improving the frame rate of the cine series.
2. The advantage of having different types of motion measures was seen in the complementary analysis between principal strains and velocities. The combined analysis of the different motion measurements is a powerful tool in understanding tongue dynamics. We believe that these motion measurements will serve well as inputs to models of speech production.
3. Lagrangian strains, in spite of errors and limitations, reflect the subtle differences of adjacent tongue surface zones. These strains can be used to investigate relationships between the local surface and internal movements.
4. Finally, HARP-MRI processing is fast. Tracking of one tissue point can be done within a second, and the calculation of strains and velocities for one tagged image can be measured within one minute.

9.6 Summary

In this chapter, we have adapted HARP-MRI to measure the tracking of tongue motion during speech. We identified the challenges and limitations in this process. We concluded that the performance measures developed in the previous chapters were not only valid in the tongue, but were pushed to their limits because of the complicated motion of the tongue. HARP-MRI was demonstrated with the use of a simple utterance, and motion measures were developed exclusively for the tongue. The observations of principal strains showed the inhomogeneity of tongue motion. The Lagrangian strains were robust to loss of spatial resolution and imprecision artifacts. The use of HARP-MRI in the tongue was justified by reducing the number of repetitions for image acquisition, its speed, and its ability to provide a variety of different motion measurements.

Story continues in appendix. The main goal of understanding speech production is to understand the relation between the tongue surface and tongue's interior muscles. This requires high quality data from both the surface and the interior. While HARP-MRI can provide strain and tracking in the interior of the tongue, the surface measures still suffer from partial volume errors. Therefore, to supplement HARP-MRI data, other modalities like ultrasound can be used to measure the surface of the tongue. Ultrasound is widely used to track tongue surface shapes because tongue surface contours are readily extracted and visualized. One goal in the future should be the fusion of MRI and ultrasound into a single visualization tool. As a first step toward this goal, the author has worked on spatiotemporal visualization of ultrasound contours of the tongue. Since, the focus of this work does not fall into the scope of HARP-MRI, the details are included in the Appendix chapter.

Chapter 10

Conclusions and Future Work

In this dissertation we used theory and simulations to characterize the optimal and peak performances of HARP-MRI. The optimal performance was characterized using simulations in Chapter 3. The observations made in Chapter 3 were corroborated using both theory and simulations in Chapters 4 through 7. In Chapter 8, we explained the presence of artifacts in HARP strain maps and proposed an algorithm to reduce them. In Chapter 9, we pushed HARP-MRI into a new realm by applying it track the motion of the tongue during speech. In this chapter, we summarize the key points of the four contributions of this dissertation: optimal performance, peak performance, artifact reduction, and application to imaging tongue motion.

10.1 Optimal performance of HARP-MRI

In Chapter 3, we addressed an inverse problem: “Given the values of output (tissue displacement and strain), how to select the optimal operating parameters (tag separation and filer size)?” We answered this question using optimization methods based on simulations. The optimal operating parameters were derived for different imaging scenarios, i.e., for different values of LV sizes, different noise levels, and different strains in the myocardium. Here, we list the key results of our analysis and provide future directions.

10.1.1 Key results

- IVPD, PVE, spectral interference, and noise are the main sources of error in HARP-MRI.
- The sources of error affect different motion measurements differently. Circumferential strain is sensitive to noise and spectral interference; radial strain is largely affected by IVPD and PVE; and tracking is robust to all sources of error. The only source of significant error in tracking is tag jumping, which occurs due to insufficient temporal resolution.
- Noise and interference lead to reduction in the smoothness of the estimates, whereas IVPD and PVE lead to loss of spatial resolution. The loss of spatial resolution affects the accuracy more than the effects of noise and interference. Therefore radial strains are less accurate than circumferential strains.
- Different motion measurements require different strategies for optimal use. Since radial strain is the least robust to changes in operating parameters, imaging and analysis parameters should be first based on the optimal estimation of radial strain. Parameters so selected should be applicable for CS and tracking. The selection of optimal parameters can be done using the *HARP-MRI Parameter Optimization Toolbox*, which was written as a part of this dissertation.
- Selection of optimal parameters is a trade-off between spatial resolution and smoothness. Hence, the use of CSPAMM with flip angle compensation is highly recommended for HARP-MRI. The use of CSPAMM is a win-win situation in the tradeoff between the increase in spatial resolution with the decrease in spectral interference. For the same tradeoff, the use of grid tags is a lose-lose situation. Hence, separate acquisitions of horizontal and vertical tags are recommended.

10.1.2 Future research

Although this study was more comprehensive and quantitative than previous such studies, it was based on simulations. The recommendations in Chapter 3 should be considered

to be guidelines rather than rules. Future work should involve complete testing of the above recommendations using an actual moving phantom in an MR scanner. Although the optimization study cannot be as high dimensional as this computer simulated study, the results of the phantom will be closer to reality and may yield somewhat different practical tradeoffs. Further, the phantom studies should be used as an opportunity for a more comprehensive testing of the parameter optimization toolbox.

10.2 Peak Performance of HARP-MRI

In the previous contribution, we described the workings of HARP-MRI under different imaging conditions. In this contribution, we considered few extreme imaging conditions and analyzed the response of HARP-MRI. In other words, we addressed a forward question, “Given a pair of tag separation and filter size, what are ranges of motion and strain that HARP-MRI can measure?”

In order to answer this question, we set HARP-MRI in a communication-theoretic framework. We interpreted a tagged image as a monocomponent AM-FM signal and discussed the following two approximate properties about the instantaneous frequency at a point in an AM-FM signal.

- Instantaneous frequency is the frequency of the local sinusoid at that point.
- Instantaneous frequency is the average of Fourier frequencies at each point.

We used the above two properties in the study of dynamic range and resolution. The key results from the investigation of HARP-MRI’s peak performance are summarized below.

10.2.1 Key Results

Dynamic Range. In Chapter 5, we studied dynamic range of both tracking and Eulerian strain. We derived analytical expressions for calculating the dynamic range of Eulerian strain and tag rotation for a given bandpass filter size. Our expressions were validated using simulations and real *in vivo* data.

- The dynamic range of tracking is half the tag separation. If the inter-frame displacement of a tissue point is more than the dynamic range of tracking, tag jumping or mistracking occurs. The dynamic range of tracking is also a function of local strain. If the tissue is locally compressed, dynamic range of tracking decreases, and if the tissue is locally expanded, the dynamic range increases.
- For the FastHARP acquisition size, strain up to $\pm 41\%$ can be measured using HARP-MRI. Local tag rotations of 16° – 34° can be measured as well. This shows that the FastHARP Fourier acquisition size is adequate for estimation of motion and strain in both diseased and normal hearts.

Resolution. “HARP-MRI is a nonlinear system” was an often used statement in this dissertation. Indeed, the nonlinearity was a major challenge in characterizing the performance measures of HARP-MRI, especially its spatial resolution. The classical definition of spatial resolution based on FWHM does not hold for HARP-MRI. Therefore, in Chapter 6, we proposed an alternate definition for resolution based on edge models in strain. The edge models were clinically motivated as extreme cases of transitions between healthy and diseased myocardial tissue. Spatial resolution of HARP-MRI was defined as its ability to accurately estimate the size of a diseased myocardial tissue; the amount of blurring of the strain edge quantified this ability. The spatial resolution of both Eulerian strain and tracking were studied.

- The spatial resolution of Eulerian strain is limited by the intrinsic resolution of the bandpass filter. In other words, an edge in strain was blurred out by a distance equal to FWHM of the filter, thereby introducing errors at the strain edge. In a realistic setting, however, the transition of strains are not abrupt; the smoothness of transition from healthy to diseased tissue is dictated by the size of the functional border zone. If the width of the functional border zone is equal to or more than the FWHM of the filter, Eulerian strain is reproduced faithfully, up to the effect of noise and artifacts.
- The resolution of tracking is independent of the bandpass filter size. Tracking is not affected by the blurring of the edge by the bandpass filter, and hence the estimates

of tracking are robust even at the edge. Errors in tracking occur only when the tissue motion has exceeded the dynamic range of tracking. The robustness of tracking explains the results in Chapter 3.

Detectability. In Chapter 7, we used simulations to address the question “What is the smallest infarction that can be detected in a HARP-MRI Eulerian strain map?” The simple answer is that it depends on noise. The detailed answers are given below.

- If the infarction size is equal to the FWHM defined by the filter, then the detected strain contrast is 50% of its original. In spite of this 50% contrast reduction, the infarction can still be detected.
- Detectability of an infarction is not limited by spatial resolution of the strain map, but by the noise level in the background.
- For CNRs typical of CSPAMM images, infarction as small as 0.3–0.5 times the FWHM can be detected.

10.2.2 Future research

Realistic simulations. The study of peak performance of HARP-MRI depended on results of simple simulations. But in order for these measures to be accepted widely, more realistic simulations and phantom studies need to be performed. The realistic simulations must not only incorporate models of normal heart motion, but should also take into account the presence of ischemia or infarction. This is a challenge because it is difficult to derive an analytical model of motion for a diseased heart. One way is to use finite-elements-based dynamical simulators like ANSYS and ABAQUS, which have been traditionally used in the design of mechanical structures. These simulators allow the user to design the material properties (like stiffness), which can be used to control the material properties of healthy and diseased tissues. Size, shape, and transitions regions of the abnormality can be designed. These simulators calculate the motion on a finite element grid, which can then be given as inputs to the more realistic analysis of resolution and detectability. Further, the

detectability analysis in the future should not only be restricted to strain maps, but should also analyze detectability in tracking as well.

Complementary detectability question. In Chapter 7 (on detectability), we focussed on answering the question, “For a given strain contrast, what is the smallest infarction that can be detected?” Future work should answer the complementary question as well, “For a infarction of a certain size, what is the minimum strain contrast needed for the infarction to be detected?” The minimum detectable level of contrast is an interesting question because it quantifies the contracting ability that is still remnant in the infarcted tissue.

10.3 Artifacts in HARP

Artifacts in HARP strain maps obscure the detection of useful features and reduce the clinical usability of the strain maps. In Chapter 8, we discussed how these artifacts are produced, and how to reduce them. The key results are listed below.

10.3.1 Key results

- The zebra artifacts are manifestations of the sources of error that affect HARP-MRI. The unique spatial pattern of artifacts depends strongly on the direction in which strain is computed at each point. Artifacts in CS maps are caused by spectral interference and noise, while artifacts in RS are caused by IVPD and PVE. We observed that while artifacts in RS are severe, the artifacts in CS are comparatively mild. While the CS maps could be smoothed out using postprocessing, the artifacts in RS are practically unrecoverable.
- A 2-D filtering approach based on weighted phase unwrapping was proposed to smooth out CS maps. A preliminary analysis on an *in vivo* data set showed that the proposed method performs better than an existing 1-D filtering method. Further validation is needed to thoroughly understand the merits of this method.

10.3.2 Future research

Anisotropic diffusion. Although, the proposed 2-D filter was shown to perform better than the existing 1-D filter, it has an disadvantage of smoothing across edges because it is a linear filter. We expect this to be a problem particularly in the endocardium. A recent nonlinear method addresses this problem [2]. This method is based on anisotropic diffusion and initial results are very promising. More validation needs to be performed under different imaging conditions.

Pulse sequences and registration. Recently, the methods developed to smooth the strain maps have seen as shift in paradigm, moving from post-processing methods to clever manipulation of the k-space data acquisition. Recently, MR imaging pulse sequences have been developed that suppress all other peak except for the harmonic peak [44, 7, 156, 3]. These methods look very promising, except that they need twice the number of acquisitions of what is currently required. The increase in imaging time in one issue, but another problem is the spatial misalignment between different acquisitions. One solution is to develop optimal registration algorithms, which are optimized on their ability to suppress interfering spectral peaks.

Spectral separation. Spectral interference occurs because spectral spreading from one spectral peak interferes with the others. Therefore, every point in the spectrum is a linear combination of energies from two or more peaks. “Can this linear combination be resolved?” is the question of spectral separation. This is not a straightforward question, especially for the spectrum of a phase modulated signal. An elegant analytical separation may not be possible in this case, and the solution may need to come from iterative methods.

10.4 Tracking tongue motion using HARP-MRI

In Chapter 9, we identified the challenges of applying HARP-MRI to track tongue motion during speech. The peak performance measures that were developed for the heart were equally applicable in the tongue. We recognized that the high variability of tongue

motion stretches the performance limits of HARP-MRI. In this chapter, we demonstrated the feasibility of HARP-MRI in tracking tongue motion during utterances of simple words. We developed two HARP-based motion measurements specific to the tongue: Eulerian principal strains, and Lagrangian strains in the lines of action of muscles.

10.4.1 Key results

- HARP-MRI facilitated two key improvements: 1) the number of repetitions to collect tagged MR data in the tongue were halved 2) temporal resolution of the cine series was improved.
- Lagrangian strains in the lines of action of muscle are based on HARP tracking of endpoints of a line. Hence, these strains were robust to loss of spatial resolution. Lagrangian strains, in combination with Eulerian principal strains, can be used to investigate the relationships between the local tongue surface movements and internal deformations of the internal tongue muscles.
- Comprehensive analysis of tongue motion was greatly enhanced by the variety of motion measurements that could be measured using HARP-MRI. The fact that all the different measurements were measured using the same modality alleviated the problems of data compatibility and registration.

10.4.2 Future research

Fusion with finite element models. Tracking tongue motion using HARP-MRI is not a project in isolation; it is a part of a overall research program with headquarters at the University of Maryland Dental School, and has collaborators in University of Delaware and University of Maryland at College Park. Each group has been working on different aspects of tongue motion. While the Delaware group primarily focusses on tongue surface extraction from ultrasound images [85], the group in College Park develops finite element models to understand muscle activation [83]. The final goal is to fuse this rich collection of data from all groups in an effort to understand the complication mechanism of speech production. Fig. 10.1 shows results from a preliminary work, which tries to fuse the output

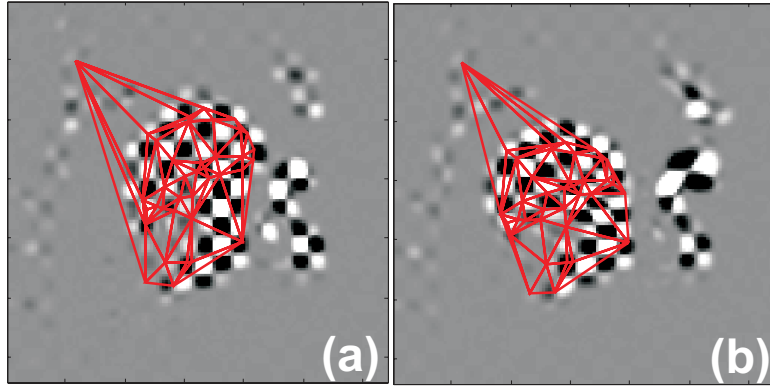


Figure 10.1: Finite element meshes manually superimposed on checkerboard images. Figs. (a) and (b) show initial and deformed time frame, respectively.

of HARP tracking to drive the finite element model. The finite element mesh is manually laid down on a tagged image at an initial time frame in Fig. 10.1(a). HARP tracking deforms the nodes of the mesh through the cine series. Fig. 10.1(b) shows an example of the deformed finite element mesh. Currently, the nodes of the finite element mesh are manually identified and registered to the tagged image. In the future, this process should be semiautomated with minimal human intervention. Tracking the finite element mesh highlights the problem of mistracking. Since many points on the finite element mesh lie on the tongue surface or the tongue tip, mistracking is highly likely. Mistracking continues to be one of the major challenges in the tongue. There are two reasons for mistracking: 1) inadequate temporal resolution, and 2) through-plane 3D motion.

Temporal resolution. Currently, there is an upper limit to the increase in temporal resolution in collecting tagged tongue data. This is because, speaker variability between utterances gets amplified at high temporal resolutions. Hence, although the technology to acquire high resolution data exists, it remains untapped. One solution is to acquire all the data required in one repetition, say using grid tags protocol. This method, however, would require tradeoffs between spatial resolution, temporal resolution, and increased spectral interference. A second solution to this problem is a post-processing of the temporally-resolved data collected across many repetitions. The post-processing should involve a kind of spatiotemporal registration, which will minimize artifacts in the tagged images. Audio

data that is collected during the MR experiment could also be a useful tool to drive the registration. A third solution is to process the final tracking output using HARP refinement [109]. This method is time intensive and its feasibility to correct tracks in the tongue should be investigated.

3-D tracking. The second reason for mistracking is through-plane motion. Through-plane motion occurs because the imaging is done in a 2-D imaging plane, while the tongue moves in 3-D. As the tongue moves through the imaging plane, existing tissue moves out and new piece of tissue appears in the image. The new piece of tissue carries with it a different HARP phase, which destroys the continuity of HARP phase maps, thereby leading to mistracking. One solution to this problem is to move to 3-D HARP techniques. Recently, many 3D HARP approaches have been developed for the heart [5, 115, 138, 136]. The feasibility of these approaches in the tongue should be investigated.

10.5 Publications

Portions of this dissertation were previously published or are presently under consideration for future publications. The material related to dynamic range, resolution, and detectability appear in [119], [120], and [121] respectively. The 2-D phase unwrapping algorithm was published in [118]. The application of the HARP-MRI to the tongue was published in preliminary form in [117], and a detailed manuscript on this topic is currently in review. The material on the selection of optimal operating parameters for HARP-MRI is a part of a manuscript under preparation.

10.6 Software contributions

Given below are the software tools that were developed as a part of this dissertation.

- HARP-MRI Parameter Optimization toolbox: A tool for selecting optimal operating parameters. It can be downloaded from
iacl.ece.jhu.edu/projects/optimHARP/

- HARP 2nd Generation: A tool that integrates HARP-MRI functionalities for both heart and the tongue.
- SURFACES: A tongue contour processing program with a attached visualization tool. This tool was written as a part of research presented in the appendix chapter. This tool is available for download from www.speech.umaryland.edu/software.

10.7 Closing Remarks

Through the years during which the theses in this dissertation were developed, there has been a conscious paradigm shift from postprocessing of tagged MR images to direct and more efficient ways of acquiring tagged MR data in k-space. This change in paradigm signals a shift from MR image processing to MR imaging. This is a very positive development, which we believe is necessary if HARP-MRI is to see the full light of the clinic. The topics in this dissertation have been motivated precisely by this challenge to make HARP-MRI clinically feasible. The characterization of peak and optimal performances of HARP-MRI has demonstrated HARP-MRI's ability to provide diagnostically significant information. It has helped us realize how HARP-MRI can supplement the existing modalities to diagnose heart disease. We believe that the work in this dissertation takes HARP-MRI one step closer to its regular clinical use.

A complete adoption of HARP-MRI will require fast and efficient 3-D methods that will provide clinicians with outputs with better resolution and lesser artifacts. This will not only require more technical research, but also the cooperation of a team of radiologists, cardiologists, technicians, and engineers in both academia and the medical imaging industry. During such a cooperative effort, the foremost objective should be the better diagnosis of the patient. It is our hope and belief that research presented in this dissertation, as insignificant it might be, will help in faster, better, and early detection of heart disease.

'Whatever you do may seem insignificant, but it is most important that you do it.'

— Mahatma Gandhi

Appendix A

Spatiotemporal Visualization of the Tongue Surface using Ultrasound and Kriging

Preface

A comprehensive analysis of tongue motion requires data from both the tongue's interior and the tongue's surface. One method to analyze surface motion is to acquire two-dimensional ultrasound images of the tongue during speech, and to extract the tongue surface contours from the images. While visualization of these extracted contours is straightforward, quantitative and statistical analysis of these contours is difficult because of the absence of physical tissue point markers, like tags in MRI. In this research, this problem is overcome by pre-processing the contours using Kriging. Pre-processing includes extrapolating and resampling the contours on a regular spatial grid. The preprocessed contours can be visualized as spatiotemporal surfaces, which can be used for quantitative and statistical analyses of speech.

A.1 Introduction

As explained in Chapter 9, the tongue can produce a variety of surface shapes through complex activation of its muscles. The imaging methods that are currently used to mea-

sure tongue surface motion can be classified into two types: tissue point techniques and non-invasive imaging techniques. Tissue point techniques include X-ray microbeam and electromagnetic midsagittal articulator, and the non-invasive techniques include ultrasound, X-ray, and MRI [143, 150]. When compared to the imaging techniques, the tissue point measurements interfere with natural speech because of their invasiveness. They also have methodological problems of extrapolating the tongue surface between and beyond the tissue points [142]. The imaging techniques, on the other hand, provide a more complete representation of the tongue surface. Among the imaging modalities, ultrasound is very attractive for producing an image sequence of tongue motion because of real-time capture rates (30 frames per second), convenience of experimentation, and cost. Ultrasound has been extensively used to analyze speech production [66, 143] and to understand the act of swallowing [30, 162].

In this chapter, we have used a sequence of two-dimensional ultrasound images to understand the motion of the surface of human tongue during speech and swallowing. The sequence of images is acquired at video frame rates and represents the mid-sagittal section of the tongue [Fig. A.1(a)]. As in MRI, multiple repetitions are acquired for the same utterance. But here, the necessity for repetitions is not for acquiring complete data, but to account for intra-subject variability, and to reduce the error in the measurement. The cine series of ultrasound images are processed using an existing automatic contour extraction and tracking algorithm [85] [Fig. A.1(b)]. Each set of these extracted tongue contours constitutes a very high dimensional data set – a dense set of points on the tongue (typically around 100 sample points on the tongue) moving over time with data collected at a rate of 30 frames per second [Fig. A.1(c)].

While such high dimensional data can be visualized in a spatiotemporal fashion [see the waterfall display in Fig. A.1(d)], quantitative comparisons like averaging are impossible because of the absence of physical tissue point markers. The absence of physical markers implies that there is no simple point-to-point correspondence between contours, which is necessary for averaging and comparing contours. Therefore, it is necessary that the contours be sampled on an identical spatial grid and that they be of the same length. If the contours are of equal length and if they are sampled on identical grids, then a spatial correspondence can be established between two spatial points on two contours that share

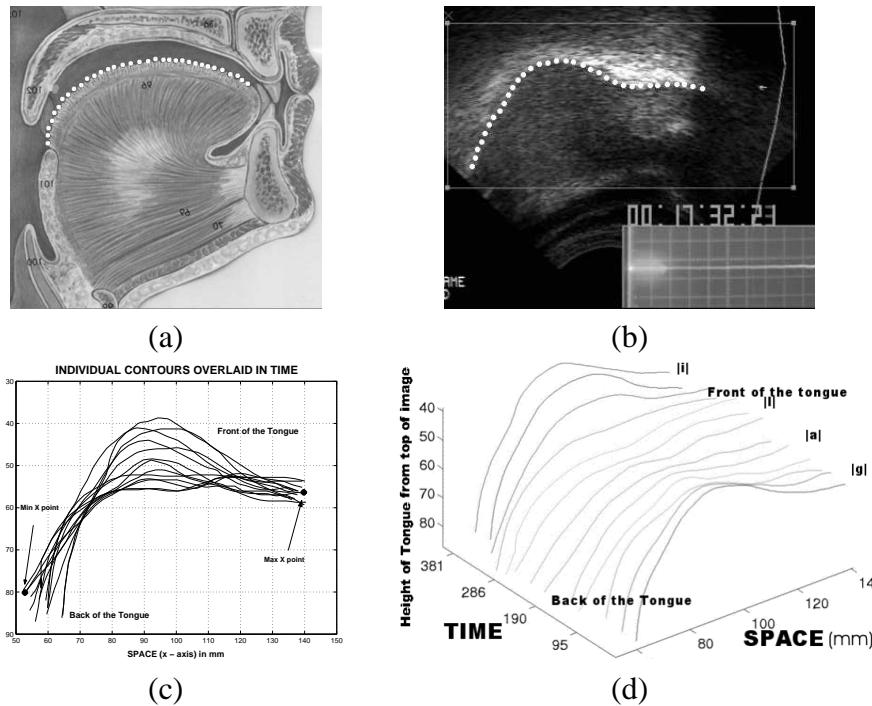


Figure A.1: (a) Midsagittal tongue schematic with superimposed surface contours points. (b) Midsagittal ultrasound image with tracked surface contour points (c) Sequence of tongue contours in time overlaid on each other. (d) Waterfall display of contours for the word ‘golly’.

the same x coordinate. But the following three factors lead to the apparent length differences and irregular sampling of contours.

1. Data loss at tongue tip and tongue root: The tongue tip and tongue root are difficult to image using ultrasound. The tongue tip is obscured by air beneath it and the tongue root is obscured by the shadow of the *hyoid* bone. This data loss might lead to a change in the apparent length of the extracted contours.
2. Change in true length of tongue contour: Due to speaker imprecision, the tongue contours may be of different lengths for different repetitions. Moreover, the tongue length can change even during one utterance due to the volume-preserving nature of the tongue. For example, vertical expansion or compression must be balanced by an front-back expansion or compression, respectively, which, as a result, changes the tongue length.
3. Contour sampling effects: An increase in the gradient of the extracted contour in a particular portion, increases the density of sampling in that portion. This behavior of the contour extraction algorithm results in differences both in the spatial sampling locations and local sampling density.

To address these difficulties, our strategy is to pre-process the contours by equalizing their lengths, and then by resampling them on the same grid. Pre-processing methods, such as registering, smoothing, extrapolating, and interpolating data, are necessary steps in many statistical applications [130]. A variety of pre-processing methods have been suggested by Stud et al. in [142] and Stone et al. in [148]. The existing methods to equalize the lengths of the contours include combinations of the following three approaches: 1) truncation of the longer contours beyond a defined region; 2) extrapolation of shorter contours to the size of longer ones through linear or spline extension; and 3) padding shorter curves with constant values. The truncation approach, although good for certain kinds of contours, neglects interesting and valid data from the longer curves. The extrapolation approach using splines was discarded by Slud et al. [142] because of the unphysiological swings in the extrapolated contours. Instead they used the “padding” approach, where the shorter curves are padded with endpoint averages. The padding techniques introduces artificial discontinuities, which

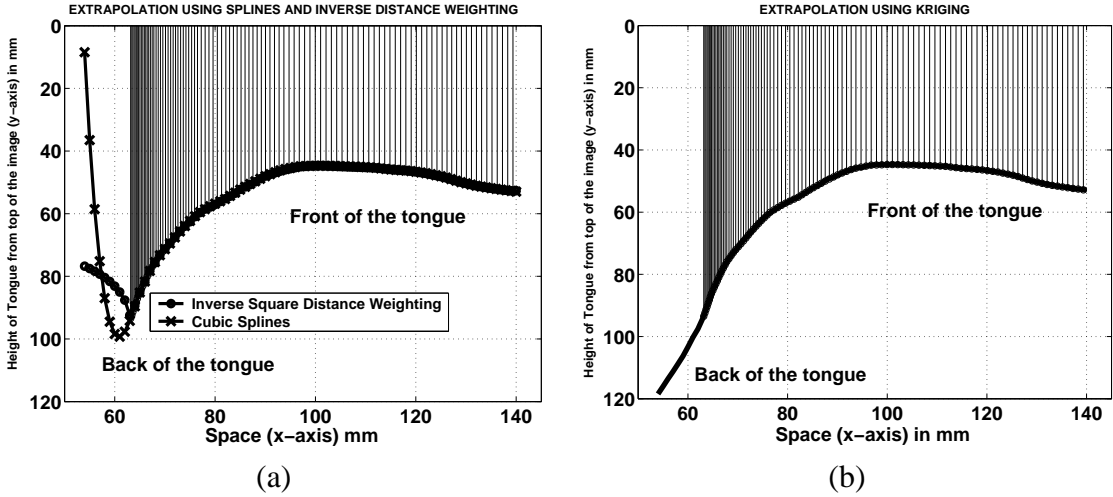


Figure A.2: Comparison of Kriging with inverse square distance weighting and cubic splines: (a) Extrapolation using cubic splines and inverse square distance weighting; note the swing in the case of cubic spline(cross) and the unsMOOTH contour produced by inverse square distance weighting methods. (b) Extrapolation using Kriging; note the improved performance of Kriging at the back of the tongue.

are not only visually unappealing, but can create problems in some statistical analyses. In this research, we take the extrapolation approach.

The problem of spatial data interpolation and extrapolation is common to many scientific areas, for example, image processing, economic forecasting and geostatistics. Various methods have been used for interpolation [65, 29, 48, 155], for example inverse distance weighting, Kriging, polynomial splines, Hardy's multi-quadratic method, and tension finite difference method. Some of these interpolation algorithms have been used directly for extrapolation, but the results differ in their accuracy. Among these methods, the inverse distance weighting method is considered to be robust in terms of estimation error. This robustness is due to the weighted averaging of data values, resulting in estimates not too far from the actual data. This method, however, introduces abrupt changes in contours, which make the contour non-differentiable, unsMOOTH, and visually unappealing [see Fig. A.2(a)]. This makes the contours difficult to be used for further analysis. On the other hand, polynomial splines, especially the higher order splines, sometimes lead to undesirable oscillations in the extrapolated values depending on the gradients of the values near

the end of the contours [see Fig. A.2(a)] [81, 74].

Fig. A.2 shows a typical extracted tongue surface contour. The data corresponding to the extracted contour is represented in the form of a stem plot descending from the top of the plot. Note that the sampling density is higher in locations where the slope is larger, such as at the back of the tongue (on the left). This occurs because the contour itself is sampled uniformly along its length. Thus, as the slope of the contour increases, the density of sampling with respect to the x axis also increases. Fig. A.2(a) shows two extrapolated methods for the same data set: one using inverse square distance weighting (a special case of inverse distance weighting where the weighting exponent is two) and the other using cubic splines. In both cases the quality of interpolation within the tongue surface is good. The problem starts to appear in the extrapolated part. In the case of inverse square distance weighting, the value of the extrapolated values are constrained to stay within the values of the data. Hence there is an abrupt change in shape, which is uncharacteristic of a tongue shape. In the case of cubic splines, clearly there is a non-intuitive and extreme fluctuation in the extrapolation.

In order to avoid the aforementioned problems, we use Kriging [31] to extrapolate the tongue shape. Kriging is a statistical estimation technique that uses the statistics of the sampled function to estimate a continuous function that interpolates between the sampled points and also extrapolates beyond the endpoints of the contours. The output of Kriging is a smooth and visually appealing fit of the data, making Kriging suitable for pre-processing the contours. Both the oscillation and the abruptness are absent in Fig. A.2(b), where the extrapolation is done using Kriging. The key to Kriging's improved extrapolation performance is its spatial asymptotic properties. Also, given the sample data points and their statistics, Kriging estimates a continuous function that best fits the data points. Therefore, the resulting continuous function can be resampled at any given spatial grid. After each contour has been extrapolated and resampled, the contours can be visualized as a spatiotemporal surface and can be analyzed using a dedicated software tool called SURFACES, which we also present in this appendix.

A.2 Methods

A.2.1 Data acquisition

We acquire a sequence of ultrasound images of the mid-sagittal section of the tongue [Fig. A.1(a)]. The sequence of ultrasound images is acquired as the subject either speaks a given utterance or swallows a particular bolus of water. One of the images in an ultrasound sequence is shown in Fig. A.1(b), with the extracted contour overlaid as white dots. The ultrasound scan rate is set to 30 images per second. Each subject is asked to repeat the utterance multiple times (usually 7 times, with the first and last omitted from further processing) in order to account for the intra-subject variability in speech production. The audio data is also recorded, but it is not directly useful in the context of this work. The sequence of images is acquired both in analog and in digital format. The images are then input into the contour extraction program, which is described in the next section.

A.2.2 Automatic contour extraction and tracking

Each image in the sequence is processed using the algorithm proposed by Li et al. [85]. The algorithm uses a discrete form of deformable contours and imposes speech, tongue, and ultrasound imaging constraints. The initial contour of the tongue shape is user-defined; it is then used as the initialization for the deformable model. Using the initial contour and the model constraints, the algorithm tracks the tongue surface over the series of images. The algorithm also imposes regularizing constraints on the deformable contours, so that the resulting contour is smooth. Each contour is represented as a set of y values, which represents the height of the tongue (calculated from the top of the image) measured at sampling locations determined by the x values [Fig. A.1(c)]. These contours are the input for the pre-processing using Kriging.

A.2.3 Introduction to Kriging

Kriging is named after the South African mining engineer D. Krige who developed it for estimating mineral deposits from scattered ore samples [116, 65]. Since then it has been

used to interpolate spatially dependent data in a wide variety of disciplines. Kriging is a modified linear regression technique that estimates a value at a point by assuming that the value is spatially related to the known values in the neighborhood of the point. Kriging computes the value for the unknown data point using a weighted linear sum of known data values. The weights are chosen to minimize the estimation error variance while keeping the average estimation error zero. Hence, Kriging is called the best linear unbiased estimator because it theoretically tries to minimize the variance of estimation error, while being an unbiased estimation procedure [116].

Direct minimization of error variance is not possible because the true values are unknown. Hence, Kriging uses a random function model, where the data points are assumed to be realizations of random variables and the point to be estimated is also a random variable. These random variables are assumed to have specific covariance structure; selection of which is crucial in the estimation procedure. So given the model, the error variance can be modelled and then minimized under the unbiasedness constraint to get the Kriging solution.

A.2.4 Derivation of Kriging solution

Given observations at spatial points $\mathbf{x}_1, \mathbf{x}_2, \dots, \mathbf{x}_p$, we want to estimate the value of the function at any spatial point \mathbf{x} . Kriging estimates a continuous function $s(\mathbf{x})$, so that the average estimation error is zero and the error variance is minimum. Since Kriging estimates a continuous function, we can get the value of the function at any point \mathbf{x} .

In our case, the observations are the ' y_i ' values that measure the height of tongue contours from the top of the ultrasound image at sampling points ' x_i '. Since the x_i 's are one-dimensional, we let $\mathbf{x} = x$, a one-dimensional variable. Kriging models the estimated function $s(x)$ as consisting of two components

$$s(x) = u(x) + \mathbf{f}^T(x)\mathbf{d}. \quad (\text{A.1})$$

The first term $u(x)$ is a zero-mean random function with known covariance function $k(x_a, x_b)$ [68]. The covariance function models the spatial correlation in the data. The second term $\mathbf{f}^T(x)\mathbf{d}$ is the mean of the function $s(x)$. The term $\mathbf{f}(x)$ is $r \times 1$ vector of known *drift functions* and

\mathbf{d} is the $r \times 1$ vector of unknown ‘drift coefficients’. The mean of the function $s(x)$ is deterministic, but unknown. Usually the drift functions are taken to be monomials of degree less than or equal to a chosen value q . In our 1-D case, $r = q + 1$. Given the shape of the tongue contours, we have selected $q = 1$, which leads to linear drift functions ($r = 2$),

$$\mathbf{f}(x) = [1 \ x]^T.$$

Intuitively, Kriging can be seen as estimating two components of the contour $s(x)$. The mean, $\mathbf{f}^T(x)\mathbf{d}$, captures the global shape of the contour, while the zero-mean random function, $u(x)$, captures the variation of the contour around its mean. The mean is a linear combination of drift functions. In this research we use linear drift functions which means that the global shape of the contours is captured with a linear function with a given slope and an intercept. The variation around the mean is captured by the zero mean random function $u(x)$. The behavior of these two components is critical in determining how the extrapolated curve will look. A brief discussion on the extrapolation properties is discussed after the Kriging solution has been developed.

Given this statistical model for the data, Kriging produces the Best Linear Unbiased Estimate (BLUE), which consists of a linear combination of the observations.

$$\hat{s}(x) = \mathbf{a}^T \mathbf{y},$$

where \mathbf{y} is a vector of the observations (y values) at x_1, x_2, \dots, x_p and $\mathbf{a}(x)$ is a $p \times 1$ vector of coefficients, which we want to estimate. The constraint of unbiasedness of the estimate leads to the constraint on the coefficients,

$$\mathbb{F}\mathbf{a}(x) = \mathbf{f}(x),$$

where

$$\mathbb{F} = [\mathbf{f}(x_1) \dots \mathbf{f}(x_p)], \quad (\text{A.2})$$

which is an $r \times p$ matrix. The Kriging estimate is then obtained by finding $\hat{s}(x)$ which minimizes the estimation error variance

$$E[(s(x) - \hat{s}(x))^2]$$

subject to the unbiasedness constraint. The constrained minimization problem can be solved using the method of Lagrange multipliers and the solution depends only on $\mathbf{f}(x)$, \mathbb{F} , data covariance matrix

$$K = \begin{bmatrix} k(x_1, x_1) & \dots & k(x_1, x_p) \\ \vdots & \ddots & \vdots \\ k(x_p, x_1) & \dots & k(x_p, x_p) \end{bmatrix}, \quad (\text{A.3})$$

and the covariance vector

$$\mathbf{k}(x) = [k(x, x_1) \dots k(x, x_p)]^T. \quad (\text{A.4})$$

The solution is

$$\hat{s}(x) = \mathbf{k}^T \mathbf{w} + \mathbf{f}^T(x) \hat{\mathbf{d}}, \quad (\text{A.5})$$

where

$$\begin{aligned} \mathbf{w} &= K^{-1}[I - \mathbb{F}^T(\mathbb{F}K^{-1}\mathbb{F}^T)^{-1}\mathbb{F}K^{-1}]\mathbf{y}, \\ \hat{\mathbf{d}} &= (\mathbb{F}K^{-1}\mathbb{F}^T)\mathbb{F}K^{-1}\mathbf{y}. \end{aligned}$$

For more details on the derivation of Kriging, please see reference [158]. Details of the algorithm implemented in this appendix are given in the following section.

A.2.5 Kriging algorithm

Given a contour in terms of x_i (spatial sampling locations) and y_i (height of the point from the top of the image), the problem is to estimate the value of a continuous function $s(\cdot)$ at arbitrary spatial position $x \in \mathbb{R}$.

Algorithm 1 1. *Form the data vector, $\mathbf{y} = [y_1 \dots y_p]$.*

2. *Select the drift function $\mathbf{f}(x)$ and calculate \mathbb{F} as defined in Eq. (A.2).*

We used the linear drift function, $\mathbf{f}(x) = [1 \ x]^T$.

3. *Select the covariance function for the data, $k(x_a, x_b)$ and calculate the matrix K and vector $\mathbf{k}(x)$ as defined in Eqs. (A.3) and (A.4) respectively. We used the generalized covariance function, $k(x_a, x_b) = \|x_a - x_b\|^2 \ln \|x_a - x_b\|^2$.*

4. Select the noise covariance matrix Σ , a $p \times p$ matrix that characterizes the statistics of the noise in the data.

In this work we assumed zero noise variance in the contour data. The contour extraction algorithm incorporates smoothing routines and hence the output contour is already smooth and noise free. But noise can be easily incorporated into the algorithm, but assuming white zero mean noise with variance equal to σ mm². Hence, $\Sigma = \sigma I$, where I is the $p \times p$ identity matrix. The use of non-zero noise variance make Kriging a smoother rather than interpolator [158].

5. Calculate the matrices

$$\begin{aligned} L &= (K + \Sigma)^{-1} \\ M &= (\mathbb{F}L\mathbb{F}^T)^{-1}\mathbb{F}L \\ G &= KL(I - \mathbb{F}^T M) \end{aligned}$$

6. Calculate the coefficient vectors

$$\begin{aligned} \hat{\mathbf{d}}_s &= M\mathbf{y} \\ \mathbf{w}_s &= K^{-1}G\mathbf{y} \end{aligned}$$

7. Calculate the desired estimate using

$$\hat{s}(x) = \mathbf{k}^T(x)\mathbf{w}_s + \mathbf{f}^T(x)\hat{\mathbf{d}}_s.$$

Thus, the solution of Kriging is a continuous function $\hat{s}(x)$, which can be resampled on an arbitrary spatial grid, thus overcoming the irregular sampling problem. Notably, the spatial grid can include extrapolated points that are beyond the original range of x_i 's over which the data was collected. This compensates for apparent length changes of tongue contours because of data loss and speaker imprecision.

A.2.6 Connection to thin-plate splines

The selection of the covariance structure of the data is important in Kriging estimation. In our algorithm, we use the generalized covariance function, $k(x_a, x_b) = \|x_a -$

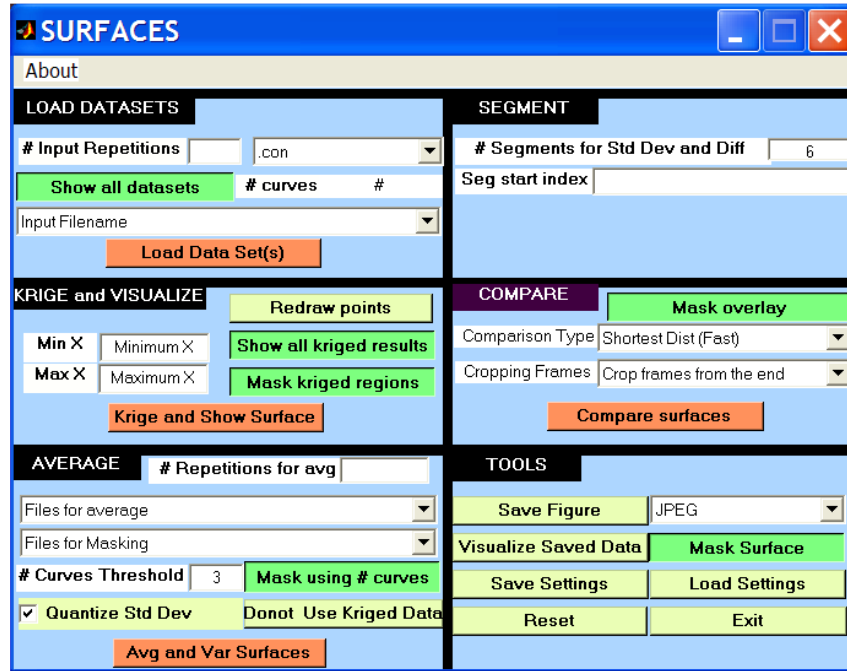
$x_b\|^2 \ln \|x_a - x_b\|^2$. The use of this covariance function makes our Kriging solution the same as the *thin-plate spline* solution [21]. Thin-plate spline is an interpolation method that estimates a smooth curve that passes through all given data points so that the final curve is minimally bent. The name ‘thin-plate spline’ refers to a physical analogy involving the bending of a thin sheet of metal, when the tongue heights are set as deflections of the metal plate in the z -direction. In our case, we deal with a 1-D analog of this bent metal sheet. It has been shown that the thin-plate spline is a special form of Kriging [67] and under certain conditions they are the same.

Thin plate splines are smooth and asymptotically parallel to the mean of the estimated function. In the extrapolated region, while the zero mean random function tends to flatten out, the mean function continues on its trend, thus dominating the behavior of the curve. So, during extrapolation the contour typically follows the global trend of the contour, which in our case is linear because of the use of linear drift terms. Since the thin-plate spline solution has a smoothing term built in, the extrapolation will be smooth. Unacceptably huge drifts can occur while extrapolating with thin-plate splines; but it happens only at points that are much further away from the data, when compared to the spread in data locations. In typical cases, we extrapolate less than 6 mm on either side of the tongue, where the extrapolation performs reasonably well. A detailed validation of the quality of the extrapolation and the estimation errors are presented later in this chapter in section A.4.

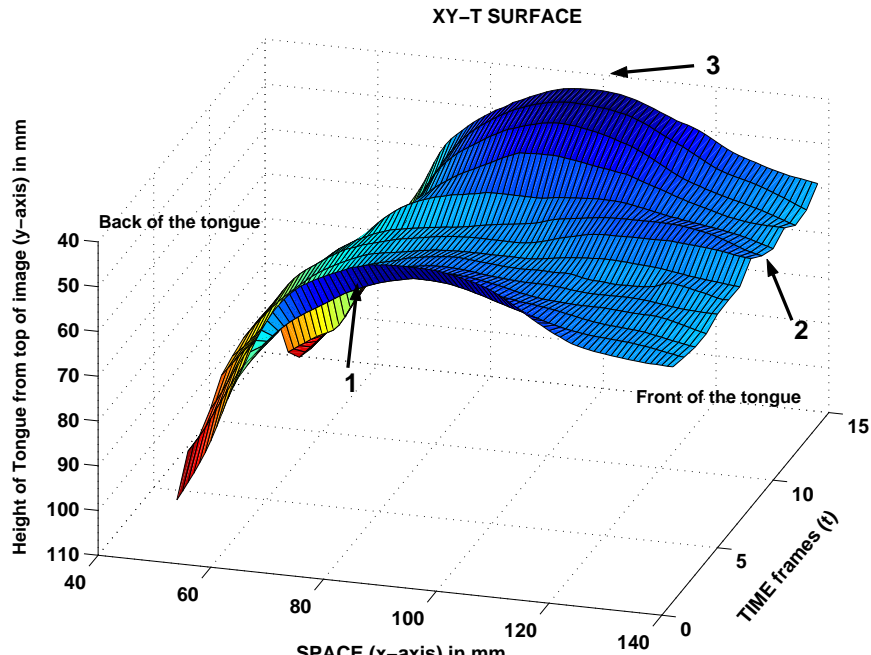
A typical ultrasound data set contains 13–40 contours depending on the length of the speech utterance or swallow and the video frame rate of the ultrasound scanner. Each contour is extrapolated and resampled using the above method. Then the contours are stacked as a spatiotemporal surface [see Fig. A.3(b)]. Similar processing can be done on different repetitions of the same speech utterance or swallow, and resulting surfaces can be averaged to yield an average spatiotemporal surface.

A.2.7 SURFACES software

Fig. A.3(a) shows a snapshot of the graphical user interface (GUI) for SURFACES (available for download at www.speech.umd.edu/software). The GUI and the algorithm were implemented in MATLAB Version 6 (Mathworks, Natick, MA, USA) and



(a)



(b)

Figure A.3: (a) A snapshot of the SURFACES software and (b) a spatiotemporal surface of the word ‘golly’.

ported to a stand-alone version. The GUI has five main panels. The functions in the first and second panels pre-processes individual contour for further analysis. The program reads in the initial contour sequences and allows the user to select maximum and minimum values of x , within which each contour will be cut or extended, smoothed (estimated) using Kriging and then resampled. The ‘*Krige and Show Surface*’ button kriges all the contours resulting in a spatiotemporal surface, as shown in Fig. A.3(b). This surface looks similar to the waterfall display in Fig. A.1(d). Unlike the waterfall display, this surface can be directly used for further processing (e.g. averages, differences etc), because all the contours have an equal number of samples on the same grid.

The spatiotemporal surfaces that are derived from the kriged contours can be used to qualitatively analyze a speech utterance. For example, Fig. A.3(b) shows the spatiotemporal surface for the word ‘*golly*’. Noting that the front of the tongue is on the right, the nearest contour shows the ‘*g*’, which is arched in the middle [see 1 in Fig. A.3(b)]. As time advances, the tongue flattens and the tip rises for the ‘*l*’ [see 2 in Fig. A.3(b)]. Finally the tongue arches again for ‘*y*’ [see 3 in Fig. A.3(b)].

Panel 3 of the software is for averaging different repetitions of the same utterance that have been kriged and resampled in Part 1. Since the samples are on a regular spatial grid, the averaging is done for different y values at each x coordinate. By averaging different y values at each x coordinate, we are implicitly making a point-to-point correspondence of different y values which share the same x coordinate. The result is an averaged spatiotemporal surface, and a variance surface. Panels 4 and 5 of the software are used for comparison of two spatiotemporal surfaces like overlaying surfaces and calculating local or global differences. These spatiotemporal surfaces can be either individual repetitions or average surfaces (see Fig. A.4(a) for an example of an overlay of two such surfaces). The current version of SURFACES implements two algorithms for calculating the difference between spatiotemporal surfaces. These include a simple difference of y at each x and a nearest-neighbor algorithm [146] to find the shortest distance between two surfaces. These distances are further used for calculating L2 difference norms and root mean squared differences. More details about the algorithms used can be found in the user manual for SURFACES (www.speech.umaryland.edu/software).

A.3 Results and Applications

Applications of the SURFACES software is demonstrated on two kinds of data: 1. speech data collected to find the effect of gravity on tongue and 2. swallowing data collected to find the effects of anterior open bite on swallowing stability.

A.3.1 Application to speech data

This application demonstrates the use of comparative analysis between two spatiotemporal surfaces corresponding to two different speech utterances. The goal of this study was to understand the effects of gravity on the tongue during speech [144]. The subjects were asked to repeat the same utterances in a supine position first and then in an upright position. Tongue contours were extracted from the ultrasound data, kriged, averaged and visualized using SURFACES. The overlaid surfaces in Fig. A.4(a) shows a typical result during the utterance of the word ‘golly’. We see that the supine surface (filled surface) is rotated backward from the upright surface (white mesh) during the entire word. A secondary effect that can also be observed is that tongue tip is elevated in the supine position during the ‘l’ (see arrow). The two surfaces can also be visualized as a difference image [Fig. A.4(b)] with the colors denoting the amount of difference (in mm) between each pixel of the two surfaces.

A.3.2 Application to swallowing data

This application demonstrates the use of visualizing the spatiotemporal surfaces and drawing qualitative physiological inferences from it. Fig. A.4(c) shows the spatiotemporal surface of water swallow. We observe that the water is initially contained in the front of the tongue, with the tongue tip depressed and the back elevated to protect the airway. Subsequently, the tongue deforms around the bolus of water as it is propelled backwards. Finally, the tongue elevates from front to back to make contact with the palate after the water’s passage. This spatiotemporal surface can also be rotated to various views. Fig. A.4(d) shows the spatiotemporal surface of Fig. A.4(c) as a 2-D image where the color denotes the tongue height. The black lines in figures A.4(c) and (d) separate the regions that contain true data from the regions that contain extrapolated data.

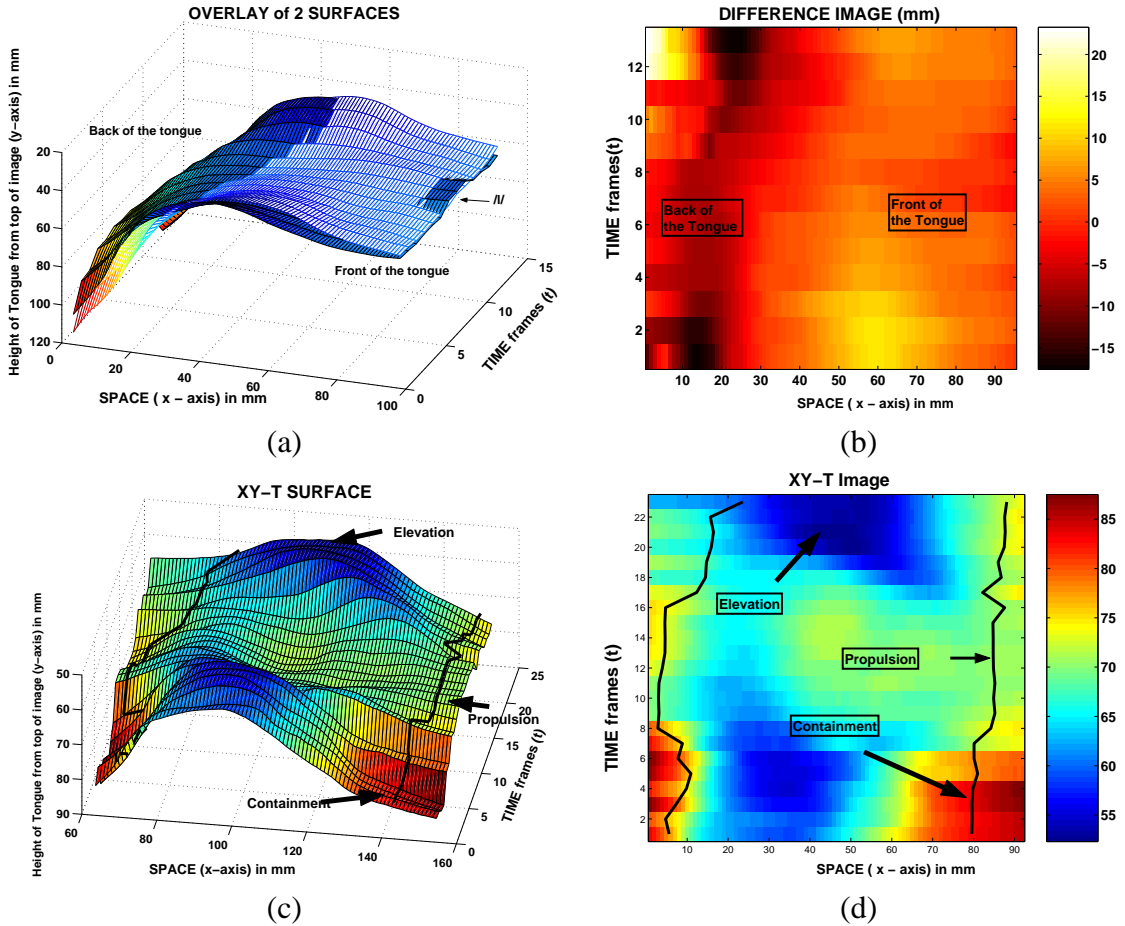


Figure A.4: Applications of SURFACES: (a) Overlay of 2 spatiotemporal tongue surfaces of the word ‘golly’. Mesh surface was spoken in ‘upright’ position and the filled surface in ‘supine’ surface. (b) Difference between the two spatiotemporal surfaces in form of an image. (c) Spatiotemporal surface of a swallow. The water is contained in front of tongue, then propelled backwards, followed by tongue surface elevation after the water’s passage. (d) Visualization of the swallow as an image with colors denoting height. Note in (c) and (d) the black lines separate the regions that contain real data from the regions that contain extrapolated data.

A.4 Validation of contour extension

Recall that given the data values at specified spatial points, a Kriging solution estimates the value at any spatial point. The Kriging estimate is the ‘best’ in the sense that it theoretically minimizes the error variance while maintaining the mean error zero. Hence it is possible to get an estimate of the minimum error variance even before the estimation is done. But this estimate of the minimum error variance is the predicted error variance of the model and cannot be completely trusted without testing the model on real data [65]. The validation test on real data is more crucial in the case of extrapolation, since the range of errors produced in extrapolation tends to be larger than in interpolation.

A.4.1 Validation materials and methods

A total of 1612 tongue contours were used for the validation test. The validation data set contained contours from 4 different words (*golly, oslo, he sought, he taught*), 5 different speakers and 2 different positions of positions of speech (subject upright and subject laying supine).

Portions of the tongue contour of length approximately 1 mm, 3 mm, 5 mm and 10 mm were artificially cut (see Fig. A.5). All the lengths are distances along the surface of the tongue contour and not along the spatial axis (x-axis). The center region combined with the green regions was the initial full contour. The artificial cuts were made from both the back and the front of the tongue contour (green) regions in Fig. A.5). These cuts simulated the loss of data and the apparent change in length as discussed in the introduction. Kriging was then used to restore these cut portions (blue regions in Fig. A.5) and the error was measured as *estimated curve minus the true curve*. This procedure was done for all the 1612 contours. The errors were also averaged separately for the front and the back of the tongue. Standard deviation of the errors was also calculated.

A.4.2 Validation results

Fig. A.6 shows the average errors (at each point) for the four different length cuts. The blue curve shows the error at the back of the tongue, whereas the red curve shows the

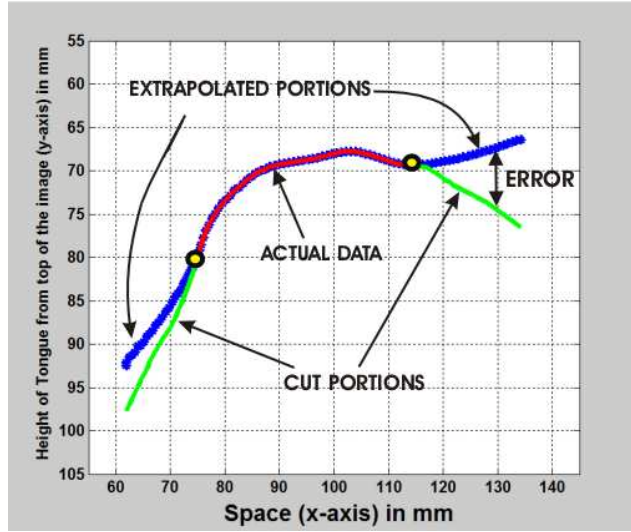


Figure A.5: Validation experiment: The center line along with the lower lines (gray) on either side is the actual tongue contour. The edges are artificially cut in order to see how Kriging performs in extrapolation. The last data points on the edge of the contour are represented as black circles. The extrapolated lines (blue) are the contours that Kriging estimated. The difference between the blue and green regions is measured as error.

error at the front of the tongue. The axis in these graphs represents the distance from the estimated point to the cut, (i.e. the last data points on the edge of the contour represented as black circles in Fig. A.5). Error bars represent standard deviation. For a given length of extrapolation, the error measures in Fig. A.6 give an estimate of the amount of confidence that can be placed on the calculated values, depending on whether the extrapolation is done in the front or in the back of the tongue. For example if the contour is extrapolated to a length of 5 mm [Fig. A.6(c)], then at a point 4 mm away from the actual data, the expected error is around -3.2 mm in the back and around -4 mm in the front of the tongue. Also, we note that in all cases the error is negative, which implies Kriging always underestimates the values. This underestimation of the true curve is because, the extrapolated contour tries to follow the global shape of the tongue contours, which in many cases, a line with a positive slope. Therefore, in the front of the tongue, the extrapolated contour curves up, whereas in the back of the tongue the extrapolated contour curves down. In the actual data the back of the tongue slopes downward, whereas the front of the tongue stays flat, in most cases [see

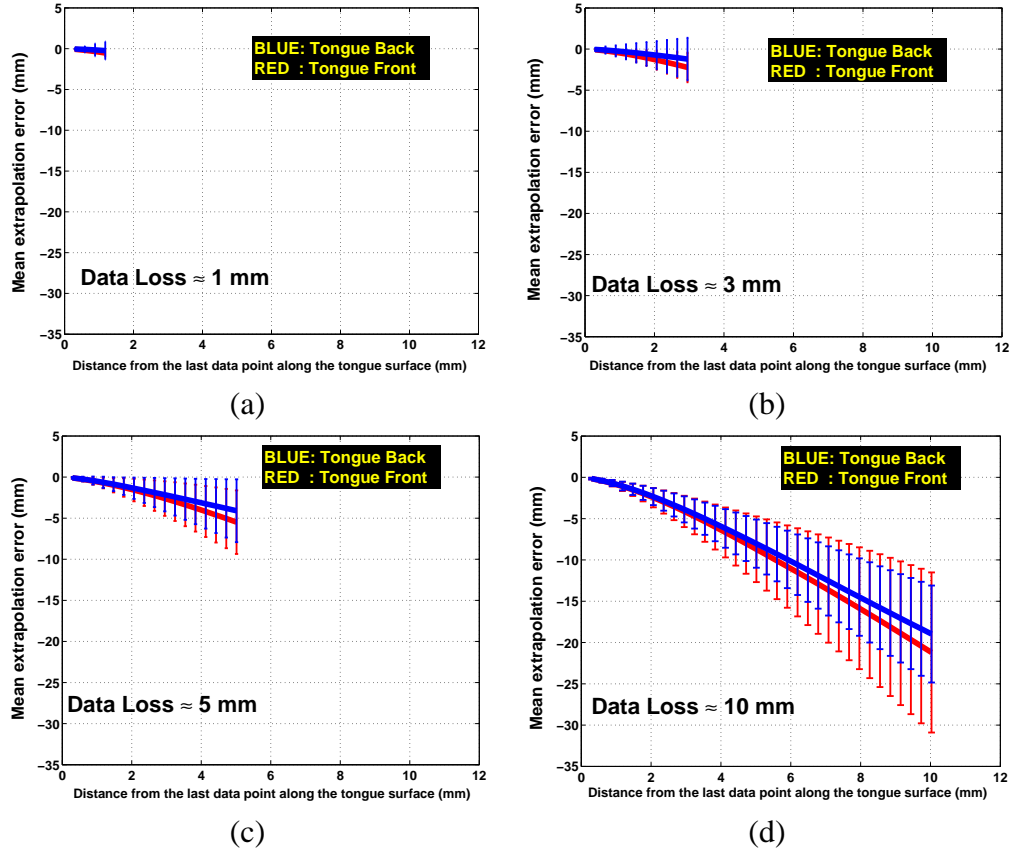


Figure A.6: Validation Results: Mean errors in estimation when the length of tongue contour cut is (a) 1 mm (b) 3 mm (c) 5 mm and (d) 10 mm. The error bars represent standard deviation. The x-axis denotes distance along the surface of the tongue, not the distance along the spatial axis (x-axis). The red curves denote the errors in the front of the tongue and blue denotes the errors in the back of the tongue.

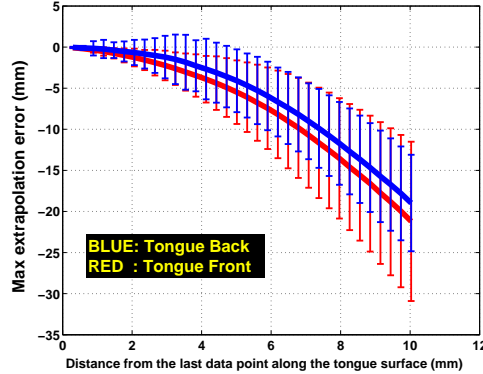


Figure A.7: Maximum Errors: Maximum expected errors in estimation as a function of the length of tongue cut.

for example Fig. A.1(c)]. Hence, we see that error at the front of the tongue is slightly, but consistently, higher than the back of the tongue. This behavior, however, depends entirely on the global scope of the particular tongue surface that is being analyzed.

Fig. A.7 represents the worst case analysis of Kriging extrapolation. Maximum expected error is plotted as a function of the length of tongue cut for both the front and the back. The maximum error occurs at the point which is farthest away from the data. The maximum error and the error variance also increase with increasing length of data loss.

A.4.3 Discussion

We notice that the errors are large when the amount of extrapolation is large. It is natural to expect this trend because we are moving away from where actual data exists. The inverse distance methods may provide a lower error measure because the values are always constrained to be within the data values. But this lower error measure does not have a physical meaning and is only of statistical interest. This is because the curve estimated using inverse distance methods has large discontinuities, thus ignoring the physical reality of the tongue. Moreover the contours that are estimated using inverse distance methods can neither be used for averaging repetitions nor for doing comparative studies.

It is also important to note that the errors mentioned in this section are extrapolation errors. Using Kriging with the generalized covariance function for interpolation is extremely

robust and the estimates have a very low value of errors [65] [see Fig. A.2(b)]. So, the values estimated in the interior of the tongue have low errors (see the central overlapping region of the red and blue curves in Fig. A.5).

Even though the Kriging solution is useful for visualization, averaging and comparative analysis, physiological inferences derived using these extrapolated regions should be used with caution because of the extrapolation errors. On the other hand, interpolation error is very small and hence the quantitative measures in the non-extrapolated regions of the tongue can be used with high degree of confidence. With regard to the issue of knowing which regions of the contours are extrapolated, the ‘SURFACES’ software has two important features: 1) When visualizing a spatiotemporal surface a mask is generated which tell the user which data points are real and which have been artificially kriged [Fig. A.4(c) and (d)]; 2) when averaging different repetitions, rules have been implemented so that an averaged value will be generated only at those x points where a certain number of real (non-extrapolated) y values are available.

One of the limitations of Kriging is that its solution, like all spline-based interpolation methods, becomes unstable if there are two points with the same x value, but different y values. This situation can occur when the tongue surface curls or when the tongue surface becomes exactly vertical. In these cases, Kriging might fail to give reasonable contours. Therefore, for such cases, the ‘SURFACES’ software implements a local contour adjustment routine. The tongue contour is locally tweaked by changing the x -coordinate of one of the two points. Different amounts of tweaking were tried on locally vertical contours from data sets of the upright-supine study. The minimum of these local tweaks that provided reasonable results for all contours was ± 0.3 mm. Therefore a bias of ± 0.3 mm was chosen as final amount of tweaking. This bias is within the typical ultrasound measurement error of ± 0.5 mm [149]. The adjusted contour is then subsequently kriged and visualized.

A.5 Conclusion

We described a method of visualizing, quantifying and comparing tongue surface features from contour sequences. Kriging was used to extrapolate the tongue surface contours

that are extracted from ultrasound image sequences of the tongue. The resulting Kriged contours are then stacked and visualized as a spatiotemporal surface. A dedicated software tool, SURFACES, which incorporates the Kriging algorithm is presented. The tool is used for averaging and comparative analysis of different tongue shapes. The calculation and visualization of spatiotemporal mid-sagittal tongue surfaces helps in understanding tongue deformations during speech and swallowing.

The main problem that was overcome by this research is the lack of point-to-point correspondence between the extracted tongue contours. This problem was solved by equalizing the length of the contours and resampling them on an identical grid, thus establishing a correspondence of two points which share the same x coordinate. Ongoing research in this field is to design algorithms for estimating true point-to-point correspondences based on curvature and other shape properties of the tongue. These correspondences can also be used for registering the data in time and space. In the future, these algorithms can be combined with Kriging to further improve the quantitative measures of tongue shapes.

Finally, it is hoped that in the future, advances in the area of ultrasound will complement the advances in HARP-MRI to enhance the understanding of the tongue's role in speech production .

Bibliography

- [1] “Preventing Heart Disease and Stroke: CDC report,” 2005.
- [2] K. Z. Abd-Elmoniem, V. Parthasarathy, and J. L. Prince, “Artifact reduction in harp strain maps using anisotropic diffusion,” in *SPIE Int. Symp. Med. Imag.*, Feb. 2006. San Diego.
- [3] K. Z. Abd-Elmoniem and J. L. Prince, “Quickcansel: Reduced scan time cansel to eliminate artifact-generating echoes in cardiac MRI,” in *Proceedings of the International Society of Magnetic resonance in medicine*, 2005.
- [4] K. Z. Abd-Elmoniem, S. Sampath, N. F. Osman, and J. L. Prince, “Algorithms for real-time fastharp cardiac function analysis,” pp. 516–524, 2003.
- [5] K. Z. Abd-Elmoniem, M. Stuber, N. F. Osman, and J. L. Prince, “Zharp: Three-dimensional motion tracking from a single image plane,” pp. 639–651, 2005.
- [6] T. P. Abraham and R. A. Nishimura, “Myocardial strain: Can we finally measure contractility,” *Journal of the American College of Cardiology*, vol. 37, no. 3, pp. 731–4, 2001.
- [7] A. H. Aletras and A. E. Arai, “meta-DENSE complex acquisition for reduced intravoxel dephasing,” *Journal of Magnetic Resonance*, vol. 169, pp. 246–249, 2004.
- [8] A. H. Aletras, S. Ding, R. S. Balaban, and H. Wen, “DENSE: Displacement encoding with stimulated echoes in cardiac functional MRI,” *Journal of Magnetic resonance*, vol. 137, pp. 247–252, 1999.

- [9] A. H. Aletras, W. P. Ingkanisorn, C. Mancini, and A. E. Arai, “Dense with sense,” *J Magn. Reson.*, vol. 176, no. 1, pp. 99–106, 2005.
- [10] A. H. Aletras and H. Wen, “Mixed echo train acquisition displacement encoding with stimulated echoes: an optimized dense method for in vivo functional imaging of the human heart.,” *Magn Reson Med*, vol. 46, no. 3, pp. 523–34, 2001.
- [11] J. S. Alpert and K. Thygesen, “Myocardial infarction redefined,” *Eur. Heart J.*, vol. 21, no. 18, pp. 1502–1513, 2000.
- [12] T. Arts, W. C. Hunter, A. Douglas, A. M. M. Muijtjens, and R. S. Reneman, “Description of the deformation of the left ventricle by a kinematic model,” *Biomechanics*, vol. 25, no. 10, pp. 1119–1127, 1992.
- [13] L. Axel and L. Dougherty, “Heart wall motion: improved method of spatial modulation of magnetization for MR imaging,” *Radiology*, vol. 172, pp. 349–350, 1989.
- [14] L. Axel and L. Dougherty, “MR imaging of motion with spatial modulation of magnetization,” *Radiology*, vol. 171, pp. 841–845, 1989.
- [15] L. Axel, A. Montillo, and D. Kim, “Tagged magnetic resonance imaging of the heart: a survey,” *Medical Image Analysis*, vol. 9, pp. 376–393, 2005.
- [16] J. Ayling, “Ready to go,” *Emerg. Med. Serv.*, vol. 32, no. 4, p. 97, 2003.
- [17] T. Baer, J. Gore, S. Boyce, and P. Nye, “Application of MRI to the analysis of speech production,” *Magnetic Resonance Imaging*, vol. 5, no. 5, pp. 1–7, 1987.
- [18] B. Boashash, “Estimating and interpreting the instantaneous frequency of a signal - part 1: Fundamentals,” *Proceedings of the IEEE*, vol. 80, pp. 520–538, April 1992.
- [19] B. Boashash, “Estimating and interpreting the instantaneous frequency of a signal - part 2: Algorithms and applications,” *Proc. of the IEEE*, vol. 80, pp. 540–568, April 1992.

- [20] J. Bogaert, A. Maes, F. V. de Werf, H. Bosmans, M. Herregods, J. Nuyts, W. Desmet, L. Mortelmans, G. Marchal, and F. E. Rademakers, “Functional recovery of subepicardial myocardial tissue in transmural myocardial infarction after successful reperfusion,” *Circulation*, vol. 99, pp. 36–43, 1999.
- [21] F. L. Bookstein, “Principal warps: thin-plate splines and the decomposition of deformations,” *IEEE Transactions on Pattern Analysis and Machine Intelligence*, vol. 11, pp. 567–585, June 1989.
- [22] A. V. D. Bos and A. J. D. Dekker, “Resolution reconsidered - conventional approaches and an alternative,” *Advances in Imaging and Electron Physics*, vol. 117, pp. 241–360, 2001.
- [23] A. V. D. Bos and A. J. D. Dekker, “Resolution reconsidered,” *Advances in Imaging and Electron Physics*, vol. 117, pp. 241–360, 2001.
- [24] E. Braunwald, D. P. Zipes, P. M. Libby, and R. Bonow, “Heart disease: A textbook of cardiovascular medicine, 7th ed.,” An imprint of Elsevier, 2005.
- [25] T. Buck, P. Hunold, K. U. Wentz, J. Nesser, and R. Erbel, “Tomographic three-dimensional echocardiographic determination of chamber size and systolic function in patients with left ventricular aneurysm: comparison to magnetic resonance imaging, cine-ventriculography, and two-dimensional echocardiography,” *Circulation*, vol. 69, pp. 497–505, 1997.
- [26] T. F. Budinger, A. Berson, E. R. McVeigh, R. I. Pettigrew, G. M. Pohost, J. T. Watson, and S. A. Wickline, “Cardiac mr imaging: report of a working group sponsored by the national heart, lung, and blood institute,” *Radiology*, vol. 208, no. 3, pp. 573–576, 1998.
- [27] M. H. Buonocore and H. Bogren, “Factors influencing the accuracy and precision of velocity-encoded phase imaging,” *Magnetic Resonance in Medicine*, vol. 26, pp. 141–154, 1992.

- [28] A. E. Burgess, F. L. Jacobson, and P. F. Judy, “Human observer detection experiments with mammograms and power-law noise,” *Medical Physics*, vol. 28, no. 4, pp. 419–437, 2001.
- [29] C. Caruso and F. Quarta, “Interpolation methods comparison,” *Computers Math. Applic.*, vol. 35, no. 12, pp. 109–126, 1998.
- [30] G. Chi-Fishman, M. Stone, and G. N. McCall, “Lingual action in normal sequential swallowing,” *Journal of Speech, Language, and Hearing Research*, vol. 41, pp. 771–785, 1998.
- [31] R. Christensen, *Linear Models for Multirate, Time series, and Spatial Data*. New York, USA: Springer-Verlag, 1991.
- [32] N. R. Clark, N. Reichek, P. Bergey, E. A. Hoffman, D. Brownson, L. Palmon, and L. Axel, “Circumferential myocardial shortening in the normal human left ventricle,” *Circulation*, vol. 84, pp. 64–74, 1991.
- [33] L. Cohen, *Time-Frequency Analysis*. Prentice Hall Signal Processing Series, 1995.
- [34] G. Constantine, K. Shan, S. D. Flamm, and M. U. Sivanathan, “Role of mri in clinical cardiology,” *The Lancet*, vol. 363, pp. 2162–71, 2004.
- [35] P. Croisille, R. M. Judd, J. A. C. Lima, C. C. Moore, R. M. Arai, C. Lugo-Olivieri, and E. A. Zerhouni, “Combined dobutamine stress 3D tagged and contrast enhanced MRI differentiate viable from non-viable myocardium after acute infarction and reperfusion,” *Circulation*, vol. 92, no. 8, 1995.
- [36] J. Dang and K. Honda, “A physiological model of the tongue and jaw for simulating deformation in the midsagittal and parasagittal planes,” in *Journal of the Acoustical Society of America*, vol. 102, p. 3167(A), 1997.
- [37] T. S. Denney Jr. and E. R. McVeigh, “Model-free reconstruction of three-dimensional myocardial strain from planar tagged MR images,” *J. Magn. Res. Imag.*, vol. 7, pp. 799–810, 1997.

- [38] J. A. Derbyshire and N. F. Osman, “Cardiac motion encoding using harp and DENSE: Tagging or phase contrast,” p. 1875, 2001.
- [39] L. Desponds, C. Depeursinge, M. Grecescu, C. Hessler, A. Samiri, and J. F. Valley, “Image quality index (iqi) for screen-film mammography,” *Phys. Med. Biol.*, vol. 36, no. 1, pp. 19–33, 1991.
- [40] D. Dick, C. Ozturk, A. Douglas, E. McVeigh, and M. Stone, “Three-dimensional tracking of tongue motion using tagged-MRI,” in *International Society for Magnetic Resonance in Medicine, 8th Scientific Meeting and Exhibition*, 2000. Denver.
- [41] T. Edvardsen, B. D. Rosen, L. Pan, M. Jerosch-Herold, S. Lai, W. G. Hundley, S. Sinha, R. A. Kronmal, D. A. Bluemke, and J. A. Lima, “Regional diastolic dysfunction in individuals with left ventricular hypertrophy measured by tagged magnetic resonance imagingthe multi-ethnic study of atherosclerosis (mesa),” *American Heart Journal*, vol. 151, no. 1, pp. 109–114, 2006.
- [42] O. Engwall, “Modeling of the vocal tract in three dimensions,” in *Proceedings of the Eurospeech Meeting*, pp. 113–116, 1999.
- [43] O. Engwall, “A revisit to the application of MRI to the analysis of speech production - testing our assumptions,” in *6th international seminar on speech production*, 2003.
- [44] F. H. Epstein and W. D. Gilson, “Displacement-encoded cardiac MRI using cosine and sine modulation to eliminate (cansel) artifact-generating echoes.,” *MRM*, vol. 52, no. 4, pp. 774–81, 2004.
- [45] L. M. Fink, “Relations between the spectrum and instantaneous frequency of a signal,” *Problemy Perekachi Informatsii*, vol. 2, no. 4, pp. 26–38, 1966.
- [46] S. E. Fischer, G. C. McKinnon, S. E. Maier, and P. Boesiger, “Improved myocardial tagging contrast,” *Mag. Res. Med.*, vol. 30, pp. 191–200, 1993.
- [47] D. J. Fleet and A. D. Jepson, “Stability of phase information,” *PAMI*, vol. 15, no. 12, p. 1253, 1993.

- [48] R. Franke, “Scattered data interpolation: test of some methods,” *Mathematics of Computation*, vol. 38, no. 157, pp. 181–200, 1982.
- [49] G. Freeman, M. M. LeWinter, R. E. Engler, and J. W. Covell, “Relationship between myocardial fiber direction and segment shortening in the mid-wall of the canine left ventricle,” *Circ. Res.*, vol. 56, pp. 31–39, 1985.
- [50] J. Garot, D. A. Bluemke, N. F. Osman, C. E. Rochitte, B. L. Gerber, J. L. Prince, and J. A. Lima, “Detailed analysis of transmural lv function and recruitable myocardial deformation in subendocardial vs transmural infarcts using tagged-MRI,” *Circulation*, vol. 102, Oct. 2000.
- [51] J. Garot, D. A. Bluemke, N. F. Osman, C. E. Rochitte, E. A. Zerhouni, J. L. Prince, and J. A. Lima, “Transmural contractile reserve after reperfused myocardial infarction in dogs,” *J. Amer. Coll. Cardiol.*, vol. 36, no. 7, 2000.
- [52] D. C. Ghiglia and L. A. Romero, “Robust two dimensional weighted and unweighted phase unwrapping that uses fast transforms and iterative methos,” *Journal of Optical society of America A*, vol. 11, pp. 107–117, January 1994.
- [53] M. J. W. Gotte, A. C. van Rossum, J. W. R. Twisk, J. P. A. Kuijer, J. T. Marcus, and C. A. Visser, “Quantification of regional contractile function after infarction: strain analysis superior to wall thickening analysis in discriminating infarct from remote myocardium,” *Journal of the American College of Cardiology*, vol. 37, no. 3, pp. 808–817, 2001.
- [54] H. Gray, *Gray's Anatomy*. 1980.
- [55] W. Grossman, “Assessmen of regional myocardial function,” *J. Am. Coll. Cardiol.*, vol. 7, no. 2, pp. 327–238, 1986.
- [56] M. A. Guttman, J. L. Prince, and E. R. McVeigh, “Tag and contour detection in tagged MR images of the left ventricle,” *IEEE Transactions on Medical Imaging*, vol. 13, pp. 74–88, Mar. 1994.

- [57] E. Heijman, G. J. Strijkers, J. Habets, B. Janssen, and K. Nicolay, “Magnetic resonance imaging of regional cardiac function in the mouse,” *MAGMA*, vol. 17, pp. 170–178, 2004.
- [58] D. A. Herzka, M. A. Guttman, and E. R. McVeigh, “Myocardial tagging with SSFP,” *Magnetic Resonance in Medicine*, vol. 49, pp. 329–340, 2003.
- [59] B. R. Hunt, “Super-resolution of images: Algorithms, principles, performance,” *International Journal of Imaging Systems and Technology*, vol. 6, pp. 297–304, 1995.
- [60] P. J. Hunter, “Myocardial constitutive laws for continuum mechanics models of the heart.,” *Adv Exp Med Biol*, vol. 382, pp. 303–18, 1995.
- [61] P. J. Hunter, A. D. McCulloh, and H. E. ter Keurs, “Modelling the mechanical properties of cardiac muscle,” *Prog Biophys Mol Biol*, vol. 69, no. 2-3, pp. 289–331, 1998.
- [62] P. J. Hunter and B. H. Smaill, “The analysis of cardiac function: a continuum approach,” *Prog Biophys Mol Biol*, vol. 52, no. 2, pp. 101–64, 1988.
- [63] D. Iny, A. Lundberg, W. S. Levine, and M. Stone, “The dynamics and control of the tongue during speech,” in *Proceedings of the ACC*, pp. 246–251, 2001.
- [64] W. is a Multicomponent Signal?, “L. cohen,” in *Proceedings of the IEEE*, pp. V113–V116, 1992.
- [65] E. H. Isaaks and R. M. Srivastava, *An introduction to Applied Geostatistics*. New York, NY: Oxford University Press, 1989.
- [66] E. Keller and D. J. Ostry, “Computerized measurement of tongue dorsum movements with pulsed-echo ultrasound.,” *Journal of the Acoustical Society of America*, vol. 73, pp. 1309–1315, 1983.
- [67] J. T. Kent and K. V. Mardia, “The link between kriging and thin-plate splines,” in *Probability, Statistics and Optimization – A Tribute to Peter Whittle*, pp. 325–338, John Wiley and Sons, 1994.

- [68] W. S. Kerwin, *Space-Time Estimation of left Ventricular Motion from Tagged Magnetic Resonance Images*. PhD thesis, Johns Hopkins University, 1999.
- [69] W. S. Kerwin, N. F. Osman, and J. L. Prince, “Image processing and analysis in tagged cardiac MRI,” *Handbook of Medical Image Processing*, pp. 375–392, 2000.
- [70] W. S. Kerwin and J. L. Prince, “Kriging filter for space-time interpolation,” *Advances in Imaging and Electron Physics*, vol. 124, pp. 139–193, 2002.
- [71] W. M. Kier and K. K. Smith, “Tongue, tentacles and trunks: the biomechanics of movement in muscular-hydrostats,” *Zoological Journal of the Linnean Society*, vol. 83, pp. 307–324, 1985.
- [72] D. Kim, W. D. Gilson, C. M. Kramer, and F. H. Epstein, “Myocardial tissue tracking with two-dimensional cine displacement-encoding MR imaging: Development and initial evaluation,” *Radiology*, vol. 230, pp. 862–871, 2004.
- [73] S. Kim, C. Ozturk, and G. Chi-Fishman, “Application of tagged MRI in the study of synergistic actions of lingual muscles during contraction tasks,” in *Proc of ISMRM*, p. 1514, 2004.
- [74] P. K. Kitanidis, *Introduction to Geostatistics*. Cambrige, UK: Cambrige University Press, 1997.
- [75] A. L. Klatsky, “Moderate drinking reduced risk of heart disease,” *Alcohol Research and Health*, vol. 23, 1999.
- [76] D. L. Kraitchman, S. Sampath, E. Castillo, J. Derbyshire, R. C. Boston, D. A. Bluemke, B. L. Gerber, J. L. Prince, and N. F. Osman, “Quantitative ischemia detection during cardiac magnetic resonance stress testing by use of fastsharp,” *Circulation*, vol. 107, pp. 2025–30, Apr. 2003.
- [77] C. M. Kramer, W. J. Rogers, T. M. Theobald, T. P. Power, G. Geskin, and N. Reichek, “Dissociation between changes in intramyocardial function and left ventricular volumes in the eight weeks after first anterior myocardial infarction,” *Journal of the American College of Cardiology*, vol. 30, pp. 1625–1632, 1997.

- [78] J. P. Kuijer, E. Jansen, J. T. Marcus, A. C. V. Rossum, and R. M. Heethaar, “Improved harmonic phase myocardial strain maps,” *Magnetic Resonance in Medicine*, vol. 46, no. 5, pp. 993–999, 2001.
- [79] W. M. Lai, D. Rubin, and E. Krempl, *Introduction to Continuum Mechanics*. Butterworth-Heinemann, 1996.
- [80] W. M. Lai, D. Rubin, and E. Krempl, *Introduction to Continuum Mechanics*. Butterworth-Heinemann, 1996.
- [81] P. Lancaster and K. Salkauskas, *Curve and Surface Fitting - An Introduction*. London, UK: Academic Press, 1986.
- [82] B. P. Lathi, *Modern Digital and Analog Communications Systems*. New York, USA: Oxford Press, 1998.
- [83] W. S. Levine and C. E. Torcaso, “Controlling the shape of a muscular hydrostat: a tongue or tentacle.” to appear in New Directions in Control Theory and Applications.
- [84] M. M. LeWinter, R. S. Kent, J. M. Kroener, T. E. Carew, and J. W. Covell, “Regional differences in myocardial performance in the left ventricle of the dog,” *Circ. Res.*, vol. 37, pp. 191–199, 1975.
- [85] M. Li, C. Kambhamettu, and M. Stone, “Snake for band edge extraction and its applications,” in *Intl. Conf. on Computers, Graphics and Imaging*, August 2003.
- [86] Z.-P. Liang and P. C. Lauterbur, *Principles of Magnetic Resonance Imaging*. SPIE Press, 2000.
- [87] A. N. Liberman, J. L. Weiss, B. I. Jugdutt, L. C. Becker, and M. L. Weisfeldt, “Two dimensional echocardiography and infarct size: relationship of regional wall motion and thickening to the extent of myocardial infarction in the dog,” *Circulation*, vol. 63, pp. 739–746, 1981.
- [88] W. Liu, J. Chen, S. Ji, J. S. Allen, P. V. Bayly, S. A. Wickline, and X. Yu, “Harmonic phase MR tagging for direct quantification of lagrangian strain in rat hearts after

- myocardial infarction,” *Magnetic Resonance in Medicine*, vol. 52, pp. 1282–1290, 2004.
- [89] C. H. Lorenz, J. S. Pastorek, and J. M. Bundy, “Delineation of normal human left ventricular twist throughout systole by tagged cine MRI,” *J Cardiovasc. Magn. Reson.*, vol. 2, no. 2, pp. 97–108, 2000.
- [90] P. J. Loughlin and B. Tacer, “Instantaneous frequency and the conditional mean frequency of a signal,” *Signal Processing*, vol. 60, pp. 153–162, 1997.
- [91] C. H. Lugo-Olivieri, C. C. Moore, M. A. Guttmann, J. A. C. Lima, E. R. McVeigh, and E. A. Zerhouni, “The effects of ischemia on the temporal evolution of radial myocardial deformation in humans,” *Radiology*, vol. 193, 1994.
- [92] A. J. Lundberg and M. Stone, “Three-dimensional tongue surface reconstruction: Practical considerations for ultrasound data,” *Journal of the Acoustical Society of America*, vol. 105, pp. 2858–2867, November 1999.
- [93] L. Mandel, “Interpretation of instantaneous frequencies,” *Am. J. of Physics*, vol. 42, pp. 840–846, Oct. 1974.
- [94] S. Masaki, M. Tiede, K. Honda, Y. Shimada, I. Fujimoto, Y. Nakamura, and N. Ninomiya, “MRI-based speech production study using a synchronized sampling method,” *J. Acoustic Science Japan*, vol. 20, pp. 375–379, 1999.
- [95] R. Mazhari and A. McCulloch, “Integrative models for understanding the structural basis of regional mechanical dysfunction in ischemic myocardium,” *Annals of Biomedical Engineering*, vol. 28, pp. 979–990, 2000.
- [96] A. McCulloch and R. Mazhari, “Regional myocardial mechanics: Integrative computational models of flow-function relations,” *Journal of Nuclear Cardiology*, vol. 8, no. 4, pp. 506–19, 2001.
- [97] E. R. McVeigh, F. W. Prinzen, B. T. Wyman, J. E. Tsitlik, H. R. Halperin, and W. C. Hunter, “Imaging asynchronous mechanical activation of the paced heart with tagged MRI,” *Magn. Res. Med.*, vol. 39, pp. 507–513, 1998.

- [98] T. Moser and M. Smith, “A dante tagging sequence for the evaluation of translation sample motion,” *Magn. Reson. Med.*, vol. 2, pp. 334–339, 1990.
- [99] E. Nagel, M. Stuber, M. Lakatos, M. Scheidegger, P. Boesiger, and O. M. Hess, “Cardiac rotation and relaxation after anterolateral myocardial infarction,” *Coronary Artery Disease*, vol. 11, no. 3, pp. 261–267, 2000.
- [100] E. Nagel, M. Stuber, C. Matter, M. Lakatos, P. Boesiger, and O. M. Hess, “Rotational and translational motion of the heart after myocardial infarction,” *J. Cardiovasc. Pharm.*, vol. 28, no. Suppl. 2, 1996.
- [101] V. J. Napadow, Q. Chen, V. J. Wedeen, and R. J. Gilbert, “Biomechanical basis for lingual muscular deformation during swallowing,” *American Journal of Physiology*, vol. 277, pp. G695–G701, 1999.
- [102] V. J. Napadow, Q. Chen, V. J. Wedeen, and R. J. Gilbert, “Intramural mechanics of the human tongue in association with physiological deformations,” *Journal of Biomechanics*, vol. 322, pp. 1–12, 1999.
- [103] S. Narayanan, K. Nayak, S. Lee, A. Sethy, and D. Byrd, “An approach to real-time magnetic resonance imaging for speech production,” *J. Acoust. Soc. Amer.*, pp. 1771–1776, 2004.
- [104] M. NessAiver and J.L.Prince, “Magnitude image cspamm reconstruction (MICSR),” *Magnetic Resonance in Medicine*, vol. 50, pp. 331–42, Aug. 2003.
- [105] M. NessAiver and J. L. Prince, “Visualization of myocardial motion using MICSR trinary checkerboard display,” in *Inf. Processing in Medical Imaging*, vol. 18, pp. 573–85, July 2003.
- [106] W. Nho and P. J. Loughlin, “When is instantaneous frequency the average frequency at each time,” *IEEE Signal Processing Letters*, vol. 6, no. 4, pp. 78–80, 1999.
- [107] M. Niitsu, M. Kumada, G. Campeau, S. Niimi, S. J. Riederer, and Y. Itai, “Tongue displacement: visualization with rapid tagged magnetization-prepared MR imaging,” *Radiology*, vol. 191, pp. 578–580, 1994.

- [108] D. Nishimura, *Principles of Magnetic Resonance Imaging*. 1996.
- [109] N. F. Osman, *Measuring regional cardiac function using harmonic phase magnetic resonance imaging*. Electrical and computer engineering, Johns Hopkins University, Baltimore, MD, Feb. 2002.
- [110] N. F. Osman, W. S. Kerwin, E. R. McVeigh, and J. L. Prince, “Cardiac motion tracking using CINE harmonic phase (HARP) magnetic resonance imaging,” *Mag. Res. Med.*, vol. 42, pp. 1048–1060, 1999.
- [111] N. F. Osman, E. R. McVeigh, and J. L. Prince, “Imaging heart motion using harmonic phase MRI,” *IEEE Trans. Med. Imag.*, vol. 19, pp. 186–202, March 2000.
- [112] N. F. Osman and J. L. Prince, “Visualizing myocardial function using HARP MRI,” *Phys. Med. Biol.*, vol. 45, pp. 1665–1682, June 2000.
- [113] N. F. Osman and J. L. Prince, “Improving HARP to produce smooth strain maps of the heart,” in *Proceedings of the International Society of Magnetic resonance in medicine*, p. 605, 2001.
- [114] C. Ozturk and E. R. McVeigh, “Four-dimensional b-spline based motion analysis of tagged MR images: introduction and *in vivo* validation,” *Physics in Medicine and Biology*, vol. 45, pp. 1683–1702, 2000.
- [115] L. Pan, J. L. Prince, J. A. C. Lima, and N. F. Osman, “Fast tracking of cardiac motion using 3D-harp,” *IEEE Transactions on biomedical Engineering*, vol. 52, no. 8, pp. 1425–1435, 2005.
- [116] R. Parrot, M. R. Stytz, P. Amburn, and D. Robinson, “Towards statistically optimal interpolation for 3-d medical imaging,” *IEEE Eng. in Medicine and Biology*, pp. 49–59, September 1993.
- [117] V. Parthasarathy, M. NessAiver, J. L. Prince, and M. Stone, “Tracking tongue motion from tagged magnetic resonance images using harmonic phase imaging (HARP-MRI),” in *Proc. of 15th Intl. Cong. of Phonetic Sciences*, Aug. 2003.

- [118] V. Parthasarathy and J. L. Prince, “Artifact reduction in harmonic phase (HARP) strain maps,” in *Proceedings of the International Society of Magnetic resonance in medicine*, 2004.
- [119] V. Parthasarathy and J. L. Prince, “Dynamic range of harmonic phase magnetic resonance imaging (harp-MRI),” in *Proceedings of the International Society of Biomedical Imaging*, 2004.
- [120] V. Parthasarathy and J. L. Prince, “Strain resolution from HARP-MRI,” in *Proceedings of the International Society of Magnetic resonance in medicine*, 2004.
- [121] V. Parthasarathy and J. L. Prince, “Harp-mri detectability contrast detail analysis using simulations,” in *Proceedings of the International Society of Magnetic resonance in medicine*, 2005.
- [122] V. Parthasarathy, M. Stone, and J. L. Prince, “Spatiotemporal visualization of the tongue surface using ultrasound and kriging (surfaces),” *Clinical Linguistics and Phonetics*, vol. 19(6-7), pp. 529–544, 2005.
- [123] P. M. Pattynama and A. D. Roos, “MR evaluation of myocardial ischemia and infarction,” *Top. Mag. Res. Imag.*, vol. 7, no. 4, pp. 218–231, 1995.
- [124] L. R. Pelc, J. Sayre, K. Yun, L. J. Castro, R. J. Herfkens, D. C. Miller, and N. J. Pelc, “Evaluation of myocardial motion tracking with cine-phase contrast magnetic resonance imaging,” *Investigative Radiology*, vol. 29, no. 12, pp. 1038–1042, 1994.
- [125] N. Pelc, R. Herfkens, A. Shimakawa, and D. Enzmann, “Phase contrast cine magnetic resonance imaging,” *Magnetic Resonance Quarterly*, vol. 7, no. 4, pp. 229–254, 1991.
- [126] N. J. Pelc, F. G. Sommer, D. R. Enzmann, L. R. Pelc, and G. H. Glover, “Accuracy and precision of phase-contrast MR flow measurements (abstr),” in *Radiology*, p. 181(P); 189.

- [127] B. W. Pogue, C. Willscher, T. O. McBride, U. L. Osterberg, and K. D. Paulsen, “Contrast-detail analysis for detection and characterization with near-infrared diffuse tomography,” *Medical Physics*, vol. 27, no. 12, pp. 2693–2700, 2000.
- [128] J. L. Prince and J. Links, *Medical Imaging Signals and Systems*. Upper Saddle River, N.J: Prentice Hall, 2005.
- [129] P. Radeva, A. Amini, and J. Huang, “Deformable B-solids and implicit snakes for 3D localization and tracking of MRI-SPAMM data,” vol. 66, no. 2, pp. 163–178, 1997.
- [130] J. O. Ramsay and B. W. Silverman, *Functional Data Analysis*. New York, USA: Springer, 1997.
- [131] S. Ryf, *2D and 3D Magnetic Resonance Myocardial Tagging for the Assessment of Cardiac Motion*. PhD thesis, Swiss Federal Institute of Technology, Zurich, 2004.
- [132] S. Ryf, K. V. Kissinger, M. A. Spiegel, P. Bornert, W. J. Manning, P. Boesiger, and M. Stuber, “Spiral MR myocardial tagging,” *Magnetic Resonance in Medicine*, vol. 51, pp. 237–242, 2004.
- [133] S. Ryf, M. A. Spiegel, M. Gerber, and P. Boesiger, “Myocardial tagging with 3D-cspamm,” *Journal of Magnetic Resonance Imaging*, vol. 16, pp. 320–325, 2002.
- [134] S. Sampath, *Magnetic Resonance Pulse Sequences for Rapid Imaging of Myocardial Motion and Strain*. PhD thesis, Johns Hopkins University, 2004.
- [135] S. Sampath, A. Derbyshire, N. F. Osman, E. Atalar, and J. L. Prince, “Real-time imaging of two-dimensional cardiac strain using a fastHARP pulse sequence,” *Magn. Res. Med.*, vol. 50, pp. 154–63, July 2003.
- [136] S. Sampath, N. F. Osman, and J. L. Prince, “Imaging the evolution of 3-d myocardial strains using a combined harp-senc MRI pulse sequence,” 2005.
- [137] S. Sampath, V. Parthasarathy, and J. L. Prince, “A phantom validation of the fashharp pulse sequence,” pp. 117–120, 2002.

- [138] S. Sampath and J. L. Prince, “3D tracking of cardiac material points using a combined slice-following harmonic phase (SF-HARP) magnetic resonance imaging approach,” 2004.
- [139] J. D. Schuijf, T. A. M. Kaandorp, H. J. Lamb, R. J. van der Geest, E. P. Viergever, E. E. van der Wall, A. de Roos, and J. J. Bax, “Quantification of myocardial infarct size and transmurality by contrast-enhanced magnetic resonance imaging in men,” *Am. J. of Cardiology*, vol. 94, pp. 284–288, 2004.
- [140] C. Shadle, M. Mohammad, J. Carter, and P. Jackson, “Dynamic magnetic resonance imaging: New tools for speech research,” in *Proceedings of the 14th Int. Cong. Phon. Sci.*, pp. 623–626, 1999.
- [141] Y. Shimada, I. Fujimoto, H. Takemoto, S. Takano, S. Masaki, K. Honda, and K. Takeo, “4d-mri using the synchronized sampling method,” *Jpn. J. Radiol. Technol.*, vol. 53, no. 12, pp. 1592–1598, 2002.
- [142] E. Slud, M. Stone, P. Smith, and M. G. Jr., “Principal components representation of the two-dimensional coronal tongue surface,” *Phonetica*, vol. 59, pp. 108–133, August 2002.
- [143] M. Stone, “Imaging the tongue and vocal tract,” *British Journal of Disorders of Communication*, vol. 26, pp. 11–23, 1991.
- [144] M. Stone, U. Crouse, and M. Sutton, “Exploring the effects of gravity on tongue motion using ultrasound image sequences,” in *J. Acoust. Soc. Am.*, vol. 111, p. 2476, May 2002.
- [145] M. Stone, E. P. Davis, A. S. Douglas, M. NessAiver, R. Gullapalli, W. S. Levine, and A. Lundberg, “Modelling the motion of the internal tongue from tagged cine-MR images,” *Journal of Acoustic Society of America*, vol. 109, no. 6, pp. 2974–2982, 2001.
- [146] M. Stone, E. P. Davis, A. S. Douglas, M. NessAiver, R. Gullapalli, W. Leving, and

- A. J. Lundberg, “Modeling tongue surface contours from cine-MRI images,” *J. of Speech Language and hearing research*, vol. 44, no. 5, pp. 1026–1040, 2001.
- [147] M. Stone, D. Dick, E. Davis, A. Douglas, and C. Ozturk, “Modelling the internal tongue using principal strains,” in *Proceedings of the 5th Speech Production Seminar, Kloster-Seeon*, pp. 133–136, 2000. Germany.
- [148] M. Stone, M. H. Goldstein, and Y. Zhang, “Principal component analysis of cross sections of tongue shapes in vowel production,” *Speech Communication*, vol. 22, pp. 173–184, 1997.
- [149] M. Stone, T. Shawker, T. Talbot, and A. Rich, “Cross-sectional tongue shape during the production of vowels,” *J. Acoust. Soc. Amer.*, vol. 83, no. 4, pp. 1586–1596, 1988.
- [150] B. H. Story, I. R. Titze, and E. A. Hoffman, “Vocal tract area functions from magnetic resonance imaging,” *J. of Acoust. Soc. Am.*, vol. 10, no. 3, pp. 537–554, 1996.
- [151] B. H. Story, I. R. Titze, and E. A. Hoffman, “Vocal tract area function for an adult female speaker based on volumetric imaging,” *J. of Acoust. Soc. Am.*, vol. 104, no. 1, pp. 471–487, 1998.
- [152] M. Stuber, M. A. Spiegel, S. E. Fischer, M. B. Scheidegger, P. G. Danias, E. M. Pedersen, and P. Boesiger, “Single breath-hold slice following cspamm myocardial tagging,” *MAGMA*, vol. 9, pp. 85–91, 1999.
- [153] H. Takemoto *Journal of Speech, Language, and Hearing Research*, vol. 44, pp. 95–107, 2001.
- [154] C. Tang, D. D. Blatter, and D. L. Parker, “Accuracy of phase-contrast flow measurements in the presence of partial-volume effects,” *Journal of Magnetic Resonance Imaging*, vol. 3, pp. 377–385, 1993.
- [155] H. Theil, *Applied Economic Forecasting*. Amsterdam: North-Holland Publishing Company, 1966.

- [156] J. Tsao and D. Laurent, “N-spamm for efficient displacement-encoded acquisition in myocardial tagging,” in *Proceedings of the International Society of Magnetic resonance in medicine*, 2005.
- [157] Z. Wang and A. C. Bovik, “A universal image quality index,” *IEEE Signal Processing Letters*, vol. 9, no. 3.
- [158] G. S. Waston, “Smoothing and interpolation by kriging and with splines,” *Math. Geo.*, vol. 16, no. 6, pp. 601–615, 1984.
- [159] V. J. Wedeen, “Magnetic resonance imaging of myocardial kinematics: Techniques to detect, localize, and quantify the strain rates of the active human myocardium,” *Magn. Reson. Med.*, vol. 27, pp. 52–67, 1992.
- [160] V. J. Wedeen, R. M. Weisskoff, and B. P. Poncelet, “MRI signal void due to in-plane motion is all-or-none,” *Magnetic Resonance in Medicine*, vol. 32, pp. 116–120, 1994.
- [161] D. Wei and A. Bovik, “On the instantaneous frequencies of multicomponent am-fm signals,” *IEEE Signal Processing Letters*, vol. 5, pp. 84–86, April 1998.
- [162] B. Wein, S. Klajman, W. Huber, and W. H. Doring, “Ultrasound examination of co-ordination disorders of the tongue during swallowing,” *Nervenzart*, vol. 59, pp. 154–158, 1988.
- [163] R. L. Wolf, R. L. Ehman, S. J. Riederer, and P. J. Rossman, “Analysis of systematic and random error in MR volumetric flow measurements,” *Magnetic Resonance in Medicine*, vol. 30, pp. 82–91, 1993.
- [164] A. A. Young, D. L. Kraitchman, L. Dougherty, and L. Axel, “Tracking and finite element analysis of stripe deformation in magnetic resonance tagging,” *IEEE Trans. Med. Imag.*, vol. 14, pp. 413–421, Sept. 1995.
- [165] E. A. Zerhouni, D. M. Parish, W. J. Rogers, A. Yangand, and E. P. Shapiro, “Human heart: tagging with MR imaging – a method for noninvasive assessment of myocardial motion,” *Radiology*, vol. 169, pp. 59–63, 1988.

- [166] Y. Zhu, M. Drangova, and N. J. Pelc, “Estimation of deformation gradient and strain from cine-pc velocity data,” *IEEE Transactions on Medical Imaging*, vol. 16, no. 6, pp. 840–851, 1997.

Vita

Vijay Parthasarathy was born in Thiruvananthapuram, India on October 21, 1977. He received his B.E. degree in Electrical and Electronics Engineering from Sri Venkateswara College of Engineering, University of Madras, India 1999. He received his M.S.E degree in Electrical and Computer Engineering from the Johns Hopkins University, in Baltimore, MD in 2001. He is currently pursuing a Ph.D degree in Electrical and Computer Engineering at the Johns Hopkins University. His research interests include cardiovascular imaging, vocal-tract imaging, medical image analysis, and signal processing.